Understanding and optimising the formation of local chemical heterogeneities in large forging ingots used by the nuclear industry

Lucie Gutman

Understanding and optimising the formation of local chemical heterogeneities in large forging ingots used by the nuclear industry

THÈSE

soutenue le 16 Juillet 2024

pour l'obtention du

Doctorat de l'Université de Lorraine

spécialité Sciences des Matériaux

par

Lucie Gutman

Composition du jury

Président :	Denis Najjar	LaMcube, Villeneuve-d'Ascq, France
Rapporteurs :	Henri Nguyen Thi	IM2NP, Marseille, France
	Menghuai Wu	Montanuniversität, Leoben, Autriche
Examinatrice :	Oriane Senninger	CEMEF, Sophia Antiposlis, France
Invités :	Jean Cauzid	GeoRessources, Nancy, France
	Arthur Marceaux dit Clément	Framatome, Courbevoie, France
	François Roch	Framatome, Courbevoie, France
Directeur :	Julien Zollinger	IJL, Nancy, France
Co-directeurs :	Miha Založnik	IJL, Nancy, France
	Jacob Kennedy	IJL, Nancy, France

Aux gens cools,
A Maman et Papa.

A Mamie Lucette,
merci de m'avoir emmené à la piscine,
j'ai adoré ça, d'lascousse c'est devenu une habitude.

Acknowledgements

Vous être sur le point de lire les paragraphes de cette thèse qui ont été les plus édités. La n-ième version d'un truc qui ne sera jamais à la hauteur de mes attentes. Cet exercice des remerciements m'est si difficile car je suis consciente que seule je ne serai jamais arrivée au bout de cette thèse. Alors à face à cet exercice où il est question d'exprimer toute ma gratitude, j'ai essayé, échoué, pleuré, recommencé. Promis, cette fois les larmes n'étaient pas tristes.

Je tiens à commencer cet exercice par remercier mon jury. Dans une vie, on n'a qu'une soutenance de thèse (en général), j'ai beaucoup apprécié la mienne et c'est en partie grâce à vous. Henri Nguyen Thi et Menghuai Wu, mes rapporteurs, nos échanges étaient un plaisir pour moi. Mes remerciements vont également à Denis Najjar qui a accepté d'être le président de mon jury de thèse. Enfin Oriane Senninger, j'espère avoir été à la hauteur pour votre premier jury de thèse. J'ai eu la chance de présenter mes travaux face à un jury au complet, présent dans cette salle avec moi, je vous remercie tous et toutes d'avoir fait le déplacement, lu mon manuscrit, et de m'avoir posé des questions intéressantes qui m'ont permis de pousser encore plus loin ma réflexion sur mes travaux.
J'aimerai également remercier mes directeurs de thèse: Julien et Miha. Merci de m'avoir fait confiance pour ce projet de thèse et de m'avoir accompagnée pendant cette aventure. Grâce à vous j'ai repoussé mes limites pendant presque 4 ans, participé à plusieurs conférences, collaboré avec de multiples équipes sur des sujets toujours plus variés, voyagé de l'autre côté de l'océan, appris tant de choses. Je vous remercie pour ce projet si enrichissant.
Il y a ceux qui était là dès le début et il y a ceux qui vous rejoignent en cours de route. Jacob, tu as été pour moi le co-encadrant surprise: la personne "pas prévue" et qui devient un grand soutien dans une aventure difficile. Je te remercie pour nos cafés du lundi, le petit avocatier, les recettes de boulettes sans viande, les encouragements et les conseils avisés.
François, je te remercie d'avoir fait naître ce projet de thèse et de m'avoir fait confiance pour le mener à bien. Travailler avec toi et Arthur était très agréable, toujours enrichissant et intéressant. Grâce à vous je me sentais toujours la bienvenue à la Tour et ça voulait dire beaucoup pour moi.

Sur cette thèse, de nombreuses personnes ont collaboré. C'est en partie grâce à elles que j'ai pu fournir un travail dont je suis fière. À ce titre, je souhaite remercier:

- Laurent et Mélodie (CRMC, Industeel) pour m'avoir accueillie au CRMC pour discuter de préparation d'échantillons, me donner des astuces et d'avoir même préparé quelques échantillons pour moi.
- Jean, Lise et Andreï (GeoRessources, Université de Lorraine) grâce à qui j'ai pu réaliser les analyses en µXRF. Merci pour l'accueil chaleureux, votre curiosité pour mon sujet, la formation sur la µXRF et votre présence pour répondre à mes nombreuses questions.
- Laurent (CRMC, Industeel), Miha et Ahmed (IJL, Université de Lorraine) d'avoir réalisé les simulations SOLID qui ont servi de base à mon chapitre 5.
- Nicolas, Théo et Maxi (PCM, Framatome) d'avoir réalisé les essais de forgeage numérique ce qui m'a permis d'écrire mon chapitre 6 et d'ouvrir la voie vers de nouvelles perspectives.

On parle souvent de la thèse comme d'une aventure solitaire, c'est peut-être le cas de certain.es. Ma chance a été de trouver des personnes fantastiques pour m'accompagner le long de ce chemin solitaire, difficile et effrayant.
Jules, Maman et Papa, je vous remercie sincèrement de m'avoir toujours encouragée, même lorsque vous ne compreniez pas forcément les trucs obscurs que je faisais (parfois, je ne comprenais pas non plus). J'ai aussi profité de vos vacances, souvent en dernière minute, et c'était une véritable bouffée d'air frais dans ma thèse. En plus de mes parents fantastiques et de mon petit frère bien trop grand, j'ai aussi été entourée de grand-parents merveilleux. Papy Joseph, Mamie Lucette, merci d'avoir toujours été mes fans N°1, d'avoir été là dans le meilleur et dans le pire et d'avoir essayé de comprendre ma thèse à maintes reprises (j'espère que mes explications à base de marbré au chocolat ont fini par vous convaincre).
Sur mon chemin, j'ai aussi rencontré une nouvelle famille, celle que l'on se construit: les amis. Vous êtes si nombreux.ses à m'avoir soutenue pendant ces années, je vais essayer de n'oublier personne, même si c'est peine perdue.
Il y a ceux avec qui j'ai partagé un bureau, le bureau de l'ambiance (ambiance Nöel et moulin rouge, le mix est stimulant). Hervé, merci pour les bruits, les blagues et la bonne humeur. Victor — un ange parti trop tôt (NB. Pour le lecteur, pas de panique. Il n'est pas décédé, il est juste devenu prof ;)) — merci d'avoir apporté tant de soleil et de style dans le bureau. Enfin, Hamid merci pour toutes nos conversations philosophiques (oui j'aurai dû écrire à ce moment, non je n'ai aucun regret).
Il y a aussi ceux qui m'ont montré la voie: Corentin et Quentin, merci d'avoir semé des lanternes sur le chemin, de m'avoir surveillée de loin et d'avoir été là dans les moments qui font peur. C'est en vous voyant réussir quelques mois avant moi que j'ai commencé à croire que je pouvais vous suivre, d'abord de l'EEIGM à l'IJL puis de l'IJL à l'après-thèse. J'ai hâte de travailler avec vous.
Il y a celle qui m'a montré à quel point les femmes étaient fortes: Laura, mon amie de l'EEIGM qui est restée à mes côtés tout du long de ma thèse, même après avoir déménagé à Toulouse. Laura, je suis devenue la personne que je suis grâce à toi, à ton soutien inconditionnel, à tes conseils ponctués de "oyyyéééé" et à nos nombreuses et longues conversations. Tu es l'une des femmes les plus inspirantes que je connaisse, être ton amie est un honneur.
Il y a aussi tout ceux qui ont réussi avant moi et qui m'ont accompagné. Clovis, merci d'avoir été mon guide dans les méandres de LaTeX, de m'avoir remonté le moral tant de fois et pour tout tes conseils si avisés. Sébastien — le meilleur régisseur — tu as apporté tant de joie et de rires dans mes pauses au labo et en plus tu as même ajouté une personne cool dans ma vie (coucou Pauline!), merci pour tout. Hélène, ma thèse sans toi n'aurait pas été la même, merci pour nos nombreux cafés — à l'IJL ou ailleurs — et tous tes conseils de lectures qui mettent en colère.
Il y a ceux qui ont affronté l'adversité à mes côtés: Marco, Kiki, je nous vois un peu comme des triplés de thèse. Avec vous, je n'étais pas seule, mais nous étions ensemble dans l'adversité de

l'écriture, chacun avec nos propres démons, mais toujours là les uns pour les autres. Kiki, merci de m'avoir accueillie dans ton bureau pour des sessions de rédactions en panique et d'avoir été si souvent mon taxi en sortant du bar. Marco, merci pour les tups, les brunchs, les relectures et les batailles contre LaTeX, sans toi et Clélia, ma thèse aurait été bien moins jolie.
Il y a ceux qui ont été là pour moi les collègues doctorants qui sont devenus des amis, une équipe de soutiens incroyable. Nathan, nos escapades piscine étaient mon échappatoire, merci d'avoir été un élève exemplaire, maintenant vient le temps de la suite: trouve tes disciples et montre leur la voie vers le 5-7-5-9. Corentin, merci de m'avoir ouvert la porte de chez toi si souvent, pour une soirée jeux, film ou juste nourriture gratuite. Mariam, merci de m'avoir organisé un anniversaire en 2h, c'était l'une de mes meilleures soirées d'anniversaire. Maxence, merci d'avoir été un voisin incroyable et le meilleur référent blagues de l'IJL.
Et enfin il y a Clélia. On parle trop souvent de l'amour romantique, mais pas assez de l'amour que l'on ressent pour une amie si proche (de toute manière, l'amour fait parti d'un continuum, mais bref c'est pas le propos ici). Clélia, merci d'avoir créé autour de moi une bulle de bonheur, de m'avoir donné un endroit safe (en réalité plusieurs, si on compte le sol de ton bureau, le sol de ton salon et le rebord de fenêtre de ta cuisine) pour devenir la personne que je suis aujourd'hui. Ma thèse fut une traversée mouvementée, risquée et effrayante, mais toi tu étais là, à briller plus fort encore quand j'étais dans le noir. Tu as pris soin de moi en me nourrissant physiquement à grand renfort de brunchs, petit déjeuners et tups, mais aussi intellectuellement avec des conversations qui ont changé à tout jamais ma vision du monde. Merci pour tout ça, les roulades, les life-hacks, les tups, les éclats de rire et toutes ces émotions partagées ensemble.

Il y a tous ceux qui étaient là.
Vous étiez si nombreux.
Vous êtes incroyables.
Merci les gens cools, je vous aime :)

Je les aime, mes amies.
Elles sont peu nombreuses.
Elles ont la rareté des choses précieuses.
Je les aime mais je ne leur dis jamais.
J'espère le leur montrer au moins,
sinon je ne comprends pas bien pourquoi
elles me supportent.

Serena Giuliano,
Ciao Bella

Contents

Résumé étendu en français

La construction et la mise en service d'EPR (Evolutionary Power Reactors) constituent la dernière innovation au sein de l'industrie nucléaire européenne. Les EPR ont été développés pour améliorer le rendement et la sécurité des centrales nucléaires. Au fur et à mesure des innovations, les cuves des générateurs de vapeurs nucléaires civils sont de plus en plus grandes. L'EPR n'est pas une exception avec le plus grand générateur de vapeur jamais conçu. Les différentes pièces du circuit primaire de l'EPR sont construites en partie de pièces forgées. Les pièces forgées sont réalisées dans la Forge Framatome située au Creusot à partir de lingots d'acier de nuance 16MND5, 18MND5 ou 20MND5. Avec l'augmentation de taille des réacteurs, la réalisation des pièces forgées nécessitent des lingots de plus en plus gros. L'augmentation de la taille des lingots change leur conditions de solidification, ce qui influence la formation des ségrégations chimiques au sein de ces lingots.
Les ségrégations chimiques sont des écarts entre la composition chimique nominale de l'acier et la composition chimique locale. La ségrégation des éléments d'alliage au sein des lingots d'aciers est un sujet complexe qui a déjà fait l'objet de nombreuses études. Toutefois celles-ci étaient le plus souvent focalisées sur la ségrégation à l'échelle dendiritique (la microségrégation) ou à l'échelle du lingot (la macroségrégation). Dans le cas de pièces massives, les ségrégations se forment durant la solidification et restent jusqu'à ce que l'acier refonde. Pour la construction de pièces destinées aux EPR, le forgeage ne fait pas disparaître les ségrégations mais il peut changer leur forme, leur distribution et éventuellement réduire leur intensité par diffusion. Seules des opérations de chutage peuvent supprimer certaines ségrégations, adaptées aux macroségrégations. Au contraire, les ségrégations à plus petite échelle ne peuvent pas être retirées par ce procédé et subsistent dans la pièce forgée. Elles peuvent avoir un effet délétère sur les propriétés mécaniques finales de la pièce forgée. Il est donc important et nécéssaire de comprendre la formation et la distribution des ségrégations à toutes les échelles dans ces gros lingots de forge afin d'optimiser les propriétés mécaniques finales des pièces.
De récentes études menées sur les pièces forgées utilisées pour la construction des EPR relèvent la présence de microstructures en bandes. Elles sont engendrées par la déformation des ségrégations chimiques durant le forgeage et causent une anistropie des propriétés mécaniques finales des pièces. En comparant les tailles des structures observées dans les pièces forgées et dans les lingots bruts de solidification, ainsi qu'en connaissant le ratio de forgeage, il est possible de montrer que les microstructures en bandes ne sont dues ni aux micro- ni aux macroségrégations, mais à des ségrégations d'échelle intermédiaire. Dans les gros lingots de forge, les ségrégations chimiques n'ont pas encore été caractérisées à cette échelle intermédiaire. C'est pourtant un point primordial pour la compréhension de la formation et de l'évolution de ces ségrégations.

Objectifs de la thèse

L'objectif principal de ce travail de thèse est de caractériser les ségrégations qui exsitent à l'échelle intermédiaire dans les gros lingots de forge, causant les filets de ségrégation dans les pièces forgées ou laminées. Pour cette étude, des échantillons ont été prélevés dans trois gros lingots de forge (de masse supérieure à 100 T). Ces lingots sont identiques à ceux utilisés pour la construction des EPR, mais ont été coulés spécifiquement pour fournir de la matière aux programmes de recherche en cours.
Les ségrégations à échelle intermédiaire n'ont encore jamais été étudiées dans ce type de lingot. Or la taille de ces lingots allonge leur temps de solidification, ce qui donne lieu à la formation de grandes structures de solidification (des dendrites centimétriques par exemple). Les ségrégations peuvent également être plus étendus dans ces gros lingots. La caractérisation de ces grandes ségrégations nécessite une caractérisation spatiale de la composition chimique à l'échelle centimétrique plutôt que mili- or micrométrique.
Pour atteindre cet objectif, plusieurs étapes sont nécessaires:

- Une méthode permettant de cartographier les ségrégations chimiques à l'échelle centimétrique doit être développée.
- Les ségrégations présentes à l'échelle intermédiaire doivent être caractérisées en 3D dans les gros lingots de forge.
- Les conditions de solidification, locales et globales, doivent être étudiées afin de comprendre la formation des ségrégations à l'échelle intermédiaire.
- Le comportement des ségrégations doit être étudié pendant le forgeage. Cette étude doit s'appuyer sur la simulation d'un forgeage et la comparaison des ségrégations simulées avec les ségrégrations caractérisées expérimentalement. L'idée est de comprendre quel type de ségrégation est à l'origine des filets de ségrégation dans les pièces forgées.

Chapitre 1

Le chapitre 1 présente les principales études référencées dans la littérature concernant les lingots forgés.
De nombreuses études ont été consacrées aux ségrégations qui apparaissent à différentes échelles lors de la solidification de lingots d'acier. À l'échelle dendritique, la formation de microségrégation est inévitable. Ce type de ségrégation a été étudié pendant des années et plusieurs modèles (analytiques, 1D) existent pour décrire ce phénomène. Les ségrégations à l'échelle du lingot (macroségrégations) sont bien connus. Deux types de macroségrégations co-existent au sein des lingots: les macroségrégations de masse (enrichissement en tête de lingot, cône de ségrégation en pied de lingot) et les macroségrégations localisées (veines sombres). Il est possible de réduire la présence des macroségrégations dans les pièces forgées et leur impact en adaptant le procédé de mise en forme (chutage de la tête et du pied du lingot, usinage choisi).
La simulation est un outil très employé pour la compréhension et la prédiction des macroségrégations (de masse et localisées). SOLID® est un logiciel commercial utilisé et développé par le secteur académique qui permet de modéliser la solidification de gros lingots. L'utilisation de ce logiciel permet de comparer l'impact des différents phénomènes physiques sur la formation des ségrégations. L'intérêt d'un outil de simulation robuste à l'échelle industrielle est de pouvoir comparer, à moindre coût, les différentes possibilités en terme de procédés et de guider le développement de nouveaux produits.
Dans l'industrie nucléaire, l'utilisation de traitement thermique pour homogénéiser les ségrégations des gros lingots de forges n'est pas envisageable: quelque soit leur échelle, il n'est pas possible industriellement d'homogénéiser la composition chimique des lingots. Les ségrégations subissent donc la mise en forme du lingot. Les opérations de forgeage ou de laminage changent leur taille, leur forme et parfois leur distribution dans le lingot, mais ne les éliminent pas (sauf en cas de chutage d'une partie de la matière).
Dans les pièces forgées ou les tôles laminées, des filets de ségrégation sont observés. Ces filets sont le résultat de la déformation (par forgeage ou laminage) des ségrégations présentes dans l'acier brut de solidification. Même si le processus de formation des filets de ségrégation n'est pas encore bien compris, leurs conséquences ont déjà été observées dans de nombreuses études: anisotropie des microstructures secondaires, anisotropie des propriétés mécaniques, diminution de la résilience dans la direction transverse. Les ségrégations à l'origine des filets de ségrégation semblent exister à petite échelle ou à l'échelle intermédiaire.
L'observation des ségrégations aux différentes échelles est une étape clé pour la compréhension de ces phénomènes. De nombreuses techniques ont été développées et utilisées pour la caractérisation des ségrégations. Certaines techniques sont adaptées à l'échelle du lingot et utilisées pour l'observation et la quantification des macroségrégations de masse. D'autres techniques sont plus adaptées à la caractérisation des microségrégations. Cependant, pour une caractérisation à l'échelle intermediaire, aucune technique phare ne semble exister.

Chapitre 2

Le deuxième chapitre présente les différents échantillons utilisés pour ce travail de thèse et les techniques de caractérisation et d'analyse employées.
Pour comprendre la structure de solidification des échantillons étudiés, des attaques ont été réalisées sur les échantillons afin de faire des macrographies (exemple en figure 1). Cette étape donne une première idée de la taille des structures de solidification à étudier et permet de prélever les échantillons adéquats pour l'étude.
La technique de caractérisation la plus employée dans cette thèse est la micro-fluorescence des rayons X (µXRF). Cette technique repose sur l'interaction rayonnement-matière. Un rayon X incident excite la surface de l'échantillon. En réponse à cette stimulation, les atomes de la surface émettent des photons X caractéristiques. Les photons X sont collectés par des détecteurs placés de part et d'autre de la source de rayons X. Le spectre d'émission est ensuite analysé, ce qui permet d'identifier les atomes en présence à la surface de l'échantillon étudié. La petite taille de sonde (20 µm) permet de cartographier la composition chimique d'un échantillon avec grande précision. La µXRF utilise des détecteurs EDS (Energy Dispersive Spectrometry), il est donc impossible de détecter des éléments légers tels que l'hydrogène, le carbone ou l'oxygène.

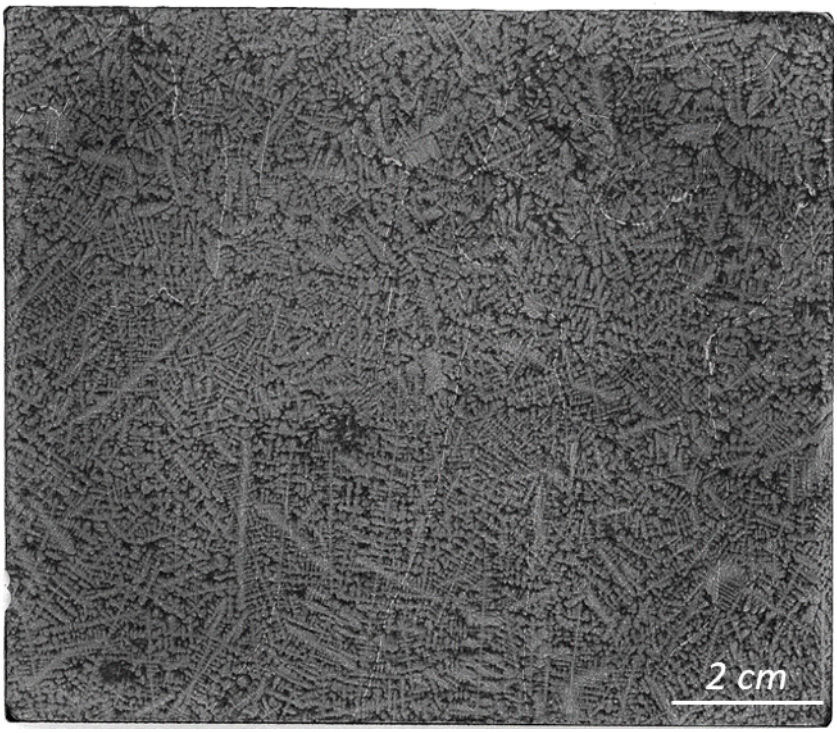

Figure 1: Macrographie de l'échantillon C2_1. Le solide appauvrit en soluté apparait en gris clair, les régions enrichies sont plus foncées. Les fines lignes brillantes sont les joints de grains austénitiques primaires.

Chapitre 3

Ce chapitre expose le processus suivis pour l'adoption d'une nouvelle technologie de caractérisation : durant cette thèse, une nouvelle méthodologie pour la caractérisation des ségrégations a été développée. L'étude de la bibliographie sur le sujet a mis en évidence le besoin d'une technique de caractérisation permettant de cartographier les ségrégations à l'échelle centimétrique. Pour répondre à ce besoin, nous avons choisi d'adapter une technique pré-existante et bien connue notamment dans le domaine de la géologie : la µXRF. L'adaptation de la µXRF au secteur de la métallurgie rend possible l'étude des ségrégations présentes dans des échantillons d'aciers centimétriques.
L'emploi d'une technique de caractérisation sur de nouveaux matériaux requière quelques ajustements. Trois aspects principaux ont été traités et sont documentés dans le manuscrit : la préparation des échantillons, les réglages du faisceau de rayons X incident et l'acquisition (le pas et le temps passé par point acquis). Toutes les conditions d'analyses ont été optimisées pour analyser des échantillons centimétriques d'acier faiblement allié. Les différents essais réalisés révèlent qu'un polissage au papier Si-C P800 (granulométrie de 21.8 µm) est suffisant pour l'analyse par µXRF. Les réglages du canon à rayons X ont été optimisés pour l'analyse du Mn et du Mo, les éléments d'intérêt pour cette étude. Pour réduire les artéfacts de mesure, le faisceau réglé à 200 µA, 50 keV était également filtré avec un filtre en aluminium de 100 µm d'épaisseur. Différents pas et temps d'analyse par point ont également été testés sur les échantillons de l'étude afin de déterminer les meilleures conditions. Avec un pas d'analyse de 100 µm, l'aspect visuel des cartographies de ségrégations obtenues est acceptable jusqu'à petite échelle (les dendrites sont observables), tout en conservant un nombre de point raisonnable. Pour ce qui est du temps d'acquisition par point, l'idée était de le maximiser tout en respectant une limite pratique : la possibilité d'analyser une plaquette en une nuit d'occupation machine (15 h dans notre cas). Le temps passé par point a donc été fixé à 45 ms.
L'utilisation de la µXRF pour la cartographie des ségrégations a été validée par comparaison avec des cartographies réalisées en microsonde de Castaing. Plusieurs échantillons ont été analysés avec les deux techniques avant comparaison. Les cartographies obtenues en µXRF présentent plus de bruit que les cartographies réalisées en microsonde de Castaing, mais les mêmes motifs de ségrégation sont obtenus. Les courbes de fraction solide cumulée des cartographies obtenues avec les deux techniques sont également similaires, ce qui valide l'utilisation de la µXRF pour l'analyse des ségrégations lorsque utilisée dans la conditions testées (faisceau: 200 µA, 50 keV, filtre Al 100µm, acquisition: 100 µm, 45 ms).
Avec cette nouvelle technique, rapide, facile d'utilisation et nécessitant peu de préparation d'échantillons, un grand nombre d'échantillon a pu être analysé. Plusieurs échantillons montrent la présence de canaux de ségrégation, comme montré dans la figure 2. Grâce à un prélèvement d'échantillon successif, il est possible d'observer l'évolution des canaux de ségrégation en fonction de la hauteur. Un traitement d'image en deux étapes (application d'un filtre gaussien et binéarisation) a été imaginé pour isoler les canaux de ségrégation du reste des ségrégations présentes sur les cartographies µXRF. Avec l'empilement de 30 cartographies traitées, nous avons pu reconstruire en 3D les différents types de ségrégation. Le volume reconstruit ($110 \times 95 \times 145\text{mm}^3$ pour $x \times y \times z$), figure 3, montre différentes échelles de ségrégations : d'un côté les canaux de ségrégations, centimétriques et continus d'un échantillon à l'autre et, de l'autre côté, des ségrégations intermédiaires ressemblant aux canaux de ségrégations sur les coupes 2D, mais n'étant pas continues d'un échantillon à l'autre.

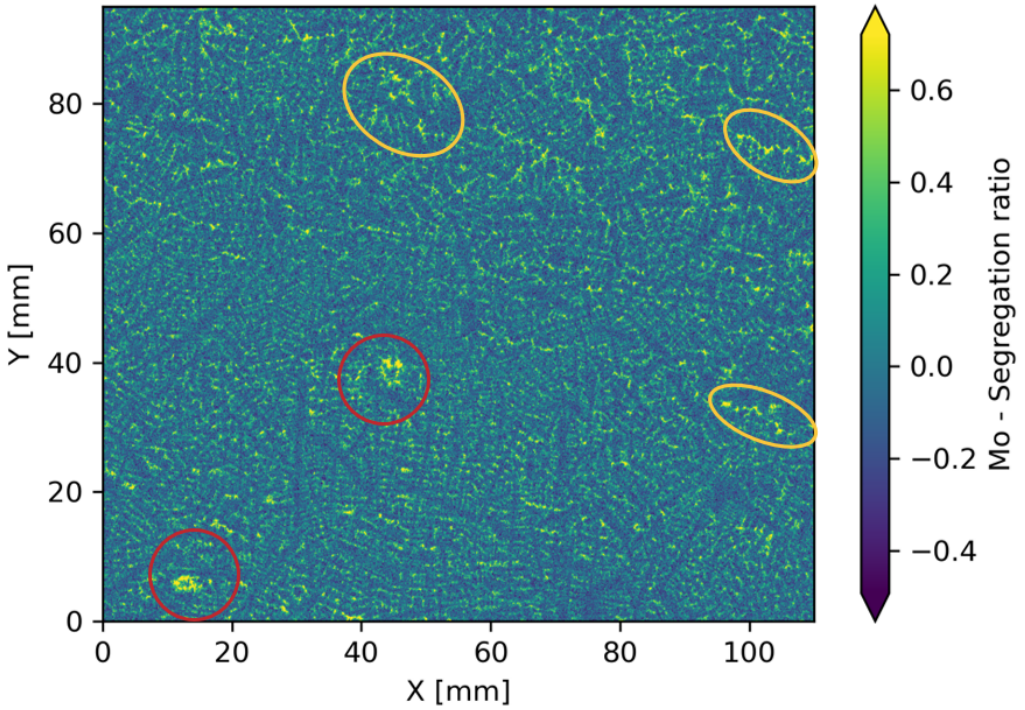

Figure 2: Cartographie des ségrégations en Mo sur l'échantillon C2_1. Les disques enrichit correspondant aux canaux de ségrégation sont entourés en rouge et les ségrégations d'échelle intermédiaire sont entourées en jaune.

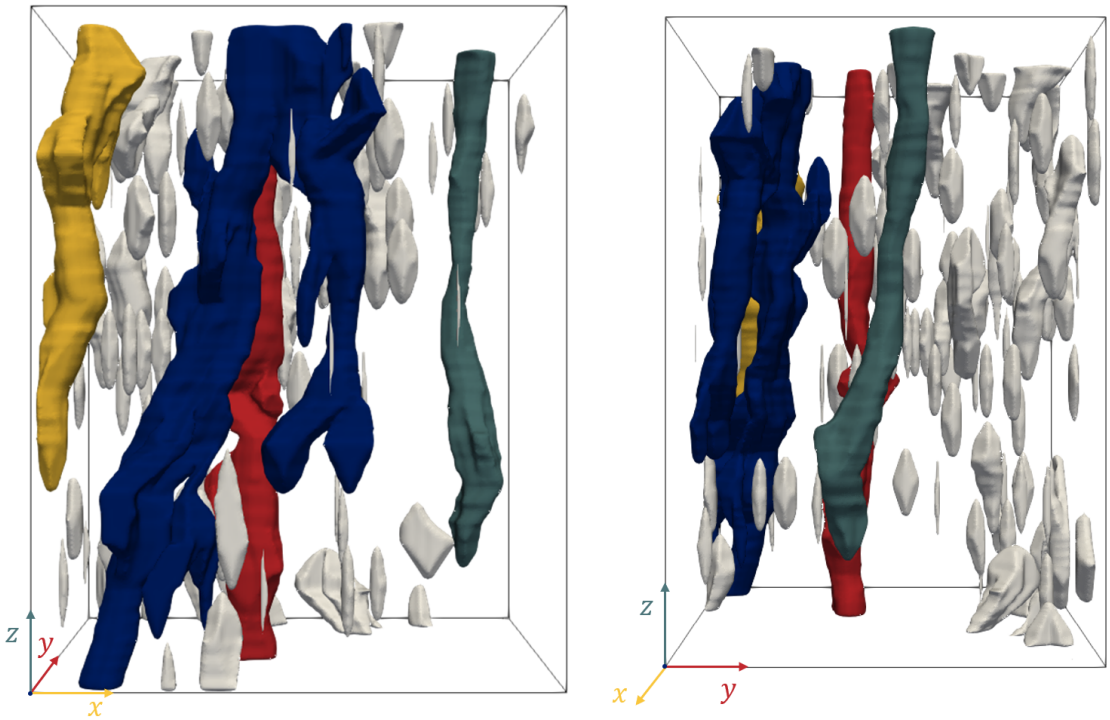

(a) Vue xz (b) Vue yz

Figure 3: Ségrégations selectionnées au court du traitement et reconstruites en 3D. L'axe y est parallèle au rayon et l'axe z pointe le haut du lingot. Les dimensions du volume représenté sont: $110 \times 95 \times 145\text{mm}^3$ pour $x \times y \times z$.

Chapitre 4

Dans le chapitre 4, la méthodologie développée dans le chapitre précédent et reposant sur l'utilisation de la µXRF est utilisée pour caractériser différents types de ségrégation. Cette technique a permis l'analyse en 3D de ségrégations sur des échantillons prélevés dans un lingot court (116 tonnes). D'autres échantillons ont été prélevés dans différents lingots afin de comprendre l'influence du type de lingot sur la formation des ségrégations.
L'observation 3D des canaux de ségrégations donne de nouvelles informations, notamment sur leur forme et leur distribution dans l'espace. Les canaux observés sont sinueux, ramifiés et parfois fusionnent ensemble. Cette représentation diffère de celle traditionnellement rapportée dans la littérature. En effet, la probabilité d'observer des ramifications ou la fusion de deux canaux ensemble est très faible lorsque l'on étudie des échantillons 2D. Les observations 2D réalisées sur des coupes de la reconstruction 3D des canaux montrent qu'il est également possible qu'un canal apparaisse discontinu en observation 2D en raison de leur forme complexe (comme démontré dans la figure 6).
Des canaux de ségrégation ont été observés dans les trois lingots étudiés (le lingot court de 116 t, le lingot long de 170 t et le lingot creux de 173 t). Pour les lingots court et long, la largeur des canaux observés est similaire et de l'ordre du centimètre. Dans le cas du lingot creux, les canaux observés sont légèrement plus petits. Cette observation pourrait être liée à deux effets: (1) l'observation a été faite en 2D et le canal pourrait avoir été coupé proche de son bord, la largeur observée n'est pas forcément le diamètre du canal mais pourrait être plus petite, (2) la taille des canaux de ségrégation est liée aux conditions locales de solidification, or dans les lingots creux le temps local de solidification est plus court que dans les lingots à solidification dirigée comme le lingot court et le lingot long.
A côté des canaux de ségrégations, des ségrégations d'échelle intermédiaire ont été observées. Il est difficile d'identifier ce type de ségrégation sur des échantillons 2D puisqu'en 2D elles pourraient aisément être confondues avec des canaux de ségrégations coupés par le plan d'observation. Les ségrégations d'échelle intermédiaire ont été observées dans le volume reconstruit en 3D, elles sont plus petites que les canaux de ségrégation mais présentent un aspect similaire dans le plan horizontal. Les ségrégations d'échelle intermédiaire mesurent environ 5 mm de diametre, avec un espacement de 5 mm entre les plans observés, il n'a pas été possible de les observer en 3D ou de déterminer avec précision leur forme.
La reconstruction 3D des canaux de ségrégation a également permis d'observer l'évolution de leur taille et de l'intensité de la ségrégation en fonction de leur hauteur. Les analyses conduites ne montrent aucune corrélation entre la hauteur au sein du canal et la taille des canaux ou l'intensité de la ségrégation.
Dans tous les lingots étudiés, des canaux de ségrégation ont été observés. Tous les canaux étaient inclinés par rapport au centre du lingot et localisés dans des zones de solidification équiaxe dendritique. Dans les quelques échantillons prélevés dans une zone équiaxe globulaire, ni canal de ségrégation, ni ségrégation d'échelle intermédiaire n'ont été observé.
Pour conclure, les analyses µXRF permettent une caractérisation 2D des ségrégations et des structures de solidification sur des échantillons centimétriques. Toutefois pour une compréhension complète de la forme et de l'orientation des canaux de ségrégation, une observation 3D est recommandée.

Figure 4: Image binaire obtenue après un traitement d'image (décrit dans le chapitre 3) réalisé sur la cartographie de ségrégations de l'échantillon C3_A.

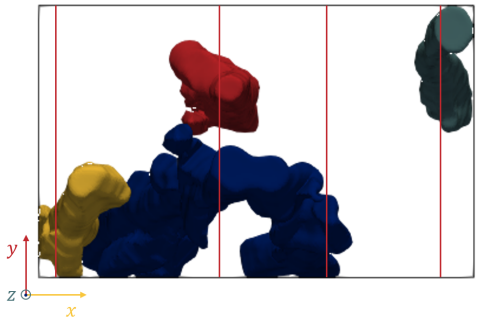

Figure 5: Emplacement des découpes verticales faite des canaux de ségrégation reconstruits en 3D pour les observations longitudinales et comparaisons avec l'échantillon C3_A.

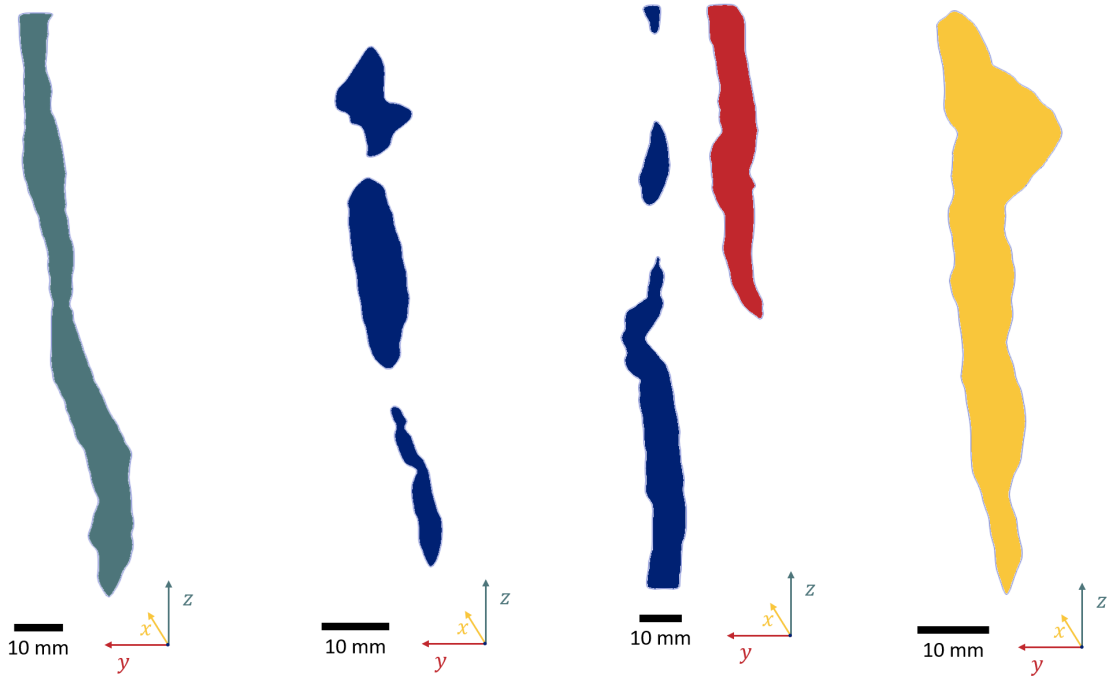

(a) (b) (c) (d)

Figure 6: Coupes verticales du volume reconstruit pour l'observation des canaux de ségrégation.

Chapitre 5

Ce chapitre utilise des simulations Solid® pour comprendre les conditions de solidification du lingot *court*. Dans les chapitres précédents (**??** et **??**), des canaux de ségrégation et des ségrégations d'échelle intermédiaire ont été caractérisées en 3D à partir d'échantillons prélevés sur le lingot *court*. La simulation permet de comprendre les conditions dans lesquelles ces ségrégations apparaissent au cours de la solidification. Les simulations Solid® ont été utilisées pour étudier d'un point de vue général la solidification du lingot, puis les conditions locales de solidification à la position C, où des ségrégations ont été observées.
La simulation de la solidification du lingot *court* indique un temps de solidification long (41 heures nécessaires pour atteindre la solidification complète). Le lingot se solidifie de l'extérieure vers le centre, radialement et de bas en haut. Au cours de la solidification, l'écoulement et du transport des grains de solide forme la macroségrégation. Les grains se déplacement dans le liquide avant de se bloquer mutuellement et de former un réseau cohérent. L'immobilisation des grains se produit progressivement de bas en haut, comme illustré sur la figure 7. Les grains immobiles ne bloquent pas l'écoulement du liquide qui continue de se produire au travers du réseau cohérent. La macroségrégation se forme pendant la solidification, c'est l'orientation relative de l'écoulement par rapport au gradient thermique qui détermine si cet écoulement cause une ségrégation, positive ou négative. La moindre variation d'orientation peut causer la formation de ségrégation.
Avec simulations Solid® nous avons pu étudier les conditions de solidification qui ont conduit à la formation de canaux de ségrégation et de ségrégation d'échelle intermédiaire à la position C dans le lingot *court*. La solidification du lingot *court* à l'emplacement C se déroule en 3 étapes, représenté sur la figure 8:

1. Dans un premier temps, les grains de solide se déplacent librement et le liquide s'écoule sans contrainte. Aucune ségrégation n'existe.

2. Puis les grains s'immobilisent, la température est constante et la fraction solide varie très peu pendant plusieurs heure: c'est le plateau de solidification (délimité par des lignes verticales jaunes sur la figure 8). Durant ce plateau, la composition est stable, l'écoulement du liquide et le gradient thermique sont faibles et ne cause pas de ségrégation.

3. Au bout d'un certain temps, le plateau se termine: la température chute, la fraction solide augmente. Le gradient thermique et la vitesse du liquide changent: ce qui créer des ségrégations.

C'est durant la dernière phase de la solidification que les canaux de ségrégation et les ségrégations d'échelle intermédiaire semblent se former. Pour confirmer cette hypothèse, les simulations Solid® pourraient être utilisées pour étudier l'évolution de critères de ségrégations en fonction du temps, de la température et de la fraction solide. Il pourrait être intéressant de comparer les critères de Flemings [1] et de Kumar [2].

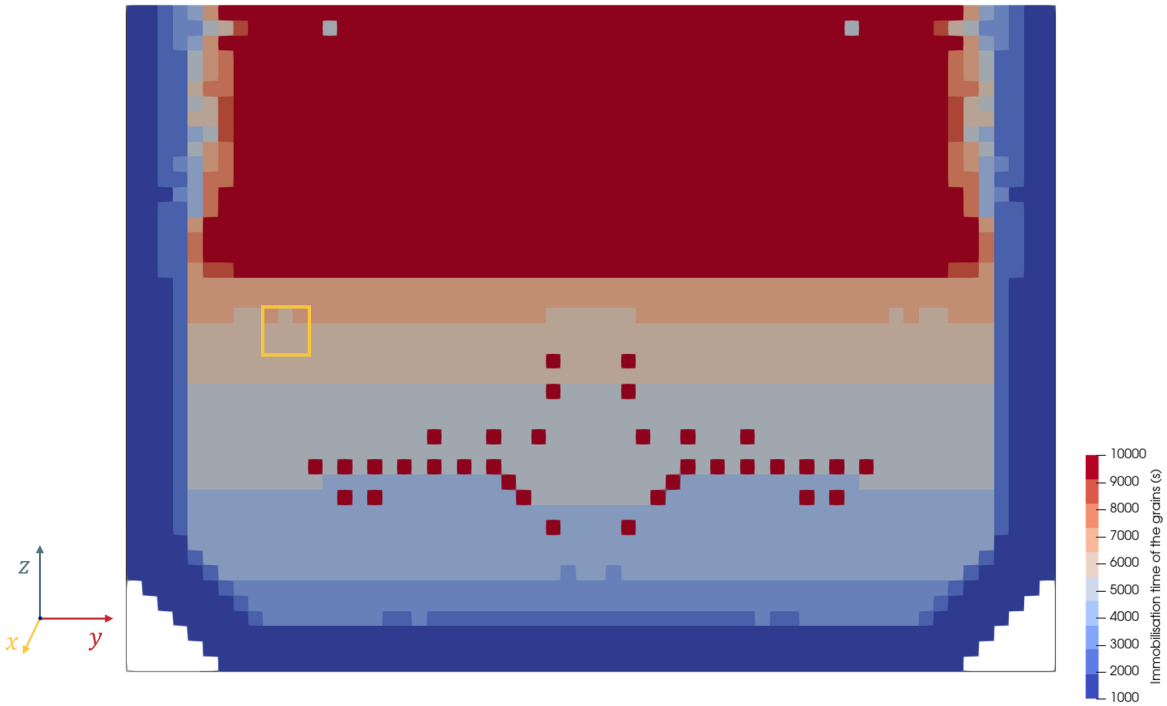

Figure 7: Prédictions du moment auquel les grains equiaxes s'immobilisent. L'échelle a été adaptée pour mettre en valeur les différences dans le partie inférieure du lingot.

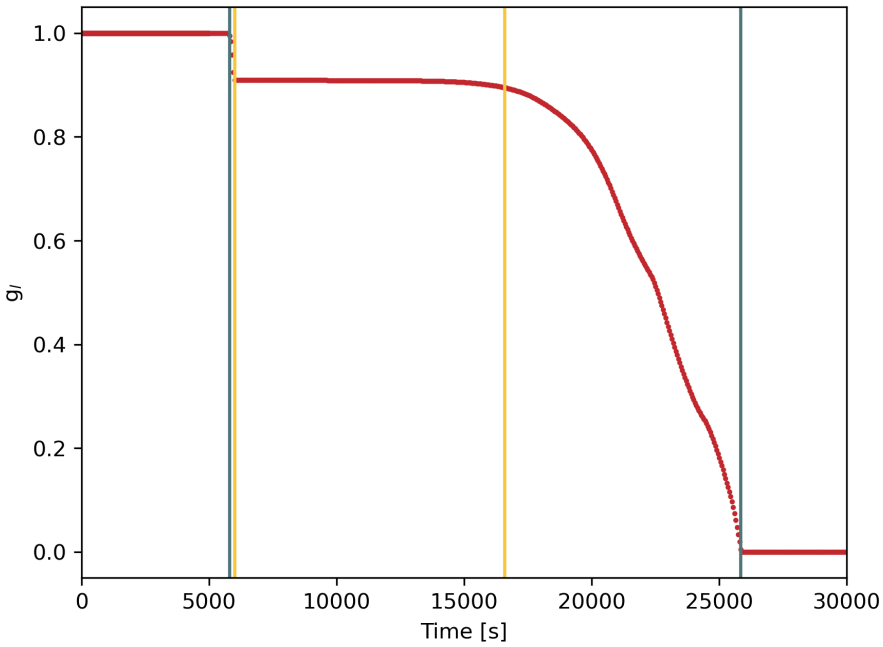

Figure 8: Zoom on the evolution of g_l with time in the cell 1502.

Chapitre 6

Dans le chapitre 6, l'aspect des ségrégations avant et après forgeage sont comparés. Deux approches différentes ont été employées et combinées afin d'étudier les effets du forgeage sur les ségrégations.
Dans un premier temps, des échantillons prélevés dans une pièces forgée (calotte de cuve) ont été analysés par µXRF afin de cartographier les ségrégations dans le matériau forgé. Les cartographies de ségrégations obtenues ont été traitées via un traitement d'image similaire à celui employé dans le chapitre 3 pour l'identification des ségrégations (canaux et d'échelle intermédiaire) sur les échantillons 2D. Cependant, le traitement d'image n'est pas adapté à l'observation et à la caractérisation des formes ellipsoïdales et déforme les ségrégations observées après forgeage.
La seconde approche employé est numérique: le logiciel Forge NxT® a été utilisé pour simuler le forgeage d'un lingot court, analogue au lingot duquel sont issus les échantillons ayant servis à la reconstruction 3D des ségrégations. Dans le lingot simulé, les ségrégations reconstruites ont été implémentées. Si dans la littérature Forge NxT® a déjà été utilisé pour simuler le forgeage d'un lingot contenant des indicateurs pour les ségrégations (Loucif and coworkers, en 2018 [3]), c'est la première fois qu'une représentation si précise des ségrégations est employée. La figure 9 donne un exemple de l'aspect des canaux après le forgeage numérique. Les simulations de forgeage étudiées durant cette thèse, permettent d'étudier avec une grande précision l'effet du forgeage sur les canaux de ségrégation et les ségrégations d'échelle intermédiaire. Elles peuvent également être directement comparées aux cartographies de ségrégation réalisées sur des échantillons de matière forgée (figure 10).
Les filets de ségrégation observés dans le cadre de cette thèse sont plus larges que ceux rapportés par Delattre dans sont travail de thèse [4] (il y indique une largeur de filet de ségrégation de 200 µm). Cependant, le forgeage employé n'est pas le même: il étudie une virole de cuve forgée à partir d'un lingot creux (identique au lingot étudié dans le chapitre 4). Or nous avons montré dans le chapitre 4 que la forme et la taille des ségrégations peuvent varier avec les conditions de solidification et donc le type de lingot. Le manque de données de caractérisation de ségrégations dans des pièces analogues à celle de notre étude freine la compréhension de la mise en place des filets de ségrégation lors des étapes de forgeage.
A ce jour, nous pouvons confirmer l'effet du forgeage sur la forme des ségrégations. Après forgeage, les ségrégations observées (sur les pièces forgées et par forgeage numérique) montrent des ségrégations de forme ellipsoïdale. Cette observation pourrait correspondre à la description des filets de ségrégation faite dans la littérature [4–7]. Toutefois, la taille des filets de ségrégation rapportée dans la littérature est plus petite que les filets observés dans cette étude. Cette différence de taille peut-être liée au ratio de forgeage ou à la taille des ségrégations dans la matière brut de solidification.

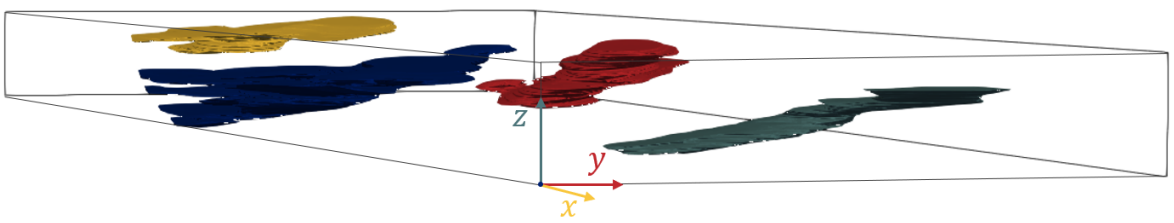

Figure 9: Observation des canaux de ségrégations reconstruits (voir chapitre 4) après forgeage numérique. Le volume observé est de $346 \times 146 \times 22$ mm^3.

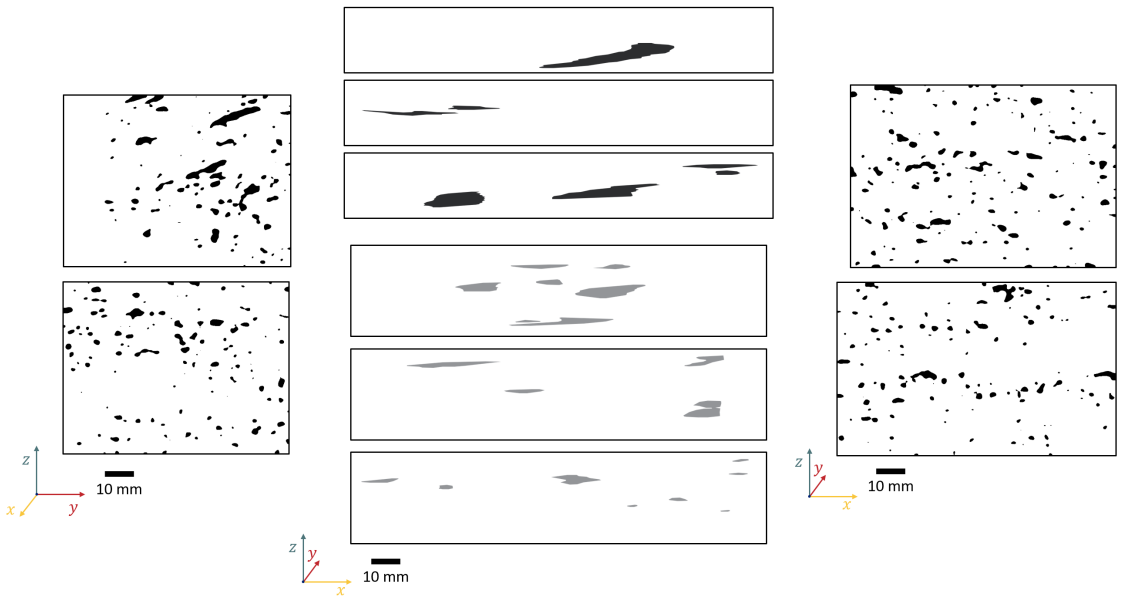

Figure 10: Au centre : les canaux de ségrégations (en noir) et les ségrégations intermédiaires (en gris); Sur les côtés : les cartographies de ségrégations des échantillons prélevés dans la matière forgées.

Conclusion et perspectives

La méthodologie de caractérisation basée sur la µXRF offre un moyen rapide, facile et non-destructif de caractériser des échantillons métalliques à l'échelle centimétrique avec une résolution de 20µm. Cette nouvelle manière d'étudier des échantillons de grande taille ouvre de nouvelles possibilités de recherche.
Grâce à la µXRF, nous avons pu étudier en 3D les ségrégations présentes à l'échelle centimétrique. La reconstruction en 3D des ségrégations a mis en évidence la complexité des canaux de ségrégations et leur coexistence avec des ségrégations plus petites, d'échelle intermédiaire. Cette observation en 3D, la première du genre à notre connaissance, a également montré les limites des observations 2D pour la caractérisation des ségrégations.
Durant cette thèse des échantillons issus de 3 gros lingots différents ont été étudié. Nous avons observé des canaux de ségrégations en zone équiaxe dendritique dans chacun des lingots. Notre étude a également montré l'absence de ségrégations à échelle intermédiaire dans la région globulaire équiaxe du lingot *creux*.
Les conditions de solidification des zones ségrégés ont été étudiés grâce à Solid®. Au terme de cette étude il semble que les ségrégations en fin de solidification, lorsque le plateau de solidification est terminé.
Enfin, cette thèse a également mis en évidence la difficulté d'identifier les ségrégation qui conduisent à la formation de filets de ségrégation dans les pièces forgées. Une compréhension complète de ce phénomène nécéssite plus de données pour comparer les résultats en fonction de différentes conditions (de segrégations, de forgeage, de laminage, ...). Toutefois, cette thèse propose une nouvelle approche d'étude couplant observations expérimentales et simulation de forgeage.

Introduction

The latest innovation in nuclear power plants is the implementation of the EPR (initially called the European Pressurised Reactor then renamed Evolutionary Power Reactor for world markets). The EPR was developed to improve the productivity and safety of nuclear power plants. The pressure vessels of the EPR are the largest ever designed for nuclear power plants. Over time, and successive innovation, the pressure vessels and steam generators in nuclear power plants became larger and larger. Both the pressure vessels and the steam generators are made of 16MND5, 18MND5 or 20MND5 steels, cast into large ingots, which are then forged. As these nuclear power plant components became larger, the size of the steel ingots required to forge them also increased. The increase in size of the ingots changes its solidification conditions and thus the chemical segregation and the microstructure in the cast material.
Chemical segregation can be defined as a local departure from the nominal chemical composition of the steel. The segregation that occurs during the solidification of large steel ingots is complex and has been the subject of countless studies. These studies, however, have mainly focused on segragations on the dendritic scale (microsegregations) or on the ingot scale (macrosegregations). When looking at the large ingots (macro-scale) used for EPR construction, any chemical segregation that forms during solidification remains: the forging process changes the shape of the segregation patterns but cannot change their intensity or number. Because of the scale of the segregations it is not possible to homogenise them by diffusion processes. Segregations formed during solidification remain in the final forged part and can affect its mechanical properties. Thus, it is of critical importance to understand the formation and occurrence of segregations at all scales in these large ingots to ensure the required mechanical properties and to exclude failure.
Recent investigations of the forged parts used for EPR construction revealed the presence of banded microstructures corresponding to bands of segregation. These segregation bands are thought to be caused by the deformation (forging) of segregations present in the cast structure. These bands create an important anisotropy in the material: the final microstructure of the steel is affected and different microstructures can coexist in the forged part leading to anisotropic and variable mechanical properties. The study of the segregation band sizes, of the as-cast segregation sizes and of the forging ratio shows that these segregation bands arise neither from the micro-segregations nor from the macro-segregations but rather from segregations on an intermediate scale (mesosegregations). These mesosegregations exist in the as-cast ingot. Such intermediate scale segregations in large ingots have never been investigated previously. Yet precise characterisation is the first step towards understanding the formation and the behaviour of these segregations.

Objectives

The main objective of this work is to characterise the mesosegregations formed during casting and leading to segregation bands in forged parts. The investigated materials are as-cast steels from several large (>100 t) ingots sacrificed for characterisation. These ingots are the same type as used for the nuclear industry.
These mesosegregations have never been investigated before in ingots of this size. Their long solidification time leads to the formation of correspondingly large structures and segregations. Their characterisation requires the chemical mapping on a centimetric scale rather than on a milli- or micro-metric scale.
In order to achieve this, the following steps must be achieved:

- Development of a methodology to map chemical segregations in steels on a centimetric-scale.
- Application of this method to characterise in 3D the segregations found in these ingots on the centimetric-scale.
- Study of the local and global solidification conditions to help understand the occurrence of the segregations
- Compare simulations of the forging of as-cast segregations to experimentally characterised segregations in the final forged parts to understand the evolution of segregation through the forging process and to identify the as-cast segregations that cause the segregation bands in forged parts.

Manuscript Outline

The present manuscript is divided into six chapters, the present introduction, and conclusion.
The first chapter presents a literature review. The patterns, the formation and the prediction of segregations during solidification of steel ingots are described. An overview of the tools used for segregation charaterisation is proposed. Finally, the consequences of segregation patterns in the forged parts are also presented.
In the second chapter, steel ingots and the forged part studied in this thesis are described. The used characterisation techniques are also presented alongside the main used analysis methods.
The third chapter describes the development of a new characterisation methodology. This methodology is based on a pre-existing technique, well-known in geology, Micro-X-Ray Fluorescence (µXRF). The assimilation of µXRF in our research field makes the investigation of segregation patterns on a centimetric scale possible.
The fourth chapter details the characterisation of segregation patterns made with the use of µXRF. This was performed in 3D on one ingot. Other ingots were investigated in 2D to compare the influence of the ingot shape on segregation patterns.
In the fifth chapter, solidification simulations conducted using the software SOLID are used to understand the formation of these intermediate-scale segregations.
The sixth chapter compares the segregations within an as-cast material to the segregations within a forged part. A new approach is also used to understand the effects of forging on segregation patterns: the forging process was simulated with the Forge NxT software on the 3D segregation patterns investigated in chapter 4.

Chapter 1

Literature Review

> La librairie est une école,
> une fenêtre sur un monde
> que nous pensons connaitre et
> qui n'est pas vrai.
> La vérité, c'est qu'il faut lire
> pour connaître vraiment le
> monde parce que les gens qui
> écrivent partent toujours d'un
> détail qui cloche.
>
> Alba Donati
> (Translation: Nathalie Bauer),
> *La librairie sur la colline*

Contents

The purpose of this chapter on literature review is to establish the groundwork for the PhD research presented in this manuscript. This 5 sections chapter starts with the basics of steel ingot solidification. During steel solidification, chemical heterogeneities called segregations are formed. The second section of this chapter presents segregation scales, typical patterns and formation mechanisms. A short overview of modelling techniques used for segregation prediction is presented in the 3^{rd} section. Then consequences of segregation on the final product and its mechanical properties are exposed. Finally, the fifth section reviews the common characterisation techniques employed for segregation study.

1.1 Ingot solidification

As steel solidifies in an ingot, primary microstructures and segregations occur. Some of these features remain and affect the steel even in its final use. Controlling the primary microstructures forming and the segregation is key for getting sound ingots for high-precision applications such as the nuclear industry. In this section, the main features of ingot solidification are presented as an introduction to a more detailed literature review on specific mechanisms. The first part explains the different primary microstructures that can be found in a steel ingot and the segregations that appear during solidification. Then the second part of the section shows examples of ingot designs used in the nuclear industry that were invented to reduce undesired features and enhance others.

1.1.1 Primary microstructures and segregations

During ingot solidification, solids can grow in different ways. Depending on local solidification conditions (thermal gradient, solidification rate, fluid flow, ...), three types of primary solidification microstructures might appear. The microstructures that form during solidification are called *primary microstructures* and they must be distinguished from secondary microstructures, which from during subsequent transformations in the solid state (ferritic or martensitic microstructures for instance) [8–11]. The three types of primary microstructures of interest in solidification of low alloy steel ingots.

- *Columnar grains* (figure 1.1a): elongated dendritic grains that grow in the same direction. The direction of growth of their primary branches is controlled by the temperature gradient. Note that for cubic crystal materials, the growth direction of the dendrite branches follows the crystallographic direction $< 100 >$.
- *Equiaxed dendritic grains* (figure 1.1b): random orientation dendritic grains, with long branched branches and no preferred growth direction.
- *Equiaxed globular grains* (figure 1.1c): the grains, not dendritic but rather spherical, have a random orientation and no preferred growth direction.

In a cast-ingot, grain structures have a usual pattern: there are three crystallisation zones, each with a different structure, as shown in figure 1.2. These zones extend from the skin of the ingot to its core. Their extent can vary according to the casting conditions

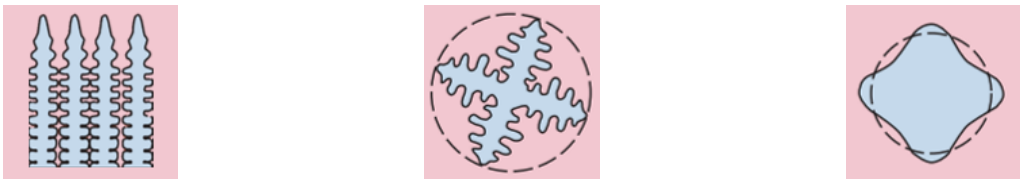

(a) Columnar grains. Adapted from [8].

(b) Equiaxed dendritic grains. From [8].

(c) Equiaxed globular grains. From [8].

Figure 1.1: Schematic of the primary microstructures of solidification.

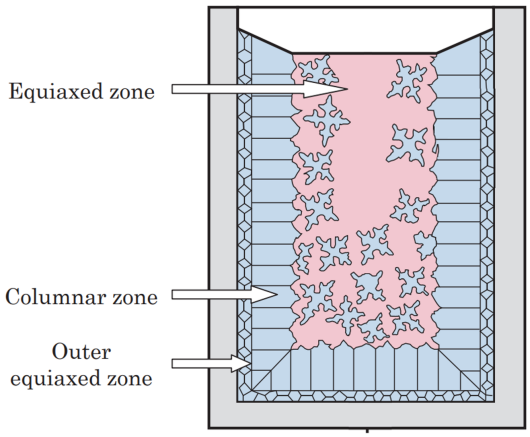

Figure 1.2: Crystallisation zone in a cast ingot. Adapted from [8, 12].

and the ingot dimensions. The skin zone is the outermost part of the ingot and is only a few millimetres thick. It is made up of numerous small equiaxed grains with no particular orientation. The large number of small grains is explained by numerous nucleation events, favoured by the high supercooling of the liquid in contact with the mould. The columnar zone follows the skin zone. In this zone, growth takes place in the form of grains oriented in the direction of the thermal gradient. The grains with one of their branch directions ($< 100 >$ crystallographic directions for steels) best aligned to the temperature gradient are selected and continue to grow. The structure becomes coarse towards the core of the ingot. The next zone is the equiaxed zone, which is sometimes absent in small-section castings. The formation of equiaxed grains in the core of the ingot is made possible by the supercooling of the liquid present in the core of the ingot and the presence of a large number of dendrite fragments detaching from the growing columnar dendrites, as well as of various types of heterogeneous nucleation sites in the liquid. The equiaxed grains formed have no particular orientation and are larger than those in the skin zone. They can freely move in the liquid. As their density is generally higher than that of the liquid, they settle to the bottom of the central ingot zone. The transition from the columnar zone to the equiaxed zone (CET) can be gradual or abrupt. The cessation of columnar grain growth can be caused by mechanical blockage of the columnar solidification front by growing equiaxed grains or by a significant solute release between equiaxed and columnar grains [8–12].

The solidification of alloys is accompanied by the segregation of the alloying elements.

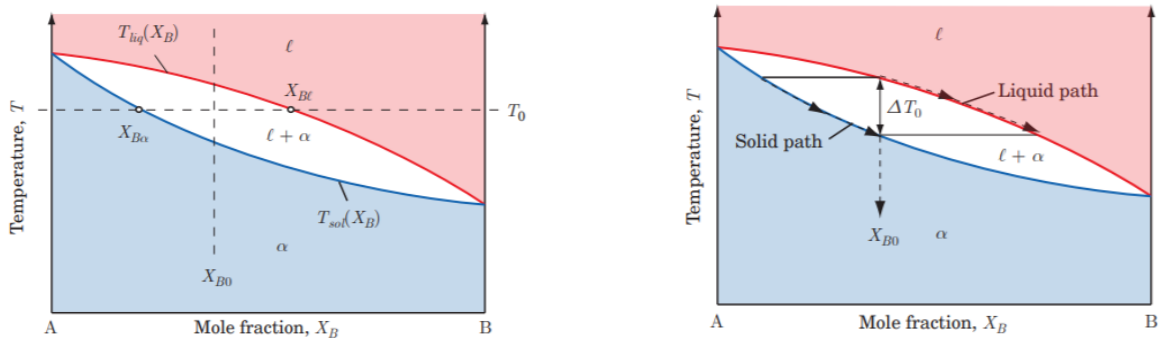

(a) Phase diagram

(b) Equilibrium solidification path

Figure 1.3: Isomorphic phase diagram of a binary alloy and it equilibrium solidification path for a X_{B0} nominal composition. Notations are α for the solid phase, l for the liquid phase, $T_{liq}(X_B)$ liquidus curve and $T_{sol}(X_B)$ solidus curve. From [8].

Each element has a different solubility in the liquid and in the solid, so during the transition from the liquid to the solid state, the distribution of the alloying elements within the new solid and the remaining liquid is not uniform [13, 14]. Figure 1.3, represents an isomorphic binary equilibrium phase diagram (where the liquid is in equilibrium with a single solid phase) and an example of a solidification path. For a fixed temperature T_0 and composition X_{B0}, the phase diagram, figure 1.3a, indicates the equilibrium compositions of the solid formed $X_{B\alpha}$ and of the remaining liquid X_{Bl}. The evolution of the equilibrium composition of the solid and liquid during solidification is described by the equilibrium solidification path presented in figure 1.3b. In the case of the diagram shown, the solute is released into the liquid during solidification, its solubility being greater in the liquid than in the solid. The first solid formed is the most depleted in solute, while the last solid formed is the richest: the concentration of solute in the liquid increases with the solid fraction [8, 15]. The partition coefficient of an element characterises the equilibrium distribution of the solute between the liquid phase and the solid phase. It is defined by equation (1.1).

$$k_0^m = \frac{X_{B\alpha}}{X_{Bl}} \tag{1.1}$$

Any difference between the local composition of the alloy (X_{B0} in the illustrative case) and its nominal (or global) composition is a chemical segregation. Segregations can be positive, in the case of local enrichment, or negative if the region is depleted in solute. The elements are not distributed homogeneously during solidification and atomic diffusion within the solid can be a slow phenomenon, so all alloys are segregated to some extent. The interest is in knowing whether the segregations present in the ingot are detrimental to the final product and its application [13, 15, 16].
Segregation exists at several scales (additionnal informaiton can be fournd in 1.2). At the dendrite scale, there are inhomogeneities in composition due to the distribution of solute during solidification. These segregations at the dendritic scale are called *microsegregations*. Compositional variations also exist at the scale of whole ingots. Generally

speaking, steel ingots are positively segregated at the top and negatively at the bottom. These segregations adopt recurring patterns and are called *macrosegregations* [8–10].
In the case of the solidification of steels, the primary solidification structures are transformed into secondary structures via solid-state transformations. The microstructures formed during these solid-state transformations replace the primary solidification structures. However, the variations in chemical composition that are the remnants of the primary structure remain [15].

1.1.2 Different types of ingots

Several types of ingots are used to manufacture nuclear components. Three major challenges are encountered when ingots are designed for nuclear component fabrication: (1) the ingots need to be large since large forged parts are required, (2) major segregations remaining in the forged parts are to be limited, and (3) ideally, no large-scale segregation would arise on the side which will be welded during the process [17].
To meet the French nuclear industry requirements, alternatives to conventional ingots were developed in the 70's by Creusot-Loire industrie. Three alternative ingots were designed: the short directionally solidified ingot, the long directionally solidified ingot and the conventional hollow ingot. All these ingots are bottom poured [17] as opposed to conventional vacuum pouring process.

- *Short directionally solidified ingots* are employed to forge the upset parts used in the steam generator. Their height-to-diameter ratio is below 0.8. The mould of such ingots was designed to encourage vertical solidification. With directional solidification, the hot top segregation is trapped beneath the top surface and A-segregates occurrence is less likely. Another advantage of this ingot is that it does not require any head feeder (hot top), thanks to exothermic powders placed on top of the ingot while it solidifies [17].

- *Long directionally solidified ingots* are used for hollow forged parts, like the sheel of the steam generator. Their height-to-diameter ratio is larger than 0.8. Their solidification mainly occurs from the sides of the ingot. Just like short directionally solidified ingots, they are cast without a head feeder, which saves liquid steel. The hot top segregation in this ingot type goes shrinkage. The aspect of the middle part of the ingot is not an issue since it is cut out to forge hollow parts. However, in the process, large-scale segregation appear on the side of the bore hole [17].

- *Conventional hollow ingots* are bottom poured in an ingot mould with a hollow mandrel. In this mould, steel solidifies from the centre and the outer sides. The inside of the mould is cooled with gas entering through the mandrel to ensure symmetric solidification and segregation patterns. Hollow ingots can be used for hollow parts that require a large-scale segregation free inside diameter [17].

1.2 Segregation patterns in ingots

During solidification, elements partition and cause segregations: an uneven repartition of elements in the solid that forms. Segregations exist at different scales: microsegregations at small scales and macrosegregations at larger scales. In ingots, segregations form recurrent patterns that have been studied for decades. This section is divided into two parts: the first one deals with the microsegregations and the different models that were proposed to predict them. Whereas the second part focuses on macrosegregations patterns and the phenomena involved in their formation.

1.2.1 Microsegregations

The different elements in alloys do not have the same solubility in the liquid and the solid. This difference, illustrated by the partition coefficient (k), is responsible for the formation of microsegregations: chemical disparities at the scale of dendritic arms. The solidification of an alloy in which the solute has limited solubility in the solid is accompanied by an enrichment of the liquid as the solid fraction increases. The solidification process also plays a role: the solidification of large steel ingots is a long process, during which liquid and solid co-exist, making the diffusion of certain elements non-negligible.
During solidification, steels also undergo a peritectic transformation. In the case of binary alloys, the peritectic point is an invariant equilibrium point of 3 phases ($l + s_1 \rightarrow s_2$). For steels, the peritectic transformation occurs between the ferrite (δ, BCC), the austenite (γ, FCC) and the liquid. Austenite growth occurs by regression of the ferrite and liquid transformation, followed by direct solidification of the austenite [8]. The solidification path is as follows:

$$l \rightarrow l + \delta \rightarrow l + \delta + \gamma \rightarrow l + \gamma \rightarrow \gamma \tag{1.2}$$

The distribution of alloying elements within the solid is influenced by the peritectic transformation. The elements are distributed a first time during the solidification of the ferrite and then a second time during the solidification of the austenite. The distribution of elements in the solid is also affected by the phase change.
Tracking the repartition of the elements in the different phases since the first phase transformation is key to understanding microsegregation and predicting its extent. The solidification path traces the evolution of the concentration of the solid formed as a function of the solid fraction. Several models exist to describe the solidification path of an alloy. These models are based on different assumptions: some neglect diffusion in the solid state, while others consider it perfect. Depending on the alloying element of interest and the process parameters, it is important to choose the right model: the model chosen for carbon, which diffuses very quickly, can be unsuitable for molybdenum, which diffuses more slowly. In the following paragraphs, the main models used to calculate microsegregation are presented as well as their hypotheses [8].

Lever rule model

The lever rule model is based on the assumption of infinitely fast diffusion in both liquid and solid phases. The composition of liquid and solid is homogeneous at each instant. In

the case of $k < 1$, the solid composition increases during solidification and immediately exceeds the composition of the first solid formed (kC_0) [8, 18].

$$C_s = \frac{kC_0}{1 - f_s(1-k)} \tag{1.3}$$

with

C_s, solid composition,
C_0, nominal liquid composition,
k, partition composition and
f_s, solid fraction.

Gulliver-Scheil's model

In the case of the Gulliver-Scheil model, the assumptions about diffusion are different. Diffusion within the liquid is still infinitely fast and the liquid is homogeneous. But the solid is not: diffusion in the solid is considered null. The first solid formed has a composition kC_0 that it retains throughout solidification. The Gulliver-Scheil's model is described with the following equation:

$$C_s^* = kC_0(1 - f_s)^{k-1} \tag{1.4}$$

with

C_s^*, solid composition at the interface between solid and liquid,
C_0, nominal liquid composition,
k, partition composition and
f_s, solid fraction.

Brody-Flemings's model

The Brody-Flemings model takes account of diffusion in the liquid and in the solid. The liquid is considered homogeneous at each time due to very rapid diffusion. Diffusion in the solid is not zero: at each instant, the solute diffuses into the solid over a diffusion distance δ, known as back diffusion. Brody-Flemings describes intermediate situations not described by lever rule or Gulliver-Scheil.

$$C_s = kC_0 \left[1 - f_s(1 - 2Fo_s k)\right]^{\frac{k-1}{1-2Fo_s k}} \tag{1.5}$$

with

$$Fo_s = \frac{D_s t_{sol}}{L_c^2} \tag{1.6}$$

where

Fo_s, Fourier number in the solid,
D_s diffusion coefficient in the solid,
t_{sol}, solidification time,
L_c, characteristic length, $^{\lambda_2}/_2$ for a dendritic growth (λ_2 is the secondary dendrite arm spacing).

As for the previous models, this equation (1.5), is only valid for $k < 1$, where k is constant (liquidus and solidus are assimilated to straight lines). This form of the equation makes it possible to find the equation of the Gulliver-Scheil model (1.4) when diffusion in the solid is neglected (by setting $Fo_s = 0$). To find the equation of the lever rule model, Fo_s should be set to 0.5, since if $Fo_s \to \infty$ leads to an indeterminate form. A drawback of this model is that it does not conserve solute. [8, 18].

Clyne-Kurz's model

In order to improve the Brody-Flemings model for systems with perfect diffusion in the liquid and intermediate diffusion in the solid (back diffusion in the solid), Clyne and Kurz proposed in 1981 to replace the Fourier number in the solid, Fo_s, by a function of the Fourier number in the solid, $f(Fo_s)$. Using this function allows the model to adopt values consistent with the limits. In other words, we find the lever arm rule when $Fo_s \to \infty$ and the Gulliver-Scheil model when $Fo_s \to 0$.
The function $f(Fo_s)$ with which to replace Fo_s in the model is the following:

$$f(Fo_s) = Fo_s \left[1 - \exp\left(-\frac{1}{Fo_s}\right)\right] - \frac{1}{2}\exp\left(-\frac{1}{2Fo_s}\right) \tag{1.7}$$

NB. Using this function does not deal with the problem of solute conservation, but only corrects the behaviour of the model when $Fo_s \to \infty$.

1.2.2 Macrosegregations

Macrosegregations are chemical composition heterogeneities at the ingot scale. Unlike microsegregation, macrosegregation cannot be resorbed during heat treatment. The macroscopic scale of these heterogeneities would require homogenization times that are impossible to reach. [8, 19, 20].
There are two main types of macrosegregation: the *mass macrosegregations* and the *local macrosegregations* [16, 21]:

- In steel ingots, the main *mass macrosegregations* are spread over the whole ingot. They are: the negative base segregation, visible at the ingot base, and the positive enrichment at the top of the ingot – the hot top segregation.

- The *localised macrosegregations* only occur in specific areas of the ingot such as channels segregates (A- and V-segregates), inverse segregations, and banding segregations

In figure 1.4, Pickering represents these macrosegregation patterns in a steel ingot. Lesoult [22] gives another representation of macrosegregation, see figure 1.5. The schema is based on a 65t ingot of 0,22 wt% C steel. On the left part of the schema, the primary microstructure is described: columnar grains near the surface and equiaxed grains in the middle of the ingot. Two different types of equiaxed grains are represented: the globular equiaxed grains forming a cone up to 75% of the ingot height, and dendritic equiaxed grains around and on top of the globular grains. The right part of the schema is a rough representation of carbon segregation patterns obtained by combustion analysis (more information on this technique is available in 1.5.1). The lower part of the ingot shows a cone of negative segregation in purple, while the upper part shows intense positive segregation in red. The A segregates highlighted by the Baumann macroetching (see 1.5.1) are shown as black lines on the schema, they are located at the boundary between the globular and dendritic equiaxed zone. A comparison of the left and right sides of the schema shows a correlation between the microstructure observed and mass segregations. When the globular grains settle, the enriched liquid is forced towards the head of the ingot and forms a positive segregation zone, which is made up of equiaxed grains.
During the solidification of alloys, mass transfers take place and cause the formation of segregations. If we consider a partition coefficient $k_0 < 1$, the liquid is locally richer in solute than the solid and the movement of one phase compared to the other causes a macroscopic mass transfer. The main causes of these transfers are listed here [8, 9, 20, 23]:

- *Convection* is a main cause of macrosegregation in ingots. It can be forced (by mixing) or natural. The natural thermosolutal convection is caused by the density difference due to temperature and composition changes in the liquid phase.
- *Motion of equiaxed grains* also causes macrosegregation. The liquid is richer in solute than the solid. Depending on their size, morphology and density, grains can either float in the liquid, settle down or be dragged by convection movements. When solute-lean grains settle, the solute-rich liquid is ejected and a negatively macrosegregated area is created.
- *Solidification shrinkage* puts enriched liquid into motion, thus creating macrosegregations. The contraction of volume due to liquid-solid transformation creates liquid suction to compensate for solidification shrinkage.
- *Mushy zone deformation* can also create a solute-rich liquid flow. A mushy zone can be compared to a sponge with a skeleton made of solid, incompressible and solute-lean, filled up with solute-rich liquid. Under pressure, the coherent mushy zone can deform and release liquid or grow and suck liquid in.

In 1973, Comon *et al.* [24] proposed an empiric formula to predict the extent of carbon segregation in an ingot, based on its nominal composition and dimensions. The empiric formula is based on the study of 152 steel ingots. The smallest ingot was 0.6 m in diameter, weighed 3.5 t, and had a carbon content of 0.1 wt%. The largest ingot considered in the study was a 0.54 wt% C ingot of 190 t, its diameter was 2.55 m. The formula predicts

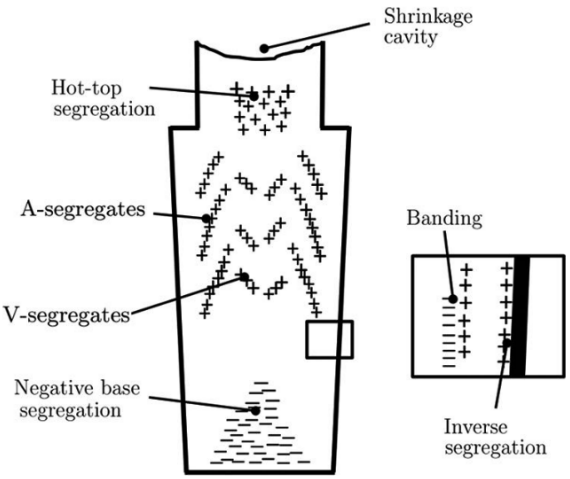

Figure 1.4: Representation of the different macrosegregation patterns in large steel ingot. Positive segregations are indicated with (+) and negative segregations with (-). From [20].

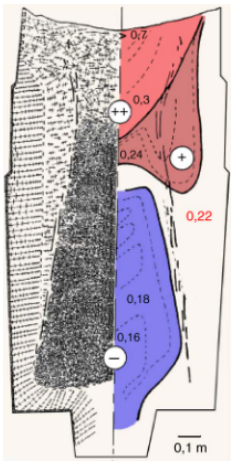

Figure 1.5: Macrosegregations and microstructures in a 65 t steel ingot. From [22].

the ingot global carbon segregation ratio (1.8).

$$\frac{\Delta C}{C}\% = \frac{C_M - C_m}{C_0} \times 100 \tag{1.8}$$

with

$\frac{\Delta C}{C}\%$, global carbon segregation ratio,
C_M, maximum carbon concentration in the ingot (without the hot-top part)
C_m, minimal carbon concentration in the ingot and
C_0, nominal carbon concentration of the cast.

According to Comon *et al.*, the global carbon segregation ratio can be predicted thanks to the formula (1.9).

$$\frac{\Delta C}{C}\% = 2.81D + 4.31H + D(28.2Si\% + 805.8S\% + 235.2P\% - 9.2Mo\% - 38.2V\%) \tag{1.9}$$

with

$\frac{\Delta C}{C}\%$, global carbon segregation ratio,
D, ingot diameter [m],
H, ingot height [m],
$Si\%$, $S\%$, $P\%$, $Mo\%$ and $V\%$, alloy elements cast concentration.

The global carbon segregation ratio depends on the ingot size: a larger ingot will be more segregated because it has a longer solidification time. The steel composition also influences global carbon segregation through changes in the liquid density or the temperature interval of solidification. Equation (1.9) gives a useful general idea. Nowadays,

complex numerical models take into account numerous physical aspects of ingot solidification, more details are given in section 1.3.
During the solidification of an ingot, macrosegregations form one after the other by various mechanisms. In the following paragraphs, the common macrosegregation patterns segregations are detailed in order of formation.

Inverse segregation and banding segregation

The inverse segregation is a surface segregation that forms near the cold mould wall. When steel solidifies against the mould wall, solidification shrinkage sucks solute-rich liquid to compensate for the volume decrease (figure 1.6). The local composition near the mould wall is enriched by the inflow of solute-rich liquid [8, 11, 19].
Banding segregation (or bands of segregation, depending on the authors) are pronounced composition variations that form during the early stages of solidification. They are caused by erratic progress of solidification when convective heat transfer is disrupted (by thermal impulse or by the formation of air gaps between the steel and the mold, for instance) [21, 23, 25].

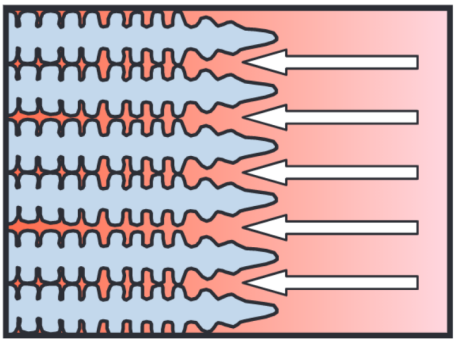

Figure 1.6: Interdendritic fluid flow caused by solidification shrinkage. From [8].

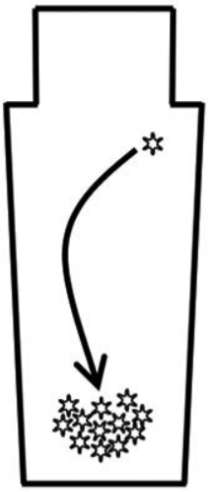

Figure 1.7: Representation of the solid sedimentation causing the negative base segregation. From [20].

Negative base segregation

Negative base segregation is a mass macrosegregation, observable at the bottom of steel ingots. The negative base segregation is formed by the grains sedimentation during the solidification of the ingot, as represented by Pickering in 2013, see figure 1.7 [20]. During solidification, liquid flow can melt off dendrite branches and take them up to the top part of the ingot. The dendritic fragments lead to formation of equiaxed grains floating in the liquid [26, 27]. The equiaxed grains grow and sediment with time since the solid

density is greater than the liquid density. Solid is solute-lean compared to liquid, hence the accumulation of solid in the ingot base forms the negative base segregation [10, 11, 13]. The formation of negative base segregation can also be encouraged by fluid flow as it was shown with numerical simulations of ingot solidification [28].

A segregates

A-segregates, also known as A segregations, channel segregates or channel segregations[1], are a type of local macrosegregations that appear in steel ingots. Freckles are defects similar to A-segregates found in directionally solidified superalloys. A-segregates form in the mushy zone, because of flow of solute-rich interdendritic liquid. In the interdendritic liquid there are differences of temperature and composition caused by the heat transfer at the scale of the casting and by solute rejection from the solid grains during solidification. These differences create density gradients in the interdendritic liquid, which causes the liquid to move, driven by buoyancy forces. This phenomenon is called thermosolutal natural convection [29].
The formation of A-segregates has been linked to the local thermal gradient or solidification rate in various studies [8, 21, 30, 31]. In 1968, Comon and Bastien [21] compared segregation patterns obtained in ingots of several sizes. The A-segregates observed in small ingots are less intense than A-segregates observed in large ingots. A-segregates appear preferably in large ingots, where the thermal gradient and the solidification rate are weak.
Permeability also influences A-segregates formation. A-segregates forms preferably in high-permeability environments, where the resistance to the flow is small: in dendritic equiaxed grains, where the secondary dendritic arms spacing (SDAS) is the largest [8]. In a 500 kg steel ingot, Chen *et al.* defined what they call a *A-segregation zone* (figure 1.8): the area in which A-segregates can form. They divided A-segregates into two categories, based on their location in the ingot:

- The first category for the A-segregates layers of the *A-segregation zone*. These A-segregates are located near the CET zone. The columnar zone is compact, the interdendritic liquid flows toward the CET zone, more permeable. The interdendritic liquid has a lower density and rises toward the centre and the top of the ingot.

- The second category for A-segregates which are located near the sedimentation cone of equiaxed grains (negative base segregation). The authors suggested that these A-segregates forms with different mechanisms: the solidification shrinkage sucks solute-rich liquid around the sedimentation cone and the sedimentation cone rejects solute-rich liquid when submitted to pressure.

[1]The term *channel* is sometimes employed for both A and V-segregates, although this can be misleading because they form by different physical mechanisms.

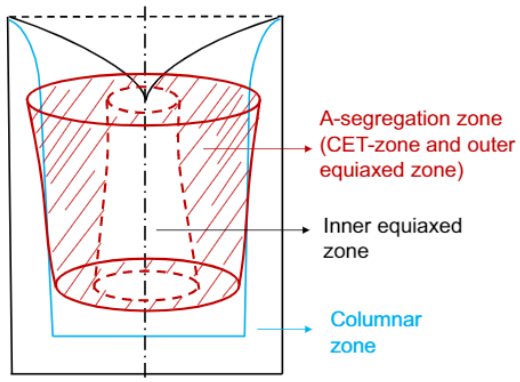

Figure 1.8: Representation of the *A segregation zone* in a 500 kg steel ingot. From [31].

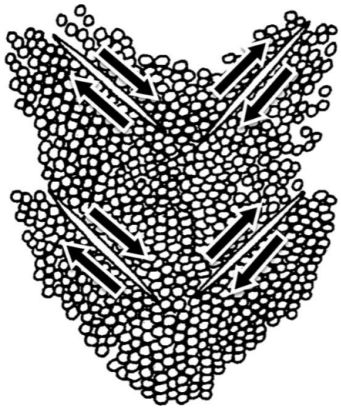

Figure 1.9: Representation of V-segregates formation. Shear planes (shown by arrows) open due to primary grain network fissuring and are filled by enriched liquid. From [23].

V segregates

V-segregates look like A-segregates but are found in the central part of the ingot and in the opposite direction compared to A-segregates. As for A-segregates, V-segregates are more common in large ingots and they are enriched in solute compared to the surrounding steel [21].
Nonetheless, V-segregates do not form with the same mechanisms as A-segregates. V-segregates appear at the end of solidification. In the centre of the ingot, dendritic equiaxed grains connect in a loose network as represented in figure 1.9. The newly formed grain network is fragile. It cracks under the weight of the steel above it. Solidification shrinkage also created voids inside the network. The cracks are filled up with surrounding enriched liquid, leading to the formation of V-segregates [13, 20].

Hot top segregation

In large steel ingots, the hot top segregation is an intense mass macrosegregation at the top of the ingot. This area is the last part of the ingot to solidify, hence it solidifies from the remaining liquid which is very rich in solute. During the solidification, the liquid density decreases as liquid is enriched in solutes (mainly due to the effect of carbon) and the liquid rises in the ingot. Hot top segregation phenomena can be worsened by bad insulation of the top part of the ingot and mould [11, 20, 32].

1.3 Simulations and predictions of macrosegregations

Simulations are a powerful tool in the solidification field to predict the final primary microstructures and segregations. With simulations, different physical theories can be tested before being compared with experimental results. From an industrial point of view, simulations are an interesting tool: with a robust modelling tool, many expensive experimental tests can be avoided. Another way to save money is to understand the physical phenomena responsible for macrosegregation to be able to act on it and reduce the defects in the ingots or move them to unused parts of the ingots.
In this part of the literature review, the works of Flemings *et al.*, pioneers in macrosegregation modelling, are first presented. Then more recent models that can model the solidification of whole ingots are introduced.

1.3.1 Local solute redistribution equation

Between 1967 and 1968, Flemings *et al.* published a 3 papers series [25, 33, 34] where they give the Local Solute Redistribution Equation (LSRE). This equation describes the segregations in a Representative Elementary Volume (REV) of the mushy zone. During solidification, the solute-rich interdendritic liquid moves to compensate for the solidification shrinkage. The LSRE equation describes the movement of the solute-rich liquid to explain the formation of macrosegregations.

$$\frac{\partial g_l}{\partial C_l} = -\left(\frac{1-\beta}{1-k}\right)\left(1+\frac{\vec{v}\cdot\nabla T}{\varepsilon}\right)\frac{g_l}{C_l} \tag{1.10}$$

with

g_l, volume fraction of liquid,
C_l, liquid composition in the REV,
$\beta = \frac{\rho_S - \rho_L}{\rho_L}$, solidification shrinkage,
k, equilibrium partition coefficient,
$\vec{v}$, local interdendritic liquid velocity relative to the solid,
∇T, temperature gradient and
$\varepsilon = \frac{\partial T}{\partial t}$, temperature change speed.

The first paper in the series [25] establishes the local solute redistribution equation. This equation is the result of a solute mass balance carried out on an REV within which the temperature and composition of the liquid are homogeneous. The equation is based on several assumptions: the solid is considered to be fixed, no pores form in the REV, and diffusion is assumed to be perfect in the liquid and zero in the solid. The solute is supplied by the flow of interdendritic liquid. Solidification shrinkage is accounted for in the mass and solute balances. The LSRE equation reflects changes in the volume fraction of the liquid with changes in composition and temperature. It takes into account the flow of the liquid and its direction relative to the temperature gradient. It is a local description of these phenomena within a REV. It does not explain the macroscale flow and heat transfer.

The following papers [33, 34] compare theoretical results obtained with the LSRE equation and experimental observations. Various configurations are tested, in particular unidirectional or bidirectional solidification as well as ingots whose cross-section varies continuously or abruptly.
In 1970, Mehrabian, Keane and Flemings published an article [1] investigating the action of gravity on the flow of interdendritic fluid. The LSRE equation was still applicable, but now it was used in conjunction with momentum and continuity equations describing the flow in the mushy zone. The model considers the action of solidification shrinkage and gravity on a fluid whose density varies during solidification. This involves defining the local velocity of the interdendritic liquid by Darcy's law and the equation for the conservation of mass within the elementary volume. The permeability of the medium is calculated using the volume fraction of liquid, a geometric factor and the number of fluid channels per unit area in a given direction. In this way, the permeability is isotropic, which may not be a very valid approximation in columnar zones. Applied to a case of unidirectional solidification, this model is used to predict liquid displacements relative to solidification shrinkage and fluid density. The effects of ingot size, paste zone thickness and composition on these liquid displacements are also studied.

1.3.2 Industrial ingot solidification simulation

Since the LSRE equation, modelling has evolved. There are now different ways of simulating the solidification of industrial ingots. Different categories of models exist depending on the physical phenomena taken into account or neglected. A review by Wu, Ludwig and Kharicha [35] published in 2018 proposes a distinction into five types of models:

1. Mixture continuum models that rely on local equilibrium models to describe the mushy zone and do not account for diffusion-controlled growth of grains,
2. Two-phase models (liquid and equiaxed grains),
3. Two-phase models (liquid and columnar trunks),
4. Three-phase models (liquid, equiaxed grains and columnar trunks) and
5. Four-phase models (liquid, equiaxed grains, columnar trunks and gas).

We can add a sixth type of model:

6. Six-phase models with moving equiaxed grains (solid, intradendritic liquid, extradendritic liquid, considered separately for equiaxed and columnar structures) [36–38].

The first three types of model are appreciated for their low computational cost. However, they have certain limitations, for example: none of them can predict a solid structure consisting of both columnar and equiaxed grains, and types 1 and 3 cannot account for the sedimentation of the crystals formed. The fourth type of model takes into account grain sedimentation, two type of rgain structures (globular equiaxed and columnar) and predicts positive segregation at the head of the ingot, negative sedimentation cone at the bottom of the ingot and segregated bands that can be related to A-segregation. However, the globular morphology attributed to the solid leads to an overestimation of

the negative segregation cone and the positive segregation at the head of the ingot. The results obtained with this kind of model are not applicable in the dendritic equiaxed zones of ingots. Only model types 5 and 6 describe the morphology of the equiaxed grains and include a prediction of the morphology transition. Only these models can account for the influence of the grain morphology on the macrosegregation .
In the following paragraphs, SOLID, a model of type 6 is presented using examples of simulations of industrial ingots. This model is also used in the thesis for the simulation of the solidification of an ingot.

SOLID® simulations: grains motion and nature influence

The SOLID® software is a multi-scale model simulation software solidification of metal alloys developed at Jean Lamour Insitute. One of the key applications of SOLID is steel ingot casting. SOLID is used in both industry and academia. Here is a short description of the phenomena taken into account at the different scales:

- For the *macroscopic scale*, heat transfer, multiphase flow, and solute transport are taken into account. The flow is driven by thermosolutal natural convection and by motion of equiaxed grains. Shrinkage can be accounted for, but is often neglected because of its small influence of macrosegregation in steel ingots and because of the complexity of simulation of shrinkage cavities and hot pipe. Equiaxed grain movement within the ingot is determined using the grain envelope fraction, g_{env}. If the envelope fraction is greater than the packing fraction parameter g^{block}, then the solid phase present in the mushy zone is considered fixed. The structure of fixed grains is permeable and the liquid flows through this porous matrix. In the opposite case, $g_{env} < g^{block}$, the grains are free floating and their motion is described by the solid phase transport equations, accounting for buoyancy, drag, and grain collisions. g^{block} is a user-defined model parameter. The equiaxed grains envelope fraction of the cell is used to predict the columnar to equiaxed transition, when the envelope fraction of the equiaxed grains reaches 0.5, the columnar front gets blocked [38].

- At the *microscopic scale*, nucleation, diffusion-driven grain growth, gain morphology and microsegregation are considered. New grains nucleate when the temperature of the elementary volume is lower than a user-defined nucleation undercooling, this is the nucleation criterion. In the model grains are described by grain envelopes that contain a solid structure and intradendritic liquid. The intradendritic liquid is assumed to be in thermodynamic equilibrium, whereas the liquid outside the envelopes (extradendritic liquid) is out of equilibrium, i.e., it is undercooled. The envelopes grow at a rate that is defined by the primary tip speed. Envelopes are considered to have an octahedral shape, i.e., with six primary tips. The growth of the solid is described by a model of diffusion-controlled solidification [39]. The different phases are represented in a volume-average sense by phase volume and mass fractions and by grain population density (number of grains per unit volume). Grain morphology is assessed by the internal solid fraction, $g_{si} = g_s/g_{env}$, the ratio between the solid fraction and the envelope fraction. This quantity estimates the

amount of solid in a dendrite envelope. For $g_{env} \to 1$ the morphology is globular, for $g_{env} \ll 1$ it is dendritic. The final morphology of the solidified structure is assessed by the internal solid fraction at the instant of grain packing.

SOLID ® can be used to investigate the influence of equiaxed grain morphology and movement on the formation of macrosegregation. Combeau *et al.* [40] simulated the same 3.3 t steel ingot in 3 different configurations: the fixed solid case ($g^{block} = 0$), the case of free dendritic equiaxed grains ($g^{block} = 0.4$) and the case of free globular equiaxed grains ($g^{block} = 0.4$). The main results are illustrated in figure 1.10. On each subfigure the macrosegregation predicted by the simulation is shown on the right and the experimental carbon segregation map on the left.

- The fixed solid simulation ($g^{block} = 0$) predicts an unreal negative segregation of the central axis, underestimates the hot top segregation and predicts A segregates.
- With free dendritic equiaxed grains ($g^{block} = 0.4$), the central axis is again predicted unrealistically negative. The underestimated hot top segregation and the A segregates are shifted higher in the ingot compared to the fixed solid simulation.
- In the case of free globular equiaxed grains ($g^{block} = 0.4$), a deeply negative unrealistic sergegation is predicted in the ingot bottom. The global segregation pattern does not match the experiment.

Their work show the importance to take into account the morphology of the grains to predict with accuracy the macrosegregation in steel ingot.
Combeau et al. [40, 41] demonstrate the influence of both equiaxed grain morphology and grain motion on the macrosegregation formation. For instance, the simulations with free globular equiaxed grains show better agreement with the experimental maps in the sedimentation cone in the bottom part of ingots, where the primary microstructure is globular, especially on large ingot simulations ([41], see figure 1.11). Other works from the same team [42], successfully simulated a transition from a globular morphology to a dendritic morphology. Predicting the evolution of the equiaxed structure makes it possible to select, on a local scale, the dominant mechanism behind the formation of segregations. Where the grains are globular, the macrosegregation is formed mainly by settling of the solute-lean grains, this creates a strong vertical segregation gradient. Where the grains are strongly dendritic (very small internal solid fraction), the packing effect is weak due to the small quantity of solid in the packing; macrosegregation forms mainly by flow of liquid through the packed layer of fixed grains. This model, which predicts the transition from a globular to a dendritic morphology, gives a good idea of the macrosegregation within a dendritic ingot.

SOLID® simulations: primary microstructure prediction

Gerin *et al.* [38] investigated the formation of the solidification structure (primary microstructure) of a 9.8 t directonally solidified steel ingot in 2020. The solidification structure can influence the final mechanical properties of the products. The software used

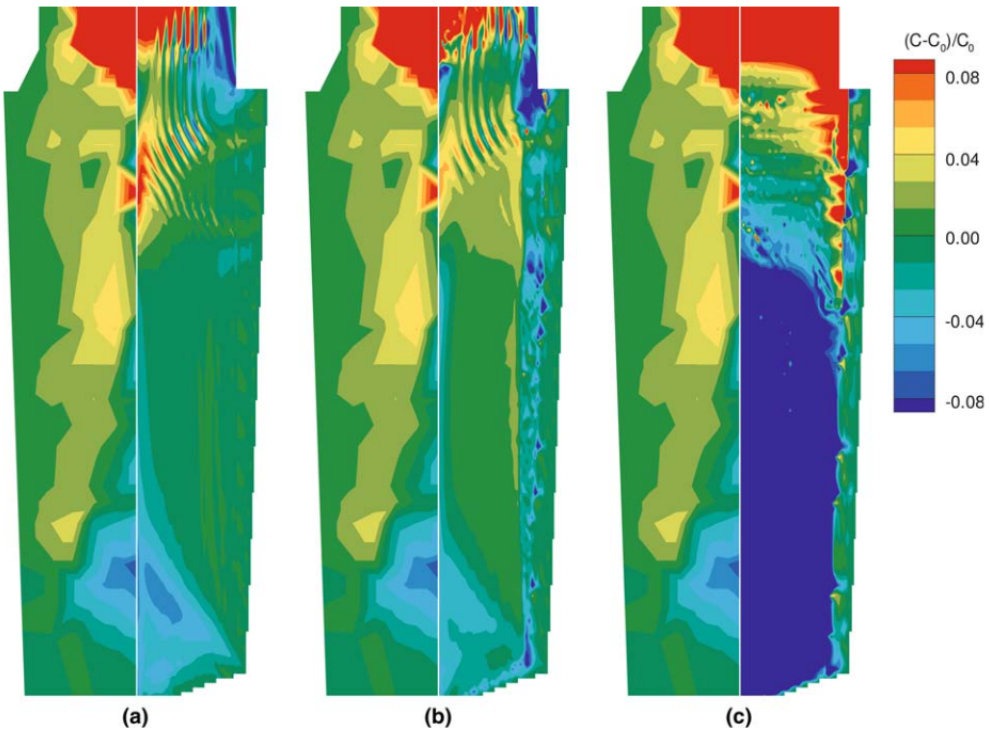

Figure 1.10: Segregation ratio map, left: experimental results, right: numerical simulation (a) Case of fixed solid, (b) Case of free dendritic grains and (c) Case of free globular grains. From [40].

for the modelling was SOLID®, although some parameters have been changed compared with the work of Combeau *et al.* [40, 41]. This time 5 different phases are considered: the liquid, the columnar solid, the equiaxed solid, the columnar interdendritic liquid and the equiaxed interdendritic liquid. This model describes the formation of the Columnar-to-Equiaxed Transition (CET) and Equiaxed-to-Columnar Transitions (ECT), accounting for the movement of the grains.

To model solidification, heterogeneous germination is neglected. The only source of grains is the fragmentation of columnar dendritic arms, which are carried away by the liquid flow and grow into equiaxed grains before settling. The smallest grains are carried away by the movement of the liquid, while the largest sediment quickly. In the CET model the columnar growth front is blocked when the envelope fraction of equiaxed grains in the mesh cell containing the columnar front reaches a defined limit (0.50). The simulation was carried out for a binary Fe-C alloy, 0.184wt% C.

Gerin et al. provide the sequence of formation of the different microstructure zones in the ingot. The flow of liquid influences the formation of segregations and structures. Initially, the columnar grains form and grow from the walls of the mould. At the bottom of the ingot, the columnar front is rapidly blocked by the accumulation of equiaxed grains. The liquid settles in an upward movement along the columnar front and down to the centre of the ingot, which has the effect of pushing the equiaxed grains to the sides of the ingot

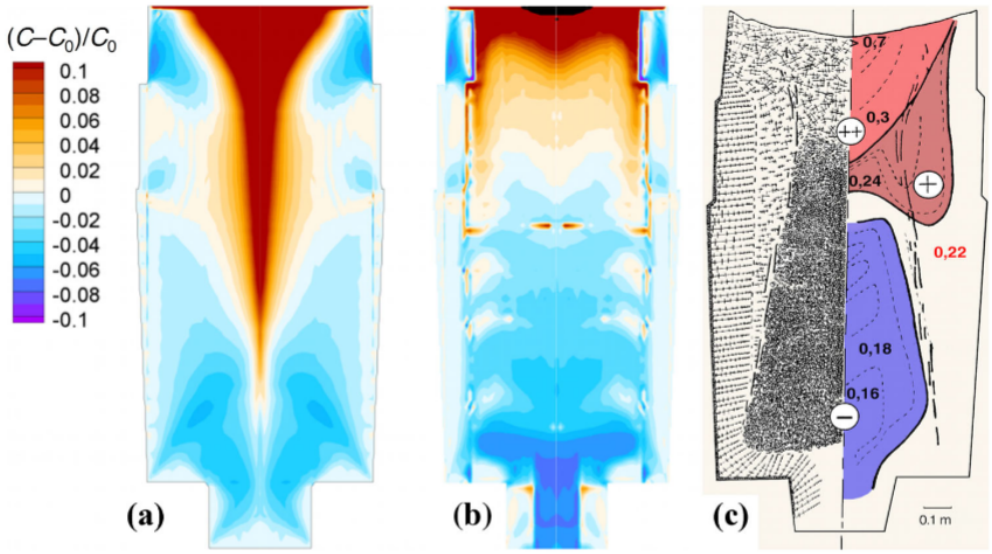

Figure 1.11: Segregation ratio map. (a) Case of fixed solid, (c) Case of free globular grains and (c) Experimental segregation map and primary microstructure. From [22, 41].

and encouraging columnar growth in the centre. The appearance of small vortices on the sides of the ingot accelerates the progression of the equiaxed zone. At the end of solidification, these vortices disappear, leaving time for the columnar zones at the top of the ingot to develop.
The simulation results are close to reality in terms of structure and segregation. Gerin et al. also conclude that this shows that secondary dendrite arm fragmentation is the dominant source of equiaxed grains in this type of ingot. The study also showed the influence of liquid movement on segregation and solidification structures.

1.3.3 Channels segregates predictions

The formation of A segregates can be modelled in two different ways: directly or using criteria. By modelling each of the flow phenomena within the ingot with a sufficiently fine mesh, it is possible to simulate the formation of segregation channels. However, the large size of ingots, their long solidification times and the complex system of equations used to describe solidification mean that calculation times are so long that it is currently impossible to apply a fine enough mesh to the entire ingot. To get around this problem, it is possible to use criteria to detect the zones in which segregation channels are likely to form. This time, a coarse mesh could be sufficient, as the A segregates are not directly described.
The two techniques are presented in the following paragraphs. First, the formation of segregation channels is modelled directly using a fine mesh over an area of a few square centimetres. The use and relevance of different criteria are then discussed.

Channels segregates direct modelling

Segregation channels can be predicted by accurately modelling the flow in the mushy zone. To do this, it is necessary to choose the appropriate mesh and calculate the local permeability accurately. Kumar *et al.* [43] have modelled the solidification of a Sn-5wt%Pb alloy in two dimensions, in a 60×100 mm^2 mold, one side of which is cooled while the others are thermally insulated. The effect of several factors on the predicted channels is analysed. They compare different discretisation methods for calculating the permeability of the medium and different mesh sizes for flow calculations.
Firstly, as the number of points increases, the different discretisation methods converge towards the same result. So the finer the mesh, the less influence the discretisation method used has on the result. As far as the mesh size is concerned, by increasing the number of calculation nodes, it is possible to calculate the flow in the channels accurately. Different mesh sizes were tested: 90×90, 150×150, and 300×300. The coarsest mesh (90×90) is used to identify areas in which segregation is likely to occur, but the flow in the channels is not calculated precisely as it is for finer meshes. The finest mesh allows the flow within the channel to be calculated, since several calculation nodes are located there, and it is also possible to estimate the width of the channel. However, the computing power required to apply such a fine mesh to the scale of an industrial ingot is too great for this solution to be considered.

Criteria for channels segregates apparition

Over the past decades, several criteria were developed for channel segregates formations. Some of them are empirical whereas others are theory-based. In this paragraph, several criteria are introduced: first the empirical criterion and then the theoretical criterion.
Several criteria were developed for freckle prediction. Freckles are solidification defect analogue to channel segregates, but form in directionally solidified gas turbine blades cast in superalloy. As freckles and channel segregates share a common origin: the remelting or a perturbation in the solid fraction.

Copley's criterion In 1970, Copley and his team [44] studied freckles in unidirectional solidification of low-melting model system (30 wt% NH_4Cl - H_2O). This study concludes that freckles form when three conditions are met at the same time:

1. The solidification is unidirectional and columnar (not equiaxed): $R < \frac{K_T G_S}{\Delta H}$,
2. The thermal gradient is low: $G < G^*$ and
3. The isotherm speed is high: $R < \frac{T_L - T_S}{\Delta t_l^* G}$.

with

R, solidification rate,
K_T, thermal conductivity,
G_S, thermal gradient, in the solid at the solidus,
ΔH, latent heat of fusion (enthalpy of fusion),

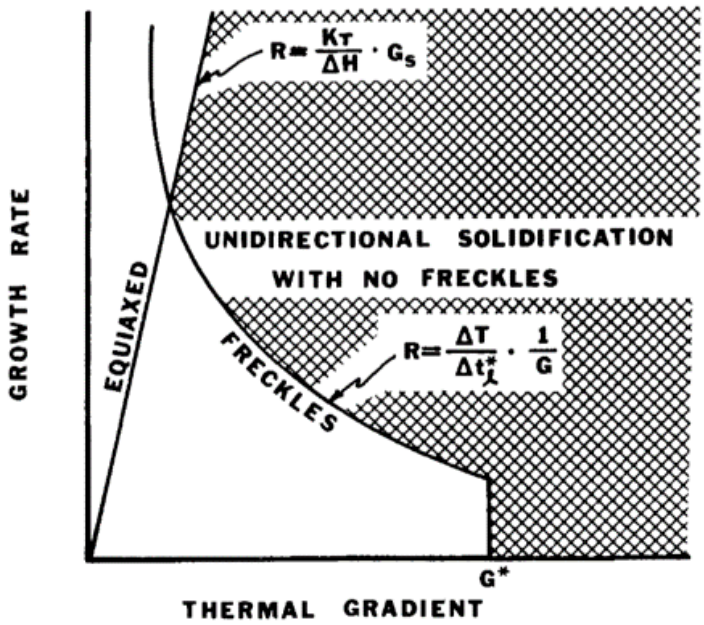

Figure 1.12: Graphical representation of the three conditions required for freckles formation according to Copley *et al.*. From [44].

G, thermal gradient,
$T_L - T_S$, solidification interval and
Δt_l^*, critical solidification time.

On a graph plotting the growth rate as a function of the thermal gradient, a specific area of the domain meets the three conditions and is prone to freckling, see figure 1.12. However, the use of Copley's criterion in steel ingot is not easy: Copley *et al.* does not give any information on the limited values of the conditions (G^* and Δt_l^*) and this approach can only be applied to unidirectional solidification.

Suzuki's criterion Suzuki's criterion is an empiric criterion based on the observation of solidification and A segregates formation in several cast steel ingots, for which some of them were dumped to stop solidification [45]. Suzuki and Miyamoto consider that A segregates form in the mushy zone, when the solid fraction reaches 0.30. They establish the following criterion to predict A-segregates formation:

$$R \times \varepsilon \leq 8.75 \tag{1.11}$$

or

$$R^2 \times G \leq 8.75 \tag{1.12}$$

with

R, advancing rate of the solidification front,
ε, cooling rate, $\varepsilon = R \times G$ and

G, thermal gradient.

Suzuki's criterion is rather simple and can easily be used on steel ingot. Nevertheless, it is important to keep in mind its limits: the criterion only acknowledges thermal conditions, the grains morphology and the liquid enrichment are neglected. It was developed on small ingots (14 kg), within specific ranges of values, $R \in [0.3; 0.7]$ mm/min and $G \in [0.45; 10]$ °C/min, and the ingot nominal carbon content was close to 0.7 wt% C.

Rayleigh's criterion In a paper from 2013, Torabi Rad and his team [46] criticise Suzuki's criterion for its validity that depends on the steel grade. They also suggest a new method of A-segregates prediction in steel ingots, based on the Rayleigh number that compares the buoyancy force to the frictional force, as it was previously done in Sn-Pb Alloys and Ni-Based Superalloys [47, 48]. They give an empirical single critical value to the Rayleigh number, under which no A-segregates forms. The authors use the same critical value for any steel ingot type or composition. The critical value was obtained after the comparison of 27 ingots. The ingots under investigation gather small experimental ingots and industrial ingots. Their C composition ranges from 0.19 wt% C to 0.88 wt% C. The approach of Torabi *et al.* differs from the approach used with previous criteria: with the Rayleigh-based criterion, they indicate the A-segregates free area of the ingots. The Rayleigh number can be calculated with the equation (1.13) [48] and the critical value found is 17±8.

$$Ra = \frac{\frac{\delta\rho}{\rho_0} g \bar{K}}{R\nu} \tag{1.13}$$

with

Ra, Rayleigh number,
$\frac{\delta\rho}{\rho_0}$, relative liquid density inversion in the mushy zone (calculated when $g_s = 0.3$),
g, gravity,
$\bar{K}$, permeability (calculated with Blake-Kozeny and Won-Thomas formulas),
R, solidification rate and
ν, kinematic viscosity.

Rayleigh's criterion is easy to implement on a production line and can be used to predict A-segregates free ingots. However, Torabi Rad and his team [46] assume that A-segregates only forms in columnar zone and the Primary Dendritic Arms Spacing is used to calculate the permeability. It is important to remember that this criterion is intended to predict A-segregates free areas, rather than to indicate the level of likelihood of A-segregate formation. In 2015, Pickering *et al.* [49], put to the test Rayleigh's criterion with two case studies. Their work shows a sensibility of the Rayleigh number to C, Si, S and P, elements that greatly influence $\delta\rho$. They also suggest lowering the critical value to 6 and they point out that Rayleigh's criterion use is easier on large steel ingots since they present more Rayleigh number variations.

Flemings's criterion In 1970, Mehrabian, Keane and Flemings [1] proposed a first theoretical criterion for the formation of segregation channels based on LSRE (1.10) [25].

Within a mushy zone between dendrites, there are numerous small and stable channels where liquid flows with a uniform velocity. However, these channels can be destabilised, leading to the formation of A-segregates. Mehrabian *et al.* focus on the conditions under which the flow instabilities occur. By rewriting the LSRE into equation (1.14), they formulate the remelting criterion.

$$\frac{\partial g_l}{\partial T} = -\left(\frac{1-\beta}{1-k}\frac{g_l}{C_l}\frac{\partial C_l}{\partial T}\right)\left(1+\frac{\vec{v}\cdot\nabla T}{\varepsilon}\right) \tag{1.14}$$

with

g_l, volume fraction of liquid,
T, temperature,
$\beta = \frac{\rho_S-\rho_L}{\rho_L}$, solidification shrinkage,
k, equilibrium partition coefficient,
C_l, liquid composition in the REV,
$\vec{v}$, local interdendritic liquid velocity relative to the solid,
∇T, temperature gradient and
$\varepsilon = \frac{\partial T}{\partial t}$, temperature change speed.

If $\frac{\partial g_L}{\partial T} > 0$, the volume fraction of liquid lowers as the temperature lowers: solidification is happening. Otherwise, if $\frac{\partial g_l}{\partial T} < 0$, the surrounding solid remelt and the liquid fraction increases as temperature decreases. A local solidification delay can lead to a slightly wider flow channel. This wider flow channel can widen by remelting the surrounding liquid and turn into visible segregation, or it can shrink if the liquid inside the channel solidifies, in that case, the flow channel reduces. How the channel evoles is described with the equation (1.14). In the equation, $\left(\frac{1-\beta}{1-k}\frac{g_l}{C_l}\frac{\partial C_l}{\partial T}\right)$, is always negative. So, solidification or remelting is controlled by $(\frac{\vec{v}\cdot\nabla T}{\varepsilon})$.

$$Remelting\_Criterion = (\frac{\vec{v}\cdot\nabla T}{\varepsilon}) \tag{1.15}$$

The remelting criterion (1.15) described by Mehrabian and his team can take different values, depending on the orientation of the fluid flow compared to the thermal gradient and this orientation determines if the channel grows or shrinks. There are three possibilities:

- $\frac{\vec{v}\cdot\nabla T}{\varepsilon} > 0$, if the fluid inside the channel flows toward the lower temperatures. The solidification inside the channel is faster and the channel size decreases. This is the *stable* configuration.
- $-1 < \frac{\vec{v}\cdot\nabla T}{\varepsilon} < 0$, in this *intermediate* configuration, the channel solidifies but at a slower rate compared to the surrounding. A solidification occurs, the channels can become unstable.
- $\frac{\vec{v}\cdot\nabla T}{\varepsilon} < -1$ is the condition for an *unstable* configuration. The fluid flow in the channel goes in the opposite direction to the thermal gradient. The liquid fraction

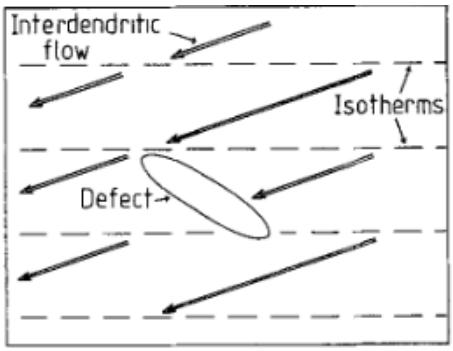

Figure 1.13: Representation of defects in the dendritic network of the mushy zone. From [50].

increases as temperature decreases: remelting happens in the channel. The channel is destabilised and grows.

In 1981, Simpson, Yerebakan and Flemings [50] studied how defects in the dendritic network can affect the channel segregates formation. The remelting criterion [1] is based on a uniform, defect-free dendritic network described by a uniformly varying permeability. In the paper of Simpson *et al.*, the dendritic network presents defects that change locally the fluid flow velocity of the interdendritic fluid, see figure This time, we're talking about an interdendritic network with a defect. The presence of this defect locally changes the flow velocity of the interdendritic fluid, see figure 1.13. It is therefore possible to satisfy locally the conditions necessary for the formation of segregation channels.
The liquid fraction difference between the inside of the defect and the outside as a function of time is given by: $\frac{\partial \delta g_L}{\partial t}$. If the expression is positive, the defect grows and a segregation channel forms. Whereas a negative value of the expression indicates the attenuation and disappearance of the defect. The expression shows the importance of the orientation of the defect relative to the temperature gradient and liquid flow. The authors conclude that the presence of small defects in the dendritic network favours the appearance of segregation channels.

Kumar's criterion The necessity to remelt solid in order to form channel segregates was also questioned by Založnik and Combeau [51] in their 2010 modelling paper on banded segregations in as-cast steel. The alternating positive and negative segregations were obtained without remelting, only a local variation of the fluid flow velocity was necessary.
Kumar *et al.* [2] came up with a new criterion inspired by Flemings' remelting criterion. Whereas the criterion developed by Flemings tracks the evolution of g_l with time, the new criterion is based on the stability of the mushy zone. It tracks the evolution of a perturbation of the liquid fraction field (δg_l) in the mushy zone with time. The evolution depends on the temperature gradient, the isotherm velocity and the velocity of the interdendritic fluid. The permeability considered in the equation is local and not global. A disturbance within the mushy zone is unstable and grows if the following condition is

met:

$$\frac{\partial \delta g_L}{\partial t} > 0 \text{ if } \vec{v_L} \cdot \nabla T > \frac{K}{g_l} \left(\frac{dK}{dg_l} \right)^{-1} (\vec{v_T} \cdot \nabla T) \tag{1.16}$$

with

$\partial \delta g_l$, small perturbation in the liquid fraction,
$\vec{v_L}$, intrinsic liquid phase velocity,
∇T, temperature gradient,
K, mushy permeability (Kozeny Carman equation),
g_l, liquid fraction and
$\vec{v_T}$, isotherm velocity.

In the paper [2], Flemings' and Kumar's criteria are compared. Both criteria are applied to solidification simulations of a Sn-5wt%Pb alloy in an experimental set-up. The simulation results are then compared with experimental data. The comparison of both criteria shows that Kumar's criterion is met before Flemings': the amplification of the mushy zone instability occurs more easily (i.e. is less restrictive) than the remelting phenomenon. The channel segregate initiation is caused by amplifications of a mushy zone instability: the remelting is a sufficient but not necessary condition for the formation of channel segregates. The comparison with experimental results confirms that Kumar's criterion accurately predicts the length and number of channels, whereas Flemings' remelting criterion underestimates their length and number.

1.4 Consequences of segregations in forged parts

Segregations, especially mass and localised macrosegregations, have consequences on the ingot and forged part quality. Segregations influence phase transformations and locally modify the final microstructure of the product. As the microstructure is not homogeneous, neither are the mechanical properties. It is worth noticing that forging operations can alter the size, shape, and distribution of segregations and inclusions within the steel, but cannot eliminate or reduce them.
This section presents the consequences of some segregation patterns on the mechanical properties of the forged or hot-rolled steel. An accentuation is put on banding segregations phenomena in forged or hot-rolled steel.
It is important to keep in mind two points: (1) some segregation patterns described in the section 1.2.2 do not influence negatively the forged parts used by Framatome, (2) the segregation banding presented in this section can be found in the forged parts and is a different phenomenon that the banding segregation (or segregation bands) presented in the section 1.2.2 which can be found in as-cast ingot and does not affect the forged part produces and used by Framatome.

1.4.1 Segregation banding in forged parts

Within forged steels or rolled sheets, banded structures, also known as segregation banding, can be observed, see figure 1.14. They should not be confused with the solidification defect called segregation banding, see 1.2.2. In forged parts and rolled steel, the banded structures are aligned parallel to the main forging or rolling direction and made up of different microstructures, as observed by Grange [52] (figure 1.14) or Pickering and Bhadeshia [5], (figure 1.15). The exact mechanism leading to banded structures is still poorly detailed in the segregation literature. However, Verhoven proposes an explanation [53]. He explains that a network linking the last points of liquid during the solidification of the dendrites can be defined. The spacings between the primary and secondary arms define the mesh of this network, as illustrated in figure 1.16. Since the orientation of the dendrites within a grain is unique, each austenite grain has its own network associated with the last liquid points. The hypothesis is as follows: during deformation, the dense planes of the network align themselves with the direction of deformation using a possible rotation.
In 2003 a correlation between secondary dendrite arm spacing (SDAS), the compressive strain and the width of segregation bands obtained was highlighted by Yamashita and co-workers [7]. The formula (1.17) was developed on laboratory-scale samples (typical microstructure scale of the samples: SDAS = 173 μm and PDAS = 318 μm). The existence of a correlation between SDAS, compressive strain and the width of the obtained bands confirmed that interdendritic segregation can cause banded segregations. In large steel ingots, the cooling is slow, leading to a wide spacing between the dendritic arms [5]. Based on Yamashita equation (1.17), a large SDAS gives large banded structures, however no experimental works on large SDAS have been documented yet.

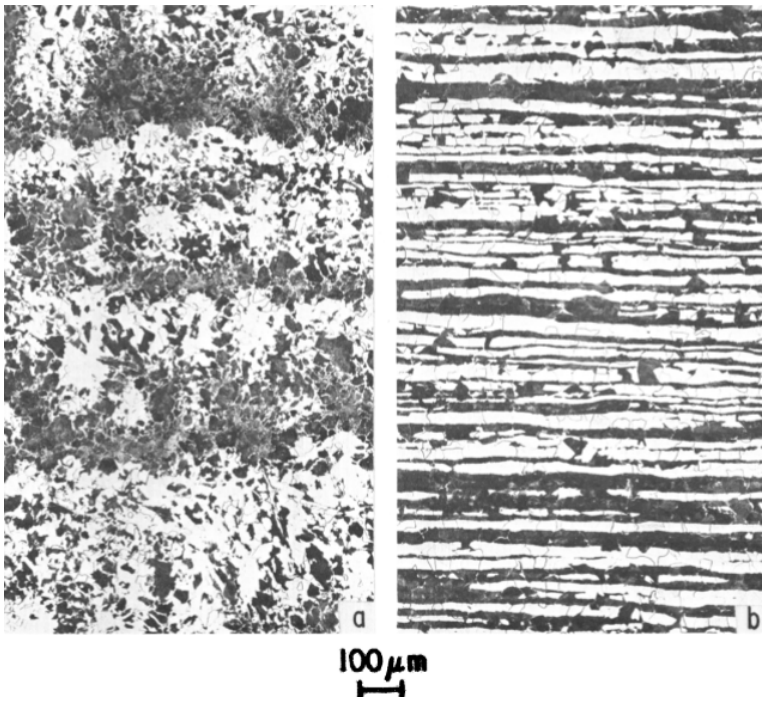

Figure 1.14: Banded structure creation, on the left the ingot structure, on the right hot rolled steel plate structure with ferrite and perlite bands. From [52].

$$L = L_0 \exp(-\varepsilon) \tag{1.17}$$

with

L, width of segregation bands [μm],
L_0, SDAS [μm] and
ε, compressive strain.

The banded structures show segregation through the bands. The richest bands are formed from the positively segregated solid from the last liquid to solidify between the primary and secondary dendritic arms. The depleted bands were formed with the first solid to form within the dendritic arms [5]. The composition differences between the segregation bands lead to the formation during solid-state transformation of different types of secondary microstructures. For instance, the right side of figure 1.14 shows an alternation of ferrite and pearlite in the bands. This observation is also reported by Kirkaldy *et al.* [54] who came up with the terms: pre-segregation and trans-segregation. The pre-segregation refers to the composition gap between the bands, whereas the trans-segregation refers to the final microstructure differences observed between the bands. The trans-segregation can also be used to refer to the potential redistribution of elements occurring during the solid-state transformation. This difference is due to 2 factors: (1) the austenite stabilisation by segregating elements such as Mn and (2) the solid-state transformation temperatures, A_{r3} (transformation of austenite to ferrite during cooling), which depends on the composition of the alloy. Since there are compositional differences between the

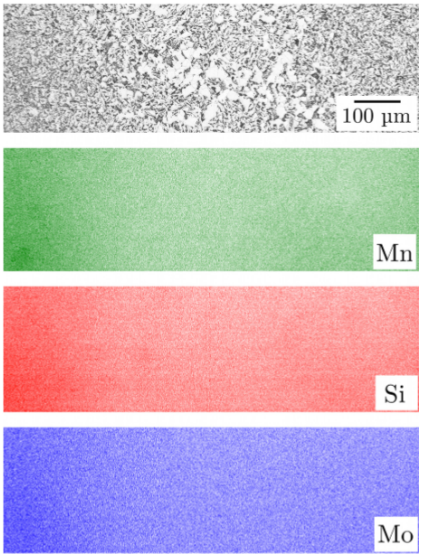

Figure 1.15: Chemical segregation measured with EPMA within a band structure. Top image: structure (A-segregation, allotriomorphic ferrite and Widmanstätten ferrite, moving from bottom left to top right). Three bottom images: chemical composition, showing highest solute concentrations in the A segregate. From [5].

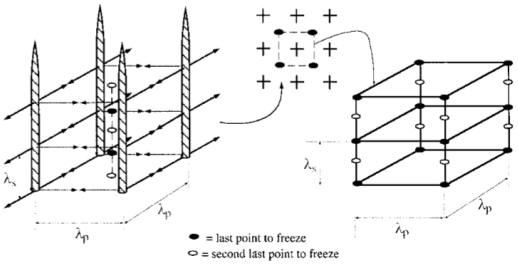

Figure 1.16: Schematic of the network formed by the last liquid points between the dendritic arms. From [53].

austenite bands, there is also a difference in transformation kinetics, ultimately leading to different secondary microstructures [7, 15, 53, 54].

1.4.2 Segregations and mechanical properties

The secondary microstructure of steels is influenced by segregations, and mechanical properties are directly linked to microstructure. Banded segregations therefore have a role to play in the mechanical properties of final parts. This subject has been studied by several authors, on a variety of different grades.
The main consequence of the banded segregations is anisotropy of secondary microstructure: bands of different microstructures exist in forged parts and rolled steel sheets. The more bands in the material, the greater the anisotropy, and the greater the influence of the sampling direction on the results [55]. The influence of sampling direction is especially visible on impact test samples (see figure 1.17). Resilience in the transverse direction (perpendicular to the segregation bindings) is much weaker than resilience in the longitudinal direction. In the transverse direction, cracks propagate easily along the bands. In the longitudinal direction, however, the bands are perpendicular to the cracks and hinder their propagation, as shown in the diagram in Figure 1.18 [55]. Grange [52] demonstrated that the inclusion presence worsens the deleterious influence of segregation banding in transverse samples.

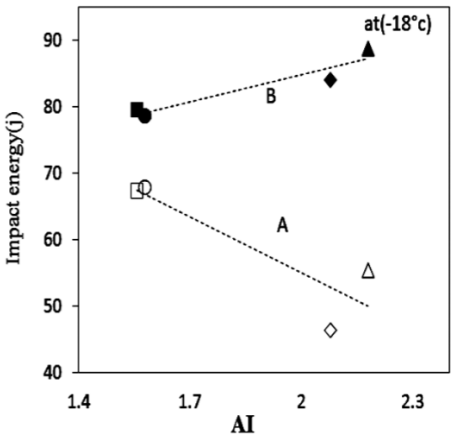

Figure 1.17: Effect of sampling direction and banded segregation on impact strength. Charpy specimen taken in (A) transverse direction, (B) longitudinal direction. AI stands for Anisotropy Index, AI = 1 is homogenous, AI > 1 is anisotropic. From [55].

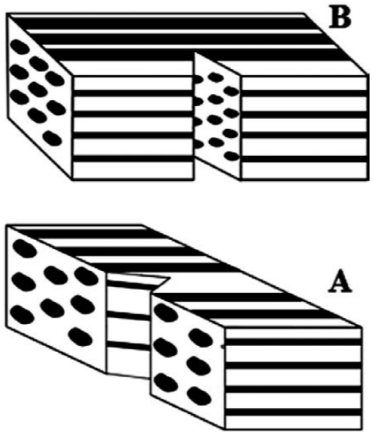

Figure 1.18: Spatial representation of band structures within Charpy specimens taken in (A) the transverse direction and (B) the longitudinal direction. From [55].

The anisotropy caused by the banded structure also affects other mechanical properties. Yan *et al.* [6] shown its impact on the hardness: the hardness of the positively segregated bands is greater than that of the negative bands (figure 1.19). The hardness changes are also related to secondary microstructure disparities between the different bands in the structure.

A study show the presence of segregation banding in forged or hot-rolled parts designed for the French nuclear industry [56]. The segregation bands cause banded structures with differences of final microstructures in the parts strudied. The mecanical properties are affected by the banded structure: the impact toughness and the tenacity values are dispersed. Indeed the presence and location of segregation banding in the sample can be critical by the either their location or their density. The segregation banding can cause the brittle fracture of the sample.

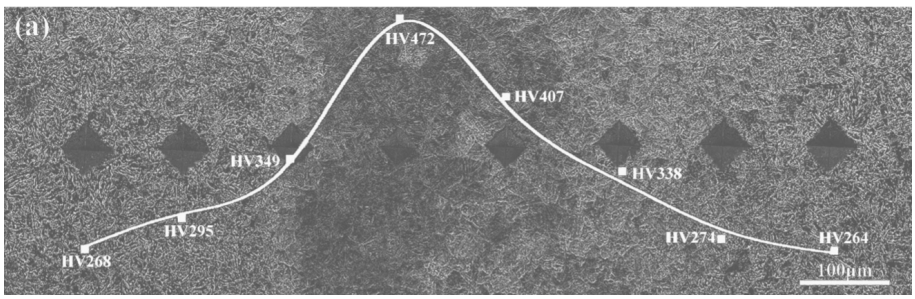

Figure 1.19: Microhardness profile through a band structure, the darkest part is positively segregated. From [6].

Mass macrosegregation (at the top of the ingot, the carbon concentration is higher than at the bottom, where negative segregation is observed) also influences the mechanical properties homogeneity. According to a study from Thornton and Colangelo [57], the mechanical properties of parts from the bottom section of an ingot are weaker than those of the parts from the head of the ingot. The carbon segregation causes the mechanical properties gap: carbon concentration is key for mechanical properties and its segregation over the ingot size is important. The pattern of macrosegregation determines the mechanical properties of the forged parts.

1.5 Characterisation of segregation patterns

In order to understand the formation of segregation patterns and to find ways to control them, there is a need for reliable characterisation tools. The observation is the first step toward the understanding. Segregation in ingots is a multiscale issue: because of this, diverse characterisation techniques are employed to track steel composition at different scales. There is a multitude of characterisation techniques, and choosing the characterisation technique that suits a study can be a difficult step. In this section, several techniques are presented, so an informed choice can be made when comes to the technique choice. The techniques presented are divided according to their investigation scale (large scale or small scale) and a comparison table is available at the end of the section (table 1.1).

1.5.1 Large scale investigations

Large-scale investigations of the chemical composition are crucial for macrosegregation characterisation. As explained in section 1.2, macrosegregation can be mass macrosegregations or local macrosegregations. The characterisation techniques presented in the following part can be used for mass macrosegregations, local macrosegregations or both. Other techniques exist, but in this work, only the more popular are reviewed.

Macroetching

Macroetching techniques make possible the observation of segregations at the ingot or the forged part scale. For a global observation of macrosegregation patterns, ingots are cut in half and the cross-section is etched, large samples can also be used for local observation or practical reasons (size, weight,...). The steel composition and the primary and secondary microstructures influence the choice of the etchant. Common macro etching techniques include sulfur print (also known as Baumann print), Nital etching or picric acid etching. Baumann print or sulfur print shows the sulphur segregation of the etched surface, see figure 1.20. The surface needs a coarse grinding and is put in contact with film paper soaked with aqueous sulphuric acid solution (1 to 10%). The sulphuric acid in the paper reacts with the sulphides present on the sample surface and creates a gaseous release of hydrogen sulphide (H_2S). The hydrogen sulphide reacts with the silver salts (such as bromides) present in the paper to form silver sulphides, making a black mark on the film [58]. Several examples of sulphur print are available in literature [20, 21, 24, 31, 59]. Sulphur print was used to track A and V segregates. This technique is based on a correlation between sulphur segregation and carbon segregation. It cannot be used on modern low sulphur-content steels.
To study the macrosegregation pattern in low sulphur-content steels, without using sulphuric acid, several macroetching techniques were developed such as picric acid or Nital etching. Different procedures exist for picric acid and Nital etching, each steel grade needs its specific procedure to be sure to distinguish the primary microstructure from the second. A procedure for picric acid is briefly described in [60], researchers use picric acid to reveal Mn-segregation and fine cracks on a commercial steel with very low S and

P content. A picric acid solution (60g of picric acid, 15g of $CuCl_2$), 60 mL of soap (no additional information is provided in the paper) and 3 000 mL of water) is applied to the coarsely ground sample surface, let for 30 min and then the surface is washed out with water, dried and polished (fine Emery polishing paper of N° 1000). That step pushes fine steel particles into the etch pits, the particles are then collected on transparent adhesive tape which is placed on white paper for observation. The segregated area appears marked with the steel particles on the white paper.
Concerning the Nital etching procedure for primary microstructure observation, a multitude of procedures exist. Depending on the steel grade, repeated or single applications of Nital are needed to reveal the segregations. Pickering used Nital etchant on its as cast-samples to reveal A-segregates in his PhD work [61] and to observe segregation in forged part [20].
The change in the composition of modern steel and the shift toward low S-content steel forced researchers to develop new techniques for macroetching. With picric acid or Nital, macroetching can be used on modern steel to investigate macrosegregation. However, it only provides qualitative information and the imaging of some large etched surfaces can be a challenge.

Figure 1.20: Baumann print of a 30 t steel ingot, carbon content: 0.33%, height: 2,140 mm and diameter: 1,315 mm. From [21].

Local chemical analysis

Local chemical analysis provides quantitative information on macrosegregation. Several solutions exist to investigate the local composition in specific spots of the ingot: Optical

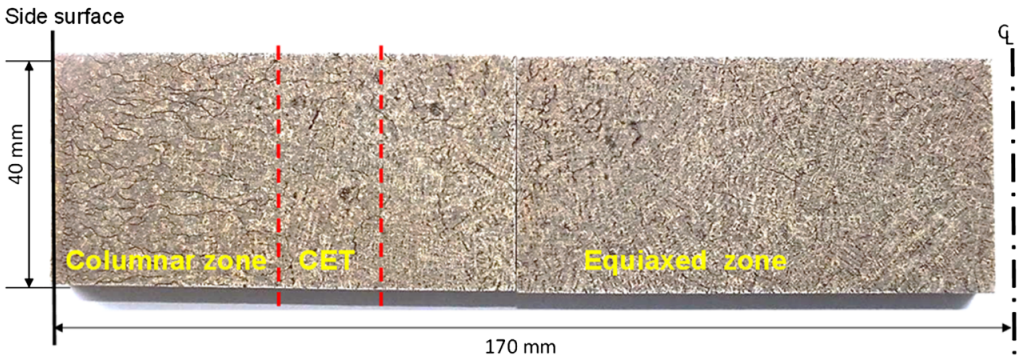

Figure 1.21: Macroetching carried out on a transverse section of ingot, different crystallisation zones are indicated, segregations in A appear as black dots. From [31].

Emission Spectrometry (OES) can be employed for heavy element quantification and combustion analysis is usually employed for Carbon and Sulphur quantification.
OES is a common technique for analysing Mn, Si, Cu, Ni and other heavy elements. It can be done in a laboratory with samples taken directly on the ingot, or with mobile instrumentation to carry out the measures directly on the ingot surface, without sampling required. The latest option is easy to implement and requires little preparation. The Spectrotest mobile equipment was used by Tkadlečková et al. to analyse Mn, Ni, Cu and Ni on specific lines on a 90 t ingot cross section [62–64]. With this technique, there is no need to take samples from the steel ingot.
With OES mobile equipment, sampling can be avoided for heavy elements, but this is not the case for C and S analysis. Combustion analysis is a reliable technique for C and S analysis, that has been used in metallurgy for a long time [30]. The analysis is performed on steel chips (0.5 to 2.0 g are needed). Carbon segregation were extrapolated from grid analysis: the cross-section surface of the ingot was trapanned in the carefully selected area before extrapolation into isoconcentration lines [65] or maps [40, 66]. The obtained segregation maps are useful for ingot-scale solidification simulation calibration.
There are limitations to OES and combustion analysis. The technique presented is time-consuming (sampling, surface preparation, preparation) and expensive since numerous steel chips need to be analysed in a laboratory for a signal segregation map. Moreover, the accuracy of the segregation maps obtained is open to doubt since it is an interpolation and local macrosegration such as channel segregates can easily be missed or misinterpreted with the grid analysis.

X-ray fluorescence

X-ray fluorescence (XRF) was used by Pickering et al. to map a whole ingot vertical cross-section [49, 67, 68]. The authors used a mobile device fixed on an instrumentation bench to perform large surface scanning. The technique is easy to use since it does not require vacuum or heavy surface preparation. Large distances were analysed with a 5 $\times$ 7 mm^2 cell, providing complete segregation maps. An advantage of the device developed by Pickering et al. is its adaptability to extremely large samples, making sampling a

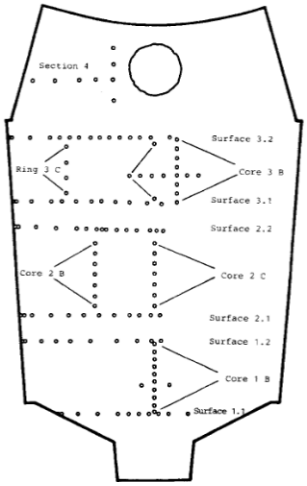

Figure 1.22: Location of chemical analysis points on a 180 t ingot, 20 MnMoNi 5.5. From [65].

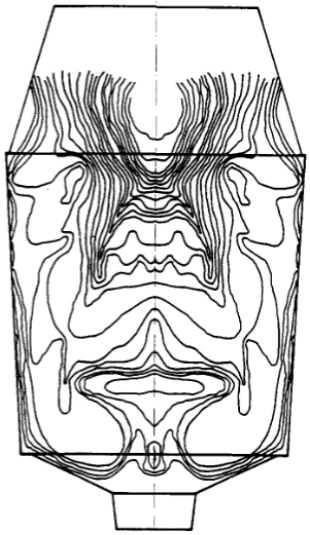

Figure 1.23: Carbon isoconcentration lines for a 180 t, 20 MnMoNi 5.5 ingot plotted based on the sampling plan shown in figure 1.22. From [65].

facultative step. Other XRF devices, fixed laboratory devices, require samples to be taken, prepared and inserted into the machine. When samples are required, they can be taken in specific positions of the ingot or part to assess the macrosegregated state of the ingot or the part [69].

XRF pieces of equipment, mobile, fixed or mounted on an instrumentation bench, are very useful for macrosegregation analysis. However, the size of the analysed cell (around 5 mm in diameter) is too large for the characterisation of some segregation patterns, as local macrosegregation (depending on the ingot size) or smaller segregation patterns (microsegregation).

The spatial resolution of the segregation maps produced with XRF can be increased by using a beam with a smaller spot. Spot size can go down to a few µm, in that case, the equipment is called a micro-X-ray fluorescence (µXRF). With µXRF, cutting samples is required to fit the samples in the sample chamber. Sengupta et al. [70] mapped centerline segregation in an Advanced High Strength Steel (AHSS) slab using a µXRF device from IXRF. The specificity of their equipment is a spot size that can adapt from 40 µm to 2 mm. The larger zone investigated in their study is 200 × 40 mm^2 on a 200 × 100 mm^2 (the thickness is not indicated, but with this sample dimension it should not be greater than 20 mm for device requirement). The quantification of the device used was tested on OES steel standards [70], several surface finishes were tested and measurements were compared to OES and Electron Probe Micro Analyser (EPMA) (see 1.5.2) [71]. The use of µXRF for centerline (which is a type of macrosegregation) investigation was a success. The M4 Tornado Bruker device is another µXRF device, common in the field, several examples on its use are reported in literature:

- The work of Li *et al.* on cladded layers in addictive manufacturing, they tracked the composition evolution in the cladded layers with a 20 µm step size, leading to a high-resolution centimetric (30 × 26 mm^2) composition map [72].
- In 2021, Jabar and co-workers used µXRF and map segregation banding in ex-service boiler components. Their paper present quantitative millimetrics (6.8 × 5.8 mm^2) maps of Mo, Cr, Nb and V realised with a 20 µm spot size [73].
- Small scale samples were also characterised to study segregation in Ni-based Superalloy. For this study a larger spot size was used (170 µm) was used to map millimetric samples [74].

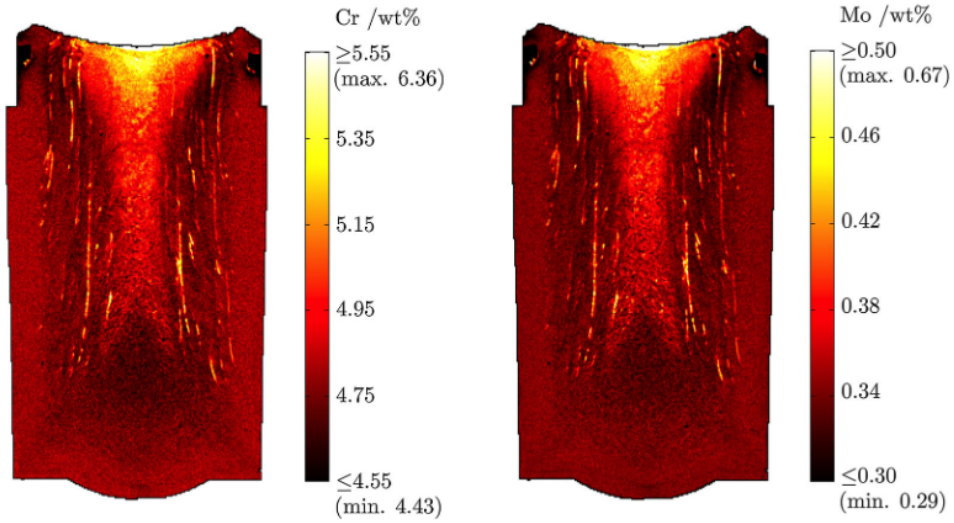

Figure 1.24: Chromium and molybdenum mapping using X-ray fluorescence spectrometry on the slice of a 12 t high-carbon ingot. From [68].

1.5.2 Small scales investigations

The techniques previously introduced cannot be used for microsegregation characterisation. The characterisation of such segregations requires precise tools and equipment. A short selection of techniques popular for the investigation of segregations at the microscale is presented in the following part.

Optical microscopy

Optical microscopy is a useful tool for microsegregation characterisation. During the solidification of alloys, microsegregation occurs and marks the primary microstructures. The primary microstructure (columnar, dendritic equiaxed or globular equiaxed) can be characterised with optical microscopy. Samples need to be ground, polished and etched before the observation. Based on the structures to observe, the alloy and its composition, the etching procedure needs to be adapted: it can reveal primary microstructure or

secondary microstructure (structure obtained after solid-state transformation) or both at the same time. For low alloy steels, Bechet-Beaujard warm etching [75] can be employed to reveal solidification grains. Based on optical microscopy images, dendrites can be measured [76]. Dendrite characterisation also includes secondary dendritic arms spacing (SDAS) measurement [77] (an example of dendritic microstructure is presented in figure 1.25). On some alloys such as Al-alloys, dendrites are visible without etching. Still, color etching is used to investigate complex microstructures obtained after compression, heat treatment, incomplete remelting, etc [78].
Optical microscopy is also a useful tool for secondary microstructure characterisation. In ingot solidification, macrosegregations such as A-segregates can cause local differences in secondary microstructures: since solid-state transformation depends on carbon content, the obtained microstructure can be different inside and outside of the A-segregate. Pickering and Bhadeshia investigated this difference in 2014 [5].
The understanding of the forged parts' mechanical properties needs an extensive characterisation of the microstructure of the parts. Segregations still exist in forged parts and influence the microstructure development. Once again, optical microscopy is a key technique when combined to specific sampling, sample preparation and etching [6].

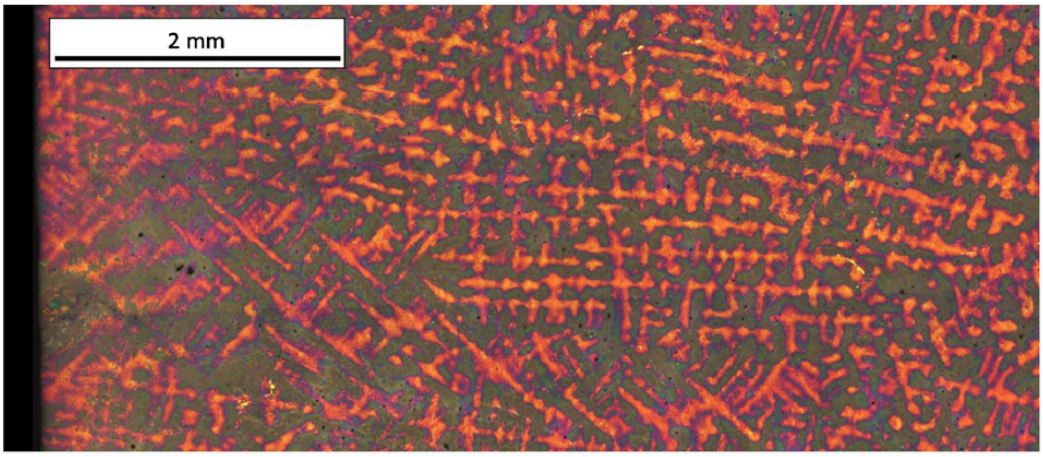

Figure 1.25: Solification microstructure reveal by colour etching. From [77].

Electron Probe Micro Analyser

With an Electron Probe Micro Analyser (EPMA), it is possible to measure the composition of steel, precisely, at a small scale. The interaction volume of the measure is usually 1 μm^3, and light elements such as C can be measured with EPMA. For these reasons, EPMA is a common tool for the characterisation of segregation at a small scale. EPMA can be used in point analysis, line scans or grid scans to provide segregation maps. In many applications, the different EPMA modes are combined. For instance, Pickering and Bhadeshia used EPMA to map qualitatively Mn, Si and Mo on samples containing A-segregates. The sample mapped is approximately 300 $\times$ 900 μm^2 was previously selected with optical microscopy analysis. On the presented sample, 3 different areas are distinguished and quantitative EPMA point analyses were done in each area to complete

the study [5]. In another study, EPMA modes are combined: a line scan and qualitative map are realised over a banding segregation phenomenon observed in a steel plate. The purpose of the study was to investigate the effects of Mn segregation on strength and ductility in quenched and partitioned steel. The EPMA provides a precise quantification of Mn in the segregated area and the matrix that explains the different final microstructures obtained in both areas and the mechanical properties differences [79]. The work of Yan et al. is another example of line scan over banding segregation phenomenon [6].
Quantitative maps realised with EPMA are found in the literature. Yamashita et al. mapped Mn on as-cast and compressed steel samples to see the deformation of the primary microstructure during compression. As the microstructure is coarser before compression, they adapted the sport size. For as-cast samples a 5 μm spot was used, whereas for compressed samples the sport size was 1 μm to adapt to the finer structure [7].
If there is enough data point on microsegregated samples, the data can be used to calculate thermodynamics constants, such as the partition coefficient, k [80].

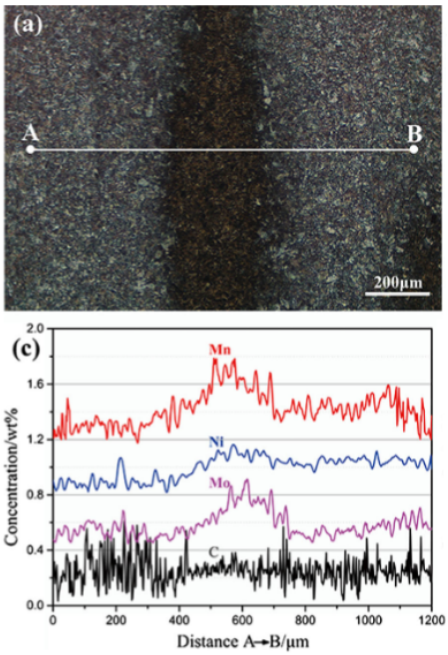

Figure 1.26: EPMA analysis along a line, optical microscopy image of the zone studied in (a) and variation in concentration from point A to point B in (c). From [6].

1.5.3 Comparison of the characterisation techniques

In table 1.1, the different characterisation techniques previously described are summed up. The table helps with the comparison of the techniques: each technique has advantages and drawbacks. The appropriate technique varies based on the size of the sample, the segregation scale and the microstructure size to investigate.

Table 1.1: Summary and comparison of the different characterisation techniques used for segregations.

Technique	**Qualitative or quantitative**	**Sample scale**	**Observed segregations patterns**	**Destruction of the sample**	**Major drawbacks**	**Examples in the literature**
Macroetching	Qualitative	cm^2 to m^2	Mass macrosegregations (Hot top, negative base segregation)	Surface alteration	Qualitative information Challenging imaging	[20, 21, 24, 31, 59–61]
OES	Quantitative	cm^2	Mass macrosegregations (Hot top, negative base segregation)	Surface alteration	Time consuming Extrapolation from grid to maps	[62–64]
Combustion analysis	Quantitative	cm^2	Mass macrosegregations (Hot top, negative base segregation)	Yes	Time consuming Extrapolation from grid to maps Expensive Destructive	[30, 40, 65, 66]
XRF	Both	cm^2 to m^2	Mass and located macrosegregations (Hot top, negative base segregation , channel segregates)	No (surface preparation)	Large spot size (5 mm) Non trivial quantification	[49, 67, 69]
µXRF	Both	cm^2	Located macrosegregations (Centerline segregation)	No (surface preparation)	Non trivial quantification	[70–74]
Optical microscopy	Qualitative	cm^2 to μm^2	Microsegregations (Small grains and dendrites)	Surface alteration	Qualitative information Reproducibility of etching	[5, 6, 76–78]
EPMA	Both	mm^2 to μm^2	Microsegregations (dendrites, dendritic arms)	No (surface preparation)	Time consuming Limited to a few elements / analysis Extrapolation from grid to maps	[5–7, 79, 80]

1.6 Summary

This chapter presented the literature on segregation in forged ingots. Here are some of the main conclusions:

- In large steel ingots, segregation appears at different scales during the steel solidification. The formation of microsegregation (at the dendrite scale) is inevitable; it has been studied for decades and several models (1D analytical) exist and describe microsegregation. The formation of macrosegregation (at the ingot scale) follows well-known patterns. Two types of macrosegregation co-exist: mass macrosegregation (top hop, negative base segregation) and located macrosegregation (A and V segregates). Careful ingot process selection can help reduce the extent of macrosegregations.

- Modelling is a useful tool for the understanding and the prediction of macrosegregation (mass and located). SOLID® is a commercial software, used and developed in academia, which models the solidification of large ingots. It makes it possible to test the influence of different physical phenomena on segregation formation. A reliable modelling tool can be used to compare different processing possibilities and guide industrial development.

- In large-scale ingots, some segregation patterns are definitive: it is not possible at the industrial scale to homogenise neither intermediate-scale segregation nor macrosegregation in ingots. Segregations go with the ingot through the whole shaping process. Forging or rolling operations can alter the size, shape, and distribution of sergegations within the steel, but it is difficult eliminate or reduce them.

- In forged parts banded structures (segregation bandings) appear after the deformation of segregation during the forging process. The formation mechanism of the banded structures is still uncertain; however, its consequences are real: anisotropic secondary microstructures, anisotropic mechanical properties and weakening of resilience in the transverse direction. The segregations that cause banded structures in forged ingot seems to be microsegregations or intermediate scale segregations.

- The observation of segregation is key to their understanding. Through the years, numerous characterisation techniques were developed and used for segregation characterisation. Some techniques are adapted to the ingot scale and efficient in mass macrosegregation visualisation and quantification. Others are useful for microsegregation characterisation. However, for intermediate segregation and localised macrosegregation, there is no star technique. On of the goal of this PhD work is to adress this issue.

Chapter 2

Materials and Methods

1 pot de yaourt
3 oeufs
3 pots de farine
1 sachet de levure
1 pot et demi de sucre
1 jus de citron
Un demi pot d'huile
180 °C, 40 min

Maman
Gâteau au yaourt
- Mon premier protocole
expérimental

Contents

To understand intermediate-scale segregations in large steel ingots, specific techniques and materials are needed. This chapter intends to present the material used for this investigation, as well as the characterisations and analysis techniques used to observe and understand the segregation patterns. Three sections form this chapter. The first one is dedicated to the samples, examining which kind of samples are required. The different ingots and parts are described, and the motivations behind the location of the samples are also discussed. Then the characterisation techniques used to observe segregations at the solid state are presented in the second part. The presented techniques cover a large-scale range of macroscale to microscale observations. Finally, the last section reviews the analysis techniques employed to process the data and understand the segregation patterns observations.

2.1 Materials

In an experimental process, once the field of the study is defined, it is crucial to carefully select and prepare the samples. In that section, the different ingots under investigation are presented, as well as the forged part examined. The selection of collection locations for samples is also discussed. Specific preparations employed to produce user and characterisation-friendly samples are presented in the last paragraph.

2.1.1 Steel grades

This study focuses on the solidification of steel used for the pressurized water reactors in nuclear power plants. The different parts of the reactor pressure vessel and steam generator are manufactured from ingots such as the ones studied in the present work. The ingots are cast with low-alloy Mn-Ni-Mo steel known as 16MND5, 18MND5 and 20MND5 according the AFNOR designations [81]. The requirements of such grades are described by the norm NF A 36-603 [82]. The targeted compositions for the studied steels are recorded in tables 2.1, 2.2 and 2.3.

2.1.2 Sample selection

For this study samples were taken in three different ingots and one forged part. From now on the ingots will be referenced to as the *short* ingot, the *long* ingot and the *hollow* ingot. Both ingots and forged parts were industrially produced. For instance, the *long* and *hollow* ingots can be used to forge the shell (hollow part of the vessel), the *short* ingot is used to build up the upper and lower vessel heads (also called the upset parts of the vessel). The forged part under investigation is an upper vessel head. The 3 ingots and the forged part were studied with the same method, with the idea of being able to compare the different samples between them. The comparison of samples taken from the different ingots can help to understand how the solidification and segregation formation are influenced by the shape and height of the ingots which influence the local and global solidification rates, the heat and solute transport on a long scale, ... The comprehension of the segregation formation in the different ingots is crucial to select the most suitable ingot for each industrial application. Finally, on some ingots, samples were taken in

C	**Al**	**Si**	**P**	**S**	**V**
0.155 - 0.175	0.010 - 0.025	0.150 - 0.250	$\leq$ 0.008	$\leq$ 0.005	$\leq$ 0.010
Cr	**Mn**	**Co**	**Ni**	**Cu**	**As**
0.120 - 0.220	1.350 - 1.550	$\leq$ 0.030	0.650 - 0.800	$\leq$ 0.080	-
Nb	**Mo**	**Sn**	**Sb**		
-	0.450 - 0.550	-	-		

Table 2.1: Targeted composition in wt% for 16MND5.

C	**Al**	**Si**	**P**	**S**	**V**
0.185	0.015 - 0.040	0.200	$\leq$ 0.008	$\leq$ 0.008	$\leq$ 0.010
Cr	**Mn**	**Co**	**Ni**	**Cu**	**As**
0.170	1.450	$\leq$ 0.030	0.725	$\leq$ 0.120	-
Nb	**Mo**	**Sn**	**Sb**		
-	0.500	-	-		

Table 2.2: Targeted composition in wt% for 18MND5.

C	**Al**	**Si**	**P**	**S**	**V**
0.190 - 0.210	0.020 - 0.036	0.150 - 0.250	$\leq$ 0.008	$\leq$ 0.005	$\leq$ 0.010
Cr	**Mn**	**Co**	**Ni**	**Cu**	**As**
0.150 - 0.250	1.275 - 1.500	$\leq$ 0.010	0.730 - 0.790	$\leq$ 0.080	$\leq$ 0.008
Nb	**Mo**	**Sn**	**Sb**		
$\leq$ 0.010	0.460 - 0.540	$\leq$ 0.010	$\leq$ 0.002		

Table 2.3: Targeted composition in wt% for 20MND5.

several locations and directions so the segregation formation was observed in the same ingot, in different directions, at the same nominal composition but with different thermal history and solidification structures.

The purpose of the study is to investigate intermediate-scale segregation. Thus, samples need to be large enough to contain several grains. Industrial scale ingots such as the ones under study undergo long solidification times (more than 24 hours), hence presenting large solidification structures. That is why samples taken were of the order of magnitude of thousands of square centimetres.

Both *short* and *long* ingots are directionally solidified ingots and were cast in the same type of ingot mould. The mould is made with cast iron, its inside is lined with refractory bricks that can be changed to extend the mould's life. The kind of mould used for *short* and *long* directionally solidified ingots has an internal diameter of 3 meters it is filled up from the bottom with a unique central casting hole. To make a long ingot a larger amount of steel will be cast in the mould resulting in a longer ingot. The *hollow* ingot is cast in a hollow cast steel mould which is distinguished by its 2 internal diameters: the outer part of the steel ingot produced being 3 m and the diameter of the hollow middle part of the ingot being 1.3 m. The feeding of that ingot is made with 4 casting holes evenly distributed around the hollow cylinder. In the middle part of the mould, air is blown during the cooling of the ingot to approach an even solidification rate between the middle wall and the outer wall.

The most studied ingot, is the *short* ingot, it is a low alloy steel 16MND5 ingot of 116

t which was directionally solidified, see figure 2.1. In this ingot, samples were taken at 3 different locations in different directions. Two batches one of 30 samples and another of 2 were taken at mid-height, and one-third in radius, the C position on the drawing. According to some internal previous studies, at this position, the columnar solidification zone is supposed to be over. The samples are supposed to be located close to the columnar to equiaxed transition (CET) zone or in a fully equiaxed zone. 3 other samples were taken on the central axis near the ingot top (D position) and finally, a last sample was taken on the central axis near the bottom of the ingot (E position). The 30 samples taken near the CET were serial cut horizontally whereas the other samples are independent and were taken vertically in the ingot. All the samples were taken on a central axis plan containing the mould feeding hole.
This second ingot, the *long* ingot, is also directionally solidified. It weighs 170 t and was cast with 18MND5 steel. In this ingot 4 adjacent samples were taken vertically close to the CET zone, as can be seen in figure 2.2. The interest of these samples is to provide a direct comparison with the samples taken from the short ingot. The samples were also taken on a central axis plan containing the mould feeding hole.
The last ingot included in this study was a 173 t low alloys steel *hollow* ingot. It was cast with 20MND5 steel and conventionally solidified. In this ingot, 4 samples were taken vertically at mid-thickness, as represented in figure **??**. Two samples were taken in the upper part of the ingot and two in the lower part of the ingot. These 2 sampling locations were selected for their different solidification structures. In the upper part, the structure is expected to be equiaxed whereas in the lower part, globular structure is expected. This ingot will provide a comparison with the long ingot structures and segregations since both can be used to produce the same final parts. For that ingot, the mould used has 4 feeding holes, the samples were taken form a plan containing one of the feeding holes.
Finally, a forged part was investigated, see figure 2.3. This part is forged from a 116 t directionally solidified ingot, identical to the one studied in this work. Four samples were taken in the part at the L-position. The samples were taken vertically in two different directions in an area forged close to the area corresponding to the as-cast section where the 30 serial cut samples were taken in the as-cast ingot. This selection enables us to compare the as-cast steel with the forged steel.

2.1.3 Sample preparation

From the 116 t ingot, three cubes with approximately 20 cm side of steel were cut out using a blowtorch. The cube's sides were cleaned with a saw cut. One of the cubes was cut into 4 different blocks, and one was serial cut to give the 30 successive samples used in this study. The samples were cut using wire electron discharge machining, which technique enables to cutting of thin samples with a minimal loss of matter. The final samples are $110 \times 95 \times 4.65$ mm^3 between each sample, 0.35 mm of matter was lost with the cutting, hence the distance between two investigated surfaces is 5 mm. On the adjacent block, two samples were taken vertically with the same techniques. Their size is similar to the size of the horizontal samples. The remaining samples taken at different places in the ingot were sawed, they are smaller than the previously introduced and were used for

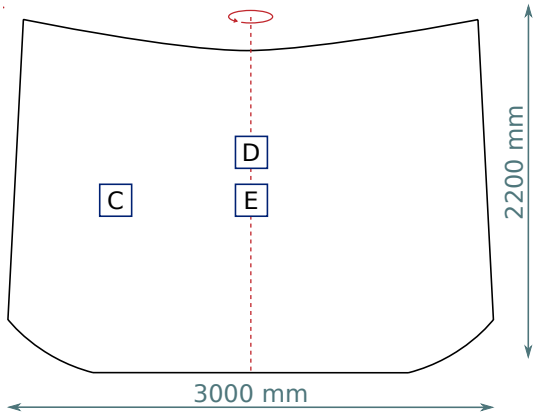

Figure 2.1: Sectional diagram of the short 116 tons ingot.

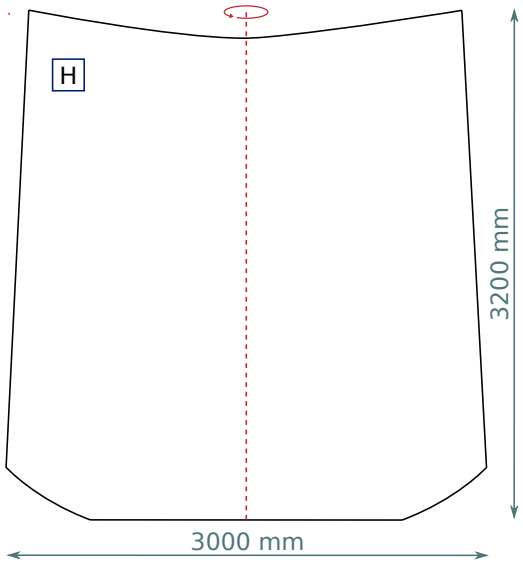

Figure 2.2: Sectional diagram of the long 170 tons ingot.

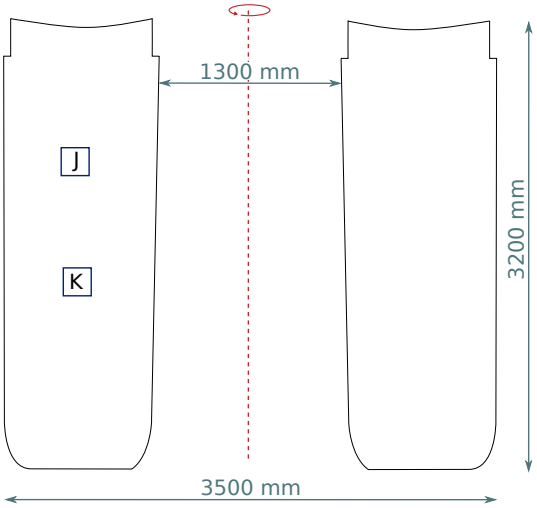

(a) Sectional view

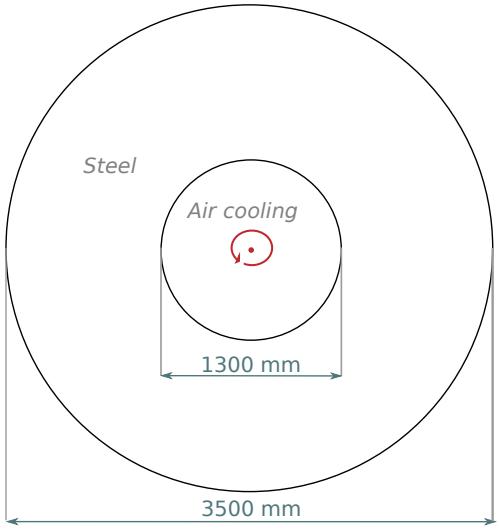

(b) Top view

Figure 2.3: Diagrams of the hollow 173 tons ingot.

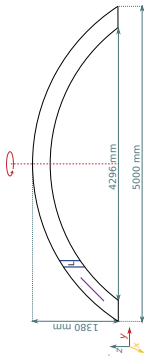

Figure 2.4: Schematic of the forged part manufactured from a *short* ingot similar to the one described in figure 2.1.

methodological purposes.
In the two other ingots, steel plates of approximately 22 x 20 cm were cut out with a blowtorch and were sawed in smaller samples. Each plate was cut into 4 samples. During the study, some small-scale samples (around $1cm^2$) were taken from the plates to investigate smaller surfaces.
The forged part sampling process was also multi-step: first, a steel block with approximately 20 cm side was taken with a blowtorch on the whole thickness of the part. Then from this block, sub-blocks were sawed and samples were cut using wire electron discharge machining. The obtained samples are 1 cm thick and measure approximately $5 \times 7cm^2$.
All the samples studied in this work are summed up in table 2.4.

Ingot	**Sampling location**	**Sampling direction**	**Number of sample taken**	**Approximative sample size (mm)**	**Usage**
Short ingot	C	xy	30	$100 \times 110 \times 5$	3D reconstruction
Short ingot	C	xz	2	$100 \times 110 \times 10$	Ingot comparison
Short ingot	D	yz	3	$10 \times 15 \times 2$	µXRF trials and EPMA
Short ingot	E	yz	1	$40 \times 40 \times 5$	µXRF trials
Long ingot	H	xz	4	$100 \times 110 \times 10$	Ingot comparison
Hollow ingot	J	xz	2	$100 \times 110 \times 10$	Ingot comparison
Hollow ingot	K	xz	2	$100 \times 110 \times 10$	Ingot comparison
Forged part	L	xz and yz	2 and 2	$90 \times 60 \times 10$	Forging effect,

Table 2.4: Summary of the samples studied in this work

2.2 Characterisation techniques

The sample collection and preparation are the first steps toward characterisation. Segregations exist at different scales, and for each scale, different characterisation techniques enable the observation of the segregation patterns. The suitable techniques for a project depend on many factors for instance: the scale to observe, the size of the sample, the accessibility of the devices, the time available, the elements to investigate, and so on. In the following section three characterisation techniques used for this study are presented. For macroscale observations, the samples were etched and macrographs were taken. For intermediate-scale characterisation, micro-X-Ray Fluorescence (µXRF) was used to map Mn or Mo content on the surface of the samples. Finally, several samples were investigated at a microscale with Electron Probe Micro Analyser (EPMA).

2.2.1 Large scale: Etching and macrography

Etching is a fast and cheap technique that produces an overview of the structures. Macroscopic etching can help to make decisions concerning samplings, such as cutting directions, sizes or geometry of the future samples. A first batch of samples is usually taken for the ingot under investigation, this batch of samples provides an overview of the structures observed in the ingot. Then areas of interest can be selected and more samples can be taken. During that study, some samples were taken in the ingots based on previous macroscopic observations, whereas some samples were directly selected from the macroetched ones.
The principle of etching in solidification studies is to reveal the chemical segregation that appears around the primary structures during solidification. Etching procedures are diverse. Choosing the most suitable procedure ensures appropriate results. In this study, low alloy unforged and forged steel was investigated. Several etchants were tested with different application techniques. The béchet-beaujard solution was applied hot or cold on the sample's surfaces, and different compositions of the Bécher-Beaujard were also tested [83]. The Villela etchant was also tried on the samples [84]. However, neither Villela nor béchet-beaujard solutions gave satisfying results. For these kinds of steel (16MND5, 18MND5, or 20MND5), it is repeated Nital etching that highlights the solidification structure the best. Nital etching is known to reveal both solidification structures and solid-state transformation structures. However, with the suitable procedure, 3% Nital mainly highlights the solidification structure even if primary austenitic grain boundaries remain visible. Room temperature 3% Nital solution was applied generously on the sample surface that was previously coarsely ground (up to a P1200 SiC paper is enough). After a few seconds, the Nital solution was wiped out from the surface of the sample with cotton, and a new solution was applied to the sample. Several passes are required, every time the Nital is applied on the sample for a longer time. The solidification structures appeared after a few repetitions of these steps, the number of repetitions and the time of Nital application can vary depending on the steel grades. On the last pass, Nital was wiped off and the sample was rinsed with Ethanol, dried with compressed air, rinsed again with Ethanol and dried again until there was no liquid left in the eventual porosities. Spray lacquer was used on the surface of the etched samples, it protects the sample from corrosion (for longer conservation) and also improves the contrast between

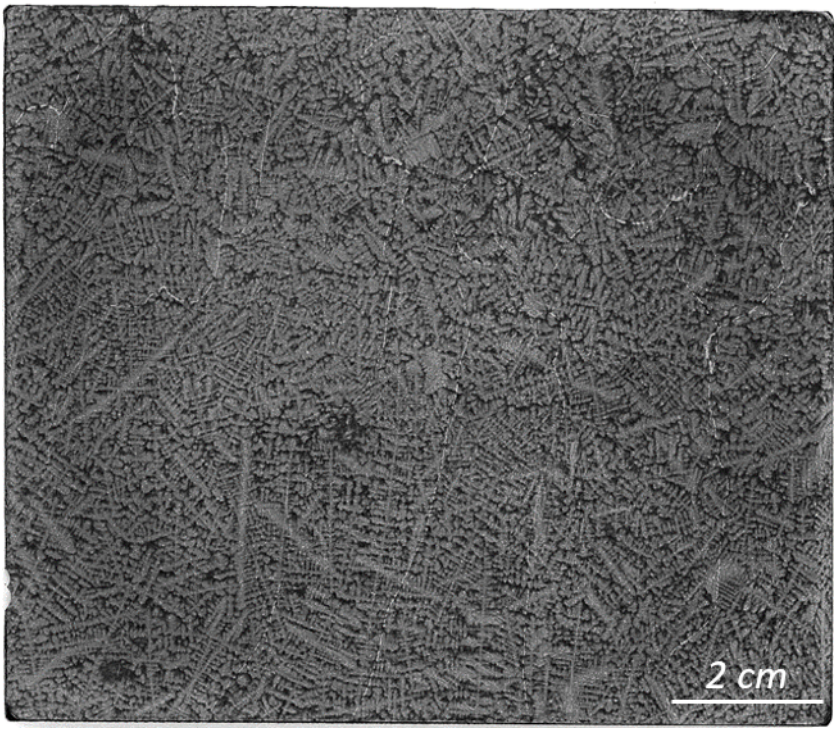

Figure 2.5: Optical macrograph of the sample C2_1. Solid depleted in solute appears in light grey, while enriched regions appear in dark. The thin bright lines are primary austenitic grain boundaries.

dark (solute-depleted) areas and light (solute-enriched) areas. A sample etched with this procedure is shown in figure 2.5.

2.2.2 Intermediate scale: Micro-X-Ray Fluorescence

To map composition on centimetric samples, a fast-intermediate scale technique is needed. The investigation of that scale is not common in solidification studies yet; however, it is a common scale in geology. Geologists use µXRF to map the chemical composition of centimetric samples with a high resolution [85]. Based on their experience, µXRF was adapted to metallurgical studies. The following paragraph describes how the µXRF device works, more information on the methodology developed to adapt µXRF to metallurgical samples can be found in the following chapter.
Radiation interaction with matter is used in several characterisation techniques including µXRF. The primary source: a high-energy X-ray excites the atoms of the sample, and electrons are shot out from the inner shells. Then relaxation occurs, and outer electrons change shells to fill the inner ones which cause the emission of secondary photons, also known as X-ray fluorescence. The energy emitted by the relaxation is specific to one atom and can be used to characterise the atoms in the presence. Based on that phenomenon µXRF identifies and quantifies the elements in a non-destructive way.
On the technical aspect, the Bruker M4 Tornado device for Goeressources laboratory was used to perform analysis. The Rh X-ray source (30 W power) is fixed and produces a

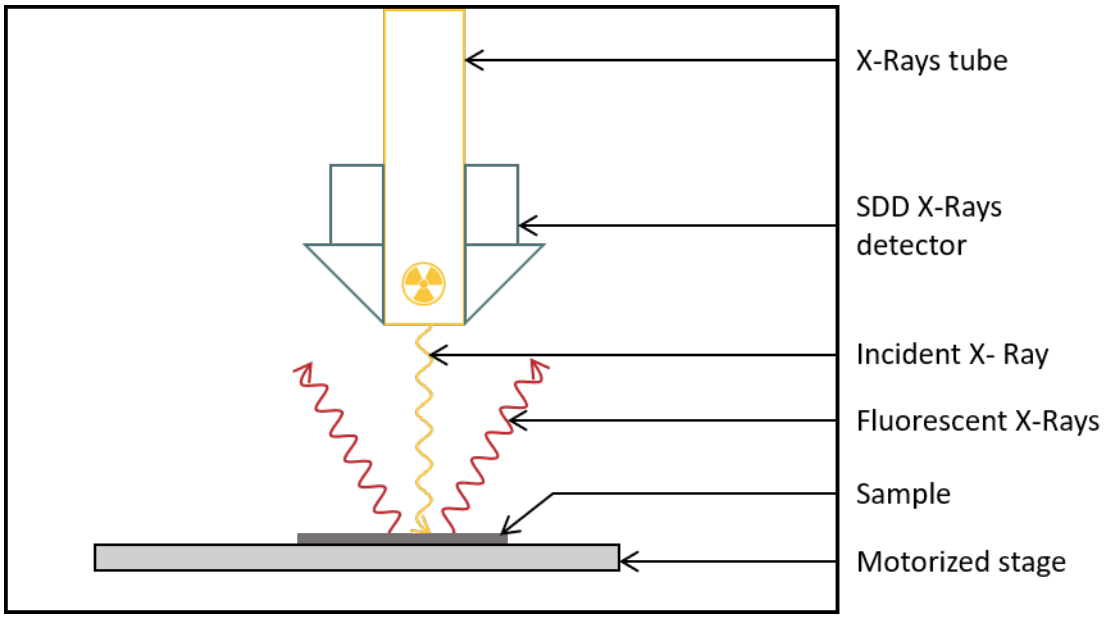

Figure 2.6: Schematic of the Bruker M4 Tornado µXRF device

20 µm-sized spot on the sample. An Energy Dispersive Spectrometry (EDS) detector is located on either side of the primary source. Detectors and primary source are fixed and the samples are placed on a motorized stage, the whole system is contained in a vacuum chamber (20 mbar vacuum). With the possibility to move the sample under the X-ray, µXRF can provide point analysis, but also line and grid scanning with a maximal surface of analysis of 190 x 160 mm^2. µXRF is based on EDS hence the analysis of light elements such as Hydrogen (H), Carbon (C) or Oxygen (O) is not possible.
To process µXRF data into segregation ratios maps, several steps are followed. Spectra are deconvolved using PyMCa 5.6.7 [86], then the maps are processed with Python codes. The first Python code to be used in a code developed by GeoRessources which is called *ProccesSeveralMaps.py*. *ProccesSeveralMaps.py* generates multiple outputs for each element of interest in a sample, using the µXRF output files and additional files created with PyMca. These outputs include a visual map displaying the raw intensity of the element peak across the sample, as well as a text file containing the peak intensity of the element at each point on the map. This text file is used for all of the data treatment realised on the µXRF analysis. Pythons codes were developped by the author to process visual maps, do image processing and produce corresponding cumulative solid fraction curves. For large scale samples, the raw data are converted to segregation ratio (see 2.3.1) and the scale bar set from the 1^{st} to the 99^{th} percentile of the segregation ratio distribution to ensure a clear visualisation of the segregation patterns. Unless specified, all maps presented in this work are processed the same way.

2.2.3 Small scale: Electron Probe Micro Analyser

At a smaller scale, EPMA is already a widespread technique for the characterisation of small samples and microsegregation. EPMA is a quantitative technique, the analysis

Element	Beam conditions	Crystal	Standard for calibration
C	7,5 kV and 100nA	SP1 – LDE2H	Calibration curve
C	7,5 kV and 100nA	SP3 – LDE2	Calibration curve
Cr	20 kV and 100nA	SP5 – LiFH	Pel6080 - Cr
Fe	20 kV and 100nA	SP2 – LiF	Pel6080 – Fe
Mn	20 kV and 100 nA	SP4 – LiF	Pel6080 – Mn
Mo	20 kV and 100 nA	SP4 – PETJ	Pel6080 – Mo
Ni	20 kV and 100 nA	SP2 – LiF	Pel6080 – Ni
Si	20 kV and 100 nA	SP5 – PETH	Pel6078 – Si

Table 2.5: Crystals used to isolate wavelengths and standards used for quantification for EPMA measurement

points can be unique on the sample surface, but thanks to the moving stage, the samples can also be moved to perform several points in a row, forming lines or grids of analysis. EPMA is popular for its precision in non-destructive quantification.
EPMA is a precise quantitative technique based on radiation interaction with matter. An electron beam is focused on the sample surface, excites the matter and causes the emission of Secondary Electrons (SE), BackScatter Electrons (BSE) and characteristics X-rays. The interaction volume of the electron beam is roughly 1 µm3, each emission corresponds to a specific location in the sample: SE are emitted by the closed-surface matter, then BSE from the intermediate depth and finally characteristics X-Rays are linked to the deeper layers of the interaction volume. With EPMA, characteristics X-rays are used to investigate the sample composition. Under electronic excitation, each element releases characteristics of X-rays identifiable with their wavelengths and energies. The characteristics of X-rays are studied with EDS or Wavelength Dispersive Spectrometers (WDS). EPMA is equipped with both solutions. EDS collects all emitted X-rays and analyze their energy dispersion. With WDS, crystals are used to separate one specific wavelength using the Bragg's law. The analysing crystals, having a known and fixed interticular distance, are placed on the Rowland circle with a specific angle between the sample and the detector to select a unique wavelength. A schematic of WDS detector is presented in figure 2.7b. Which means only one element is investigated per detector. Quantification is made possible by the use of standards for calibrations.
For this study, JEOL JXA-8530F Electron Probe Micro Analyser was used. It is equipped with a Field Emission Gun (FEG) source, one EDS detector and five WDS detectors. Figure 2.7 show a schamtic of the EPMA device. Depending on the element investigated, different operating conditions were used. The quantification of Carbon (C) requires a low acceleration voltage, hence the operating conditions were 7,5 kV and 100 nA and the measurements were quantified with calibration curves. For the quantification of Chromium (Cr), Iron (Fe), Manganese (Mn), Molybdenum (Mn), Nickel (Ni) and Silicon (Si), the beam settings were 20 kV and 100 nA, the crystals used to isolate wavelengths and standards used for quantification are summed up in table 2.5.

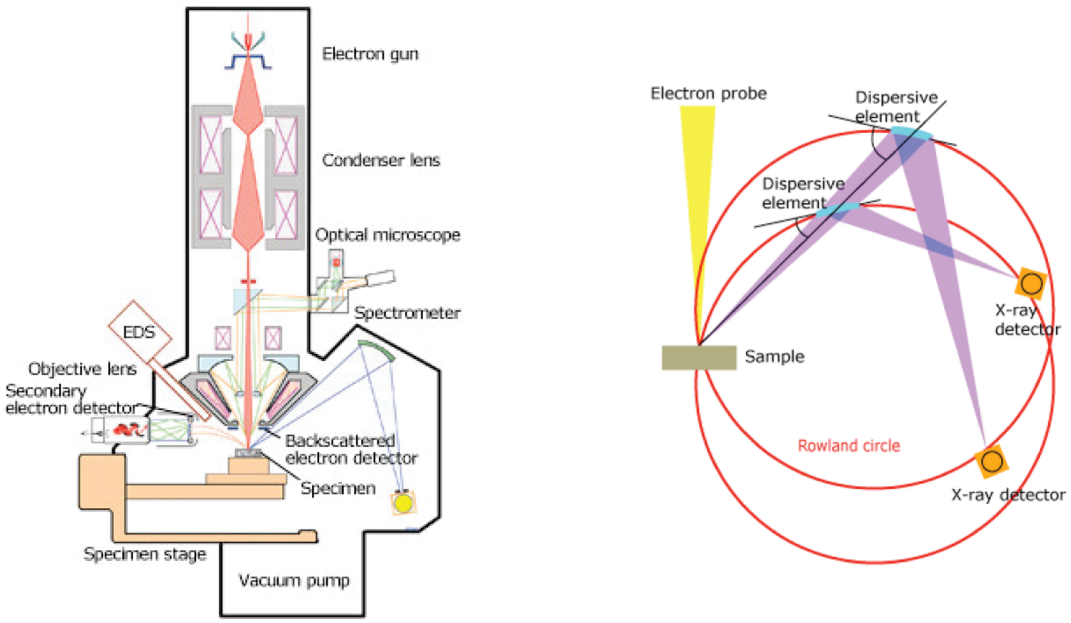

(a) EPMA device (b) WDS detector

Figure 2.7: Schematic diagrams of EPMA and WDS detector. Images taken from http://www.jeol.com.

2.3 Analysis techniques

The previously mentioned characterisation techniques produce raw data that needs to be processed and analysed to understand the segregations. Several tools can be used to understand the segregation formation and evolution through the shaping process. This section lists and explains the analysis tools used during the study to understand the segregation formation.

2.3.1 Segregation ratio

Segregation ratio is common tool for segregation analysis. It makes possible the comparison of different techniques, even if they use different measurement systems. The segregation ratio maps are also easy to interpret: enriched zones have a positive segregation ratio whereas depleted zones have a negative segregation ratio. Another advantage of the segregation ratio conversion is the possibility to compare the segregation patterns even on samples from different grades.
For that study, segregation ratios were calculated using the following equation:

$$S_i = \frac{C_i - \overline{C_s}}{\overline{C_s}} \tag{2.1}$$

avec

S_i, segregation ratio on the i-th point,

C_i, local composition on the i-th point and
$\overline{C_s}$, average composition of the sample.

A way to process µXRF maps is to compute segregation ratios to obtained sergegation ratio maps, as in figure 2.8

2.3.2 Cumulative solid fraction curves

Cumulative solid fraction curve is a microsegregation analysis tool. When partition coefficients of the studied elements are smaller than one, the solute concentration in the liquid increase as the solidification occurs. The first solid to form is the most depleted in solute and the last liquid to remain forms the richest solid. The evolution of the liquid concentration as solidification occurs can be plotted in cumulative solid fraction curves. The curves can also be relative cumulative solid fraction curves (normalised with the average value of the data set) so different maps, from different samples or analysed with different techniques, can be compared together. To plot the curves, the data must be ranked to correspond to a solid fraction. Different ranking techniques exists, based on the one or several elements of the sample studied. In the present study, only one element was coincided to plot its corresponding cumulative solid fraction curve. The data points are arranged monotonically into ascending order according to the studied element (Flemings-Grungor method) [87]. Then a corresponding liquid fraction is assigned to each data point and the cumulative solid fraction curve can be plotted. An exemple of cumulative solid fraction curve can be found in figure 2.9

2.3.3 Post-processing of µXRF data

With µXRF, each point analysed lead to a spectrum. Each spectrum is made of different peaks, in figure 2.10, an example of spectrum is given. There are 4 different peaks identified: 2 peaks for Fe, on for Mn and one for Mo. This the present study, both Mo and Mn are matter of interest. To quantify the peaks corresponding to each elements, there is different options. First, it is possible to use the machine software (Esprit form Burker) and quantify the peaks by ROI (Region of Interest). The second option is to fit the spectrum with mathematical function and to deconvolve each peak, it is possible with the help of PyMCa 5.6.7 [88].
If grid or linescan are done with µXRF, the output is a data cube: there is a full spectrum obtained on each grid points. To process the data with ease, the team working with the µXRF machine developed a python code named *ProcessSeveralMaps.py* that can process the data for several maps at once. The python code works with PyMCa 5.6.7 to deconvolve the spectrum on each point. Each peak can be analysed and the corresponding peak intensity is recorded in text file without losing the location of the spectrum on the map. At the end of the data post-treatment, one text file is obtained per peak of interest and contain for each analysed point on the map, its location and the corresponding peak intensity.
In this study, the peaks used for the analysis were: Mn (Kα, 5.900 keV) and Mo (Kα, 17.480 keV). The text files containing the relevant information were processed with home-

made python code to plot maps, convert it to segregation ratios, plot cumulative solid fraction curves, or even do image treatments on the different maps.

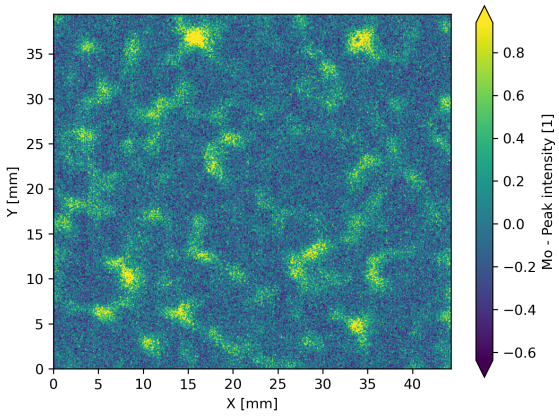

Figure 2.8: Exemple of a µXRF map. More details about this map can be found in the section 3.1.1.

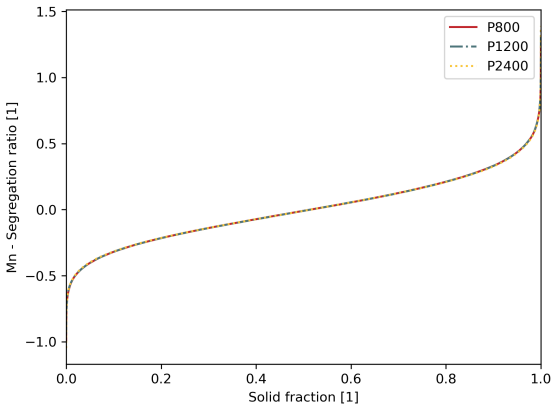

Figure 2.9: Exemple of cumulative solid fraction curve for Mn. More details about this graph can be found in the section 3.1.1.

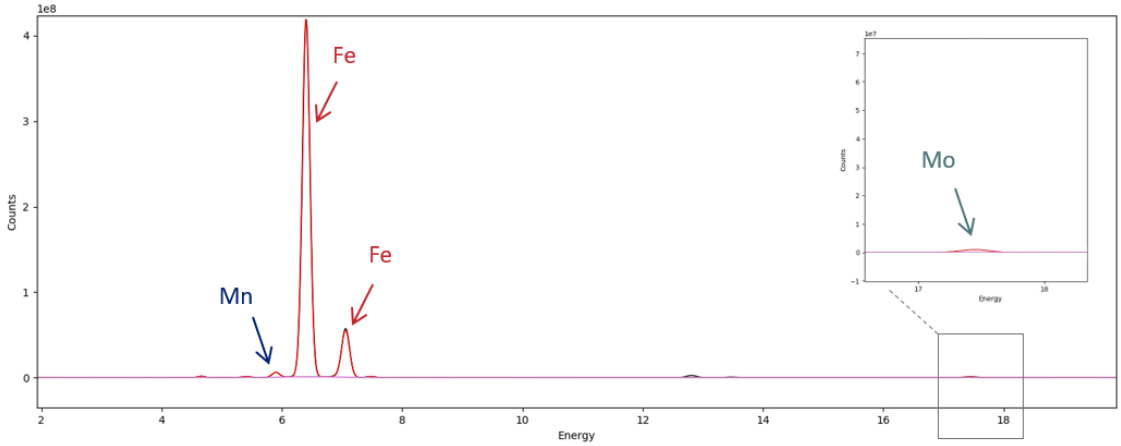

Figure 2.10: Example of average spectrum obtained on 16MND5 sample with µXRF analysis.

Chapter 3

Adaptation of the µXRF to metallurgy

Ce qui allait pas j'ai pris du temps pour le changer
J'ai pris du temps, ça prend du temps d'essayer
C'est tellement rare quand ça marche
C'est tellement rare que quand ça marche, faudra
Battre le fer tant qu'il est chaud, le fer tant qu'il est chaud
Parce que l'enfer, c'est pas d'échouer
C'est d'pas tout faire pour essayer

Ben Mazué, Gaël Faye et Grand Corps Malade,
On a pris le temps

Contents

The literature review, see chapter 1, reveals a gap in the techniques used for segregation analysis. Several techniques are used at large scale, EPMA is a common one at a small scale, however, the well-known techniques cannot be used for intermediate scale investigation, especially on centimetric samples. In this chapter, a technique that is not widely used in metallurgy, the µXRF, is adopted for intermediate-scale segregation characterisation. To ensure the reliability of the measurements based on µXRF, the parameters of the technique were first adapted to low-alloy steel samples.Then the µXRF was validated against a well-known accurate quantitative technique, the EPMA. The first section of this chapter describes the different experimental configurations that were tested, their advantages and drawbacks, and concludes with the best experimental conditions for the µXRF analysis of centimetric low-alloy steel samples. In the second section, µXRF is compared to EPMA to ensure its reliability and test its capacity to map segregation in steel samples. Finally, intermediate scale segregation maps are presented as well as a method to investigate segregation patterns in 3D based on reconstruction of successive 2D segregation maps.

3.1 Technical aspects

While µXRF is a well-known characterisation technique in geology, its use in metallurgy is not so common yet. Before being able to compare it to established metallurgical characterisation techniques, the µXRF technique should be adapted to the sample material and the best experimental conditions should be determined. In this section, the adaptation of the µXRF to metallurgy is described through 3 aspects. First, the sample preparation was investigated to produce samples suitable for µXRF. Then the different settings for experimental conditions are investigated to determine the optimal beam settings and the acquisition step and time for the characterisation of centimetric scale low alloy steel samples.

3.1.1 Sample preparation requirements

The sample preparation for XRF analysis is known to be minimal [67]. However only little is known about the use of µXRF for steel sample investigation. Thus the investigation of several sample preparation finishing was important to determine the preparation to use for all the samples analysed with µXRF.
Based on recommendations from the µXRF machine users, 3 different final surface grinding were tested. Samples were ground flat with Si-C paper down to P800 (21.8 µm granulometry), P1200 (15.3 µm granulometry) and P2400 (10 µm granulometry). The samples used for the preparation tests were taken for the *short* ingot, at the E position, 3 samples were used: one for each final surface quality.
Samples were tested all at once in the µXRF machine. The samples were mapped with an acquisition step of 20 µm and an acquisition time of 15 ms. As for the beam settings, the acceleration voltage was set to 50 keV, the current to 350 µA and the beam was unfiltered. Whatever the surface finish, the samples presented grinding scratches, but for none of the samples the scratches appeared on the segregation map obtained with

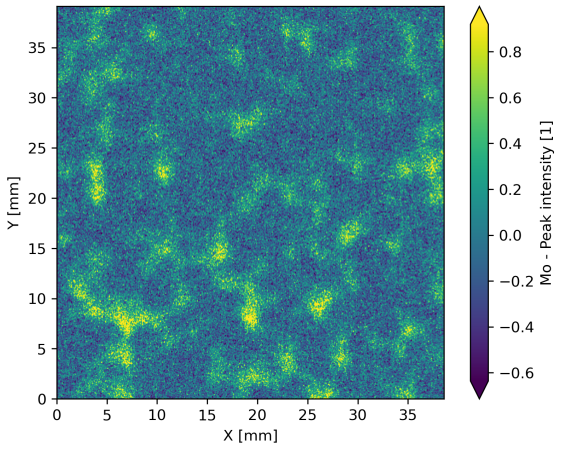

(a) P800 (21.8 µm granulometry)

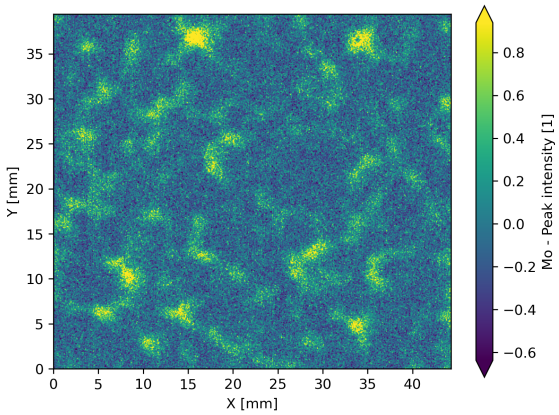

(b) P1200 (15.3 µm granulometry)

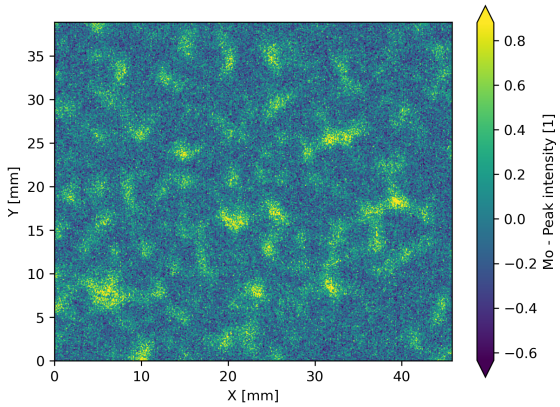

(c) P2400 (10 µm granulometry)

Figure 3.1: Chemical maps obtained on the samples prepared in different conditions.

µXRF, as it can be seen in figure 3.1. No scratches were observed, the map appearance was similar for all the samples and no visual distinction linked to the sample preparation could be made on the maps. Cumulative solid fraction curves were also plotted for all 3 of the samples (figure 3.2). The curves overlap perfectly: there is no difference in the quality of the information collected on the different samples. In figures 3.2b and 3.2d, cumulative solid fraction curves were shifted for better observation. Since there is no difference between the quality of the information collected nor the visual quality of the maps, it is safe to assume any sample ground flat down to P800 at least can be analysed with µXRF.

Later on in the study, larger samples were to be analysed with µXRF. Their preparation was done with semi-automatic grinding on MD grinding disks from Struers. The MD disk equivalent to P800 was not available, hence the larger samples were ground down to P1200 on MD-disks.

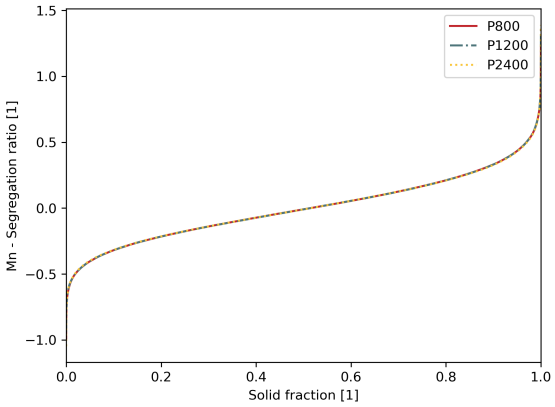

(a) Solid fraction curve for Mn

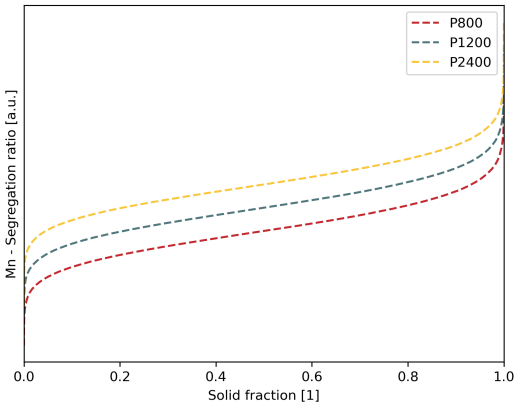

(b) Shifted solid fraction curve for Mn

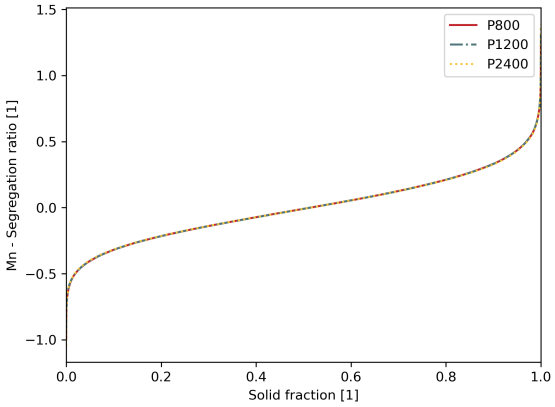

(c) Solid fraction curve for Mo

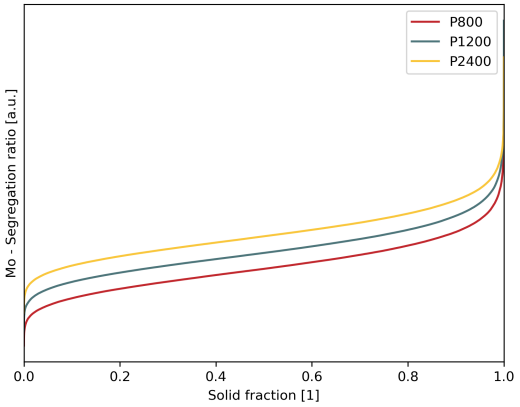

(d) Shifted solid fraction curve for Mo

Figure 3.2: Classic and shifted cumulative solid fractions curves obtained with the data of the maps realised on samples prepared in different conditions. Curves were shifted for better visualisation.

3.1.2 Beam current and filtering

Different beam settings were also tested to find the best experimental conditions for centimetric low-alloy steel samples.
Using an acceleration voltage of 50 keV, different combinations of filters and associated currents settings were investigates. Filters are thin films that absorb part of the incident X-Rays, they decrease the excitation intensity and the spectrum intensity in some parts of the spectrum. They can be used to prevent saturation of the detector or to improve the peak-to-background ratio. They come in various materials and thicknesses. The thicker ones decrease the intensity of the spectrum more than the thinner ones [89]. Five different filters were tested and an additional test was done without filter. Table 3.1 lists the different filters and the associated current used. With filter the beam current can be increased without saturating the detectors which would cause artefacts in the measure. The dead time of the measure is a good indicator of artefact minimisation: artefacts are minimised when the dead time approaches 20% [90]. Dead time is usually balanced with

Filter	Current
Empty	150 µA
Al 12.5 µm	150 µA
Al 100 µm	200 µA
Al 100 µm, Ti 25 µm, Cu 25 µm	600 µA
Al 100 µm, Ti 25 µm	400 µA
Al 630 µm	600 µA

Table 3.1: Filter tested and associate currents set to approach 20% of dead time.

current, acceleration voltage and the use of filters. In this study, the acceleration voltage was set to 50 keV and for each filter the current was maximed to an extend that keps the dead time closest to 20%.
The sample ground down to P800 for previous tests was used to test different beam settings. The maps realised for that test were always the same: same sample, same coordinates, same analysed surface, same acquisition time (10 ms) and same acquisition step (20 µm).
The quality of the outgoing signal depends on the incoming signal and therefore on the beam settings. Each tested configuration gives different results. On one hand, the use of a filter allows to work with a higher current, hence obtaining a stronger outgoing signal. The thicker the filter, the stronger the current, and the stronger the outgoing signal. On the other hand, filters are high-pass filters and damage low-energy peak information. In low-alloy steels, Fe is the major element, hence it will produce a strong Fe-peak in the XRF spectrum. Such a strong peak affect the quality of the measure on other elements, hence it is interesting to reduce the intensity of the Fe peak with filters. However, the use of filters can also decrease the intensity of other elements of interest such as Mn whose peak (5.900 keV for $K\alpha$) is close to Fe peak (6.405 keV for $K\alpha$). To choose the best option, the maps obtained in the different experimental conditions were compared visually and quantitatively based on the cumulative solid fraction curves of the data.
Visually, the maps obtained in the different experimental conditions are very similar and cannot be told apart. The cumulative solid fraction curves give more information. Figures 3.3a and 3.3b show the cumulative solid fraction curves obtained from the maps realised in different experimental conditions. Figure 3.3a confirms that the use of filters globally decreases the intensity of the Mn-peak. The filter Al 100 µm, Ti 25 µm, Cu 25 µm and the filter Al 630 µm are the filters that cause the greatest decrease in the peak intensity. The filter Al 100 µm, Ti 25 µm and the filter Al 100 µm give similar results and finally, the thinner filter causes the smallest decrease in peak intensity of Mn compared to the empty beam. Figure 3.3b shows the cumulative solid fraction curves obtained in the same conditions but on Mo maps. The first observation is that the peak intensity of the Mo is lower than the one of Mn, regardless of the filter used. Indeed the Mo-peak is smaller and as the Mn-peak is close to the Fe-peak, it has a higher baseline. Concerning the effect of the filters on Mo detection, they are completely different from the effects on Mn detection. As the Mo peak has higher energy (17.4800 keV for $K\alpha$), the peak intensity is not negatively affected by the filters. Instead, the use of filters can be beneficial since

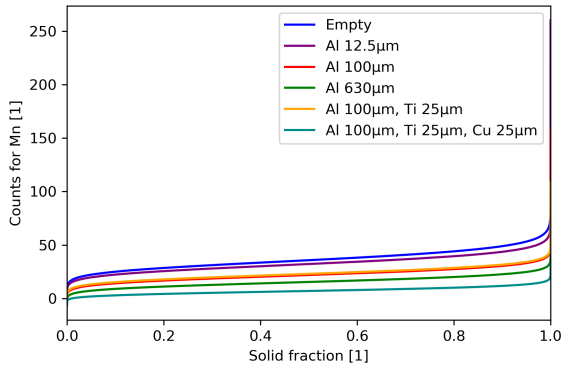

(a) Solid fraction curve for Mn

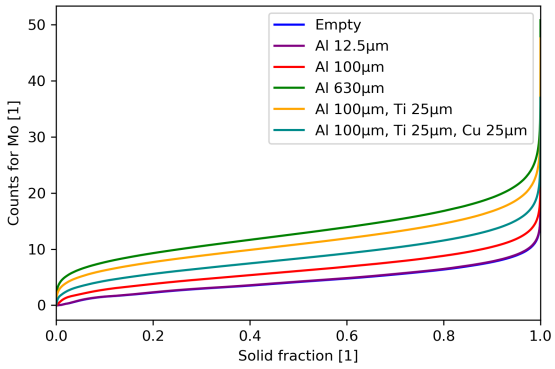

(b) Solid fraction curve for Mo

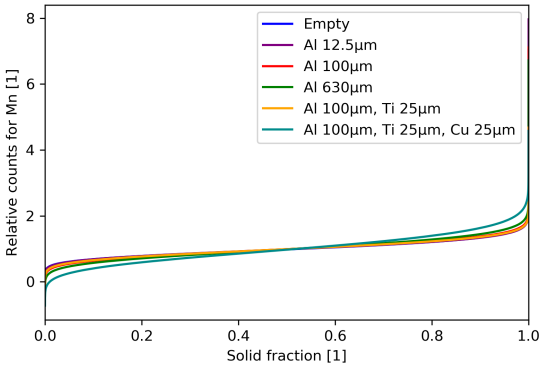

(c) Relative solid fraction curve for Mn

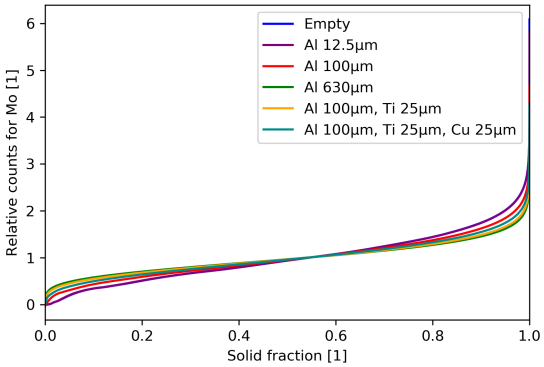

(d) Relative solid fraction curve for Mo

Figure 3.3: Classic and relative solid fractions curves obtained with the data of the maps realised in different experimental conditions.

the current can be increased without any additional artefact. Only one curve coincides with the empty beam curve, it is the curve obtained with the thinnest filter (Al 12,5 µm). This filter requires a 150 µA current, which is the same as used on an empty beam. Since both Mn and Mo are of interest for the study, a balance between degrading the Mn signal and improving the Mo signal is to be found.

The two main candidates are the filters Al 100 µm and Al 100 µm, Ti 25 µm. Both of them decrease the Mn signal but not as much as thicker filters and they allow the current to be increased up to 200 µA and 400 µA, which improves the Mo signal. The Mo signal is stronger with the Al 100 µm, Ti 25 µm filter and the current set to 400 µA. However, the study of relative cumulative solid fraction curves reveals that the use of a filter changes the shape of the solid fraction curves. The benefit of a relative solid fraction curve is to be able to compare the segregation measurement without the influence of the current that increases the peak intensity since in relative solid fraction curves the intensity of the peak is not taken into account: only the intensity ratio on the whole map is a matter of interest. For Mn, the use of any of the candidates - Al 100 µm or Al 100 µm, Ti 25 µm -

does not significantly change the shape of the relative solid fraction curve compared to the one of the empty beam. For Mo, on the other hand, the use of a filter changes the shape of the relative solid fraction curve: the heavier the filter, the further away from the empty beam curve. The relative solid fraction curve obtained with the Al 100 µm filter and a 200 µA current shows a larger intensity range of other solidification and better accordance with the empty beam curve.
Based on these observations, beam settings were defined for the analysis of low-alloy steel with µXRF. The acceleration voltage is to be set to 50 keV, so the best detection precision is for elements with a $K\alpha$ around 25 keV. The filter Al 100 µm should be used to be able to set the current to 200 µA. This configuration gives a respectable outgoing signal for both Mn and Mo peaks on a large concentration range.

3.1.3 Acquisition step and time

The last experimental settings to be tested and defined before using µXRF to investigate segregation in low-alloy steel samples are the acquisition step and time. Changing the acquisition step can change the appearance of the obtained map. The acquisition step depends on the required spatial accuracy and on the total available time for the µXRF scan. A small acquisition step gives a higher resolution map, while it is faster to analyse the same surface area with a larger acquisition step. Furthermore, the quality of the measurement depends on the acquisition time spent on each measurement point: the longer the acquisition time, the better the accuracy. Indeed, with an longer acquisition time, the detectors collecte more photons emitted by the sample which improve the peak-to-background ratio. However, increasing the acquisition time comes at a cost: the overall time required for one map increases with the time spent on each point. To distinguish the segregation patterns that matter to the study and to be able to study a large number of samples, the acquisition time and step must be carefully selected.
In this study, the challenge is to map centimetric samples overnight. The study aims at mapping intermediate-scale segregation, however, such segregation has never been observed in the past. Hence a high spatial resolution is preferred: if microsegregations can be observed with the chosen experimental conditions, then larger-scale segregation would be observable too. Using a lower spatial resolution would speed up the process, but it introduces the risk of not being able to distinguish intermediate-scale segregation. That is why balance is to be found in acquisition step and time.
Before taking a look at the tests, the scanning and acquisition methods should be fully described. The beam of the µXRF device used has a fixed 20 µm focal point and the operation of the machine produces a non-homogeneous sampling in both directions. During the acquisition of a segregation map, the motorised stage, on which the sample is set, moves continuously in the x direction. The fluorescent X-rays emitted by the sample over a given time are collected while the stage moves: this given time is called the acquisition time. The continuous movement of the motorised stage is set so that at the end of each acquisition time the sample was moved from one acquisition spatial step. Thus in the x direction, the scanning is continuous, whereas in the y direction it is not: between each analysed line, there is a gap corresponding to the acquisition step minus the beam width

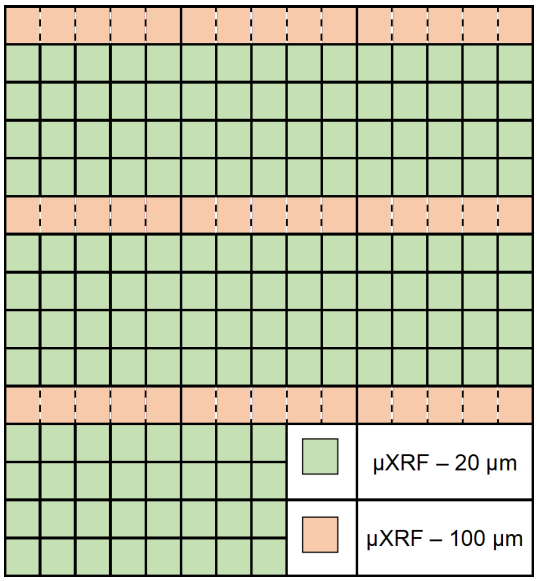

Figure 3.4: Schematic of the surface scanning during µXRF analysis with different analysis steps. When the analysis step is 100 µm, a band of 80 µm is not analysed between each analysed line of 20 µm width.

(20 µm). This gap does not exist if the acquisition step is equal to the beam width. It is the only configuration that maps the whole sample surface, although the acquisition is not homogeneous in both directions (continuous in x direction and discrete in y direction). In figure 3.4, the surface scanned with a 20 µm acquisition step is represented in green, while the surface scanned with a 100 µm acquisition step is represented in orange. Tests were performed to guide the selection of the acquisition parameters: the sample used for the P800 grinding test was used, and a specific area of the sample was scanned using different acquisition parameters. Five parameter sets were tested, with the acquisition times: 20 ms, 50 ms, 100 ms, 150 ms and 200 ms; respectively associated with the acquisition steps: 20 µm, 50 µm, 100 µm, 150 µm and 200 µm. These specific combinations of acquisition time and step use the same scanning speed, which make theire comparision easier. The beam settings were identical for all tests: 50 keV acceleration voltage, a 200 µA current and an unfiltered beam.
Figure 3.5 presents the maps obtained with the five parameter settings given above. Changing the acquisition step, changes the visual appearance of the maps. In the first map 3.5a the whole sample surface was analysed, the edges of the patterns are sharp and segregation can be observed. However, as the acquisition step increases, the shape of the structure is changed: they are spread out and distorted. As the acquisition step reaches 100 µm (3.5c), the shape of the structures is no longer representative and their edges are blurred so it is difficult to distinguish them. Consequently, acquisition steps smaller or equal to 100 µm should be favoured.
Another way to compare the acquisition step and time is to look at the cumulative solid fraction curves obtained for the maps data. The curves are presented in figure 3.6 for both Mn and Mo. The first two plots, 3.6a and 3.6b, show that the average peak intensity

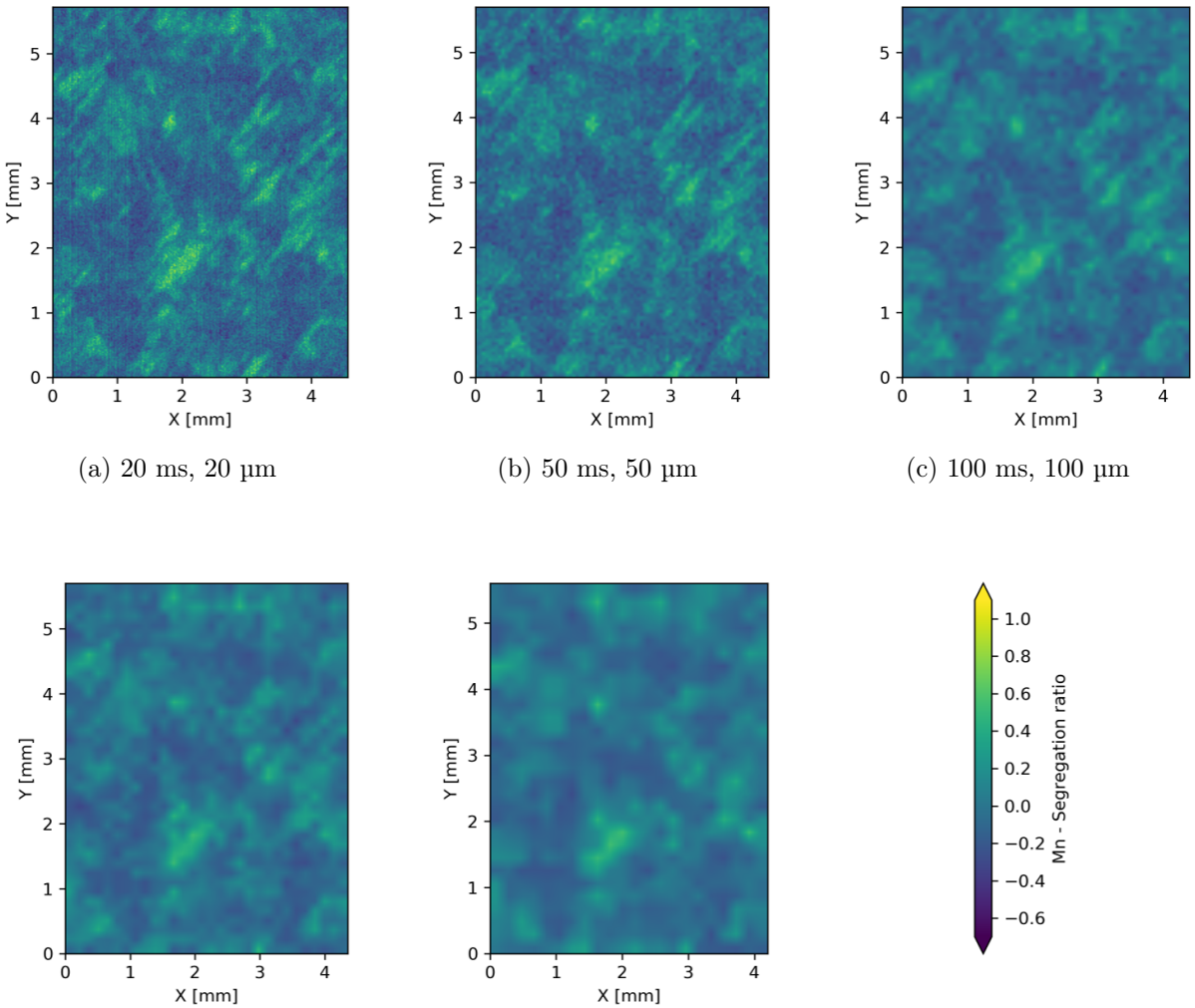

(a) 20 ms, 20 µm (b) 50 ms, 50 µm (c) 100 ms, 100 µm

(d) 150 ms, 150 µm (e) 200 ms, 200 µm

Figure 3.5: Mn segregation ratio maps of a 4.4×5.6 mm^2 sample analysed with µXRF (X-Ray beam: unfiltered, 50 keV, 200 µA), the acquisition time and step are specified under each map.

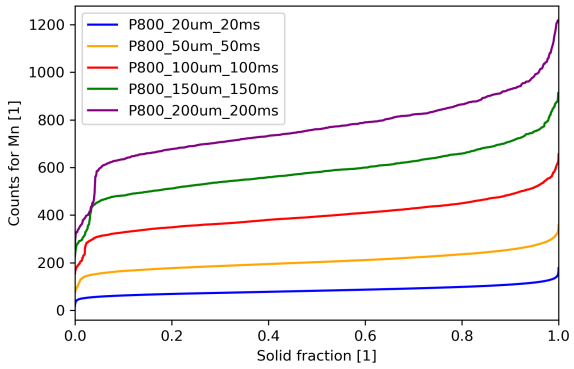

(a) Curves of Mn maps

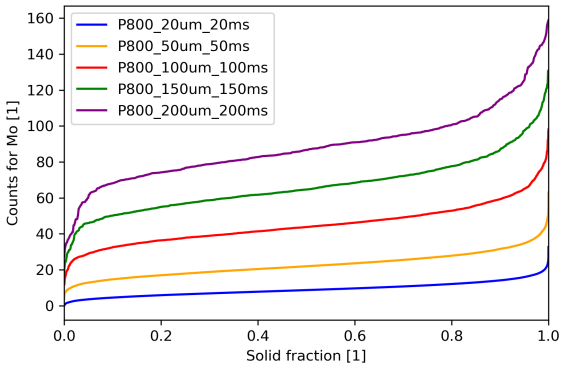

(b) Curves of Mo maps

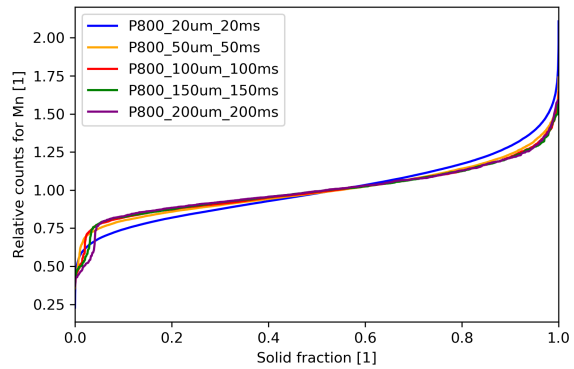

(c) Relatives curves of Mn maps

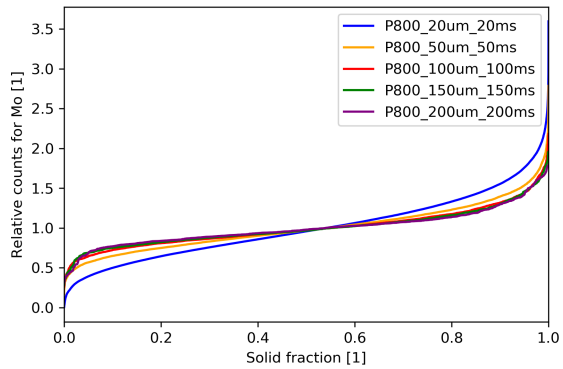

(d) Relatives curves of Mo maps

Figure 3.6: Classic and relative cumulative solid fractions curves obtained with the data of the maps realised using different filters. Refer to table 3.1 for the current setting corresponding to each filter.

increases with the acquisition time. While the peak intensity is linked to the acquisition time, the curve shape can give informations on the effect of acquisition step. One way to study the acquisition step without the influence of the acquisition time is to use relative cumulative solid fraction curves (3.6c and 3.6d). The relative curves highlight the difference in the information collected with a step that maps the whole sample (20 µm) compared to other acquisition steps. When the acquisition step increases, the curve flattens: it is less sensitive to extreme values. For both elements, the information collected with 100 µm, 150 µm or 200 µm of acquisition step are very similar. Increasing the size of the acquisition step and reducing the number of points in the map does not appear to decrease the quality of the information collected. We can conclude that the use of steps smaller than 100 µm is not justified: a 200 µm acquisition step can provide equivalent information in a shorter time.

The selection of an appropriate acquisition step and time is crucial to obtain reliable segregation maps. The main aim of the study is to map segregation patterns on large

(centimetric) steel samples, which brings the challenge of the total analysis time per sample. The number of acquisition points per sample is proportional to h^{-2}, where h is the acquisition step. For the acquisition steps tested in Figs. 3.5 and 3.6 the number of points would range from around 250,000 (for a step of 200 µm) to around 25 million (for a step of 20 µm) if applied to a 10×10 cm^2 sample. One way to keep the global analysis time acceptable is to increase the acquisition step to the largest value that gives segregation maps with sufficient resolution and to increase the acquisition time to its maximum. In this study the visual appearance of the maps was important. Thus the acquisition step was set to 100 µm, which was the high limit on visual tests. For the samples taken in the *short* ingot, the total analysed surface was 110×95 mm^2, or 1 047 051 points per sample for an acquisition step of 100 µm. For practical reasons it was necessary to be able to analyse one sample per night (15 hours), the maximal acquisition time that respected that condition was 45 ms on each point and this time was selected as an experimental condition for the centimetric maps.

3.2 Comparison of µXRF with EPMA

To validate the use of the µXRF technique, it was important to compare it with an established and calibrated characterisation technique used for segregations. µXRF is a versatile technique that can analyse small and bigger samples, hence it can be compared to several techniques, large-scale techniques or small-scale techniques. It was chosen to compare µXRF to EPMA since EPMA is a precise, non-destructive and quantitative technique. It provides concentration maps with a higher spatial resolution, i.e. with more detailed information, than µXRF. After fitting to the µXRF resolution the EPMA maps provide a quantitative reference to which µXRF can be directly compared. A specific batch of 3 samples was analysed twice: once with EPMA and another time with µXRF. In this section, the results of the 2 analyses are compared, and the differences and similarities between the techniques are highlighted, which enables us to validate the use of µXRF.

3.2.1 Experimental conditions

Samples used during previous studies [91] on the *short* ingot were selected for the comparison between µXRF and EPMA. Three samples were taken in *short* ingot, at the D-position (see figure 2.1). On each of these samples, a zone of interest (dimensions: 2×2 mm^2) was identified. The table 3.2 gives the names of the samples studied, their dimensions and the average segregation of their zone of interest (based on the previous study [91]).

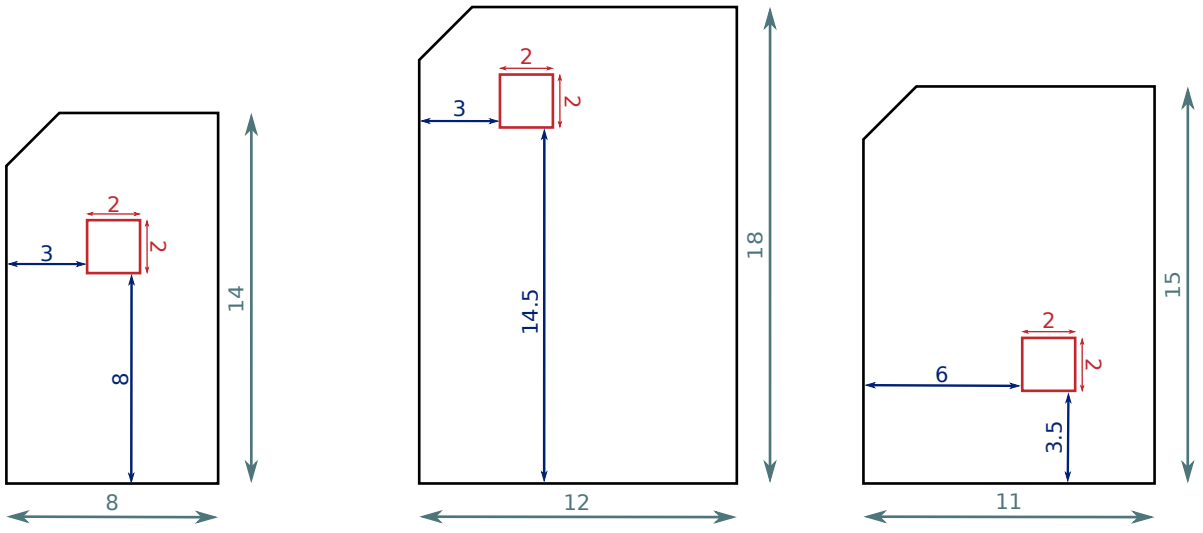

(a) Sample D6 (b) Sample D14- (c) Sample D14+

Figure 3.7: Plans of the samples selected for the comparison between µXRF and EPMA. All dimensions are mm.

Sample	Dimensions (mm)	Segregation in the zone of interest
D6	14×8	Highly positive
D14+	15×11	Positive
D14-	18×12	Highly negative

Table 3.2: Samples used to compared µXRF with EPMA.

The samples were mirror polished with 1 µm diamond slurry with a specific device, called AccuStop, which ensures parallel surfaces. While EPMA analysis requires very careful sample preparation, as described before, this is not required for µXRF, see 3.1.1. However, to reduce the differences between the 2 characterisations the samples were only prepared once so the analysed surfaces were the same.
As previously demonstrated, a 50 keV acceleration voltage, a 200 µA current and the use of the 100 µm thick Al filter give the best outcoming signal for µXRF measurement. The analysis step chosen is 100 µm and the analysis time was 45 ms on each point. These experimental conditions are the ones designed for centimetric scale sample mapping and were applied on the whole sample surface. Their comparison to EPMA was the last validation step before the application to the large samples. The EPMA settings can be found in the chapter 2. On each zone of interest EPMA analyses were done in 400 points, arranged on a uniform grid with a spacing of 100 µm. The final surface analysed with EPMA is 1.9×1.9 mm^2. The position of the zone analysed with EPMA on the samples is represented in figure 3.7.

3.2.2 Comparison of µXRF maps with EPMA maps

The samples were analysed with µXRF and EPMA, using experimental conditions described in the preceding section (see Section 3.2.1). For each sample Mo and Mn maps obtained with µXRF and EPMA were compared. To compare the two techniques, EPMA and µXRF maps were transformed into segregation ratio maps. For the sake of clarity, only the maps of D14+ sample will be presented in this chapter. As it can be observed in figures 3.8 and 3.9, even with the help of a sample plan, shown in figure 3.7, the location of the EPMA zone in the µXRF map cannot be easily identified. The samples might have moved during the analysis with both EPMA and µXRF hence the location of the EPMA zones are approximate. However, the localisation of the zone on the µXRF is crucial for the comparison between the techniques. Hence a Python code was developed to help with the localisation of the EPMA measurement zone on µXRF maps.
In figure 3.9, a red rectangle is indicated on the µXRF maps. This rectangle marks out the data analysed with a Python code to find the best match between EPMA and µXRF. In this code, the zone delimited by the red rectangle is scanned with a 20×20 point sliding window, equal to the size of the EPMA map. The sliding window is moved point by point over the µXRF measurement grid. For each position of the sliding window, the obtained µXRF map is compared to the EPMA map using two methods: (1) the point-to-point method and (2) the solid fraction curve method.

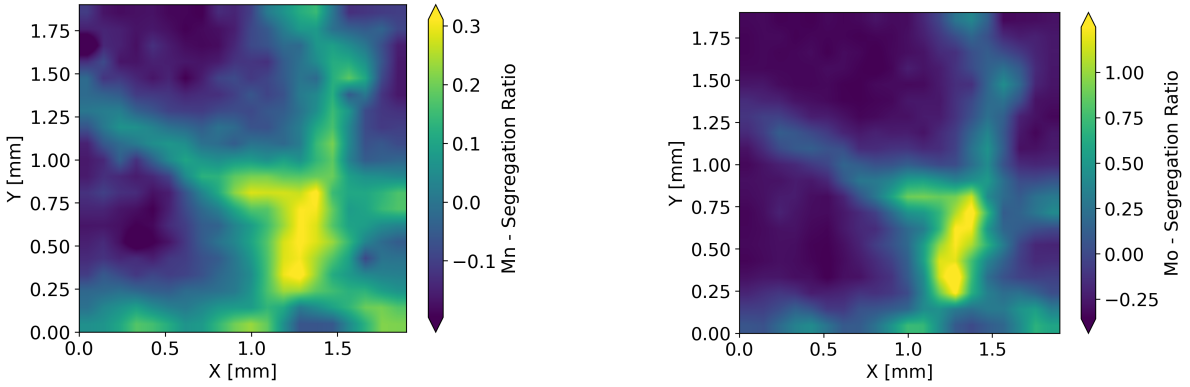

(a) Manganese map (b) Molybdenum map

Figure 3.8: EPMA maps of the sample D14+.

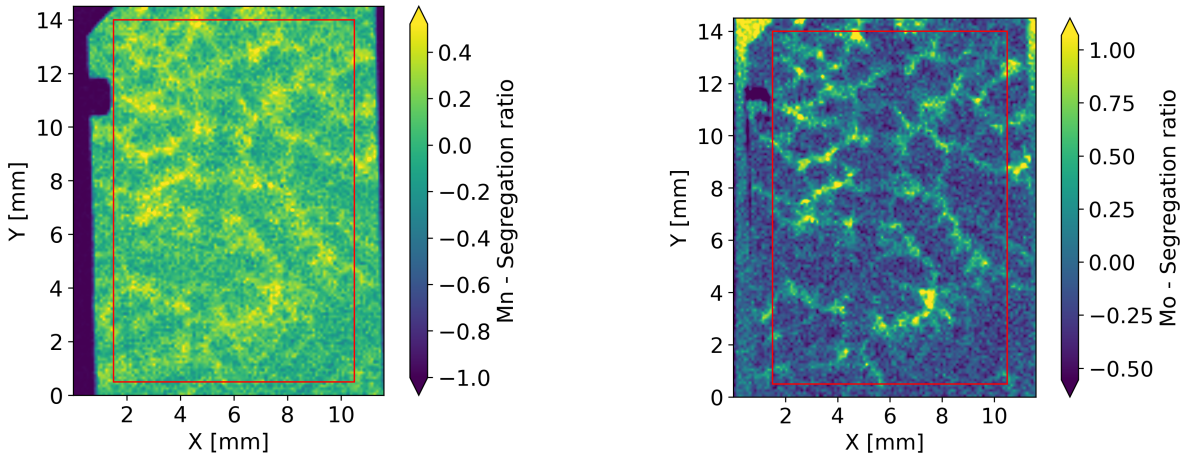

(a) Manganese map (b) Molybdenum map

Figure 3.9: µXRF maps of the sample D14+.

- For the point-to-point method, the difference of the segregation ratio measured by EPMA (S_i^{EPMA}) and µXRF ($S_i^{\mu\text{XRF}}$) is calculated for each point i in the sliding window. The overall error measure for the sliding window is the average difference, $\sum_i |S_i^{\mu\text{XRF}} - S_i^{\text{EPMA}}|$. The sliding window with the smallest average difference is selected as the best match for the EPMA zone location.

- For the solid fraction curve method, the cumulative solid fraction curve is calculated for both EPMA and µXRF, for each position of the sliding window. The average difference between the curves is then calculated in a similar way as in the point-by-point method. The window with the smallest average difference is selected as the best match for the EPMA zone location.

Each method is applied for both elements of interest: Mo and Mn, leading in 4 possible locations for the EPMA zone on the µXRF map, as can be seen in figure 3.10 (*NB*, in figure 3.10b the two point-by-point zones (calulated with Mn and Mo, represented in

yellow) are identical and therefore overlap perfectly).
In total, the point-to-point method and the solid fraction curve method were applied to 6 couples of maps: two elements Mo and Mn, and 3 samples for each technique. The main observations are the same in all samples. The zones selected with the point-to-point method match almost perfectly for both elements (the only difference is detected on the D14- sample: the positions for Mo and Mn differ by 100µm in the y direction, equivalent to one line spacing of the µXRF measurement grid). The position of these zones is also close to the expected EPMA zone positions, shown in Fig. 3.7. On the other hand, the zones selected with the solid fraction curve method are located far from those obtained by the point-to-point method and do not match for both elements. The solid fraction curve method zones are also far from the expected position of the EPMA zone. The point-to-point method seems to be the more suitable method. It leads to consistent results, independent of the chemical element and shows EPMA zones close to the expected location (figure 3.7).
In case of differences between the point-to-point method predictions for different elements, each case should be handled individually. For instance with the sample D14-, the difference between the two predictions is minimal. Mn and Mo solid fraction curves obtained for both zone locations were plotted (figure 3.11) and do not indicate any major difference. Figure 3.12 displays three Mo-maps. Mo was chosen to plot the maps since it gives better contrasts on segregation maps than Mn. One of the maps is the EPMA map that needs to be found in the µXRF maps and the two others are the two maps obtained from the point-to-point method, one on the Mn-map and one on the Mo-map. Visually, the location obtained with the point-to-point method on the Mn-map, figure 3.12c, gives better results than the one obtained with the same technique on Mo-Map (figure 3.12b), especially on the top part of the map, the enriched line is lower corresponding to the height observed on EPMA map.
Now that all the EPMA zones are located on the µXRF maps, the techniques can be compared. First visually, EPMA gives a smoother result on the maps, and µXRF measurement contains more interference. The comparison of the evolution of the segregation ratio as the solidification occurs with the solid fraction curves shows that µXRF measurements' curves are close to EPMA's curves. Some differences can be pointed out on low and high solid fractions, however, these differences do not invalidate the µXRF technique compared to EPMA. Indeed, the solid fraction curves are known to be less accurate at low and high solid fractions [80]. Also, the sampling is different for both techniques. When EPMA analyse 1µm^3 of steel every 100µm, the µXRF analyse the surface of a moving sample, continuously on 100 µm, with a spot size of 20 µm. Statistically a small very rich or very depleted area has much more chance to be collected with µXRF than with EPMA, leading to different tail shapes on solid fraction curves.
To sum up, µXRF can be used to characterise small- and intermediaite-scale segregation. µXRF is less accurate than EPMA and has a lower spatial precision, but µXRF does not require careful sample preparation and is faster and user-friendly. In this study, the aim is to investigate intermediate-scale segregation, EPMA level precision is not required, however, a fast technique, that can be applied to large samples, with low sample preparation is needed. For these purposes, µXRF is well suited.

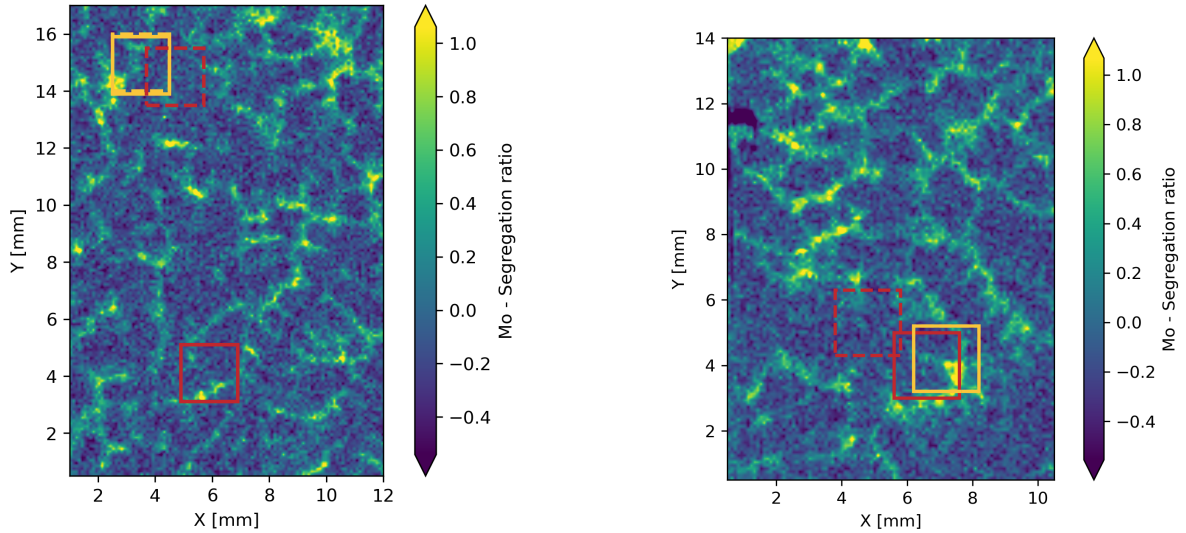

(a) Sample D14-

(b) Sample D14+

Figure 3.10: Identification on sample D14+ of the 4 possibles location of the the EPMA zone on µXRF map.
Legend: -, solid fraction curve method on Mo map; - -, solid fraction curve method on Mn map; -, point to point method on Mo map and - -, point to point method on Mn map (under the -).

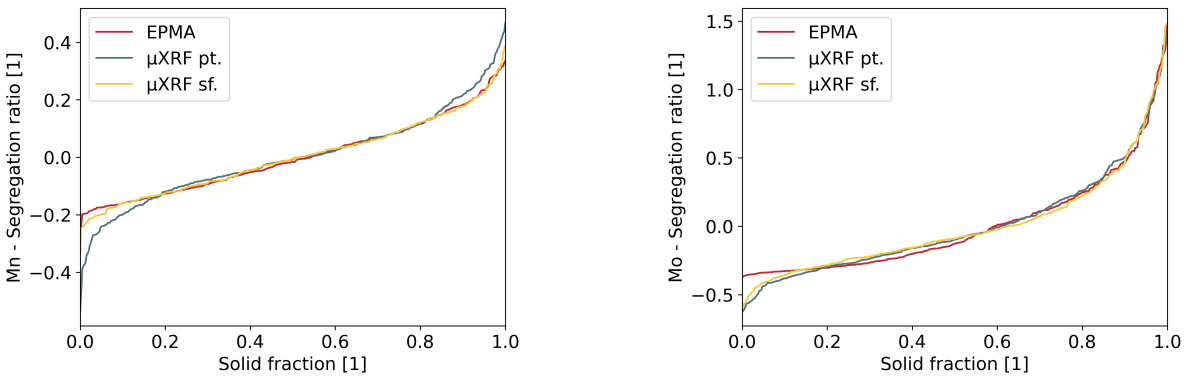

(a) Mn - Solid fraction curve

(b) Mo - Solid fraction curve

Figure 3.11: Evolution of the segregation ratio as solidification occurs for EPMA scanning and two µXRF zones both located with the point-to-point method one on Mn-map and one on Mo-map on the sample D14+.

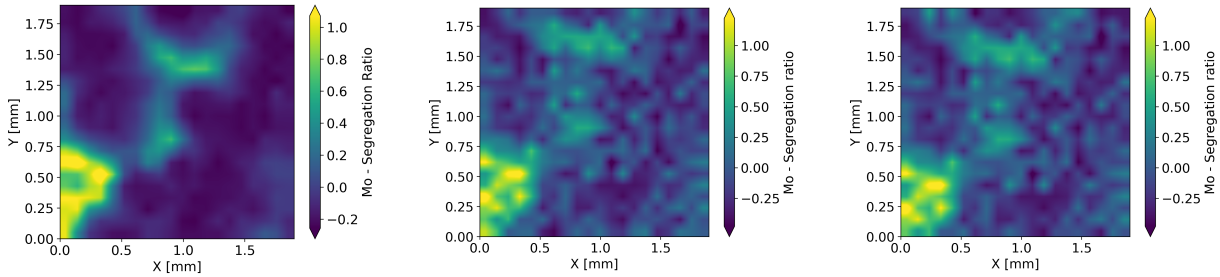

(a) EPMA map on D14- (b) µXRF map selected Mo (c) µXRF map selected Mn

Figure 3.12: Comparison of the µXRF maps obtained for the automatic localisation of the EPMA zone on µXRF maps.

In this study, we attempt to quantify the µXRF data by EPMA calibration [92]. We may not always be able to locate the EPMA zone on the µXRF map, and the lack of large calibration database encouraged us to pursue a semi-quantitative approach. We used a segregation ratio instead of relying on a weak calibration for our study.

3.3 µXRF exploitation

The previous sections explored the use of µXRF on steel samples, the best experimental conditions were determined and the ability to detect segregation was shown. Once tested, this technique was used to characterise centimetric scale samples. This section presents the application of the µXRF for the measurement of segregation in the steel ingot blocs and the processing of the measurement data. Image processing was used to highlight specific segregation patterns, which were then reconstructed in 3 dimensions based on a stack of 2D segregation maps.

3.3.1 Maps examples

In figure 3.13, the first map to be introduced is a map realised on the sample C2_1 taken in the xy direction, at the C location in the *short* ingot (see Fig. 2.1 for the position and orientation of the sample). The sample was scanned with µXRF, in the condition tested before (X-ray beam: Al-100 µm, 50 keV, 200 µA with a 100 µm analysis step and 45 ms of acquisition time per spectra).
The C2_1 map in figure 3.13 shows that three different scales of segregation can be observed at once on a centimetric scale sample. Microsegregation is distinguished by solute enrichment between secondary dendritic arms, see figure 3.14. Jacob Kennedy used this segregation maps to measure SDAS (Secondary Dendritic Arms Spacing), the average SDAS value in C2_1 sample is 0.75mm. At a larger scale, enriched areas are visible in the top right corner of the figure. These enriched areas are larger thvan dendrites (approximately 1 cm long and 1 mm thick), and smaller than any macrosegregation patterns. Hence these segregation patterns are intermediate scale segregation pointed out with yellow ellipses directly on the map in figure 3.15. Finally, enriched disks are visible on the bottom left corner of the map circled in red on the map in figure 3.15. The orientation of the sample in the ingot helps to understand that such strongly enriched disks can be channel segregates approximately perpendicular to the sample plane. Indeed, y-axis corresponds to the radius of the ingot, x-axis is in the transversal plan of the ingot. Hence, the z direction, pointing at the top of the ingot is getting out from the page, pointing at the reader. In steel ingots of such size, gravity-driven fluid flow in the channel segregates flows upward toward the top of the ingot and would be expected to be cut transversely by the C2_1 sample plane. As samples were taken successively in the z direction, channel segregates should also appear as enriched disks in sample planes located above and below plane C2_1. The red circles used to point out the enriched disks on C2_1 were copied onto the map of the following sample, C2_2, and they do encircle enriched disks, as observed in figure 3.16. Enriched disks can be found on all 30 serial cut samples analysed and form continuous segregation patterns along the height (z direction) of the analysed steel bloc. This observation confirms that the enriched disks observed in the transversal direction are indeed channel segregates. The existence of serial cut samples showing channel segregates in the transversal direction makes it possible to characterise the channels in 3 dimensions. This opportunity is exploited in the following sections.

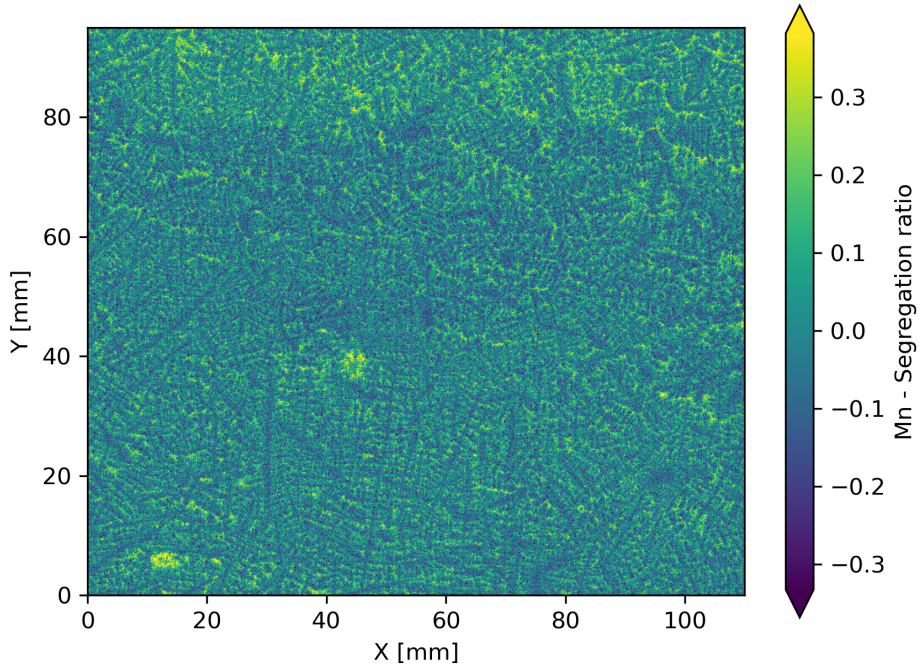

Figure 3.13: Mn segregation map of the sample C2_1.

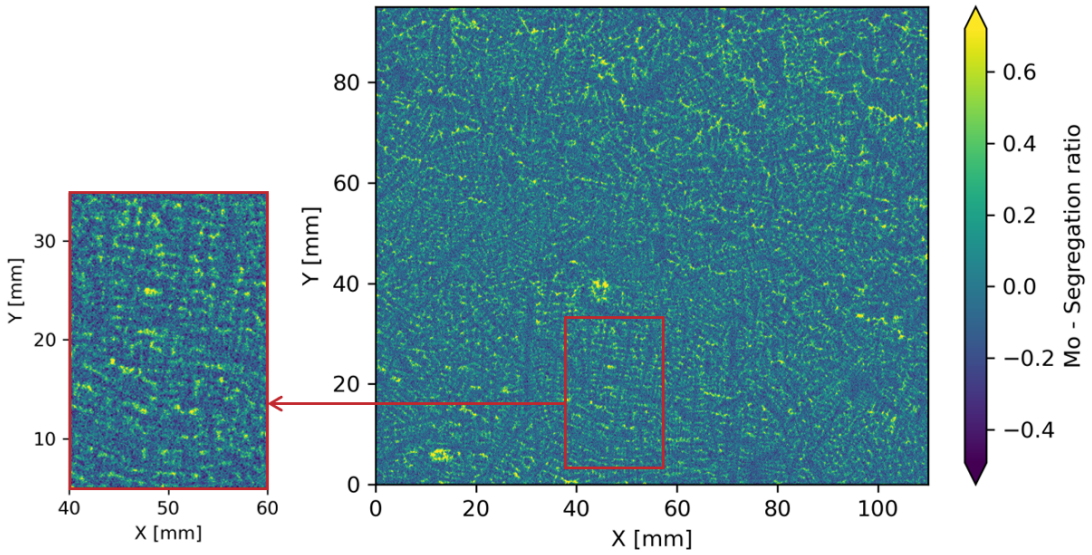

Figure 3.14: Mo segregation map of the sample C2_1 and close-up on a dentric details.

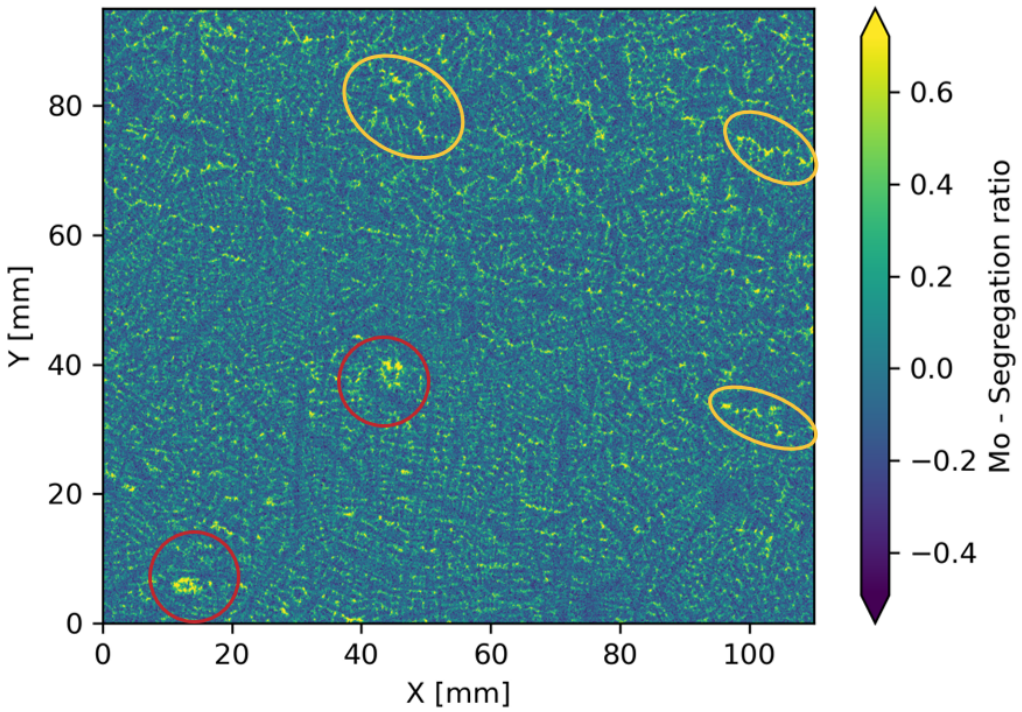

Figure 3.15: Mo segregation map of the sample C2_1 with highlighted details: circled in red enriched disks and in yellow intermediate scale segregates.

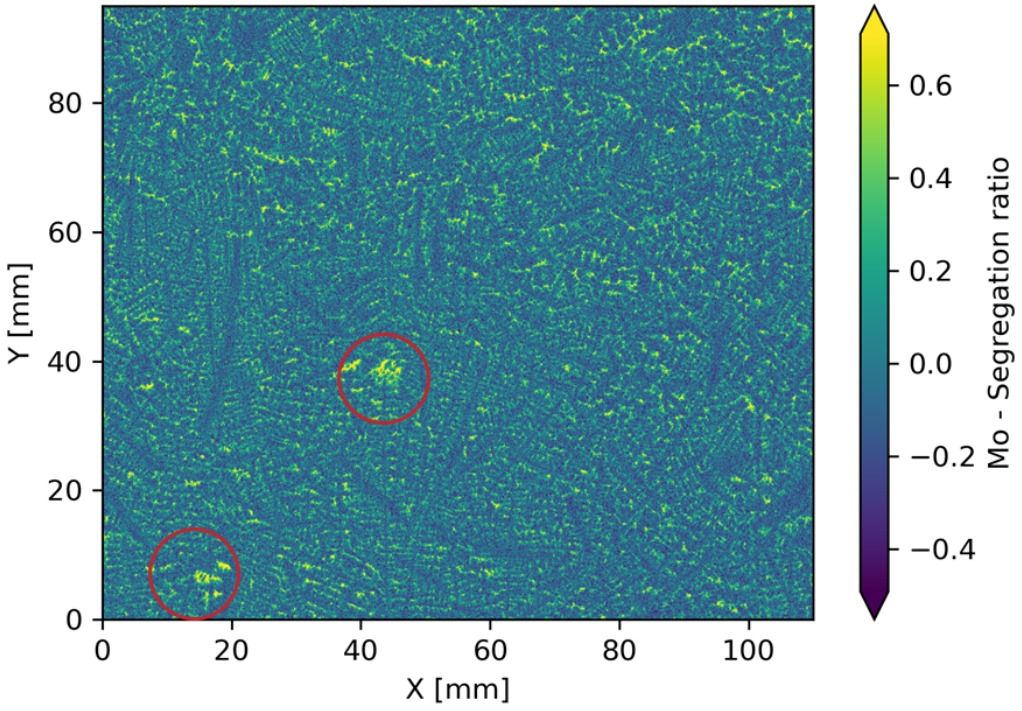

Figure 3.16: Mo segregation map of the sample C2_2 with highlighted details: circled in red enriched disks which are continuous cylindrical shape segregations between samples C2_1 and C2_2.

3.3.2 Images processing

As explained previously, different scales of segregation are visible on each µXRF map. Thus to study channels segregates on their own, it is crucial to be able to separate them from the rest of the information. This can be done with appropriate image processing applied to the segregation maps. The advantage of image processing is that it can be easily automated. As the study covers 30 successive maps, the application of an image processing that can identify channel segregates can lead to a characterisation of the channels and of their structure in 3 dimensions.
On each map, 3 scales coexist. Within each scale, different segregation patterns can exists, as explained previously in 3.3.1. At large scales, the macrosegregations can be mass segregated as the top enrichment or the depleted cone that is found at the bottom of large ingots. Channel segregates also exist at the macroscale, they are localised macrosegregations. At an intermediate scale, mesosegregations can be found in local enrichment patterns that are larger than the dendritic scale. Finally, at the smallest scale, microsegregation is characterised by a local enrichment between the dendritic arms and a depletion of the dendritic trunks. The objective of the image treatment is to isolate the channel segregates from any other segregation pattern.
On the 30 successive maps, the mass macrosegregation is not represented since the maps are processed with a segregation ratio that is calculated with respect to the average concentration of each individual map, i.e. the average composition used in the formula for the calculation of the segregation ratio is the one of the sample plane. Thus any shift of average composition between the successive sample planes is neglected. On the other hand, smaller-scale segregation such as microsegregations can be considered as experimental noise for the observation of channel segregates and intermediate-scale segregation. A common way to get rid of experiment noise is the use of a filter. A well-selected Gaussian filter helps to smooth small-scale patterns without decreasing the larger-scale information.
In this study, a truncated Gaussian filter was applied to segregation ratio maps. The Gaussian filter is determined by its standard deviation σ. The truncation of the kernel is done with a 4σ size square. Three different standard deviations were tested on the µXRF maps: 13, 25 and 50 pixels (each pixel being 100µm, the Gaussian kernels used were 0.52, 1 and 2 cm large). On the unfiltered map, the size of the enriched area corresponding to channel segregates is roughly 5 mm in diameter. As it can be seen in figure 3.17b, the first filter smooths the enrichment between secondary dendritic arms spacing, however, the solute-depleted primary dendrite trunks remain visible. Only a part of microsegregation is filtered. The second filter (figure 3.17c) fades away both enrichment between secondary dendrite arms and depletion of solute in the dendrite arms. When the Gaussian used in the filter is even larger, microsegregation is also strongly diminished, however, the filter also affects the rest of the map, as can be seen in figure 3.17d. The global differences between enriched and depleted zones are softened and the edge of the segregated channels area deteriorated. The objective is to reduce microsegregation without degrading the information on the channel segregates. The second filter ($\sigma = 0.25\,\text{cm}$) is the best option. A Gaussian filter with a 0.25 cm standard deviation and a 4σ size was applied to

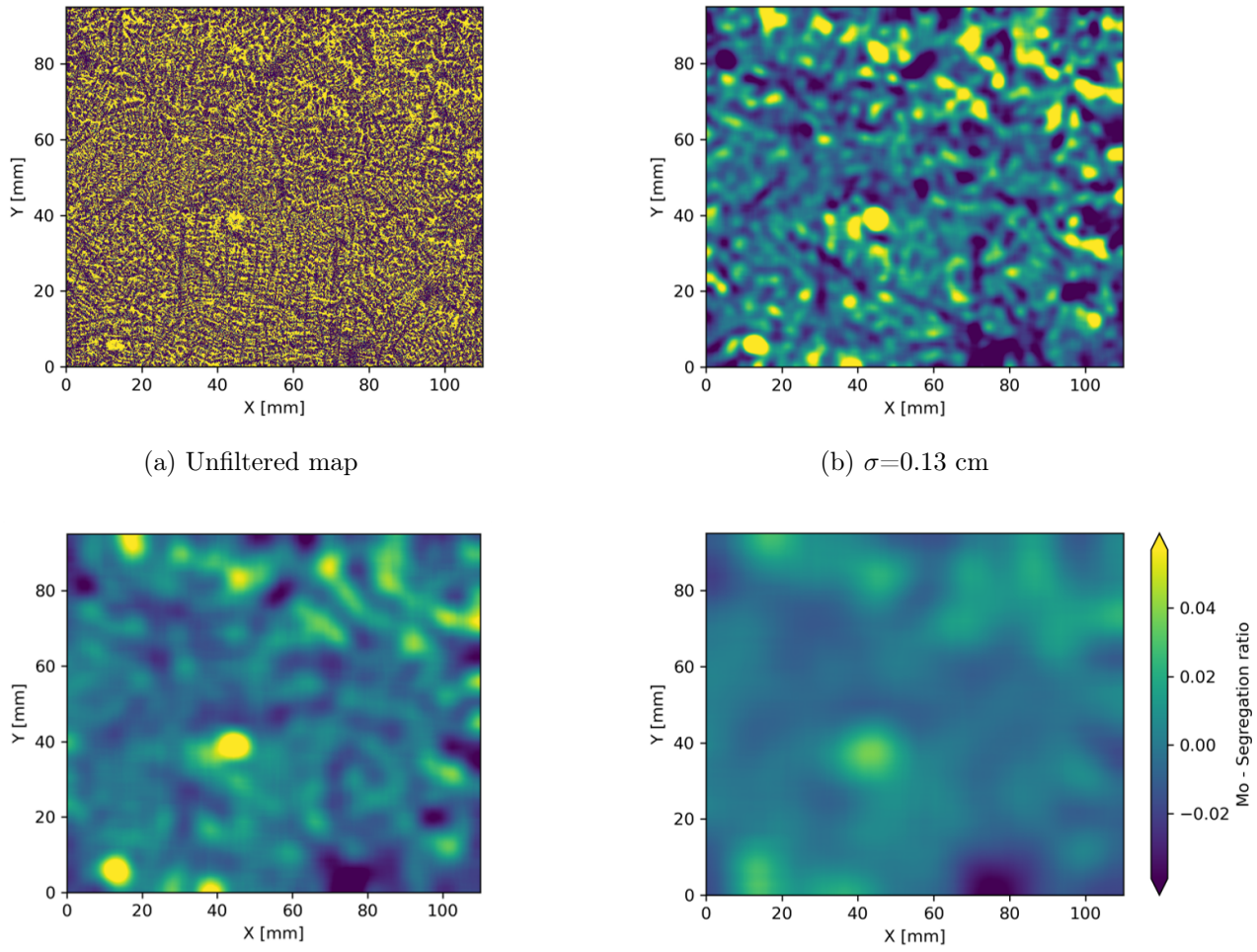

(a) Unfiltered map

(b) σ=0.13 cm

(c) σ=0.25 cm

(d) σ=0.50 cm

Figure 3.17: Mo segregation map from sample N°1 with different Gaussian filters applied. The truncation of the Gaussian kernel is 4σ and 3 standard deviation values are presented.

the 30 successive Mo-segregation maps.
On filtered maps, the enriched area corresponding to segregation channels can be identified and separated from the rest of the map with a threshold. Indeed, channel segregates are highly segregated, on each map they correspond to the most segregated area. Selecting the highest composition area should separate the channel segregates from the rest of the material. Several values for the threshold were tested. To select the threshold, the distribution of the segregation ratios of the 30 filtered maps was used and the 95^{th} quantile was selected, corresponding to a Mo segregation ratio of 0.029. This limit separates the 5% solute-richest surface from the rest of the maps. On the corresponding solute fraction curve, the 95^{th} quantile (Q95) marks the limit between the middle part of the curve and the tail of the curve. The tail of solid fraction curves corresponds to the richest solid, so the last one to solidify. This last liquid can be found trapped between dendritic arms at small scales, at larger scales the last liquid to solidify is the one flowing

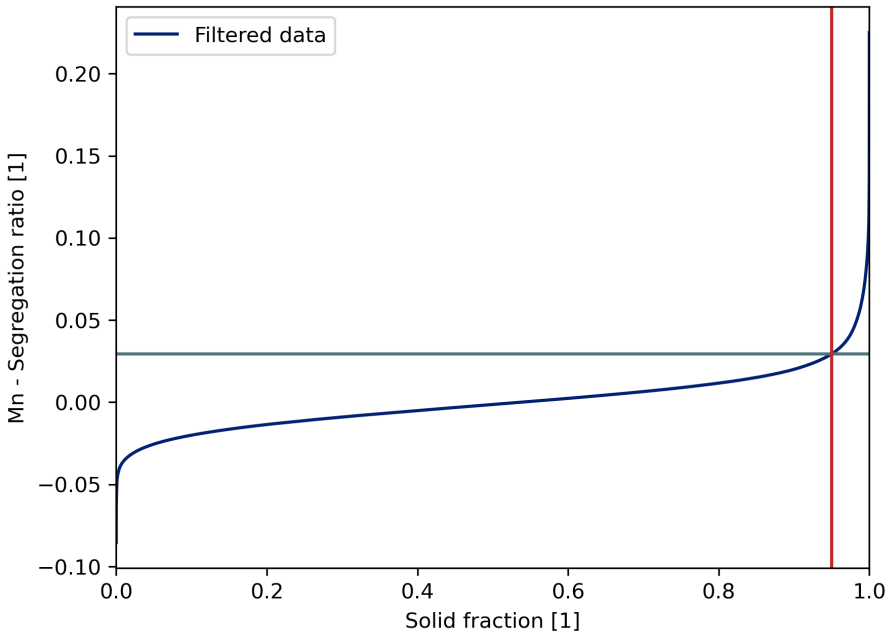

Figure 3.18: Cumulative solid fraction of the filtered data, the 30 filtered maps are considered. The red line represent the Q95 limit and the green line its associate value. Any point above theses lines is selected by the threshold.

in channels. The solid fraction curve however does not present a strong inflexion point, so several thresholds were tested. Thresholds greater than 0.029 were too restrictive and did not allow the selection of several dots corresponding to channels that were identified by the human eye. On the other hand, smaller thresholds failed to distinguish channels from other segregation patterns and led to confusing images. Maps were then binarised: every value above 0.029 was considered as potential channel segregates, whereas any value below 0.029 was not taken into account for the channel segregates characterisation. The process is illustrated with the figure 3.19, on which the threshold is represented on the filtered map (3.19a) and the second image (3.19b) shows the binary image obtained. The binary images are black and white, the black parts are the enriched areas that might be channel segregates, whereas the white parts are channel-free zones.

3.3.3 3D reconstruction

In the *short* ingot, 30 successive samples were taken at the C location in the *xy* direction. Channel segregates were observed on the µXRF maps realised on these successive samples. Images treatments described in 3.3.2 were applied to the 30 maps to separate enriched areas that might be channel segregated from channel-free areas. Figure 3.20 gives a representation of the stack of images obtained after image treatment of the 30 maps. As the spacing in the z direction between samples is known, it is possible to interpolate the 3-dimensional shape of the enriched areas selected with the image treatment. The volume interpolation was made with 3DSlicer, a free open-source software [93].
Based on the binary maps considered as slices of the volume, the software creates a 3D

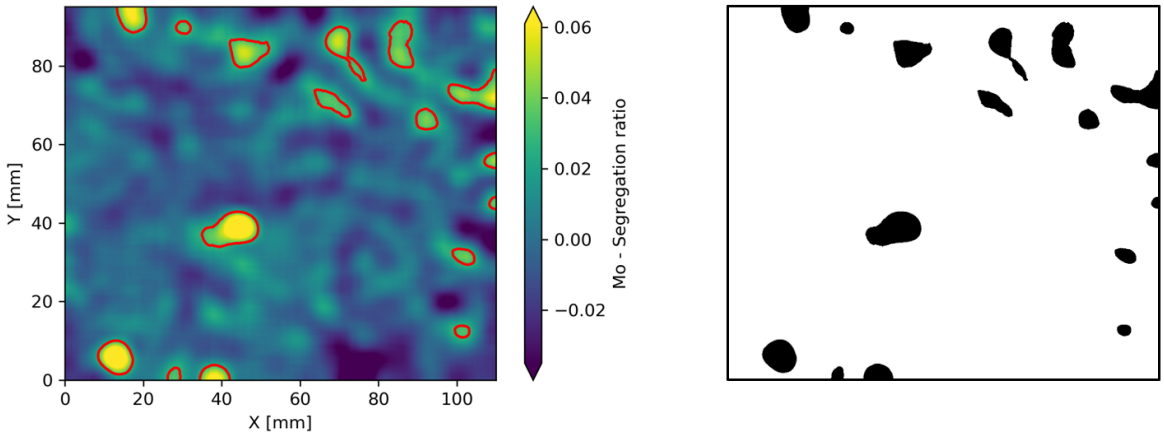

(a) Gaussian filtered chemical segregation map, with the segregation ratio threshold of 0.029 highlighted in red.

(b) Map obtained after binarisation with the 0.029 threshold.

Figure 3.19: Binarisation process for channel segregates identification and analysis.

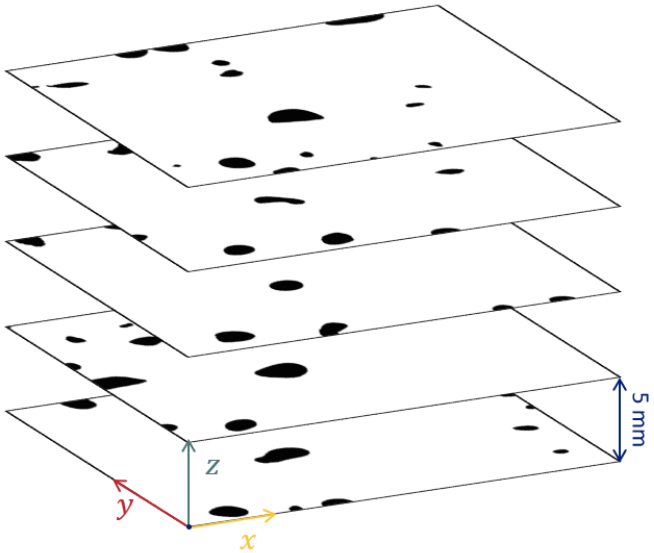

Figure 3.20: Representation of the 5 first binary images corresponding to µXRF maps after image treatment. The black areas are the enriched areas that might correspond to channel segregates, whereas the white areas are the channel-free zones.

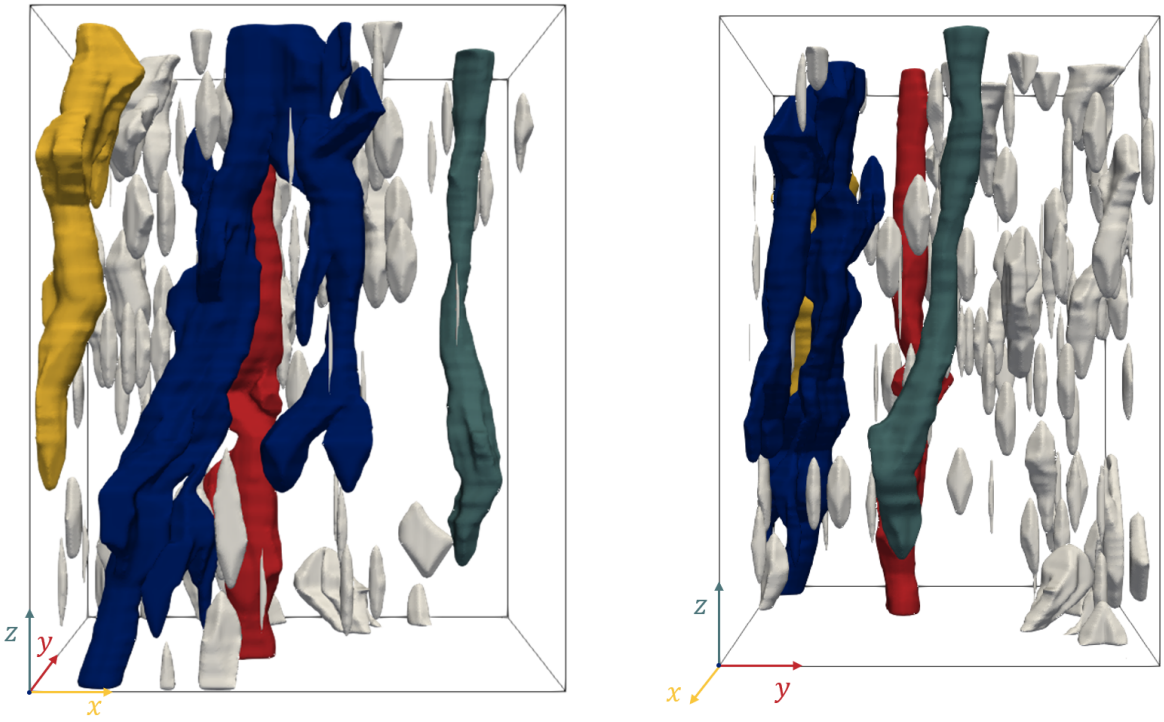

(a) View from the xz face

(b) View from the yz face

Figure 3.21: Segregations selected thought the image treatment and reconstructed in 3D. The y-axis is parallel to the radius and the z-axis point at the top of the ingot. The represented box dimensions are: $110 \times 95 \times 145$ mm^3 for $x \times y \times z$.

reconstruction of the segregations identified with the image treatment. In figure 3.21, the reconstruction of the segregations is shown.
Four different channel segregates can be observed. Two channels are continuous throughout the whole volume, one of them is made from two smaller channels that merge. Another channel segregation appears for the first time on sample C2_6 and finally the last appears on sample C2_11, both of them are observed until the last sample is analysed. In the surroundings of the long and continuous channel segregates smaller segregation volumes are observed. The smaller volumes were interpolated in 3D from non-continuous enriched areas and corresponded to intermediate-scale segregation. These intermediate-scale segregations were selected through the image treatment process. In 2D they are similar to transverse observations of channel segregates: similar intensity, shape and scale. However, they are not continuous from one sample to another.

3.4 Conclusion

This chapter exposes the process of adopting a new technique for the characterisation of chemical segregation in steel ingots. A gap in characterisation techniques was highlighted by the literature review: a different technique was required to map intermediate scale-segregation on centimetric scale samples. This observation leads to the consideration of a pre-existing technique, well-known in geology, the µXRF.
Applying a characterisation technique to a new type of material requires a few adjustments. The first section of the chapter focused on the adjustments needed for the adaptation of µXRF to metallurgical analysis, three aspects were looked at: the sample preparation, the beam settings and the acquisition step and time. All were optimised for the analysis of centimetric low-alloy steel samples. The tests revealed that a flat sample ground down to P800 (21.8 µm granulometry) is the only sample preparation required. The beam settings were optimised for the analysis of Mn and Mo, two elements of interest in our study. The beam was filtered with an Al 100 µm filter, the use of a filter enabled an increase of the current up to 200 µA for an acceleration voltage of 50 keV without increasing the artefacts on the measure. Different filters were tested. Al 100 µm was chosen since it gave the best compromise for the analysis of both Mo and Mn. This filter gives a large intensity peak range for Mo and causes only a small decrease in signal intensity on Mn-peak. Finally, the acquisition step and time were set to 100 µm and 45 ms of acquisition for each spectrum. With this acquisition step, the visual appearance of the map is acceptable down to a small scale (dendrites were still visible), without the need to increase the number of points on the map beyond practicability. With this reasonable acquisition step, the acquisition time was maximised without failing the objective of one map analysed per night and set to 45 ms.
The use of µXRF for segregation analysis was validated after comparison with EPMA. Samples were analysed with both techniques and the results were compared. Although the µXRF maps are noisier visually, they still represent the same segregation patterns as the EPMA maps. The solid fraction curves of maps obtained with both techniques are very similar, which confirms that µXRF is suitable for segregation analysis on the experimental conditions defined in 3.1.
With access to a new segregation characterisation technique, which requires little sample preparation and is fast and easy to use, numerous centimetric scale samples were analysed. Several samples reveal the presence of channel segregates. Thanks to successive sampling, the evolution of channel segregates with the height was possible. A two-step image treatment (filtration and binarisation) was designed to isolate the channel segregation patterns from the rest of the segregations on the maps. A 3D reconstruction of the channel segregates was built up from the stack of 30 treated maps. In the reconstructed volume, several scales of segregation are visible. There are continuous channel segregates and intermediate scale segregations which are similar to channel segregates in 2D binary images but are not continuous throughout the analysed height.
To our knowledge, this 3D reconstruction of channel segregates is the first of its kind.

Chapter 4

Segregation characterisation based on µXRF

I'm getting older,
I think I'm aging well
I wish someone had told me
I'd be doing this by myself
There's reasons that I'm thankful,
there's a lot I'm grateful for

Billie Eilish,
Getting older

Contents

In this chapter, the characterisation technique developed and tested in the previous chapter is used for segregation characterisation. First, segregations were observed in 3D, based on interpolation between successive centimetric segregation maps. Analysing in 3D the segregations based on µXRF maps gives a precise idea of the shape and distribution of segregations. The intensity of the segregation is also studied.
Segregations were also studied in 2D on samples taken from various ingots. The variety of samples allows studying the effect of primary microstructures on segregations and to investigate the effect of the ingot shape on segregation patterns.

4.1 Observations and analyses of segregations in 3D

In chapter 3, successive centimetric segregation maps were used to reconstruct 3D channel segregates. Along channel segregates intermediate-scale segregations were also observed. This joint observation provides new insight into segregation distribution in 3 different directions at the same position in the ingot and makes possible the study of channel segregation shape, orientation, size, etc in all directions. It is also the first observation of intermediate-scale segregation and the opportunity to compare their structure to the channel segregates structure.
In a $110 \times 95 \times 145$ mm^3 volume, four channel segregates were identified, together with 220 intermediate-scale segregation. This section presents an analysis of channel segregates and a comparison with the intermediate-scale segregations. The objectives are to characterise channel segregates shape, size, orientation and segregation distribution and to propose a first definition for intermediate-scale segregation based on their observation and comparison with channel segregates.

4.1.1 Analysis process

As mentioned previously, in the reconstructed volume 2 types of segregations exist simultaneously: channel segregates and intermediate-scale segregations, that look like channel segregates in 2D but are not continuous. To reduce bias in the results, structural investigations were carried out on the 2D images used for 3D reconstruction, rather than directly on the 3D reconstruction, which involves interpolation. However, the 3D reconstruction was needed to distinguish the 2D channel areas of each of the four channels from each other and from intermediate-scale segregation areas.
The 3D reconstruction is represented in figure 4.1 and 4.2. The first images of the reconstruction (4.1a, 4.1b and 4.1c) show both channel segregates and intermediate-scale segregations. The intermediate-scale segregations were kept in grey and a different colour was assigned to each channel segregates. In the next images (4.2a, 4.2b and 4.2c) channels were isolated for better observations. As a reminder, the 3D reconstruction is based on 30 samples with 5 mm between each analysed surface in the z direction. The samples were numbered from 1 (bottom) to 30 (top).

- The red channel segregate (visible in figures 4.1c and 4.2c) is a continuous channel segregate that goes from the bottom to the top of the analysed volume and present a few small ramifications.

- The blue channel segregate is the larger channel observed: it is continuous on the analysed volume and has large ramifications. One of the ramifications is so large it could be identified as a channel segregate merging with another. Inside channel segregates upward flow of enriched liquid flows up (in the z direction). As liquid flows up two close channels can merge.
- The green channel segregate is the only channel segregate observed in this study that does not present any ramification. The green channel segregate starts on sample N°6 and is still observed on sample N°30.
- The fourth channel segregate is the yellow one, visible on samples N°11 to N°30 and present small ramifications.

The visual analysis was complete with a quantitative investigation performed on the binary images used for the 3D reconstruction. The binary images are obtained from the image treatment described in the chapter 3. In each binary image, black areas correspond to enriched areas (channel segregates or intermediate-scale segregation) whereas the white areas only contain microsegregation.
Before analysing the binary image, each black area was identified as a 2D xy channel area or an intermediate-scale segregation area. Each 2D xy channel area was also attributed to each channel. The 3D reconstruction helps identify the nature of each enriched area, especially for channel ramification. An example of the identification and preparation process is shown in figure 4.3. Based on a binary image (4.3a), and the 3D reconstruction, each enriched area is assigned. The 2D xy channel area are coloured according to their channel segregate colour and the intermediate-scale segregation areas are kept in black. Any intermediate-scale segregation areas cut by the border of the image are suppressed. 2D xy channel areas on the edge of the images are less numerous and were kept (Otherwise, insufficient data would have negatively impacted the calculation of length and orientation).

4.1.2 Size, shape and orientation of segregation

Working with the binary images makes possible precise measurement for channel segregates and intermediate-scale segregation in the plan xy. Each 2D xy channel area part of a channel segregate was analysed individually. In case of ramifications, several 2D xy channel areas part of the same channel can be found on the same sample, in that case, each 2D xy channel area was still considered individually for individual shape and size measurement. Table 4.1, presents the main measurement realised on the channels and their 2D xy channel area. The channel length was measured by acknowledging a 5 mm distance between each image in the z direction. The measured length is minimal since no channel end is observed in the investigated volume. Maximum and minimal Feret diameters were calculated for each 2D xy channel area, as well as aspect ratios ($^{Feret_{Min}}/_{Feret_{Max}}$). The 2D xy channel areas have similar sizes and shapes in 2D: close Feret diameters and similar aspect ratios. The blue shows slightly larger 2D xy channel areas compared to the others and the green channel shows slightly smaller 2D xy channel areas. The average 2D xy channels areas surfaces confirms the previous observations:

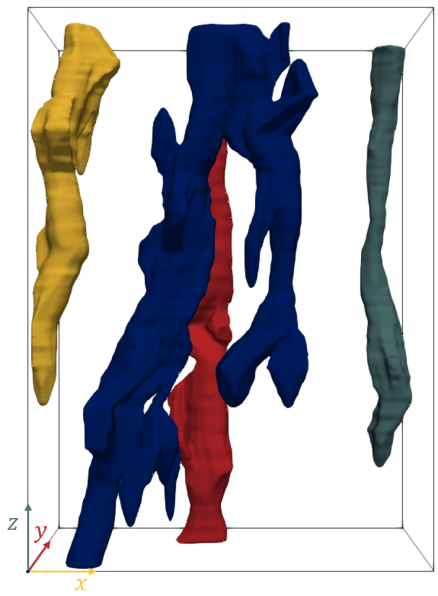

(a) View from the xz face

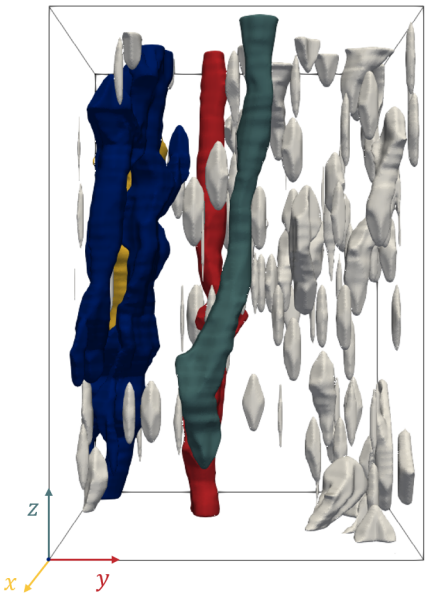

(b) View from the yz face

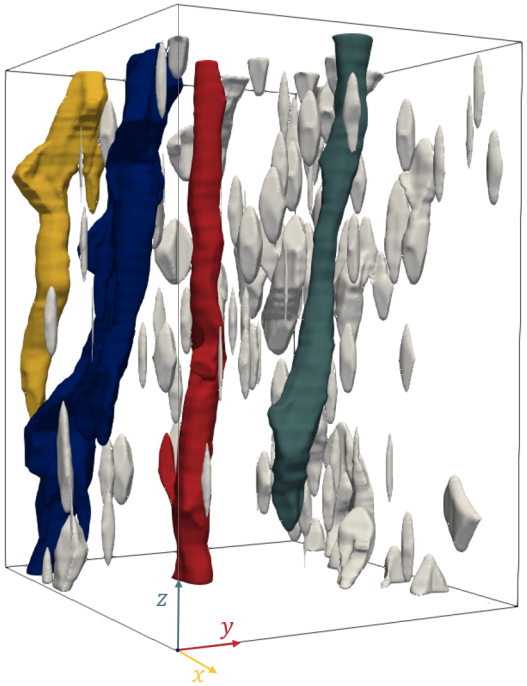

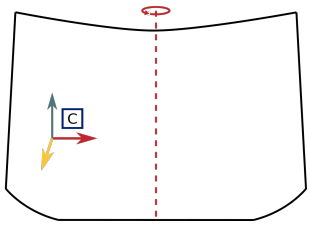

(c) Perspective

Figure 4.1: Visualisation of the 4 channel segregates (in colours) and intermediate-scale segregations (in grey) observed in the reconstructed volume based on µXRF analysis. The represented box dimensions are: $110 \times 95 \times 145$ mm^3 for $x \times y \times z$.

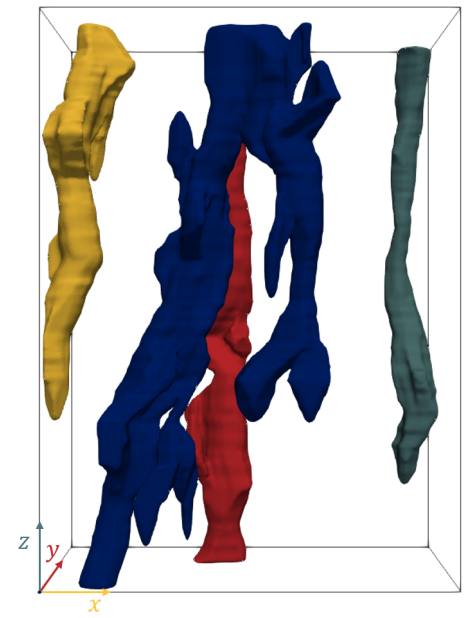

(a) View from the xz face

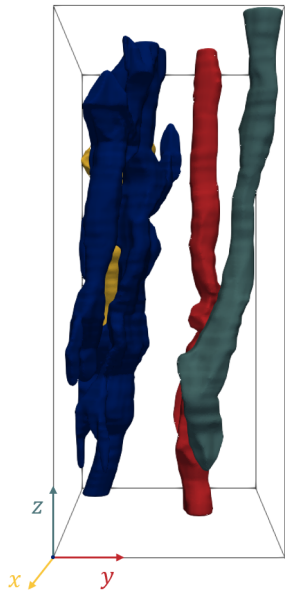

(b) View from the yz face

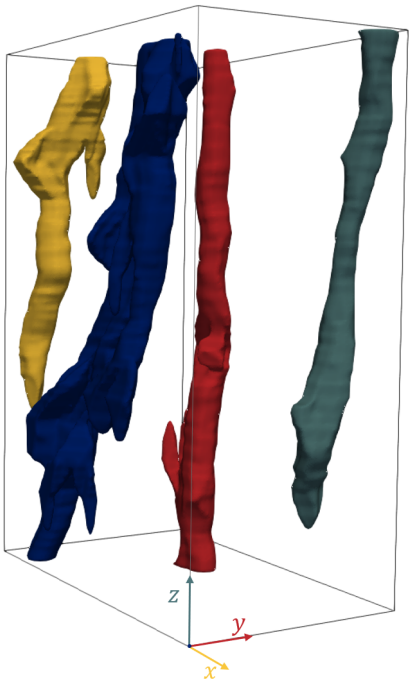

(c) Perspective

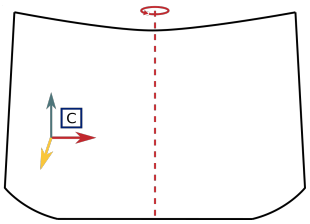

Figure 4.2: Visualisation of the 4 channel segregates (in colours) observed in the reconstructed volume based on µXRF analysis after removal of intermediate-scale segregations. The represented box dimensions are: $101.5 \times 58.9 \times 145$ mm^3 for $x \times y \times z$.

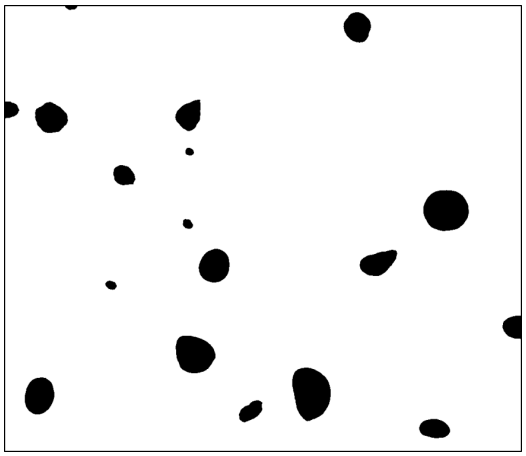

(a) Binary image, major segregations are in black

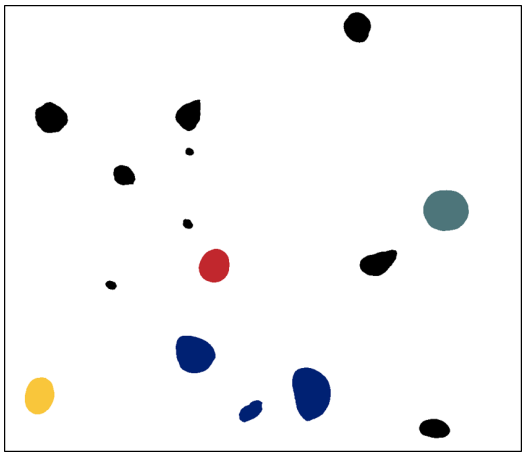

(b) Binary image, only the channel segregates dots were kept

Figure 4.3: Example of the identification process of channel segregates on the 20th slice.

Table 4.1: Comparision between the different channel segregates, based on 2D *xy* channel area (average values per channel).

Structure	**Blue**	**Green**	**Yellow**	**Red**
Number of 2D areas [1]	60	25	21	31
Minimal length [mm]	145	120	145	95
Average maximum Feret diameter [mm]	12.8	9.1	10.6	10.8
Average minimum Feret diameter [mm]	8.0	6.9	7.6	7.1
Aspect ratio [1]	0.7	0.8	0.7	0.8
Average area [mm²]	80	48	61	56

the channels are equivalents, even if the blue is slightly larger and the green one slightly thinner. The order of magnitude of their diameter is 1 cm.
Intermediate-scale segregation areas were also analysed individually, all but the ones on the edge of the image were analysed. In table 4.2, the average values of both databases are compared. Intermediate-scale segregations and 2D *xy* channel areas have equivalent shape, but the intermediate-scale segregations observed are smaller than the 2D *xy* channel areas. The average area of single intermediate-scale segregation is only a third of the average 2D *xy* channel area.
In figure 4.4 the proportion of the surface of each sample occupied by 2D *xy* channel areas is presented as a function of the *z*-position of the sample. The total occupied surface is represented in grey, whereas the surface occupied per channel is represented in the corresponding colour. The blue channel takes a bigger portion of the sample surface compared to the other channels: the 2D *xy* channel areas associated with the blue channel are larger (see table 4.1) and more numerous because of its numerous ramifications. The ramifications from the blue channel are long and can be observed on several samples, increasing the surface occupied by this channel in particular. Yet, there is no correlation between

Table 4.2: Comparision between 2D *xy* channel area (average values) and intermediate scale segregations.

Structure	**2D *xy* channel**	**Intermediate scale segregation**
Number of 2D areas [1]	137	220
Minimal length [mm]	-	<5
Average maximum Feret diameter [mm]	10.8	6.0
Average minimum Feret diameter [mm]	7.4	3.9
Aspect ratio [1]	0.8	0.7
Average area [mm²]	61	22

the z-position (height in the ingot) and the surface occupied by channel segregates on samples: the area occupied by the channel does not increase or decrease with height on the investigated volume (meaning 145 mm high). Only one major increase can be seen in the graph: between 0 and 30 mm in z-position, the surface is more than doubled. This increase is not a global attendance but the result of the appearance of a new channel segregate (the green one) on the sample N°6 (z = 25 mm) and the combined effect of several and large blue channel ramifications (from sample N°5, z = 20 mm).
The proportion of the surface occupied by intermediate-scale segregation against the surface occupied by 2D *xy* channel areas is compared in figure 4.5. No correlation either between the surface occupied and the height of the sample nor between the surface occupied by the 2D *xy* channel areas or the intermediate scale segregations. Every sample studied presented both 2D *xy* channel areas and the intermediate-scale segregations. On this set of samples, intermediate-scale segregations occupy a smaller proposition of the surface compared to the 2D *xy* channel areas. Intermediate-scale segregation contributes less than 2D *xy* channel areas to *xy* surface segregation in this batch of samples.
The 3-dimensional observation of channel segregations helps to understand better their shape and size. An additional observation can be done based on figure 4.2b: all channel segregates observed in the volume are tilted: as they rise, they bend toward the centre of the ingot. Some are only slightly tilted (the red channel, for instance, is almost straight), whereas others (the green channel) are strongly tilted. The channels' inclination and location (mid-height and mid-radius) could indicate A-segregates.
A-segregates have been investigated for decades, however, their characterisation is usually 2 dimensional. A-segregates can be studied in 2D in longitudinal cross-sections or transverse cross-sections. Pickering characterised A-segregates in two ways: macroetching and XRF measurements. Both were carried out in the longitudinal cross-section of a 12 t ingot. The observed A-segregates are 5 mm thick [68]. Transverse cross-section observations report an average 2D channel area width of 1 or 2 mm on A-segregates observed in a 500 kg ingot by macroetching [31]. Another study, reports an average 2D channel area of 20 mm² for A-segregates found in 17 kg ingots [45]. In his paper, Suzuki [45] reports that the size of 2D channel areas in transverse cross-section increases with the time spent in the mushy zone. In this study, the average area of 2D *xy* channel area (cor-

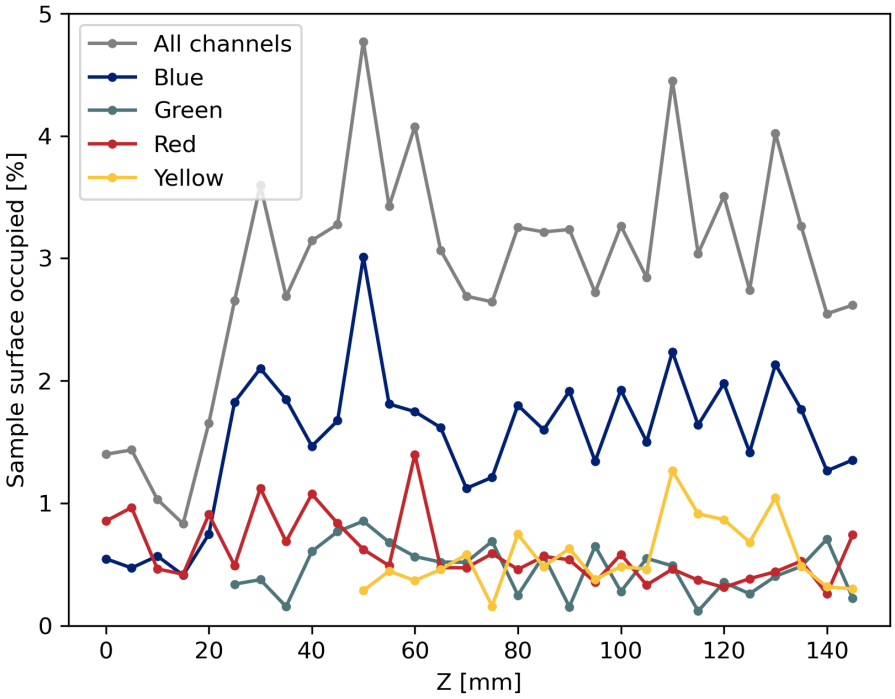

Figure 4.4: Evolution of the surface occupied by the sum of 2D *xy* channel areas on samples with height in the volume.

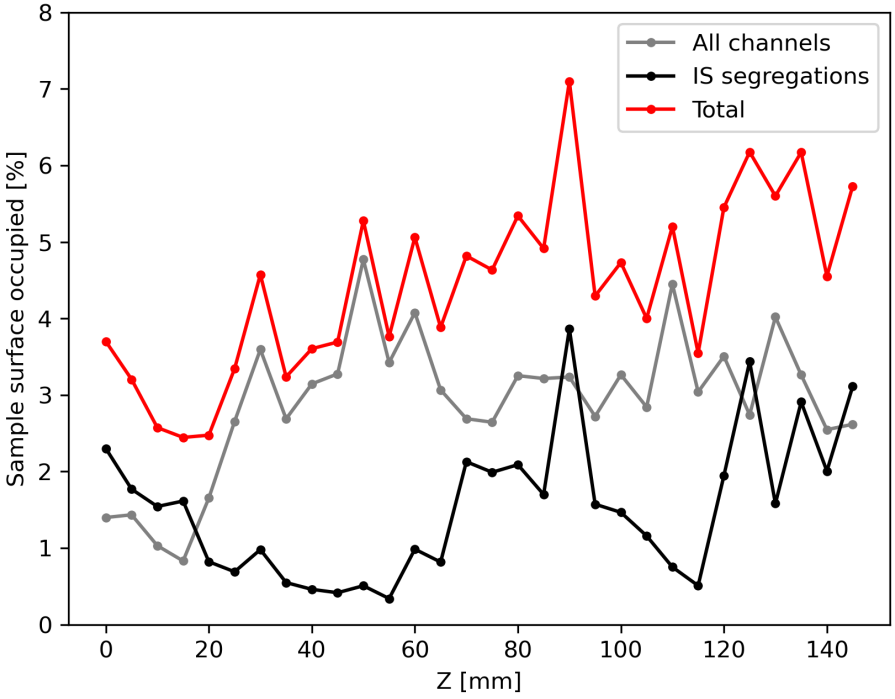

Figure 4.5: Evolution of the surface occupied by the sum of 2D *xy* channel areas and the sum of intermediate-scale (IS) segregations on samples with height in the volume.

responding to transverse cross-section) is 61 mm^2. The present observation shows larger channel segregates compared to Suzuki's, Chen's or Pickering's observation, however, our observation was carried out on a large ingot (116 t) and solidification of such ingots takes much longer than small ingots. The mushy zone takes time to fully solidify. According to Suzuki's work, it could explain larger A-segregates. The solidification history of the C-located samples will be explored in the chapter 5 with SOLID® simulations.
As for all characterisation work, there is a measurement uncertainty on the size of the channels discussed in this work. This uncertainty depends on the measurements made in µXRF and the image processing that leads to the identification of the 2D *xy* channel areas. The uncertainty is also valid for intermediate-scale segregation measurements. The precision of µXRF was optimised and discussed in chapter 3. As a reminder the image treatment applied to the segregation maps is a two-step process: Gaussian filtration and binearisation according to a threshold. The effect of the threshold upon the measured size of a 2D *xy* channel area and intermediate-scale segregation was tested on one enriched area of each kind. The two enriched areas were selected on sample N°11. The sample was filtered with a Gaussian filter, $\sigma = 0.25$ cm and then made binary with different thresholds. The thresholds tested were the quantiles of the 30 filtered map value distributions. Figure 4.6 shows the evolution of the 2D *xy* channel areas and intermediate-scale segregation with the quantiles used as thresholds. For 2D *xy* channel areas a threshold variation of 5% leads to an average difference of 1.25 mm on the equivalent diameter of the 2D *xy* channel areas (considering a round area) with a standard deviation of 0.59 mm. The uncertainty on the channel segregation diameter estimated with this method is around 12%. The uncertainty of the measure does not change the order of magnitude of the channel size (around 1 cm).

4.1.3 Segregation ratio evolution

During the investigation, another point that was studied was the evolution of segregation intensity within the channel segregates. On the original untreated map (expressed in segregation ratio relative to the sample), the areas within the channel segregates were isolated for segregation ratio analysis. The segregation ratio used for the analysis was the same used for the segregation map plotting:

$$S_i = \frac{C_i - \overline{C_s}}{\overline{C_s}} \tag{4.1}$$

avec

S_i, segregation ratio on the i-th point,
C_i, peak intensity on the i-th point and
$\overline{C_s}$, average peak intensity of the sample.

For each sample, the average segregation ratio within each channel was calculated and then plotted as a function of the height of the sample. If the channels had ramifications and so several 2D *xy* channel areas on the same sample, all were averaged together. In figure 4.7, the segregation ratio evolution within each channel and on average on all

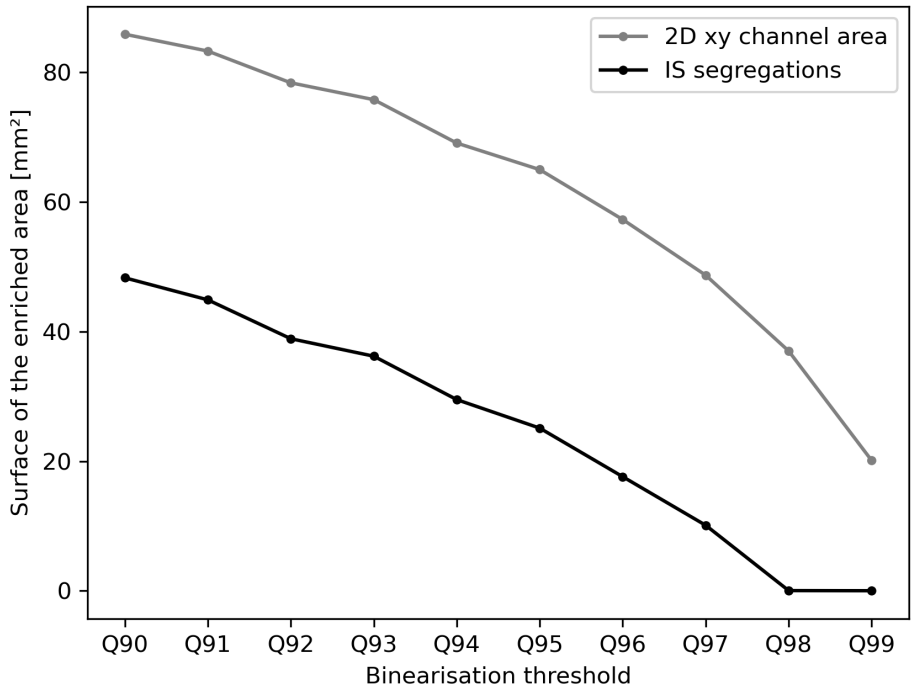

Figure 4.6: Evolution of the surface occupied by the sum of 2D *xy* channel areas and the sum of intermediate-scale (IS) segregations on samples with height in the volume.

channels is presented as a function of the height. As expected all average values are positive. There is not any clear evolution of the average segregation ratio in the channels with the height of the sample: as if the composition of the channel did not vary with the height in the ingot. A few points should be noticed in this analysis:

- The segregation ratio calculation is specific to each sample: each sample has its segregation ratio formula based on the average peak intensity of the sample.
- The segregation ratios presented are much greater than the segregation ratio limit used for binearisation in image processing. Because the binearisation is done on the filtered maps and the filtration process averages the values.

The segregation ratio of the channels was also compared to the segregation ratio of the intermediate-scale segregations. In figure 4.8, the evolution of both segregation ratios with height are plotted, as well as the average value in dashed lines. The channel segregates are slightly riched in solute than the intermediate-scale segregations: the average segregation ratio in the channels segregates is 0.075, whereas, in the intermediate-scale segregation, it is 0.070. The segregation ratio of intermediate-scale segregation does not seem to be correlated with the height of the sample: at this scale (14,5 cm), the sample height in the ingot does not influence the solute enrichment of either channel segregates nor intermediate-scale segregations.

The average segregation ratio of observed channels segregates is 0.075. In the literature, there is no comparable work to the one presented here. Studies mainly investigate channels segregated with macroetching, and only a few chemical analyses are performed: it can be qualitative, or ponctual analysis in the channel. Pickering did chemical analyses in A-segregates with EPMA and OES [5, 61]. The Mo concentration measured in the A-segregate is 0.62 wt% with EPMA and 0.87 wt% with OES, knowing the nominal composition of the steel (0.488 wt%), the segregation ratio can be calculated according to this manuscript definition (equation (4.1)). The Mo-segregation ratio measured by Pickering is 0.27 with EPMA and 0.78 with OES. These values are one order of magnitude bigger than the average segregation ratio in the channel segregates observed. Several factors can explain this difference:

1. The average segregation in the present study is computed on raw map data. The areas corresponding to channel segregates are isolated and studied. In the selected areas, there are depleted tiny zones coexisting with strongly enriched zones. Figure 4.9, shows an example of the selection on the Mo segregation map of the sample C2_20, the selected areas correspond to the the 2D xy channel areas on this sample. With this visualisation, the coexistence of enriched and depleted solid in the reconstructed channel segregates is obvious.

2. The EPMA measurement is a small-scale investigation and the result is a punctual measure, which is compared to average values of segregation ratios. In the channels segregates observed, there are local enrichment comparable to the one observed by Pickering [5, 61] (see figure 4.9, the enrichment greater to 0.4 in segregation ratio).

The difference between the OES measurement reported by Pickering, compared to the average segregation ratio measure in channel segregates observed is not explained yet.
In figure 4.10, both channels segregate, intermediate-scale segregation and all maps data were plotted in cumulative solid fraction curves. Channel segregates and intermediate-scale segregation have equivalent curves: they are almost indistinguishable from each other. The curve corresponding to the whole data set is a bit lower than the ones of the enriched areas, but has a similar shape: the areas selected with the image processing solidify the same way as the steel; local enrichment could be explained with local thermal and flow differences, this hypothesis is explored in chapter 5.

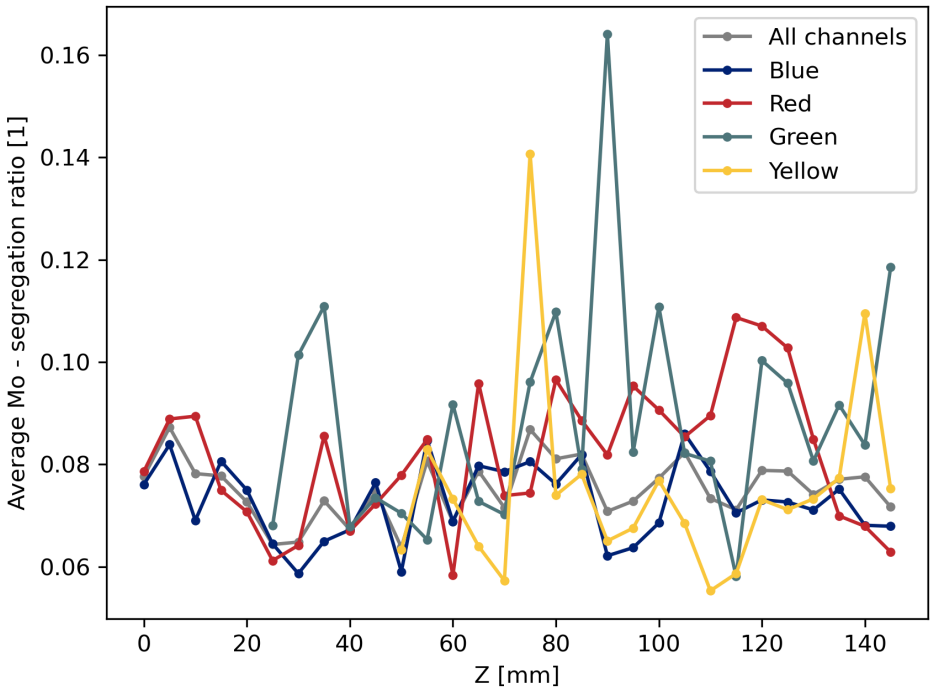

Figure 4.7: Evolution of the segregation ratio in channel segregates on samples with height in the volume.

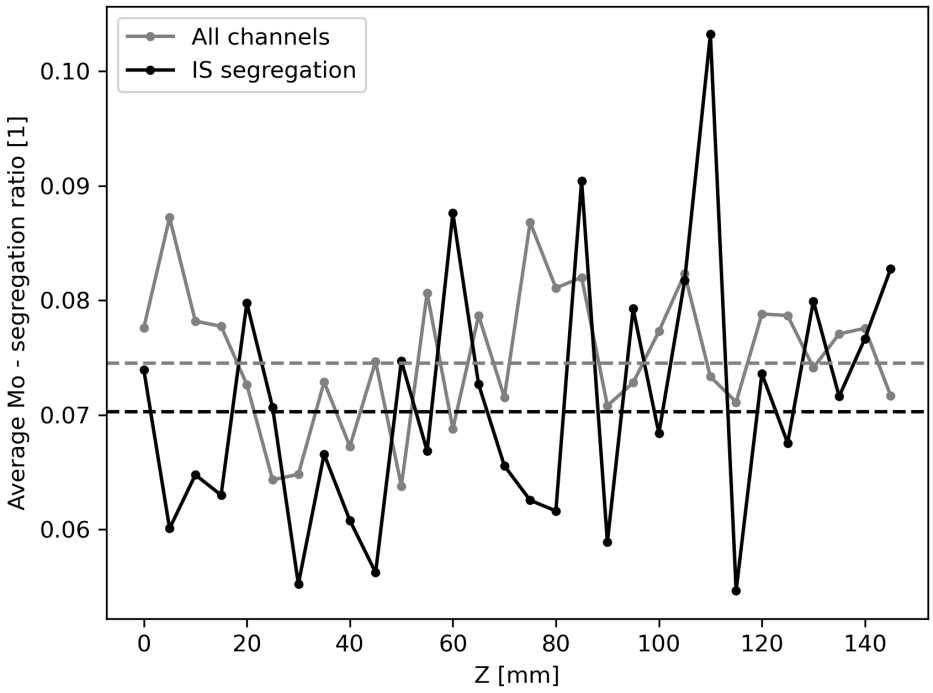

Figure 4.8: Evolution of the segregation ratio in channel segregates and in intermediate-scale (IS) segregations on samples with height in the volume. The corresponding coloured dashed lines represent the average value for both populations.

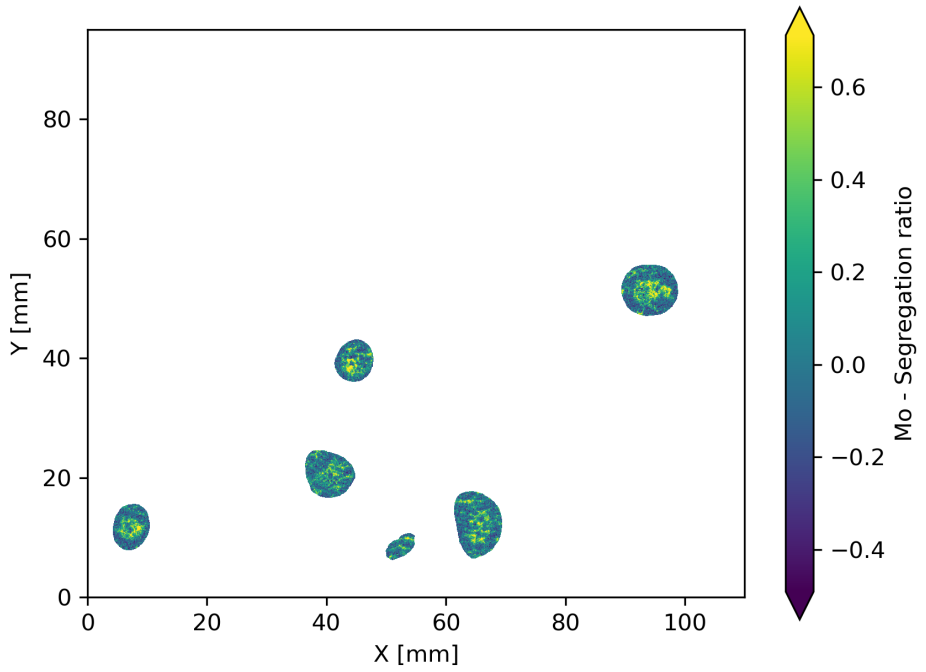

Figure 4.9: Extraction of channel segregates on Mo segregation map of the sample C2_20.

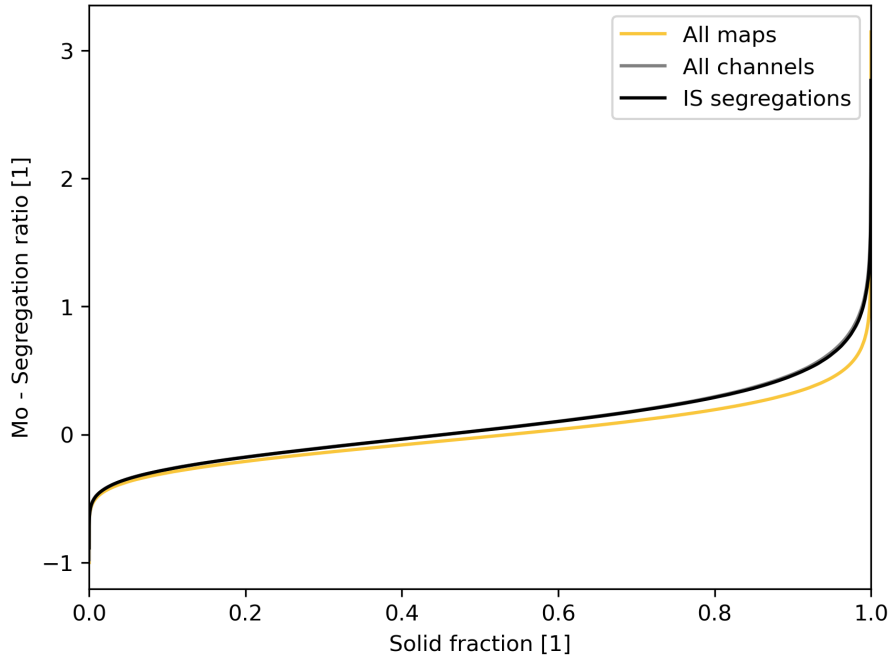

Figure 4.10: Comparison of the cumulative solid fraction curves of all the data, the channel segregation and intermediate-scale segregation.

4.1.4 Summary

Channel segregates and intermediate-scale segregations were observed in 3 dimensions based on interpolation between 2-dimensional successive µXRF maps. The observation of segregation patterns in 3D made possible the study and comparison of different segregation features:

- The size and shape of the segregations, in 3D and in the *xy* plan.
- The evolution of 2D *xy* channel area (the channel transverse cross-section) and intermediate-scale segregation area with the sample height.
- The evolution of the segregation intensity within the segregation patterns with the sample height (in total the samples covered 14,5cm in the *z*-direction).

The development of a new methodology enabled the investigation of such features with high spatial resolution. The investigation highlighted 4 main points:

- Four channel segregates were observed. Because of their location (mid-height and mid-radius) and their inclination (toward the ingot centre), we can assume that they correspond to what is usually called A-segregates. The precision of the 3D observations of the channels gives new insight into their shape: channel segregates were proven to be branched (with big and/or small ramifications), and they can be sinuous and merge together.
- The four close channel segregates observed had equivalent sizes. Their average 2D *xy* channel area is an ellipse: 10.8 mm and 7.4 mm of diameters. The 2D *xy* channel area does not follow any trend with the height in the analysed volume of steel. The segregation intensity observed within the channel segregates (though the segregation ratio) does not evolve with the height in the investigated samples.
- Intermediate-scale segregations were observed close to the channel segregates. The intermediate-scale segregations observed on *xy*-plans were on average 22 mm^2, in general, their area is smaller than the 2D *xy* channel area. Intermediate-scale segregations were not observed on successive samples as channel segregates (no continuity). Assuming a spherical segregation pattern with a diameter of 5,29 mm (based on the average surface), the distance between 2 samples (5 mm in the *z*-direction) makes the chance to catch the intermediate-scale segregation continuity difficult.
- The segregation intensities of channels segregates and intermediate-scale segregation are similar. The study of their cumulative solid fraction curves reveals a similar solidification path.

4.2 Comparison of segregations patterns in different ingots

The channel segregates observations reported in the literature are usually 2D [5, 31, 45, 61, 68, 94]. The channel segregates are cuts and observed in their longitudinal cross-sections or transverse cross-sections. The previous section presented a detailed channel segregate characterisation based on 3D observation. This section is dedicated to channel segregation observation. A comparison between 3D observation and 2D observation shows the advantages of both techniques. The 2D analysis is a faster way to observe channel segregates (only a few samples are required, against 30 for a 14,5 cm high 3D reconstruction). 2D analysis makes possible the comparison of different solidification conditions with only a few samples: in this study, segregations were mapped in 3 different ingots. Both the influence of the ingot shape and the primary solidification structure effect on segregations at the centimetric scale were studied.
In total, 4 batches of samples were taken in 3 different ingots. A first batch of samples was taken in the *short* ingot in the C position. A second batch of samples is from the *long* ingot, the samples were located in the H position. Finally, two sets of samples were taken in the *hollow* ingot: both in the middle of the bulk section of the ingot, one set near the top and the other at a lower position. In this section, the segregation maps obtained with the different samples are presented, commented and compared. This comparison leads to a discussion on primary microstructure differences and channel segregates formation.

4.2.1 *Short* ingot: 116 tons

In the *short* ingot, 32 centimetric size samples were taken: 30 were taken horizontally in the ingot and used for the 3D channel segregates reconstruction, see 4.1, and 2 more samples were taken vertically, in the YZ plan, y direction being the radius of the ingot and z the height. The samples taken vertically are adjacent to the one taken successively horizontally for the 3D reconstruction study, the spatial arrangement of the samples in the ingot is represented in figure 4.11a. The samples were taken in the C position of the ingot (see figure 4.11b). The 2 vertical samples, C3_A and C3_B were analysed with µXRF in the experimental condition defined in the chapter 3: the beam working conditions were 50 keV, 200 µA, filtered with 100 µm of Al and the sample was scanned with a 100 µm acquisition step and a 45 ms acquisition time. The segregation ratio maps obtained for Mo are presented in figure 4.12. The samples are arranged on the page the same way they were arranged in the ingot, the top part of the ingot being the top of the page and the centre of the ingot in the left direction.
Several scales of segregation are visible on the segregation ratio maps. Microsegregation can be seen between dendritic arms and reveals an equiaxed dendritic primary microstructure. Mass macrosegregation is not observable because of the local segregation ratio assumption. However, local macrosegregation: channel segregates are visible on one of the samples. On the top sample (top part of the figure) there are two strongly enriched lines: they are longitudinal cross-section observations of channel segregates. In the extension of the bottom line, there are several enriched spots both on sample C3_A (the top sample) and the top part of sample C3_B (the bottom sample). In 3D channels segregates are not straight cylinders, but they are sinuous objects as observed in the previous section

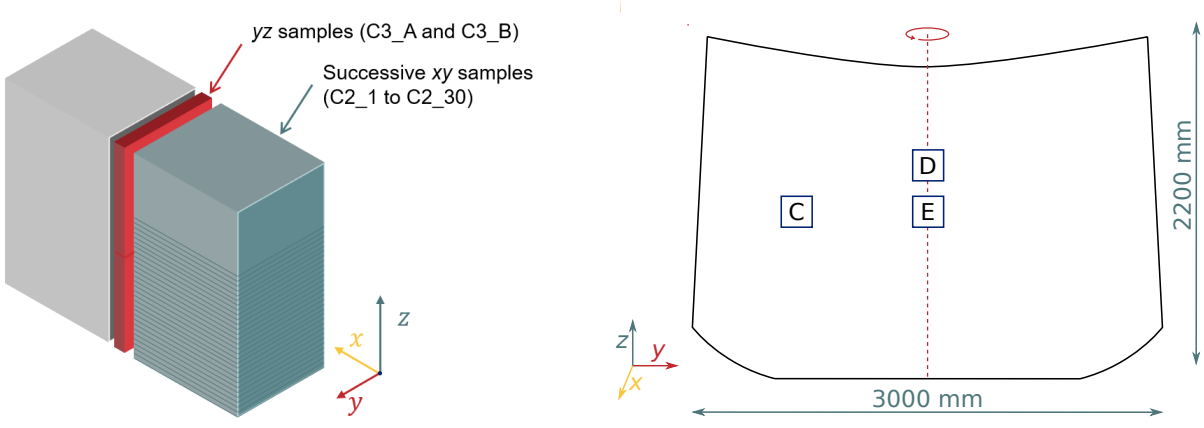

(a) Schematic view of sampling in the *short* ingot at the C position.

(b) Sectional schematic of the short 116 tons ingot.

Figure 4.11: Sampling in the *short* ingot.

(see 4.1). This sinuous shape brings the hypothesis of continuous channel segregation in both samples. In 2D observation, with only one plan observed, the channel might appear discontinuous with a succession of almost aligned enriched spots and lines. Still, it might exist beneath and above the analysed surface as a sinuous enriched channel. It can also be noticed that both channels are tilted: their upper part bending toward the centre of the ingot. This inclination is observed in the case of A-segregates.
As shown in the figure 4.11a, the samples used to produce the vertical segregations maps (figure 4.12, samples C3_A and C3_B) were adjacent to the samples used for the 3D reconstruction (samples C2_1 to C2_30). No continuous channels were observed between C2 and C3 samples, however, channel segregates were observed in both cases. The channel segregates observed in 2D (sample C3_A) were compared to the channel segregates reconstructed in 3D based on the C2 samples analysis. To compare the samples between them, the C3_A segregation map went through the image processing used to identify channel segregates and intermediate-scale segregation on C2 samples, see figure 4.13. The filter used was the same: Gaussian filter (25 pixels standard deviation and a 4σ truncation size) followed by a binarisation with a threshold at 0.029 in segregation ratio after filtration. On the binary image, the channel's horizontal width was measured to be. Two measures were done: one on an enriched area in the top part of the sample (lines used marked in grey) and one on the lower enriched area (lines used marked in purple). The average horizontal (xy) widths of the top channels are 8.9 mm (top channel, in grey) and 7.4 mm (lower channel, in purple).
To compare the observations of channel segregates made in their longitudinal direction (C3 samples), the 3D reconstructed channel segregates were sliced in the same observation plan as C3_A sample was taken (yz-plan). Lines in figure 4.14 show where longitudinal yz slices were made. The print of the channel segregates on the longitudinal slices made in the 3D reconstruction are presented in figure 4.15. The comparison between figures 4.13 and 4.15 highlight channel segregates features:

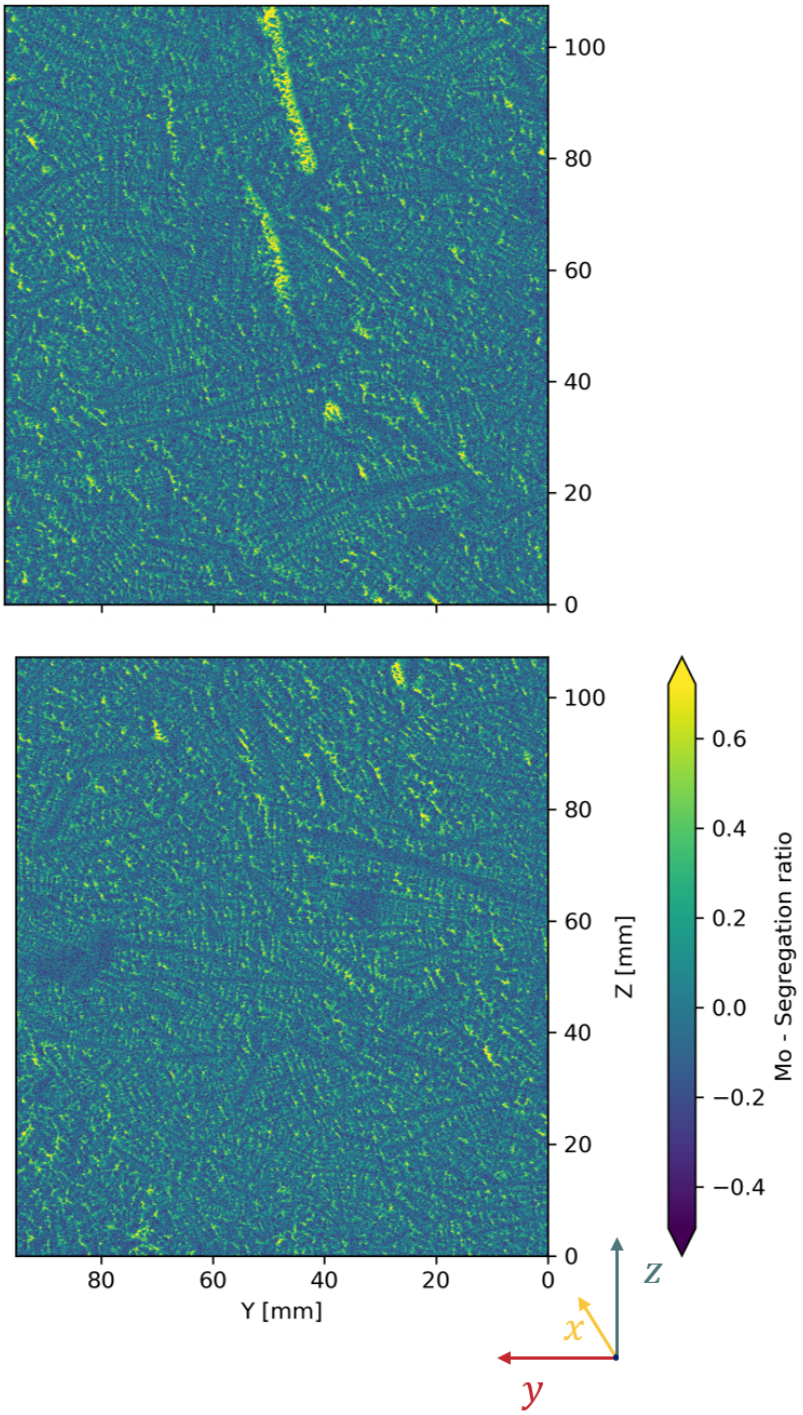

Figure 4.12: Mo segregation ratio map obtained on C3_A sample (top) and C3_B sample (bottom) with µXRF analysis.

Figure 4.13: Binary image obtained after image processing (described in chapter 3) performed on segregation ratio map C3_A.

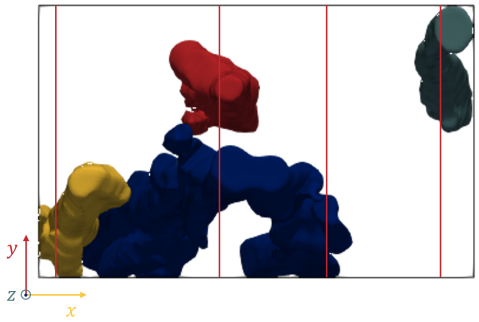

Figure 4.14: Indication of vertical slices done on the 3D reconstructed channel segregates for longitudinal observation and comparison with C3_A sample.

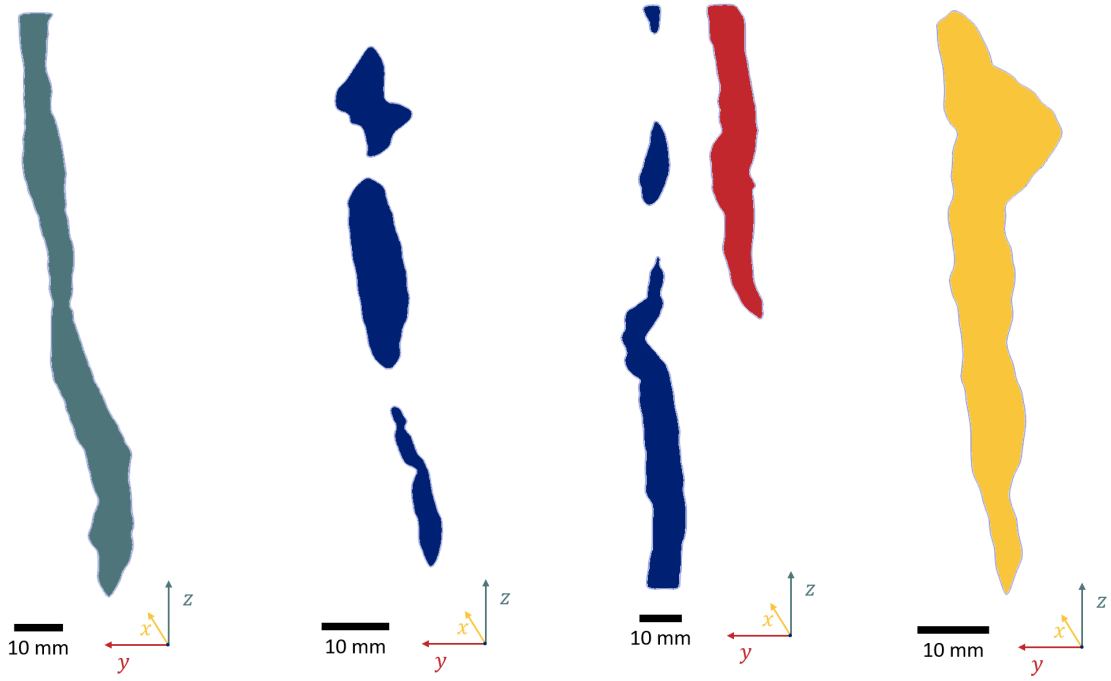

(a) (b) (c) (d)

Figure 4.15: Vertical cuts in the reconstructed volume for longitudinal channel segregate observation.

- All the observed channels show an inclination toward the centre of the ingot.
- Some channels observed continuous in 3D appear discontinuous in 2D (see figures 4.15b, 4.15c). The visual similarity between the longitudinal cuts B and C (4.15b, 4.15c) of the reconstructed volume and the alignment of enriched areas in the figure

4.13 reinforce the idea of sinuous channel segregates observed in sample C3_A.

- The order of magnitude of channel segregates width observed in 2D is the same as Feret diameters in of the 2D *xy* channel areas studied in the last section.

To sum up, in the *short* ingot, channel segregates were observed in 2D and 3D. The samples showing channel segregates were taken at mid-height and mid-radius of the ingot and exhibit globular equiaxed primary microstructure. The channel segregate width observed in both 2D and 3D in the order of magnitude of 1 cm, which is larger than the typical values reported in the literature [5, 31, 45, 61, 68, 94]. However, the large size of the ingot might encourage the channel segregates formation because of the long local solidification time and the filter used in the image processing might enlarge the segregation sizes. The 3D observation of channel segregates gives accurate observation of the channels' shape and size, while 2D observation can give partial information due to sampling: i.e. discontinuous channels segregate since they are sinuous objects. The discontinuity of the channels in 2D makes impossible to status on the number of channels observed in sample C3_A: in figure 4.13, there could be one, two or three channels (one on the left part of the image where round enriched areas align, one with the enriched area marked with purple lines and one with marked with the horizontal grey lines). 3D observation could answer that interrogation, but is much more demanding: it takes more samples and more time to get to a result.

4.2.2 *Long* ingot: 170 tons

For the study of the *long* ingot, 4 adjacent samples were taken in the top part of the ingot, see H location in figure 4.16. The samples were prepared and analysed in the same way as the ones from the *short* ingot. The experimental conditions were identical for the 4 samples: a beam filtered with 100µm of Al, working at 50 kev and 200 µA on a sample scanned with a 100 µm step for 45 ms on each scanned point. The obtained segregation ratio in Mo are presented in figure 4.17. The spacing between the top and bottom samples is scaled with the maps to correspond to the matter lost during the cutting steps. However, the exact spacing between the right and left samples is not known precisely but is believed to be around 1 cm. The represented lateral spacings are equal to 1 cm.
The obtained maps are similar to the one previously observed on the *short* ingot: several scales of segregations are visible, including microsegregation and located macrosegregation. The equiaxed dendritic primary microstructure is highlighted by the microsegregation.
There are two channel segregates on the analysed samples. One of them is continuous on the samples but was cut by sampling (see samples on the right side of the figure 4.17. The other channel segregate is visible on the samples on the left side of the figure 4.17. The left side channel segregate is not continuous on the samples. But, the alignment of enriched long areas is characteristic of 2D channel segregates observation as demonstrated with the several cuts made in the 3D reconstructed volume (see figure 4.15c). Both channels incline toward the centre of the ingot, which can indicate A-type channel segregates. A-type segregates are known to be long, sometimes observable on the whole

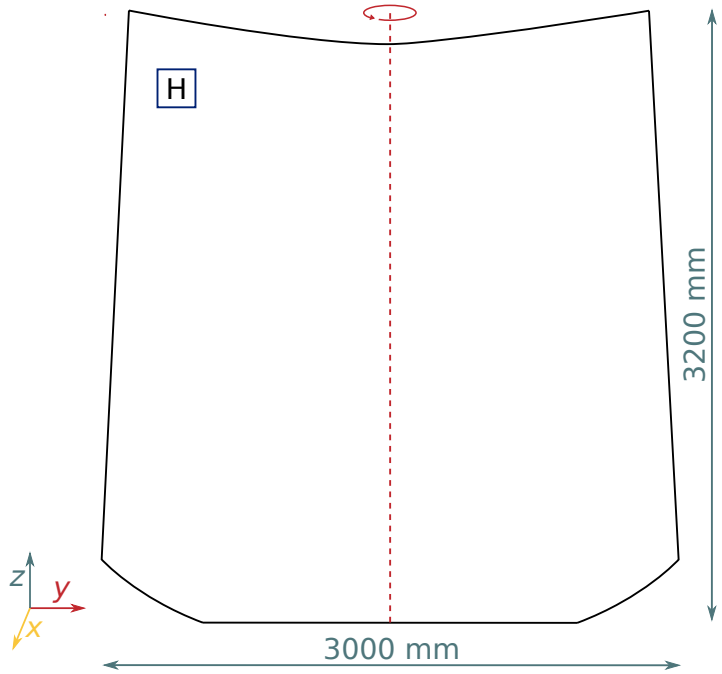

Figure 4.16: Sectional schematic of the long 170 tons ingot.

ingot length [61, 68]. However, the size of the sample is not big enough to check for the observed channel segregates continuity on such distances, still the channel segregates observed seams to spread on the whole samples observed.
In figure 4.18, the H samples segregation maps were filtered and made binary (the threshold used was 0,036, the 95^{th} quantile of the H-samples data after Gaussian filtration). In this figure, the two channel segregates observed were highlighted with grey and purple shading. Measures made to determine the horizontal average width of the channel segregates observed are reported in figure 4.18 in purple and grey lines. The channels segregates average width is 6,8 mm in both cases: the one highlighted in purple and in grey. The width measure is slightly smaller than the one measured on channel segregates observed in the *short* ingot, but the order of magnitude is the same and comparable to what is observed in 3D in the *short* ingot.
As for the observations made in 2D in the *short* ingot, the 2D observations of channel segregates in the *long* ingot do not bring a complete idea of the shape and orientation of the channels. The aspect of the channels segregates observed in 2D in both ingots (*long* or *short*) is very similar which brings the idea of centimetric sinuous 3D channel segregates as the ones observed in 3D in the *short* ingot.

4.2.3 *Hollow* ingot: 173 tons

The last ingot to be part of the study is a *hollow* ingot. In that ingot, 4 samples were taken in 2 different locations, see locations J and K in figure 4.19. The J location is in the upper

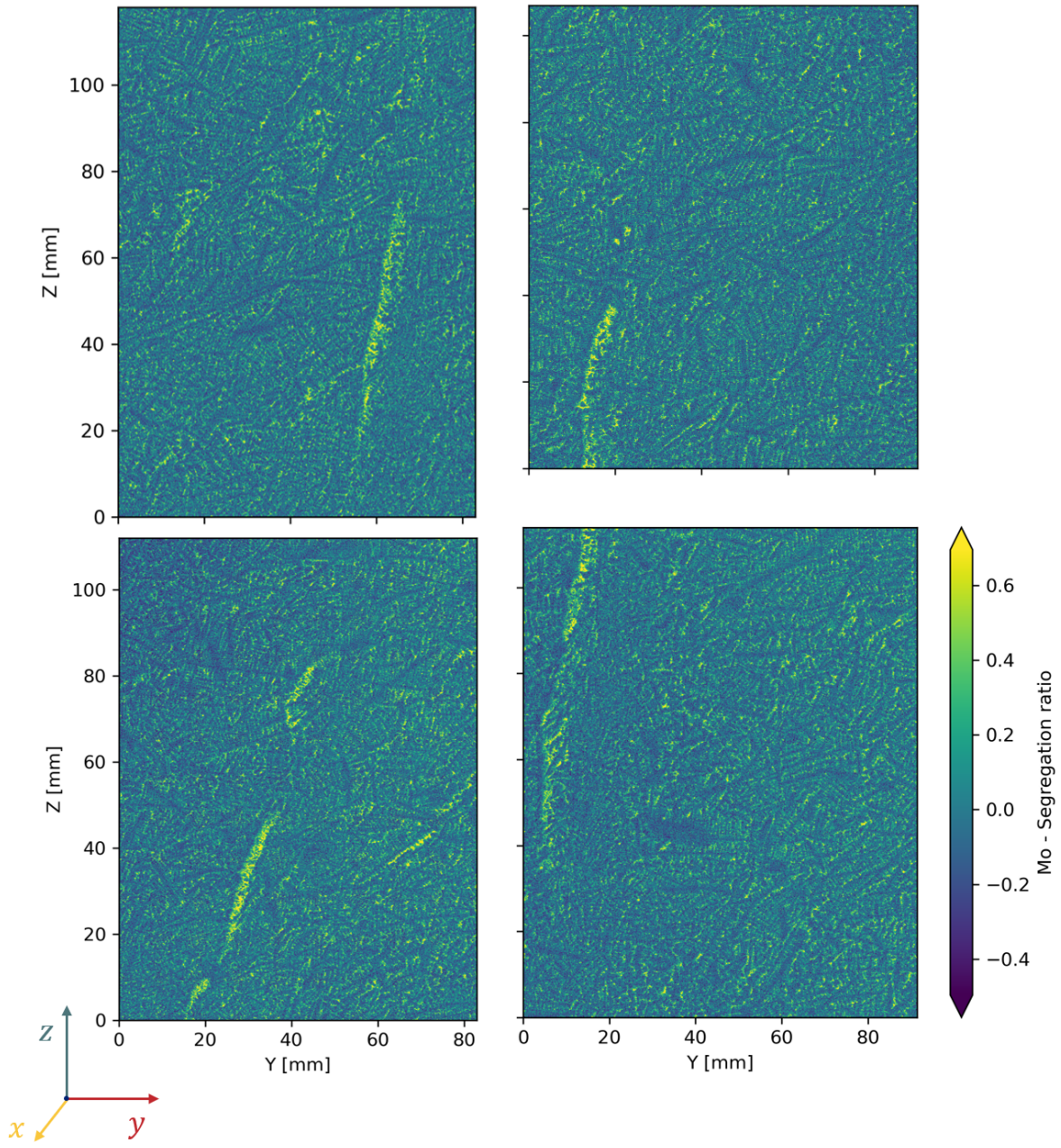

Figure 4.17: Mo segregation ratio map obtained on H2_C (top, left), H2_D (bottom, left), H3_A (top, right) and H3_B (bottom, right) samples with µXRF analysis.

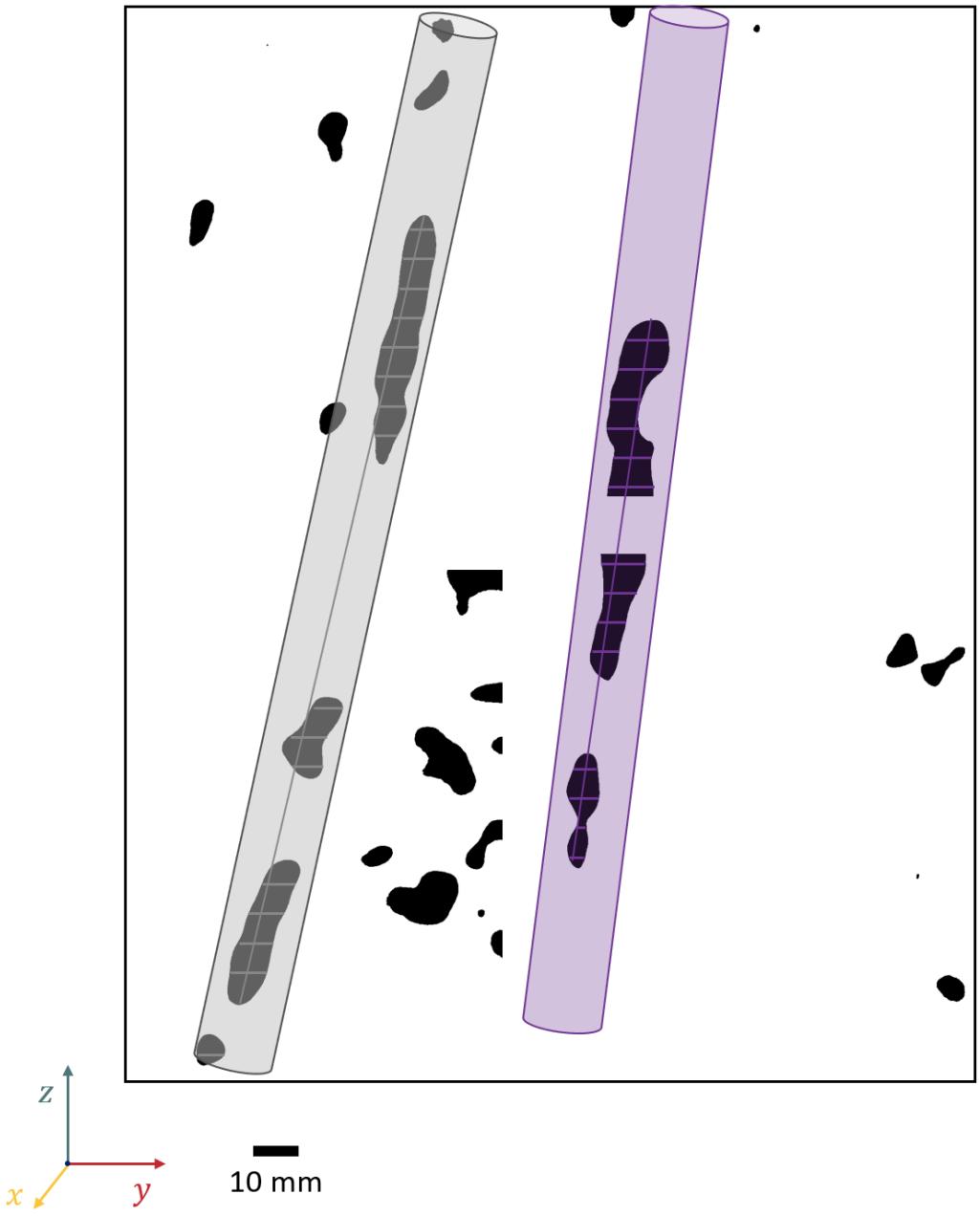

Figure 4.18: Binary image obtained after image processing (described in chapter 3) performed on segregation ratio map H2_C, H2_D, H3_A and H3_B.

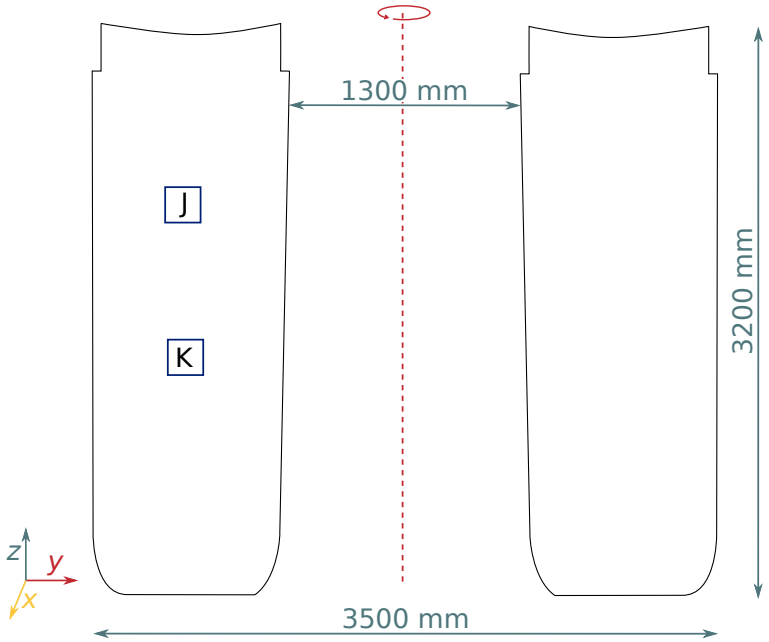

Figure 4.19: Sectional schematic of the hollow 173 tons ingot.

part of the ingot whereas the K location is in the lower part of the ingot. The motivations for such sample locations were to compare the segregations and primary microstructure differences between the top and bottom part of the ingot and to compare the segregations forming in the *hollow* ingot with other ingots (with the J location, comparable to C and H location on other ingots).
The samples were prepared and analysed in the same conditions as *short* ingot and *long* ingot samples (grinding down to P1200, beam settings: 100 µm Al filter, 50 keV and 200 µA, 100 µm step, 45 ms per spectrum). The resulting Mo segregation ratio maps are presented in figure 4.20 for samples taken in the J location and 4.22 for K location samples. Sample taken for the *hollow* ingot, were taken side by side in both locations. Both locations are close to the middle of the bulk part of the ingot. The particularity of *hollow* ingot is that it solidifies from both sides of its bulk section. The classical macrosegregation patterns (negative base segregation, V segregates, A segregates and hot top segregation) are present in hollow ingots, they are just made cylindrical by the shape of the ingot mould. Hence in a bulk section of the ingot, the classic macrosegregation patterns can be observed. However the patterns can be asymmetric, indeed even if the solidification occurs with two opposite solidification fronts, the cooling rates are different between the outside of the mould and its inside hole cooled down with gas flux. This cooling rate difference leads to different solidification driving forces and solidification speeds, as a result, the two solidification fronts do not meet in the middle of the ingot. This means that with samples taken in the middle of the ingot, the solidification front meeting line is not in between the samples.

J location samples - Ingot shape effect

For samples taken in the J location, see figure 4.20, a channel segregate is visible on the right sample, the one closer to the outside of the mould. The enriched line is almost crossing the whole sample from bottom to top. The enriched line inclines toward the centre of the bulk cross-section of the ingot, which would fit with an A-segregate inclination on this side of the cross-section. On the other sample, no obvious channel segregates can be identified with enriched line patterns. However, in the lower right corner of the sample, there is a located enriched zone. Knowing the sample location, this zone could be V or A segregates. However, without 3D information, it is not possible to solve this interrogation. It was not possible to access extra samples for 3D characterisation and the exact nature of the segregation pattern observed is unclear.
The image processing designed to highlight positive segregations was applied to both segregation ratio maps, the results is in figure 4.21. The threshold used for the binarisation was 0.046, the 95^{th} quantile of the J-samples data after Gaussian filtration. The binary images show the two segregation patterns mentioned previously: an undefined segregation on the centre side sample and a channel segregate on the outer sample. The channel segregate horizontal width was measured. the average horizontal width of the channel is 5,5 mm. The channel segregate observed in the *hollow* ingot is thinner than the ones observed in directionally solidified ingots (both *short* and *long*). It might be linked to the solidification of the *hollow* ingot: the bulk section of the ingot is smaller than the diameter of directionally solidified ingots, hence the local solidification time can be smaller. A smaller solidification time decrease see section width of channel segregates according to Suzuki [45].

J location samples - Position in the ingot effect

On the segregation ratio maps obtained with samples taken in the K location of the *hollow* ingot (figure 4.22) there is not any located macrosegregation to observe: no channel segregate. The microsegregation visible is also different compared to samples taken in the J position: it does not present any interdentric enrichment, since there is almost no dendrite to see (only one is visible, on the top right side of the left side sample). The primary microstructure observed is equixed globular: dendrites did not grow from the equiaxed grains and the grains settled in the bottom part of the ingot creating the base sedimentation cone. This part of the ingot is supposed to be globally depleted in solute, however, it is not possible to check that information with the characterisation done in this study since a local segregation ratio was used.

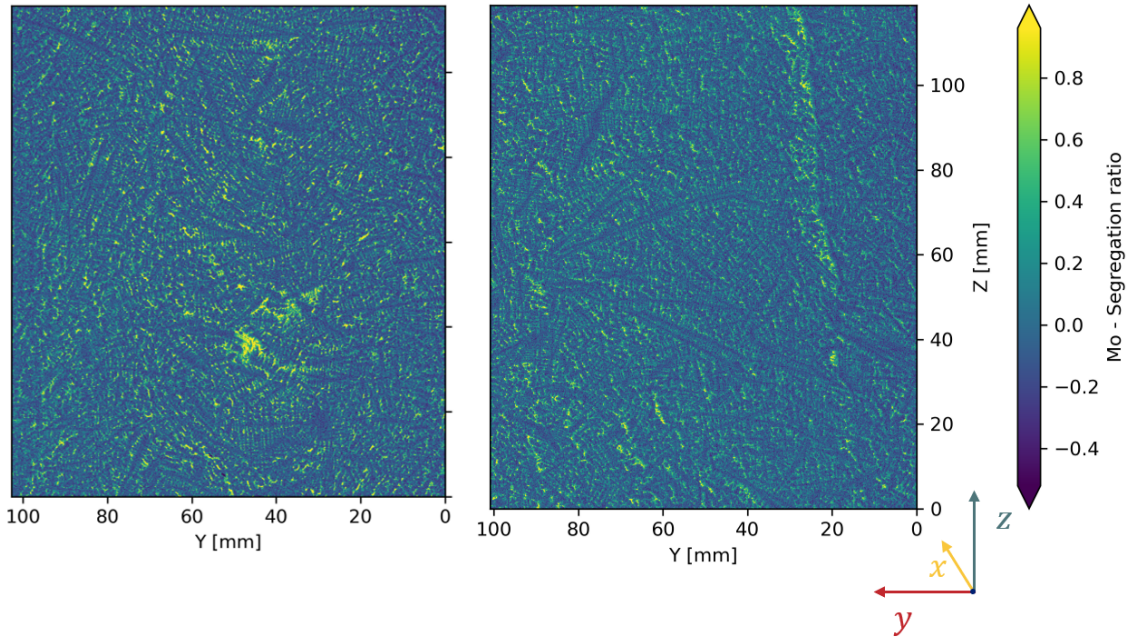

Figure 4.20: Mo segregation ratio map obtained on J_1 and J_2 (left to right) samples with µXRF analysis.

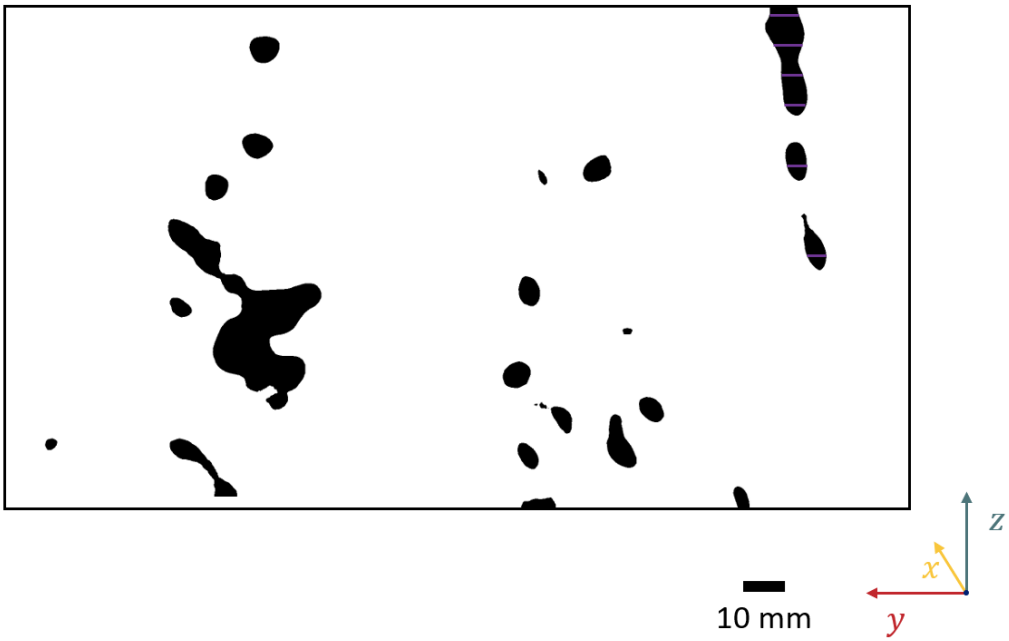

Figure 4.21: Binary image obtained after image processing (described in chapter 3) performed on segregation ratio map from J samples

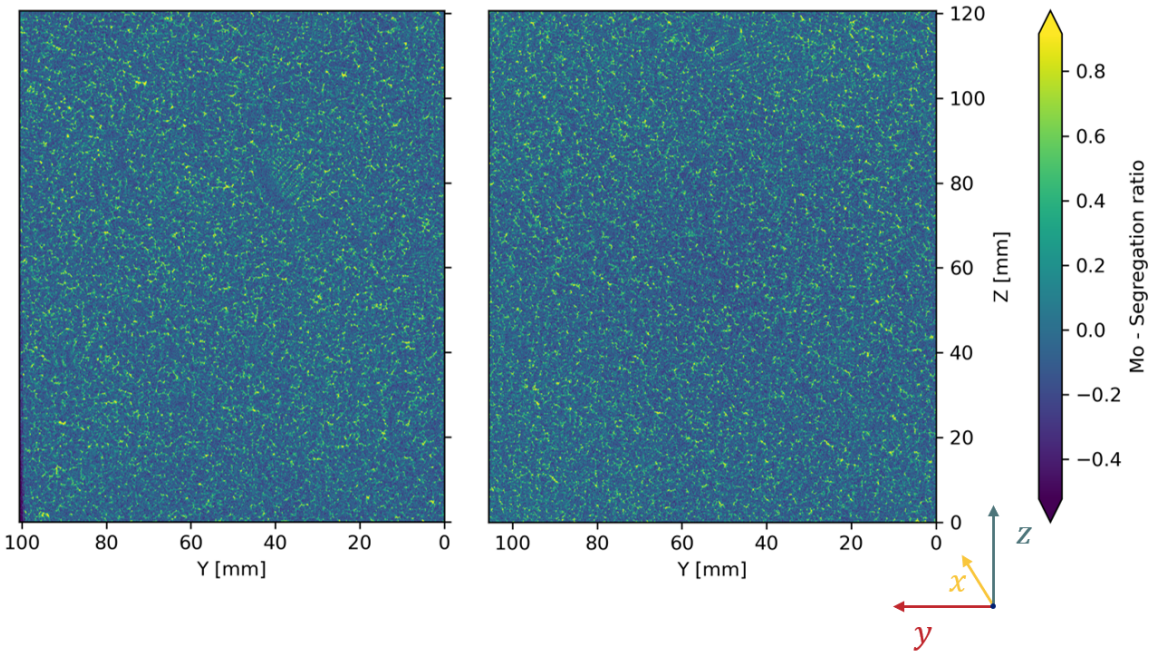

Figure 4.22: Mo segregation ratio map obtained on K_1 and K_2 (left to right) samples with µXRF analysis.

4.2.4 Similarities and differences observed between ingots

The observations carried on on 3 different ingots reveal the presence of channel segregates in all the investigated ingots (channel segregates being observed in samples groups C, H, and J, see figure 4.23). The observed channel segregates were located in dendritic equiaxed grain areas, were identifiable by their sinuous channel shape, and were inclined toward the ingot centre. Several channel segregates appear discontinuous on the segregation maps however, based on observations of the shape of channel segregates in 3D (see 4.1), the channels are now known to be sinuous. The 2D map can cut their paths in several points, causing discontinuous aligned enriched sports or lines that all belong to the same channel segregate, as demonstrated with figure 4.15. In samples groups C (*short* ingot) and H (*long* ingot), channel segregates were observed to continue from one sample to another. The last group of samples, group K, showed a different primary microstructure compared to the other samples (see summary in table 4.3). K samples show equiaxed globular grains. The difference in primary microstructure is due to the ingot solidification process. As solidification occurs, gravity settles down solute-depleted grains in a cone shape [20]. The negative segregation cone is made of globular equiaxed grains and can go up to 50% of the total height of the ingot. In the negative segregation cone, A-segregates are not expected but V-segregates can be observed [22]. Samples K, figure 4.22, show neither A-segregates nor V-segregates on the segregation maps. The samples were taken in the *hollow* ingot, at a medium height and in the middle part of the ingot. In that position, globular equiaxed grains belonging to the negative segregation cone can be found. If the texture is identified

Table 4.3: Summary of the different observations carried on for the ingot comparision

Samples	**Ingot**	**Primary microstructure**	**Segregation patterns**
C	Short ingot 116 t Directionally solidified	Equiaxed dendritic	Channel segregates
H	Long ingot 170 t Directionally solidified	Equiaxed dendritic	Channel segregates
J	Hollow ingot 173 t Conventionnally solidified	Equiaxed dendritic	Channel segregates
K	Hollow ingot 173 t Conventionnally solidified	Equiaxed globular	None

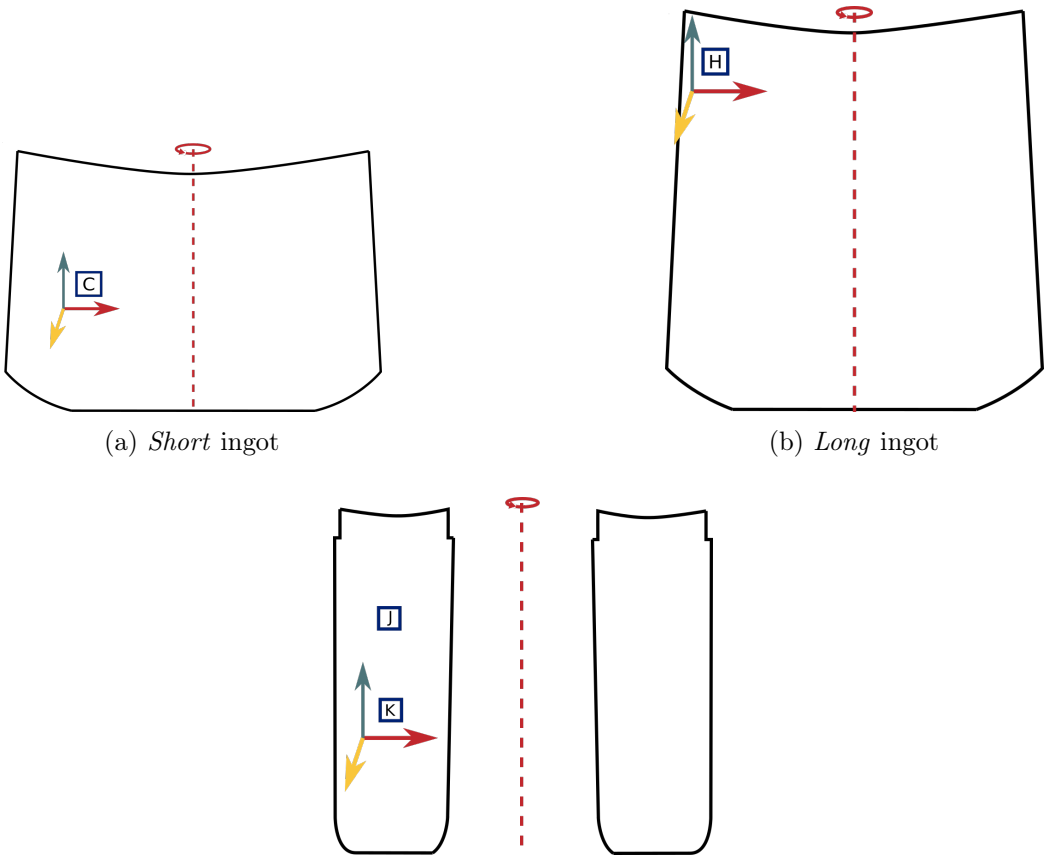

(a) *Short* ingot

(b) *Long* ingot

(c) *Hollow* ingot

Figure 4.23: Samples positions in the different ingots studied.

with the absence of dendritic arms on segregation maps, the negative mass segregation of the cone cannot be confirmed with the present measurement since µXRF analyses are not quantified in the study and maps are presented in local segregation ratio.

4.2.5 Summary

In this study, 3 types of ingot were compared through 4 sets of samples: samples C taken in a *short* ingot, samples H taken in a *long* ingot and samples J and K taken in a *hollow* ingot. Mo segregation ratios maps were realised on the samples and revealed several main points:

- In the *hollow* ingot, two primary microstructures were observed: globular equiaxed grains and dendritic equiaxed grains. Different solidification conditions in the different locations of the ingot explain the observed primary microstructures.
- Samples (group K, *hollow* ingot) taken in the globular equiaxed area show no channel segregates.
- All the other groups of samples (C, H and J) show channel segregates. The samples come from different ingots with various shapes and sizes and from different locations within the ingots. The solidification conditions beneficial to channel segregates formation are various and still unclear. The following chapter presents a comparison of existing criteria for channel segregates formation prediction.
- The channel segregates observed in 2D in directionally solidified ingots (both *short* and *long* ingot) have the same order of magnitude compared to the channel segregates observed in 3D. However, the channel segregates observed in the *hollow* ingot, are slightly thinner, which might be linked to the local solidification time. Solidification simulation could help answer this interrogation.
- Even if the different shapes do not prevent the channel segregates formation, the interest is not vain. *Hollow* ingots present channel segregates, but the channel segregates are trapped inside the ingot. Hence the channel segregates are less likely to arise to the surface of the forged part during the forging process.
- 2D observation of channel segregates is faster than 3D observation, but it fails to determine with precision the shape and size of channels segregates.

4.3 Conclusion

The use of the characterisation method based on µXRF, developed and tested in chapter 3, made possible a 3D analysis of segregation patterns in the *short* ingot. Samples were also taken in several ingots to investigate the effect of the ingot type on segregation patterns.
The 3D observation of channel segregates gave a new insight into their shape and space distribution. Channel segregates appear to be sinuous, to merge and to have ramifications. This representation is not the one usually described in the literature, indeed, with 2D observations as it was traditionally done in the past, the probability of observing ramifications or merging is low. The 2D observation carried on and the slices of the 3D reconstructed volume also showed that in 2D channel segregates can appear discontinuous, due to their complex 3D shape.
The *xy* width of the channel segregates in both *short* and *long* ingot are close, in the order of the magnitude of the centimetre. In the case of the *hollow* ingot, the channel observed was a bit smaller. Two effects could explain its small size: (1) it observation was made in 2D, and the channel might have been cut on its edge, far from its diameter, which would make it appear smaller but be the same size as the one observed in the other ingots; (2) the size of the channel is related to the local solidification time which is smaller in the *hollow* ingot compared to directionally solidified ingots [45].
Near the channel segregates, intermediate-scale segregations were observed. Intermediate-scale segregation could not be identified in 2D samples alone, because of the risk to mistake them for channel segregates cut by the sample plan. Intermediate-scale segregations were observed in the 3D reconstructed volume, they are smaller than channel segregates but have similar aspects in the horizontal plane. Intermediate-scale segregations measure around 5 mm in diameter, with a 5 mm spacing between the samples, it was not possible to observe intermediate-scale segregation in 3D and to determine with precision their shape.
Another advantage of the 3D reconstruction is that it made it possible to check the evolution of both the size and the segregation of channel segregates as a function of their height. The carried-out analyses show no correlation between segregation or size of the channel segregates and height.
In all the ingot studied (a *short* directionally solidified ingot, a *long* directionnaly solidified ingot and a conventionally solidified *hollow* ingot), channel segregates were observed. All the observed channel segregates were inclined towards the centre of the ingot and found in the equiaxed dendritic grains area. On the only set of samples taken in an equiaxed globular grains zone, no channel segregates or intermediate-scale segregation were observed.
To conclude, 2D characterisation with µXRF is a fast technique that can reveal both segregations and primary microstructures on centimetric scale samples. However, to fully understand the shape and orientation of channel segregates, a 3D observation is better.

Chapter 5

Study of solidification conditions

> Il faut se méfier des petites filles. Elles touchent le fond de la piscine, se cognent, se blessent, mais rebondissent.
>
> Judith Godreche

Contents

Sample characterisation is insufficient for an extensive understanding of solidification phenomena and consequences. Simulations help to understand the phenomena at different scales, test hypotheses and understand the physical aspects of solidification without the drawbacks of experimental work. In this PhD work, SOLID® simulations were employed to complete and support the experimental work. Chapter 4 reveals channel segregates and intermediate-scale segregations observed in the *short* ingot at the C-position. The simulations help understand the solidification conditions leading to the formation of such segregation. This chapter is divided into three parts and covers the simulation of the *short* ingot performed with SOLID®. The first section exposes the hypothesis and settings of the simulation used. The second part discusses the predicted solidification of the *short* ingot. The C-position solidification is treated specially and with more precision in the section 5.3.

5.1 Hypothesis and settings of the SOLID® simulations

SOLID® simulations are based on hypothesis and require initial setting to function. In this section, SOLID® operation is briefly described together with the main hypothesis done on the ingot solidification in the code. The settings used for the simulation of the *short* ingot solidification are also defined.

5.1.1 General operation of SOLID® simulation used

SOLID® is a multiscale and multiphase model that predicts ingots and continuous casting solidification [40, 95]. Composition, grain morphology and liquid density are predicted. The simulation combines micro- and macroscale approaches and includes 5 phases: the extradendritic (or free) liquid, the columnar grains, the equiaxed grains and interdendritic liquids for both columnar and equiaxed grains.

Microscale

At the microscale, Representative Volume Elements (REV) (that will be referred to as "cells") are used as a local approach for the prediction of nucleation, grain growth and phase changes. In each cell, at each time step, the local microscopic state is computed. The grains are not directly represented, but each cell stores average values for the different phases. A single cell can contain liquid, equiaxed and columnar grains at the same time.
The columnar growth is followed with a front-tracking method: cells can contain the growing columnar front, be behind it or contain only liquid and equiaxed grains. The tip velocity of the columnar dendrites imposes the columnar front velocity. The columnar front propagates columnar grains from one cell to the next one. The columnar grain density is a fixed simulation parameter.
SOLID® also describes the CET induced by their solutal effects or mechanical blocking [36]. The solute-induced CET is intrinsic to the model: the front growth is imposed by the tips' velocities, so it is sensitive to chemical undercooling. When equiaxed grains

grow ahead of the columnar front, the surrounding extradendritic liquid composition increases, and solutal undercooling ahead of the columnar front decreases which ultimately stops the front progression. To replicate mechanical-induced CET, a mechanical blocking parameter is introduced: if the equiaxed grain fraction (g_{eqx}) in a mixed cell containing columnar and equiaxed grains is greater than the blocking parameter (g_{CET}^{lim}), the columnar front is stopped and does not propagate to the next cell.
Equiaxed grains, unlike columnar grains cannot propagate from one cell to another. They grow from fragments injected at the columnar front to mimic the coarsening and dendritic fragmentation in the columnar zone. The surface flux of fragmentation at the columnar front is a set model parameter. In large ingots, the only equiaxed grains source required is fragmentation [38]. When a cell is empty of equiaxed grains and none exist in the surrounding liquid, ECT starts: in the adjacent liquid cells, a new columnar front starts.
At the microscale, an envelope model is included in SOLID® to study the morphology of the equiaxed grains. The morphology is evaluated with the internal solid fraction (the ratio of solid phase inside the envelope): $g_{si} = {}^{g_s}/_{g_{env}}$. When $g_{si} \to 1$, the grains are globular, on the contrary: if $g_{si} \to 0$, the morphology is dendritic [40].

Macroscale

At the macroscale, SOLID® accounts for heat and solute transport, the grain population and computes the flow with thermal and solutal influence.
The liquid flow depends on the solid phase state. In the columnar zone, the solid is always fixed, but the equiaxed grains are not and can move around or be blocked: in SOLID® if $g_{env} > g^{block}$, the solid motion is null. In that case, the liquid flows between the grains and between the dendrites' arms. The mush permeability influences the liquid flow and is accounted for in the simulation with Kozeny-Carman law. If $g_{env} < g^{block}$, the equiaxed grains are free (in the columnar grain-free area) and described by a transport equation. Buoyancy, drag forces and pressure are considered in the momentum equation used to predict solute transport. As a result, the velocity depends on the phase (liquid or solid) and the morphology of the equiaxed grains (dendritic grains float in the liquid and are easily swept away, whereas globular grains settle down easily) [40].

5.1.2 Settings and realisation of this study

The *short* ingot solidification simulation was realised at the Institute Jean Lamour. Ahmed Boukellal performed the SOLID® simulations, based on advice and previous internal work done by Laurent Carroz (ArcelorMittal, Industeel, Le Creusot). The calculations were run in the EXPLOR computing mesocentre (a computing cluster of the University of Lorraine). The author performed the analysis of the results and the comparisons with experimental observations.
The main parameters fixed in the simulation are summarised in table 5.1. The simulation represents the whole solidification system, as shown in figure 5.1: the ingot, the ingot mould, the feeding channel and the layers of exothermic powder and insulation placed on top of the liquid steel. The model is axisymmetric and 2-dimensional. This means that the model simulates a half of the geometry shown in figure 5.1. The finite-volume

mesh is uniform with cells of 5×5 cm^2. The ingot filling is not simulated, the simulation starts with a fully liquid ingot at 1550 °C. The cells in the yellow box correspond to the C position in the *short* ingot. Only the steel ingot will be represented in the following simulation images. All results are shown for the whole ingot, but note that they are necessarily symmetrical because of the axisymmetric model.

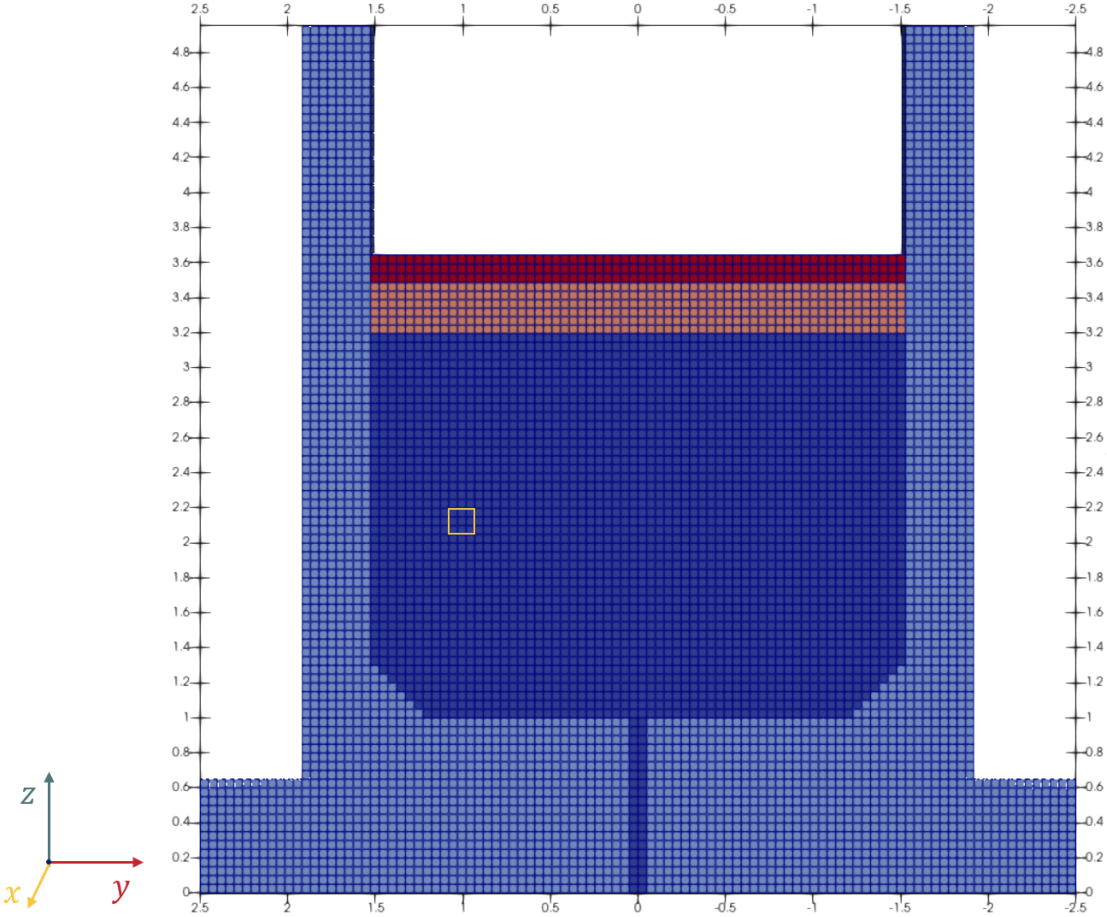

Figure 5.1: Simulation system representation.

Table 5.1: Main parameters used in the simulation

Parameter	**Value**
Carbon content [wt%]	0.18
Partition coefficient [1]	0.17
Liquidus slope [K/wt%]	81.1
Diffusion coefficient of C in the liquid [m^2/s]	2.0×10^{-8}
Diffusion coefficient of C in the solid [m^2/s]	5.187×10^{-11}
SDAS (characteristic scale for hydrodynamic permeability) [µm]	500
Limit in envelope volume fraction for grain motion [1]	$g^{block} = 0.60$
Limit in volume fraction of envelope for columnar growth [1]	$g^{lim}_{CET} = 0.50$
Flux of dendrite fragments from the columnar into the equiaxed zone [m^2/s]	50
Critical temperature gradient for fragmentation [K/m]	10

5.2 Solidification prediction of the *short* ingot

The final solidified state of the *short* ingot and the evolution of solidification with time were studied based on SOLID® simulation. The final state study informs on correlations between solidification structure and macrosegregation. Fluid flow and solid transport occurring during solidification are also crucial for macrosegregation formation. All these aspects are covered in the following section.

5.2.1 Solidified state predicted

The solidification simulation starts with an ingot mould full of liquid steel and lasts 150 000 seconds (being more than 41 hours). The solidification of the steel starts at the mould wall contact with a columnar growth oriented toward the centre of the ingot. The solidification progresses in the ingot in a U shape: the ingot solidifies from the sides and the bottom.

As the columnar front grows in front of the ingot mould wall, fragmentation releases fragments of columnar dendrites in the liquid ahead of the columnar front. In the undercooled region ahead of the columnar front, equiaxed grains grow from the fragments and stop the columnar front progression. The repartition of the different structures can be observed in figure 5.2: the primary columnar zone, the columnar-to-equiaxed transition (CET), the equiaxed zone, the equiaxed-to-columnar transition (ECT), and the columnar zone that forms as result of the ECT. Note that in all figures, C-position is marked by a yellow square. The computed solidification structure indicates a 15 cm thick columnar zone against the ingot mould wall. The centre of the ingot is mainly equiaxed and the top is a mixture of equiaxed and columnar grains. The confirmation of the solidification structure requires currently unavailable experimental data from the 116 ton ingot. However, similar distribution of solidification structure has been observed experimentally in a smaller directionally solidified (LSD type) ingot of 9.8 t [38].

As equiaxed grains grow, they settle down and get blocked as the user-provided packing fraction, g^{block}, is reached. The packing (immobilisation) of equiaxed grains happens gradually from bottom to top. Figure 5.3 maps the immobilisation moment of the equiaxed grains and shows that equiaxed grains are packed after less than an hour of solidification. Once equiaxed grains in the central zone of the ingot are blocked, it takes several hours until full solidification. This is shown by the solidification time in figure 5.4. Note that the solidification time at the C position is more than 5 hours and in the ingot center it is more than 10 hours. When the equiaxed grains get blocked, their morphology is assessed by the value of the internal envelope solid fraction (g_{si}) at that time. For $g_{si} \ll 1$ grains are considered dendritic, for $g_{si} \to 1$, they are considered globular. Figure 5.5 shows the grain morphology in the fully equiaxed zone of the ingot (other zones, i.e., columnar, and CET and ECT transition zones, are shown in grey). In the *short* ingot simulation, the equiaxed zone ahead of the columnar area is mainly dendritic. These results agree with Framatome knowleged on short directionally solidified ingots. The simulation thus successfully describes the morphology of the equiaxed grains. The simulated columnar zone is discontinuous from bottom to ingot mid-height: columnar, CET, equiaxed (a few globular grains but mainly dendritic grains), ECT and columnar grains again.
SOLID® predictions include composition maps at the end of the solidification. The simulation successfully predicts the positive central upper segregation and depletion in solute in the bottom left and right diagonals. The macrosegregation prediction is presented in figure 5.6.

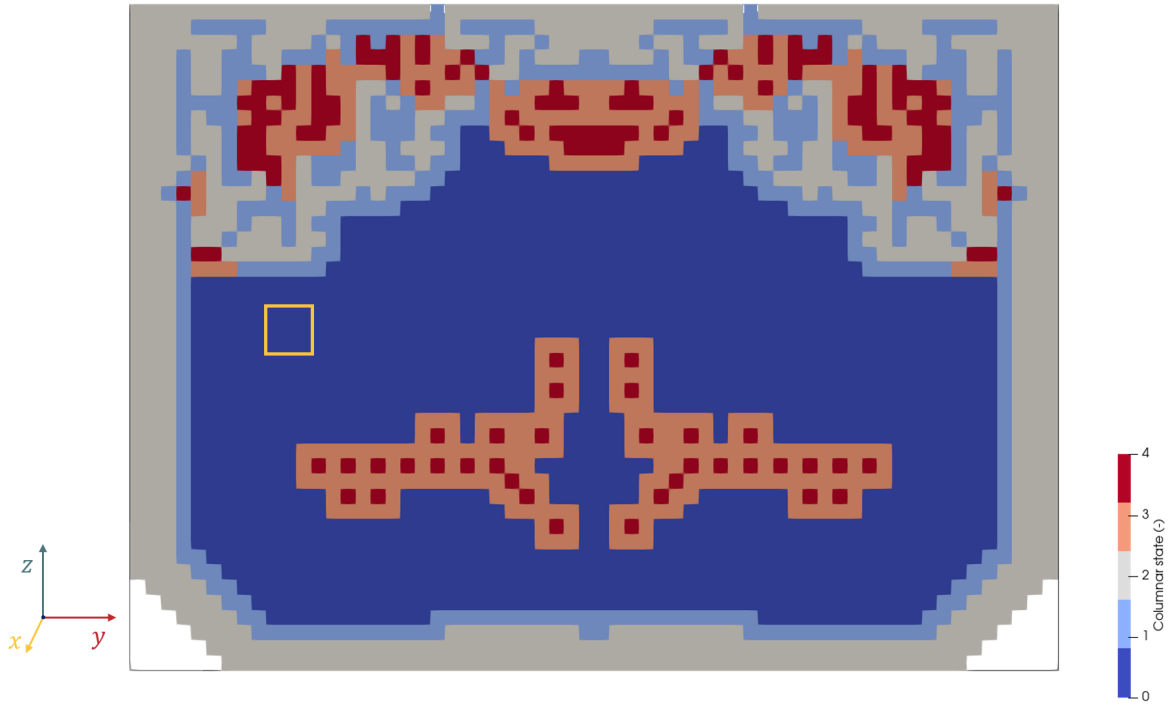

Figure 5.2: Predictions of solidification structure. Keys to the legend: Columnar (before CET) in grey (value: 2), CET in light blue (value 1), Equiaxed (both globular and dendritic) in dark blue (value: 0), ECT in orange (value: 3), Columnar (after ECT) in red (value: 4).

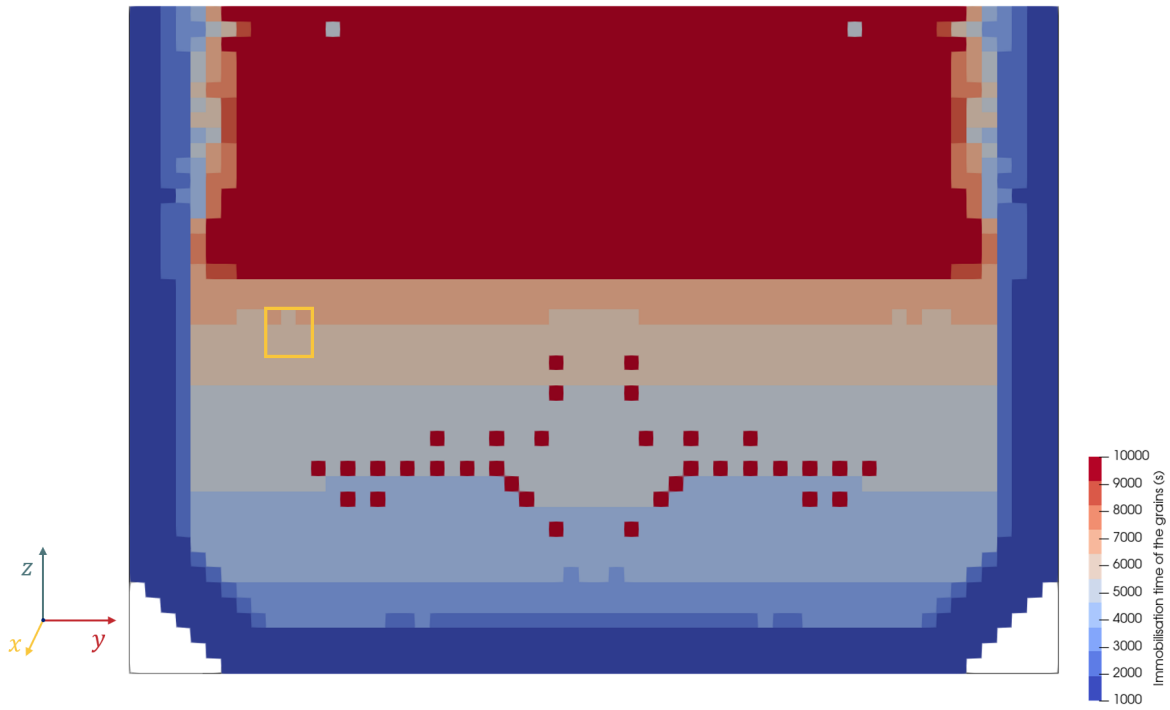

Figure 5.3: Prediction of the immobilisation time of the equiaxed grains. The colorbar scale was adapted to highlight differences in the lower part of the ingot.

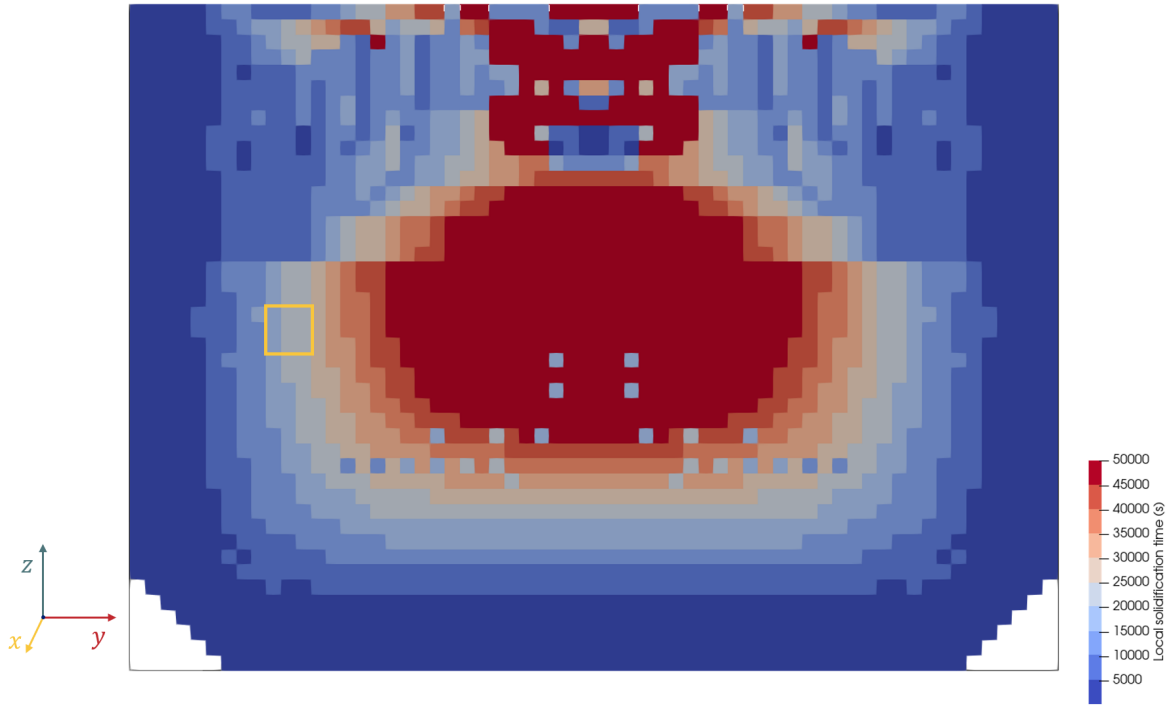

Figure 5.4: Local solidification time predicted. The colorbar scale was adapted to highlight differences in the lower part of the ingot.

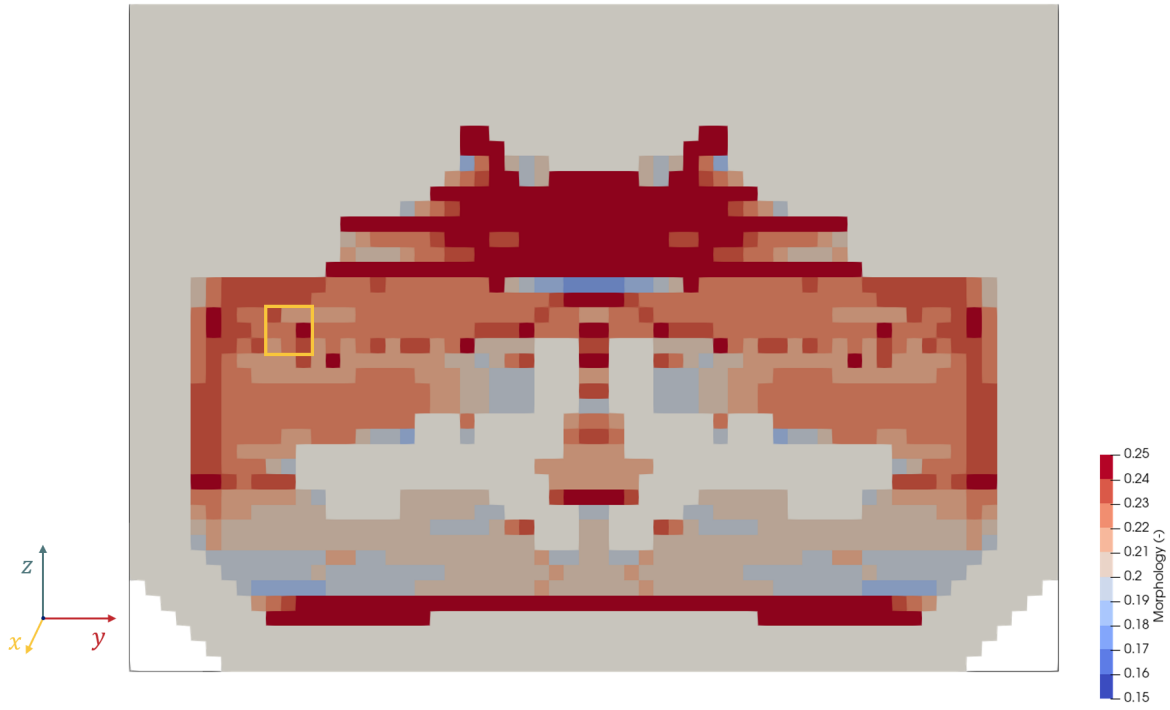

Figure 5.5: Grain morphology in the fully equiaxed zone. *Morphology* is the local internal solid fraction at packing. Note that the parts of the ingot that are not fully equiaxed (columnar or CET and ECT transition zones) are represented in grey.

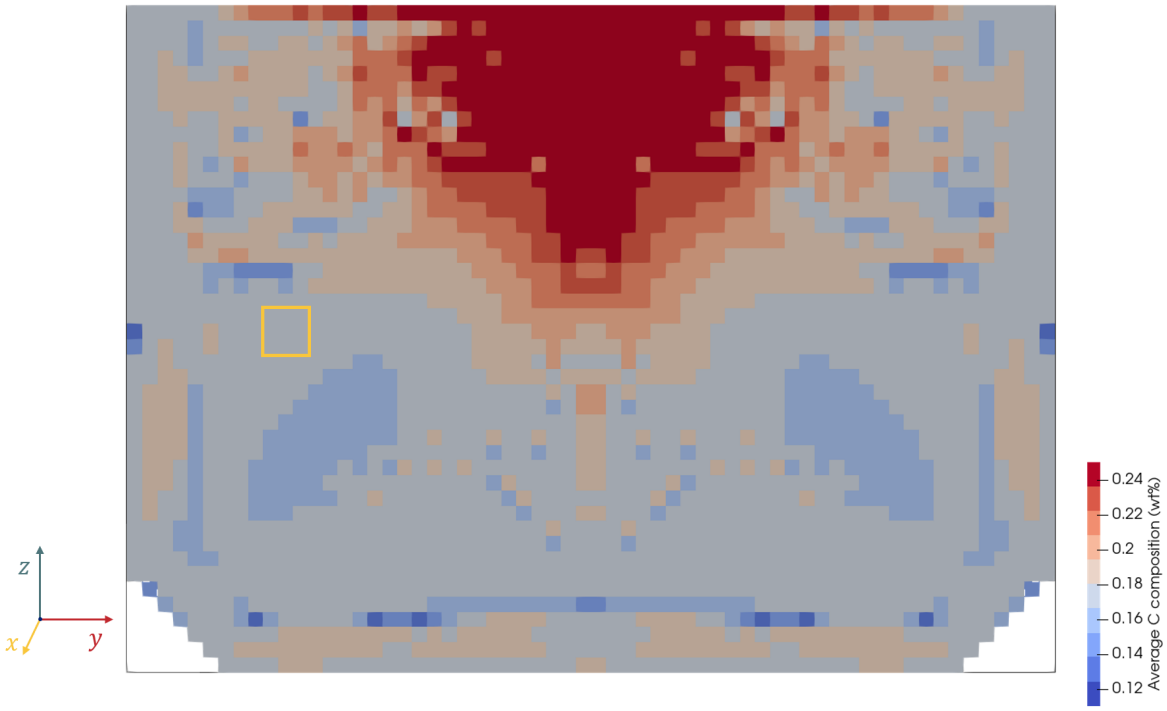

Figure 5.6: Carbon concentration predicted map.

5.2.2 Effect of fluid flow and solid transport during solidification on macrosegregation

The formation of macrosegregation during solidification is due to solute movement at the ingot scale. SOLID® simulates the liquid flow and grain movement (solid velocity vectors) during solidification that causes macrosegregation. In figure 5.7, both temperatures and flows are represented in the solidifying ingot at different times. The temperature field in the ingot is represented on the left side and the flows on the right side. Various pieces of information are represented in the flow figures:

- The segregation is represented. Note that the colour scale is different than in Fig 5.6, it is adapted to provide more detailed segregation intensity observation.
- Segregation is shown only in the packed zone. In the white space in the centre top part of the ingot (see figure 5.7b), the grains move.
- In the packed zone the liquid flow is represented by purple streamlines.
- In the area where grains move, the grain motion is represented by yellow vectors on the left part of the ingot. The magnitude of the arrows is not quantitative.
- On the opposite side of the ingot, the liquid flow is represented by green vectors where the grains are free. The magnitude of the arrows is not quantitative.

During the whole solidification of the ingot, grains movements and fluid flow patterns keep the same tendencies. The solidification occurs gradually, in a U shape from the sides and the bottom toward the centre and the top. As solidification progresses, grains settle and pack in the lower central part of the ingot, in figures 5.7b, d, f, h, j and l the progression of the layer of packed grains can be observed. In the upper part of the ingot, the grains are free to move. Under the influence of gravity, the grains in the top part of the ingot settle (with a downward movement). The liquid flow forms loops in the ingot. In the upward part of the ingot, the liquid flows upward in the centre of the ingot and downward against the columnar front. In this part of the ingot, the liquid flow is governed by the thermal gradient and dragged by grain settling against the columnar front. In the lower part of the ingot, when the liquid flows between the settled grains, it goes in the opposite direction: upward on the side near the columnar front and downward on the central axis. When the liquid flows through the zone of packed grains, the solutal effect becomes the principal driving force of the liquid: enriched liquid is rejected into the interdendritic liquid, which decreases the liquid density. Because the interdendritic liquid in the packed layer is close to thermodynamic equilibrium, given by the liquidus line,

$$T = T_m + mC_l\,, \tag{5.1}$$

with

T_m, melting temperature of pure iron,
C_l, local liquid composition, and
m, liquidus slope,

the macroscopic gradient of liquid concentration is antiparallel to the temperature gradient. The flow therefore rises on the sides of the ingot because of the lateral density gradient in the mushy zone.
In the equiaxed part of the ingot, segregation can change during the solidification: at the same position, a positive segregation can turn into a negative segregation during the solidification. In the solid network formed by the grains packed, the liquid flow orientation can vary during the solidification and the liquid flow's relative orientation to the thermal gradient governs the enrichment or depletion in solute in a specific position in the ingot. The evolution of the concentration with time is given by the solute conservation equation. For fixed solid it is given by:

$$\frac{\partial C}{\partial t} = -\nabla \cdot (g_l C_l \vec{v_l}) \tag{5.2}$$

If we account for mass conservation, $\nabla \cdot (g_l \vec{v_l}) = 0$, and we assume that the liquid in the packed zone is in thermodynamic equilibrium, given by the liquidus line, $T = T_f + mC_l$, we can write:

$$\frac{\partial C}{\partial t} = -\nabla \left(g_l C_l \vec{v_l}\right) = -\frac{g_l}{m} \vec{v_l} \cdot \nabla T\,, \tag{5.3}$$

with

C, local total composition (of solid and liquid),
g_l, volume fraction of liquid,
C_l, local liquid composition,
$\vec{v_l}$, local liquid flow,
m, liquidus slope and
∇T, temperature gradient.

For carbon in steel, m is negative. g_l is always positive, hence $-\frac{g_l}{m} > 0$, the sign of $\frac{\partial C}{\partial T}$ is directly linked to $\vec{v_l} \cdot \nabla T$.

- If $\vec{v_l} \cdot \nabla T > 0$ then $\frac{\partial C}{\partial T} > 0$, meaning that if the liquid flow has a velocity component in the same direction as the thermal gradient locally, the composition increases. When the liquid flows in the same direction as the thermal gradient, enriched liquid from the solidification front is transported and enriches its surroundings.

- If $\vec{v_l} \cdot \nabla T < 0$ then $\frac{\partial C}{\partial T} < 0$, so when liquid flow has a velocity component opposite to the thermal gradient locally, the local composition decreases. With liquid flowing in opposite direction to the thermal gradient, the liquid transported is depleted in solute and decreases the local composition of its surrounding.

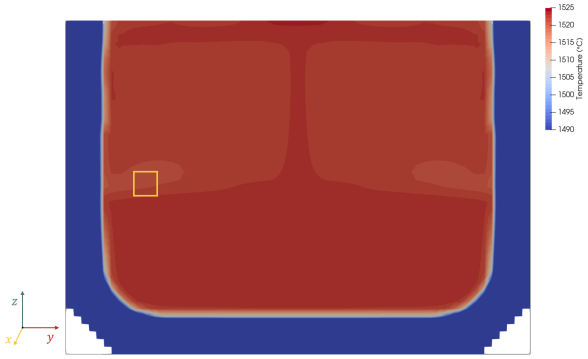

(a) Temperature field, time = 5 810 s

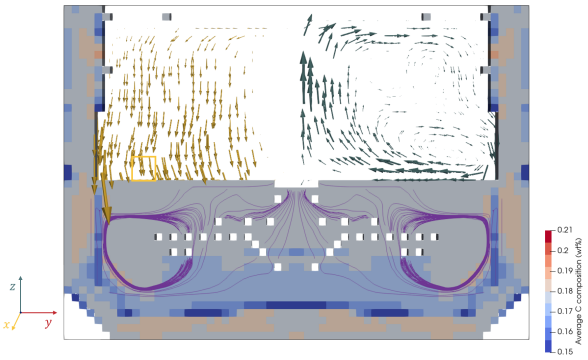

(b) Grain motion and liquid flow, time = 5 810 s

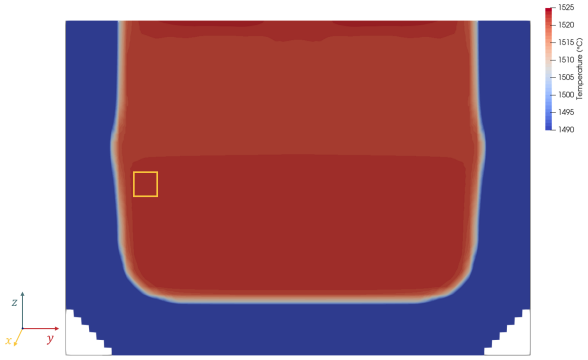

(c) Temperature field, time = 11 010 s

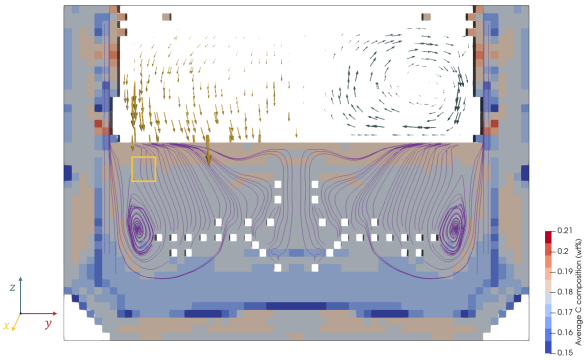

(d) Grain motion and liquid flow, time = 11 010 s

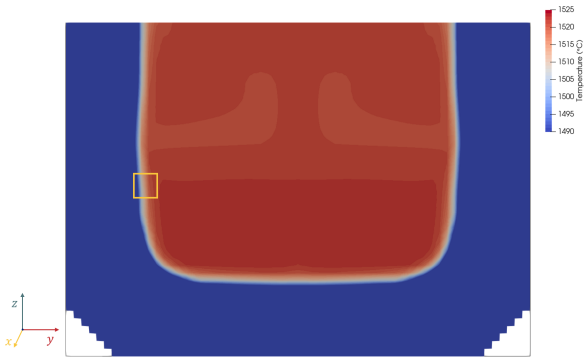

(e) Temperature field, time = 21 010 s

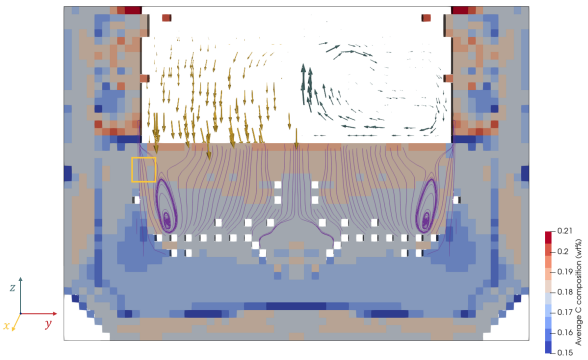

(f) Grain motion and liquid flow, time = 21 010 s

The creation of a negative macrosegregation in the lower corners of the ingot (visible on figures 5.7f, h, j and l) is a good example of the effect of $\vec{v_l} \cdot \nabla T$ on segregation formation. In the lower corner of the ingot, depleted solute flows from the centre of the ingot toward the solidification front at the bottom and on the side of the ingot. The thermal gradient points to the centre of the ingot. Liquid flow and thermal gradient are in opposite directions, this area of the ingot is fed with depleted solute and a negative segregation thus forms.

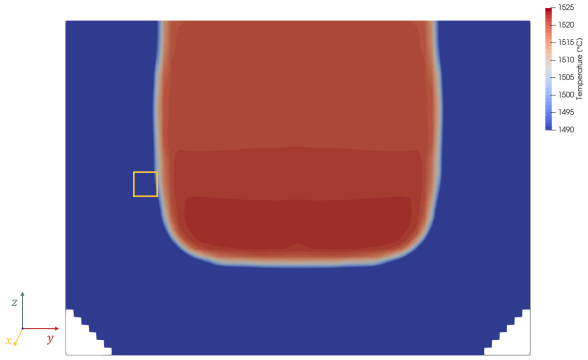

(g) Temperature field, time = 30 010 s

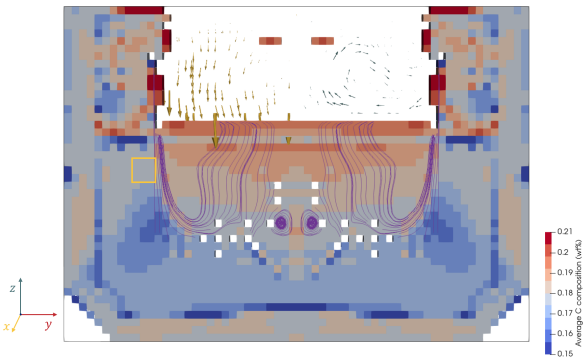

(h) Grain motion and liquid flow, time = 30 010 s

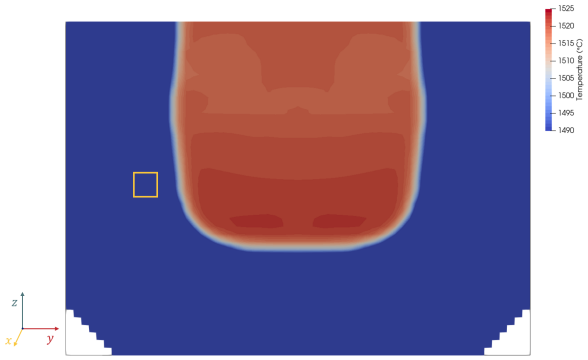

(i) Temperature field, time = 40 010 s

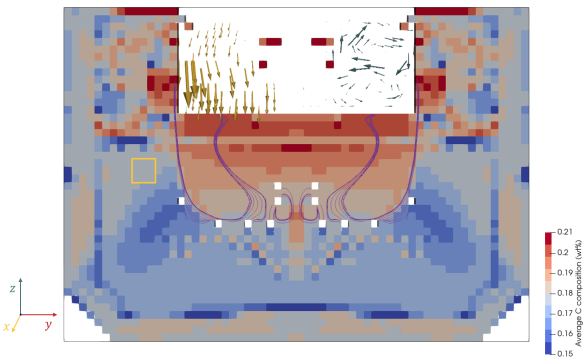

(j) Grain motion and liquid flow, time = 40 010 s

(k) Temperature field, time = 150 000 s

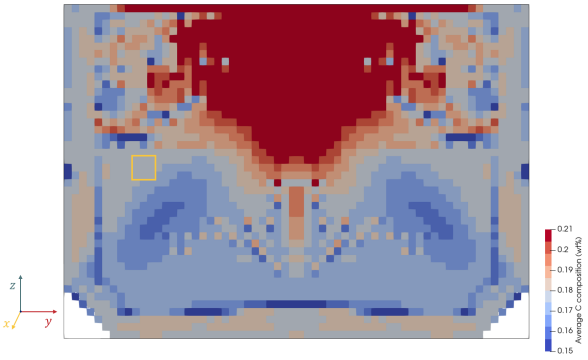

(l) Grain motion and liquid flow, time = 150 000 s

Figure 5.7: Temperature field, grain movement, liquid flow and segregation evolution during the simulated solidification. Figures on the right side show the grain movements in yellow vectors and the liquid flow in green vectors and purple streamlines. The C-position is shown by a yellow square.

5.3 Solidification prediction of the C position in the *short* ingot

In the *short* ingot, samples were taken at the C-position to be analysed and led to the observation of 3D channel segregates and intermediate-scale segregations (see chapter 4). Understanding the solidification conditions of the samples taken at the C-position will help understand the formation of the segregation pattern. In the SOLID® simulation, the sample location in the ingot is covered by 9 mesh cells (see figure 5.8). The cells are delimited by the yellow box in the figures. The values of the different variables computed during the simulation were saved with a higher frequency in the 9 C-position cells to enable a detailed analysis of the local solidification conditions. The 9 cells forming the C-position in the SOLID® simulation can be seen in figure 5.8. Each cell is $5 \times 5 \text{cm}^2$. The width of the simulated C-position is thus larger than the 3D reconstruction presented in chapter 4 (9,5 cm in as-cast steel and 15 cm in simulation). In the simulation, the 3D reconstructed volume straddles 3 cells.
The solidification of the C-position is a long process. The 9 cells solidify from edge-side cells to centre-side cells. Three groups of cells can be observed: cells 1576 to 1574 (edge cells) solidify first, then 1503 to 1502 (middle cells), and finally 1430 to 1428 (centre cells) solidify last, as observed in figure 5.9. At this height in the ingot, the solidification happens mainly from the side of the ingot toward its centre, explaining the shift in time from one cell column to another. In large ingots, solidification times are long. At the C-position, the average simulated solidification time (from $g_l < 1$ to $g_l = 0$) was 20 038 s, i.e., 5 h 34 min. Cells located closer to the centre of the ingot take more time to solidify. In the C-position, as the cell columns get closer to the centre, it takes approximately one hour more to solidify than for the previous column. The solidification is not a linear process through time. At the C-position, the solidification of each cell group is shifted in time but kept the same evolution. For this reason, the graphs showing the evolution of parameters (with time, solid fraction or temperature) in this section are presented for only one cell: the cell N° 1502, located in the centre of the C-samples location in the *short* ingot.
Figure 5.10 shows the evolution of g_l in the C-position with time as the ingot solidifies. In figure 5.9, the time stops at the end of the ingot solidification. It can be seen that solidification starts early, but stagnates in form of a plateau for a long time before starting again. In figure 5.10, the different solidification steps are marked with vertical lines.

1. The first vertical green line marks the appearance of solid in form of moving equiaxed grains in the cell (time = 5 810 s). The grains move in and out of the cell and the g_l evolution with time is erratic (not visible in the figure due to very small variations).

2. The liquid fraction drops abruptly because more equiaxed grains arrive and pack. At this point in time the plateau starts. During the plateau the liquid fraction varies only very little and stays at around 0.9 and the temperature is constant (1522 °C). Solidification does not progress during the whole plateau period, which can last for several hours (average at the C-position: 2 h 55 min). In the C-position, the plateau represents approximately half of the solidification time. All C-position cells start the plateau at approximately the same time (1 h 40 min after the beginning of the

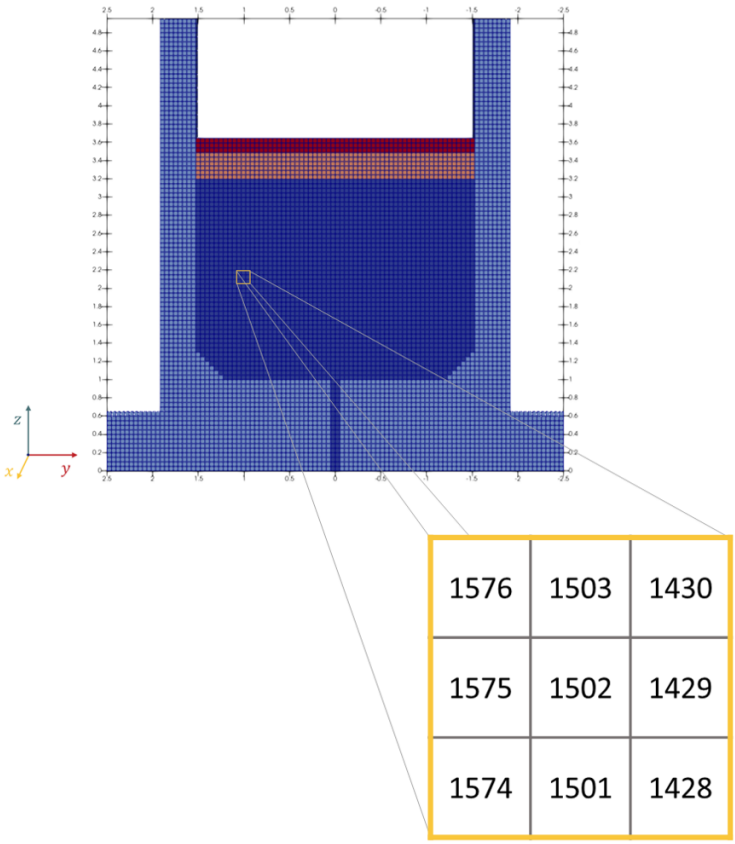

Figure 5.8: Cells belonging to the C-position representation.

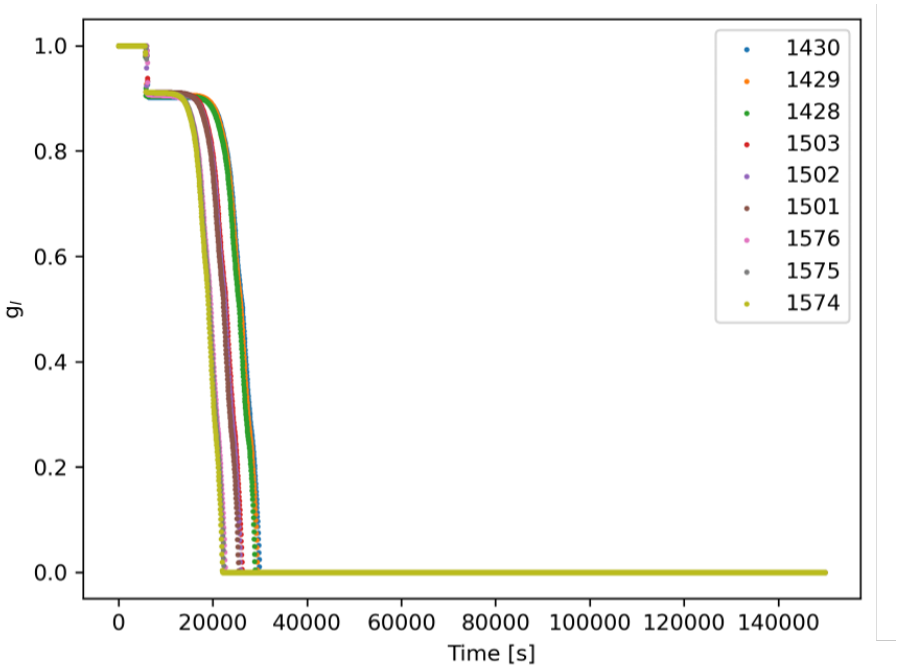

Figure 5.9: Evolution of g_l with time for the 9 cells of the C-position.

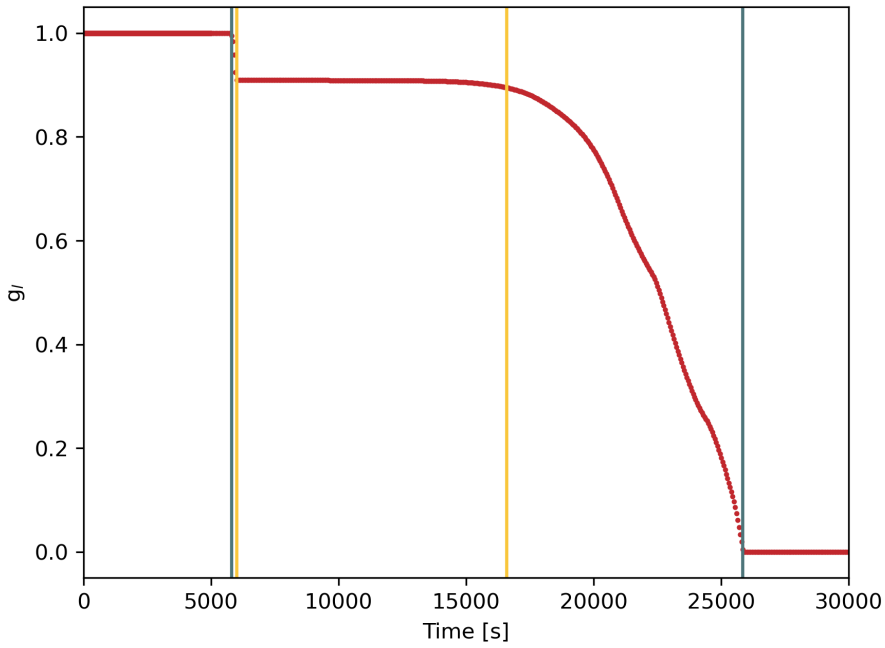

Figure 5.10: Zoom on the evolution of g_l with time in the cell 1502.

simulation). The plateau is longer for cells closer to the ingot centre. In figure 5.10, the plateau is delimited with vertical yellow lines: the first line marks the packing of equiaxed grains and is at 6 000 s and the second line marks $g_l = 0,90$ at 16 600 s.

3. Once $g_l < 0,90$ the plateau is considered to be over. The solidification speeds up and g_l reaches 0 at around 8 h 20 min of solidification. The end of the solidification for cell 1502 is indicated with a green vertical line (time = 25 850 s).

The temperature field is a key parameter of solidification. With figure 5.7, the evolution of the temperature field can be compared to the evolution of volume liquid fraction in cell 1502. Figure 5.7a shows the temperature field when the first solid grains appear in cell 1502. During the solidification plateau in cell 1502, the temperature field looks as shown in figure 5.7c, in this figure, the C-position belongs to a large isothermal area in the ingot, the temperature of the cell is constant for 2h45. The next figure (5.7e), shows the temperature field as the plateau is over and the solidification rate for cell 1502 increases. We can see the cell being crossed by the thermal front (the zone of steep temperature gradient): the solidification follows the temperature decrease. Finally, the temperature field after full solidification of cell 1502 is in figure 5.7h and the cell is fully in a colder area of the ingot. The observation of the average C concentration in the cells also gives information on the local solidification. In figure 5.11, the lines indicating the different solidification steps were kept to help the analysis. Before the plateau (vertical green line, T = 6000 s), the composition increases as a result of the surrounding solidification and enriched liquid flow. When solid grains arrive in the cells and pack, they flush away the enriched liquid and replace it with depleted solid: the average C composition drops abruptly and the solidification plateau starts. The composition is pretty stable during the

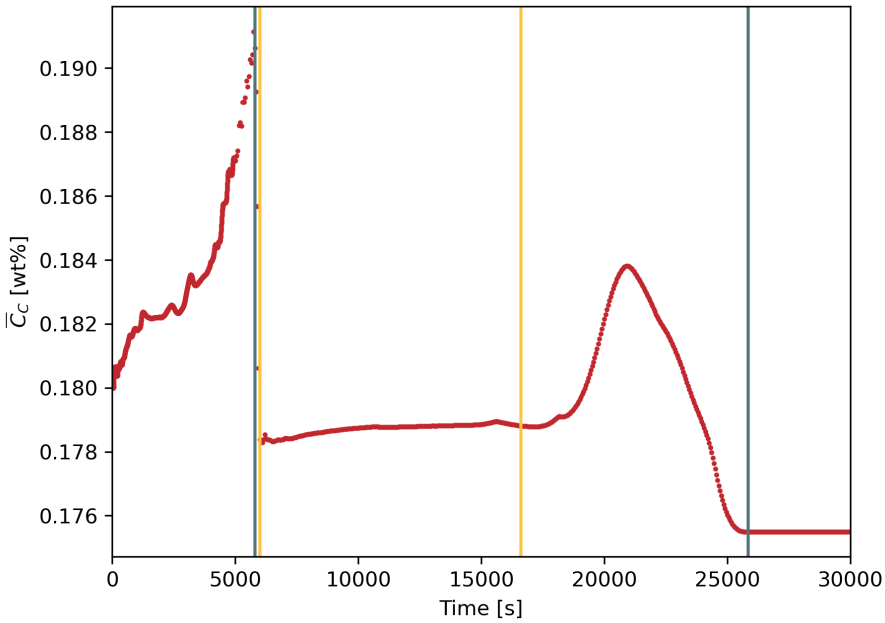

Figure 5.11: Evolution of average C composition with time in the cell 1502.

whole plateau. During the last step of solidification (large drop of g_l), the composition increases and then decreases. The evolution of thermal gradient and liquid flow directions can explain the composition evolution [1].
Before and during the solidification plateau, the thermal gradient does not evolve, the C-position is in an isothermal area of the ingot, where the temperature gradients are very small (see figure 5.7c). After 16 600 s, the temperature gradient increases, which also stops the plateau, because solidification accelerates. Figures 5.12a and 5.12b show the thermal gradient in y and z directions. The thermal gradient in the C-position is mainly lateral (in the y direction).
The liquid velocities are presented in figures 5.12c and 5.12d. The liquid flow velocities in the C-position are small (between 10^5 and 10^4 m/s), however, the orientation of the liquid flow relative to the thermal gradient creates segregations. The flow velocity is such that during the solidification time the liquid travels a distance of the order of the size of the samples taken in the C-position, i.e., 10 cm.

[1] Two different simulations were used in this PhD work, the results. The second simulation was run with tighter convergence criteria for the liquid velocity and temperature calcultations.

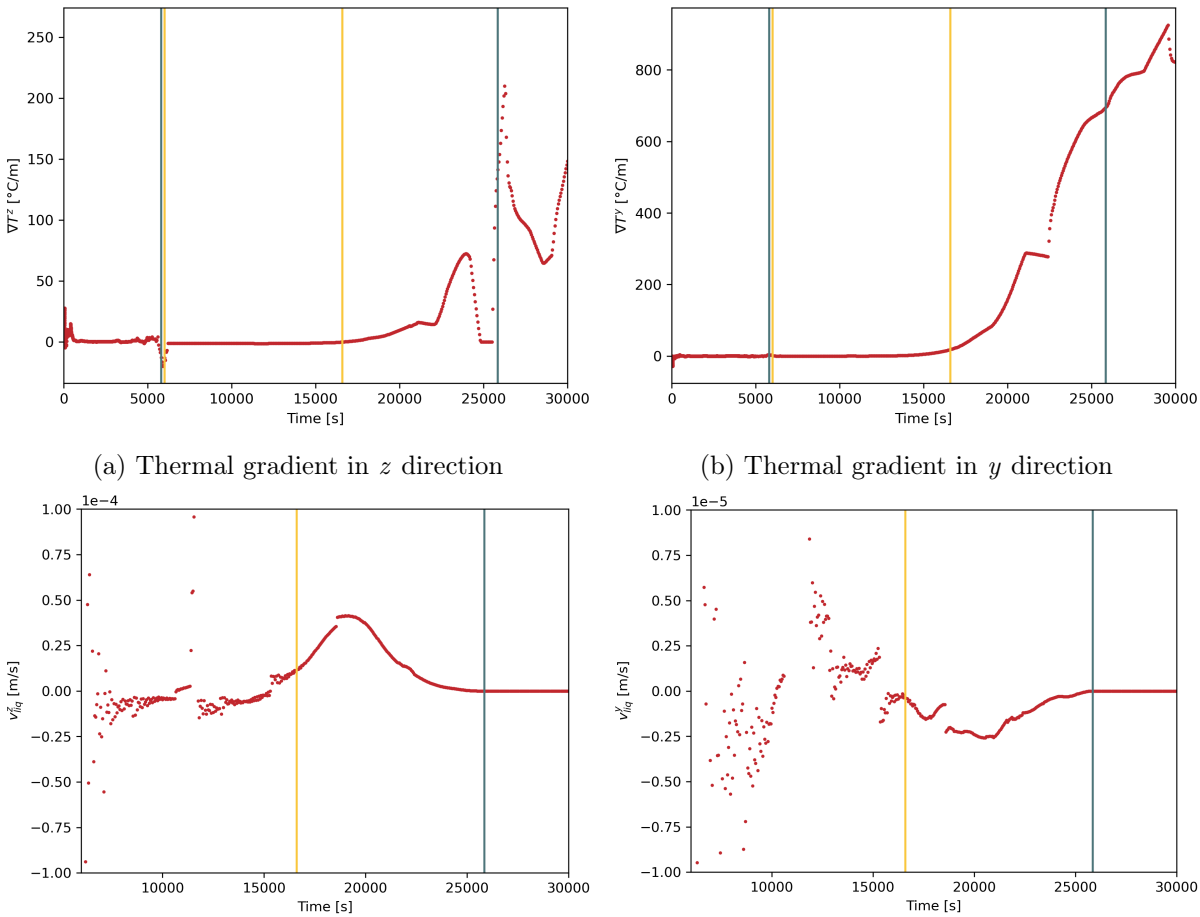

(a) Thermal gradient in z direction

(b) Thermal gradient in y direction

(c) Liquid velocity in z direction

(d) Liquid velocity in y direction

Figure 5.12: Comparision of thermal gradient and liquid flow directions. *NB.* The liquid velocity graphs start on the solidification plateau, at time $t = 6000$ s. Different ordinate axis scales are used for y and z components, both for ∇T (a-b) and liquid velocity (c-d).

5.4 Conclusion

This chapter use Solid® simulations to understand the solidification conditions of the short ingot. In previous chapter (3 and 4), *short* ingot's segregation were studied in 3D. With simulation, we can understand in which circumstance the segregations appear during solidification. Solid simulations provided an overview of the ingot's solidification, followed by an investigation of local solidification conditions at the C-position, where segregations were observed.
The simulation of the solidification of the *short* ingot indicates a long solidification time (41 h required to achieve full solidification). The solidification of the ingot occurs from the ingot's side and bottom toward the centre. During the solidification, macrosegregation forms because of fluid flow and solid transport. Grains move around in the liquid pool, and at some point, they get blocked in a coherent network. The packing of grains occurs progressively from bottom to top. In the packed areas, the grains remain stationary while the fluid flows through them. The relative orientation of the liquid to the thermal gradient causes segregation; even the slightest variation can lead to the formation of segregations. Solid® was also used to understand the solidification conditions that lead to the formation of channel segregates and intermediate-scale segregations. At the C-position a three steps solidification was observed:

1. Before the grains get blocked, the liquid flows and the solid moves freely. No segregation is caused.

2. The solidification plateau: the grains are blocked, but the temperature is constant and the solid fraction varies only very little. The plateau last several hours, during which the composition is steady, since the liquid flow and the thermal gradient very little, no segregation is formed.

3. The plateau comes to an end and the solid fraction increases. The thermal gradient and the liquid flow velocity change, and segregation are created.

Channel segregation and intermediate-scale segregation seem to occur when solidification speeds up after hours at a constant liquid fraction. To confirm this hypothesis, Solid® could be used to investigate the evolution of segregation criteria (Kumar's [2] or Flemings's [1]) with time, temperature, liquid and solid fractions. Suzuki's criterion, used to predict channel segregates, can be compared to Kumar's and Flemings's criteria, however Suzuki's criterion is to be calculated only at $g_s = 0.3$.

Chapter 6

Effects of the forging process on the segregations

> The doubt will always
> find you in the unexpected
> moments, sometimes even
> on a day that is going fine.
> But the doubt is never
> the enemy, just a reminder,
> to continue to push foward,
> with every breath
> and every moment in time.
>
> Courtney Peppernell,
> *Time will tell*

Contents

In the previous chapters, as-cast large ingots were investigated. Different segregation patterns were observed in different ingots. In large-scale ingots, such as the ones studied in this PhD work, the segregation cannot be erased or diminished by heat treatments. Hence, in forged parts made from large-scale ingots, the intermediate-scale segregation and macrosegregation patterns remain. The forging process changes the shape and distribution of segregagtion patterns. The mechanical properties of the final forged parts are affected by the presence of segregation. Therefore, it is crucial to understand how the forging process shapes and distributes segregation patterns.
In this chapter, we analyse the impact of the forging process on previously observed patterns of segregation. Different techniques and methods are combined to provide a better understanding of the segregation patterns that appear from channel segregates and intermediate-scale segregations after the forging process. First, samples were taken in a forged part and compared to as-cast samples. A second part of the work is based on forging simulations: segregation patterns observed in as-cast ingot and numerically forged. Finally, the experimental observations of forged material are compared to the result of the forging simulations on segregation patterns.
Figure 6.1 shows the forged part studied. This upset part was froged from an ingot analog to the *short* ingot. The samples in the forged part were taken at the L-position. The purple line represents the position of C-position in the *short* ingot after forging.

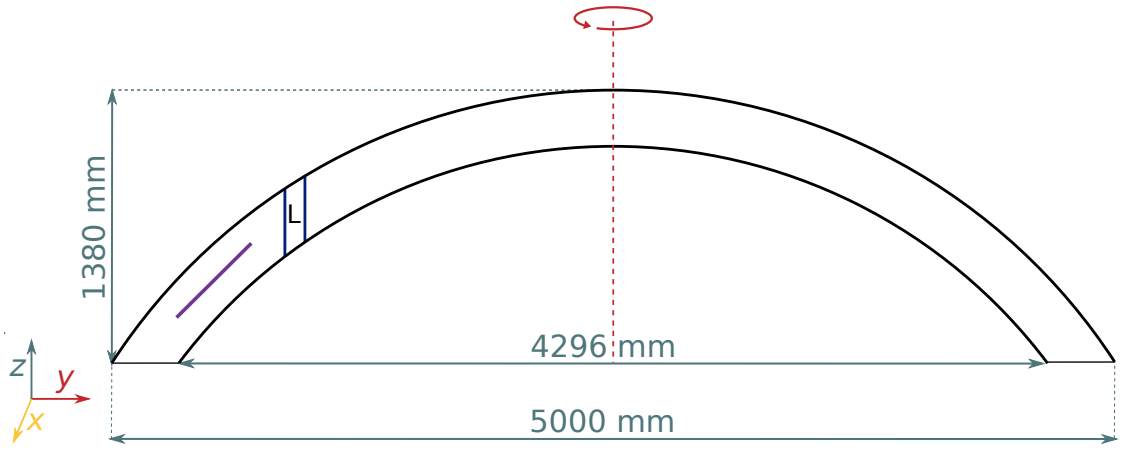

Figure 6.1: Schematic of the forged part

6.1 Forged part characterisation based on µXRF

The studied forged part is forged from a 116 t directionally solidified ingot, identical to the *short* ingot studied in this work. Four samples were taken in the L-position, in two different planes: samples were taken in the xz-direction and in the yz-direction. For each direction, 2 samples were taken, one just below the top surface of the forged part and another below the first one.
The samples were scanned with µXRF for chemical homogeneity investigation. The µXRF settings used were the same as the ones used on as-cast ingot samples (X-ray beam: Al-100 µm, 50 keV, 200 µA, with a 100 µm analysis step, and 45 ms of acquisition time per spectra). The scanning direction was changed compared to as-cast samples: for the forged part samples, the continuous scanning direction was the z-direction for the sample, indeed forged parts are known to have anisotropic segregation patterns and the vertical direction (z) is known to present bands of segregations [5].
Segregation ratio maps were computed based on µXRF results. The segregation ratio maps are presented in figure 6.2. The segregation ratio maps were processed with the Gaussian filter and threshold to isolate segregation patterns. The Gaussian filter used was smaller than the one used on the segregation maps obtained from as-cast samples: in the xz and yz directions, the forging process reduces the segregation patterns' sizes which get flattened in the z direction. The Gaussian filter size was reduced accordingly to the forging process undergone by the *short* ingot to become the forged part. A Gaussian filter with a 0.625 cm standard deviation and a 4σ size was used. The threshold was defined as the 95^{th} quantile of the segregation ratio distribution after the application of the Gaussian filter (same method as the one used on as-cast samples in chapter 3). The binary images obtained are presented in figure 6.3.
On the left side of the page, figure 6.3a shows the segregations ratio maps of samples taken in the xy-direction. The maps are quite homogenous: segregated areas exist but are evenly distributed on the samples. The primary solidification structure is no longer visible on the samples. Segregations appear as horizontal enriched areas. Their arrangement can be compared to segregation bands already described in literature [5–7]. The second pair of samples (figure 6.3b) confirms the observation of segregation bands. The samples taken in the yz-direction, are taken in the diameter of the forged part (the centre being on the right side of the page). In the upper part of the top sample, some larger segregation bands can be observed. In the upper part of the top sample, all segregation bands, small and large ones, are inclined toward the top of the forged part.
Table 6.1 records the measurements made on segregation bands identified with image processing on the binary images. The segregation bands observed are small segregation patterns. Some large segregation bands were observed (top part of top samples for both pairs), but small bands outnumber them. The average aspect ratio of the segregation ratio observed is equal to 0.6, which does not indicate strongly elongated shapes. The visual comparison of the binary images (6.3) with the original segregation maps (6.2), shows that the image processing made the segregation patterns more rounded than they appear in the segregation maps. The Gaussian filter is responsible for this smoothing of the segregation patterns, in as-cast samples, it was not an issue since the observed

Table 6.1: Measurements of the segregation bands observed in the forged part.

Segregation pattern	**Segregation bands *xz* and *yz* directions**
Number of 2D areas [1]	468
Average maximum Feret diameter [mm]	2.1
Average minimal Feret diameter [mm]	1.1
Aspect ratio [1]	0.6
Average area [mm²]	2.2

segregation patterns were rather round, but in the forged part the observed segregation patterns are elongated in the horizontal plane and get deformed by the Gaussian filter. The analysis of forged part samples produces binary images with deformed 2D segregation patterns. Based on observation carried out on as-cast material (chapter 4), it is safe to assume that 2D observation cannot provide a full description of the segregation patterns after forging. The distribution of segregations remains representative of reality, but their shape needs further investigations.

There are only a few studies in the literature that provide a comparison point for the study of segregation bands in large forged parts. Delattre [4] investigated a forged part made from a *hollow* ingot cast with 18MND5 steel. In his work, the segregation bands observed are 200 µm wide. The size of Delattre's segregation bands is comparable to the one observed on the Mo segregation maps in figure 6.2. However, the forged part is not the same, the ingot used is not the same and the forging process effect on segregation can be different. Without a better comparison point, simulation can help understand the effects of forging on the segregation in the ingot.

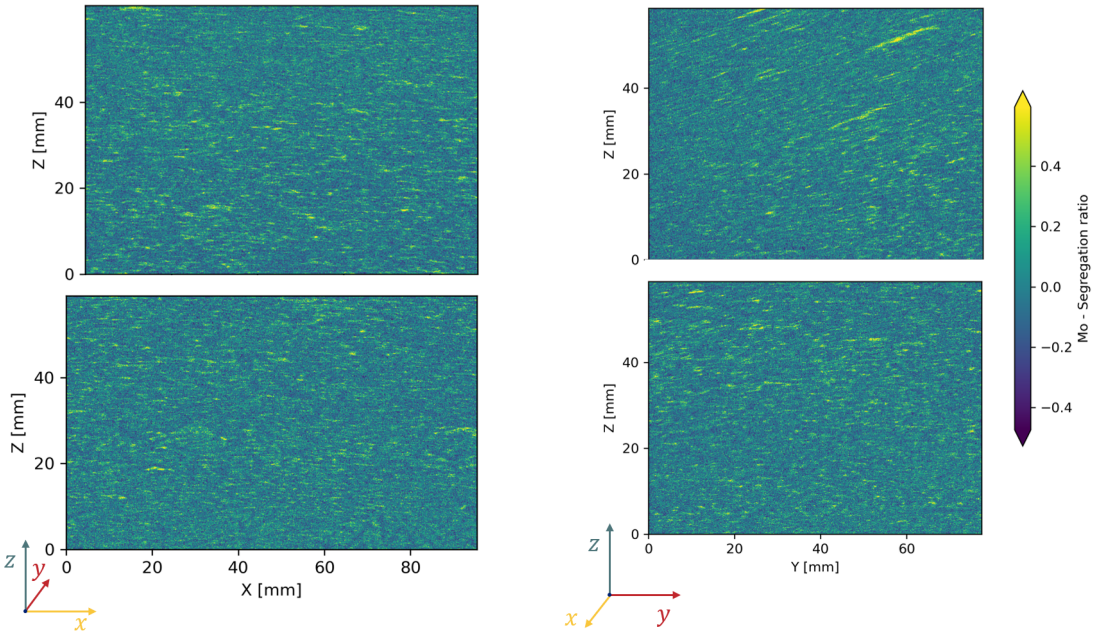

(a) Observation xz face

(b) Observation yz face

Figure 6.2: Mo segregation maps of samples taken from a forged part.

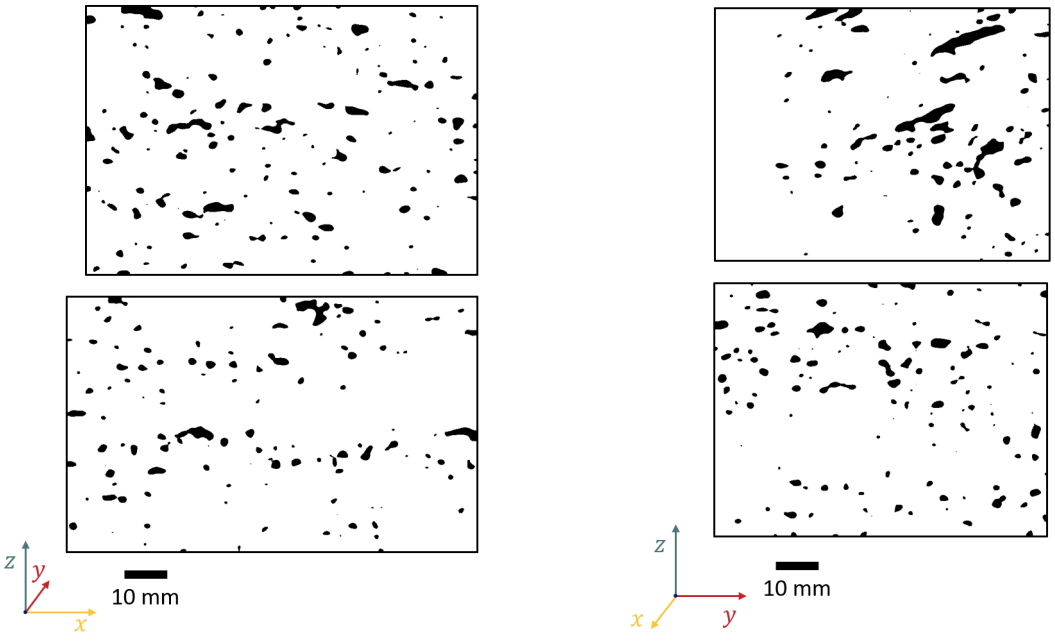

(a) Observation xz face

(b) Observation yz face

Figure 6.3: Binary images obtained after image treatment of the maps presented in figure 6.2.

6.2 Simulation of the forging process

Forge NxT® is a software used to simulate industrial forging processes. Forge NxT® is used by Framatome to simulate and investigate the forging steps of the different components implemented in civil nuclear power plans. For this study, Forge NxT® was used to study how forging affects the segregation patterns observed in as-cast material. The 3D segregation patterns reconstructed from 2D *xy* segregation maps in chapter 3 were implemented in Forge NxT®. The 3D segregation patterns were placed in the *short* ingot before forging and then Forge NxT® was used to simulate the forging process of the ingot to produce the forged part. The end position of forged segregation patterns in the forged part is marked with the purple line in figure 6.1. The simulations were realised by a Framatome team: Maxi Cadet, Nicolas Halot and Théo Picard.
In the numerical forged part, the 3D segregations patterns were deformed with the surroundings. The final aspect of the 3D segregation patterns in the simulation is presented in figures 6.4 and 6.5. Three simulations were carried out: one with the 3D channel segregates, one with the 3D intermediate-scale segregations and the last one that included both channel segregates and intermediate-scale segregations. The deformation of segregation patterns during the forging is important and creates complex shapes. This is why the analysis presented separates channel segregates from intermediate-scale segregation. Figure 6.4 shows the aspect of channel segregates after forging and figure 6.5 shows the intermediate-scale segregation after the forging process. A global observation of the forged segregation patterns indicates a major reduction in the z-direction that goes along with an augmentation in x and y-directions. In short: the segregation patterns get flattened in the z-direction.
The forged segregation patterns were sliced in two directions: to produce *xy* slices and *xz* slices. The slices of the forged segregation patterns make possible the comparison with the experimental observations of as-cast and forged steel. Table 6.2 summarises the main information about the section areas of the segregations observed on the slices. Examples of *xz* slices of the forged channel segregates are shown in figure 6.6 and figure 6.7 shows some *xz* slices of the forged intermediate-scale segregations.
The *xy* and *yz* slices show different segregation pattern shapes and sizes. The compression during forging is the most important in the z direction, *e.g.* the channel length is divided by 4 during the forging process. The forging process changes the aspect of segregation patterns: channel segregates are compressed in the z direction and appear shorter and also wider, their average area on *xy* slices is multiplied by 9 during the forging process. On the *yz* slices, the aspect ratio of the channels segregates is small: the channel segregates vertical cross-sections are elongated ellipsoidal shapes. The forged intermediate-scale segregations show the same difference between *xy* and *yz* slices: the cross-section areas are greater on *xy* slices than on *yz* slices and the aspect ratio of the intermediate-scale segregations vertical cross-section is low (equal to 0.2), meaning in the *yz* plan, the intermediate-scale segregations are elongated ellipsoids.
After the forging process, the channels segregates are larger than the intermediate-scale (the 2D *xy* channel area after forging is 5 times larger than the intermediate-scale segregation area in the same plan). The size difference was already noticeable before the forging

(a) View from the xz face

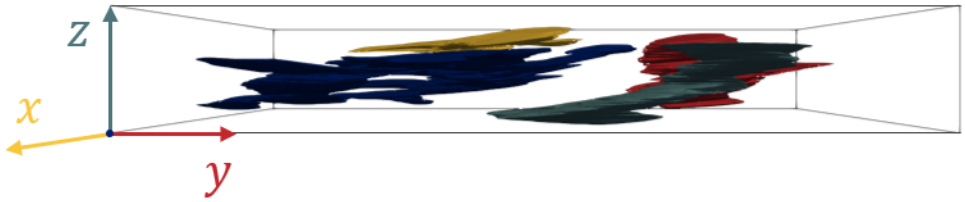

(b) View from the yz face

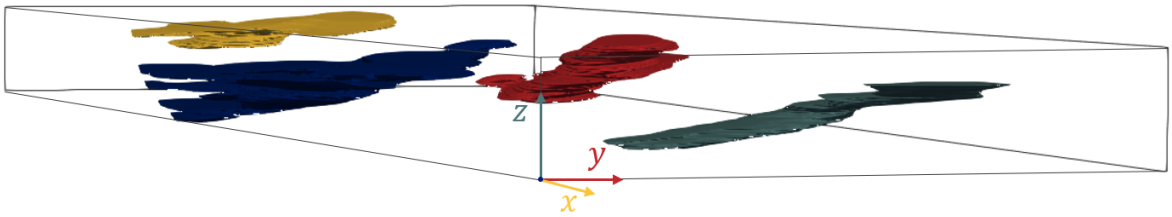

(c) Perspective

Figure 6.4: Observation of the reconstructed channels segregates (see chapter 4) after forging simulation. The observed volume is $346 \times 146 \times 22$ mm^3.

Table 6.2: Measurements of the segregation patterns after the simulation of the forging process.

Segregation pattern	**Channel segregates**		**Intermediate-scale segregations**	
Observation direction	***xy***	***yz***	***xy***	***yz***
Number of 2D areas [1]	115	87	382	242
Average maximum Feret diameter [mm]	37.1	27.4	14.1	11.4
Average minimal Feret diameter [mm]	18.1	3.3	8.1	1.7
Aspect ratio [1]	0.5	0.1	0.6	0.2
Average area [mm²]	554	62	110	15

process. Visually, the intermediate-scale segregations are elongated ellipses, perpendicular to the z-direction (the direction with the higher compression rate). The channel segregates orientation after forging is not so obvious, the channel segreates are highly deformed by the forging process. Depending on the sampling, the 2D yz observation of channel segregates can show elongated ellipses, similar to large intermediate-scale segregations 2D yz observation.

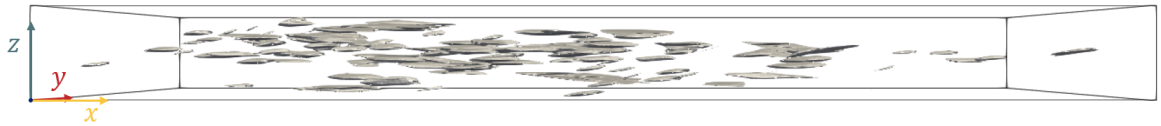

(a) View from the xz face

(b) View from the yz face

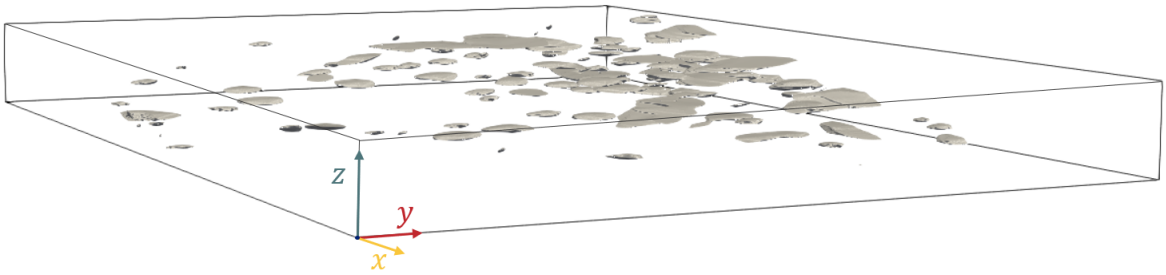

(c) Perspective

Figure 6.5: Observation of the intermediate-scale segregation (see chapter 4) after forging simulation.The observed volume is $365 \times 268 \times 31$ mm^3.

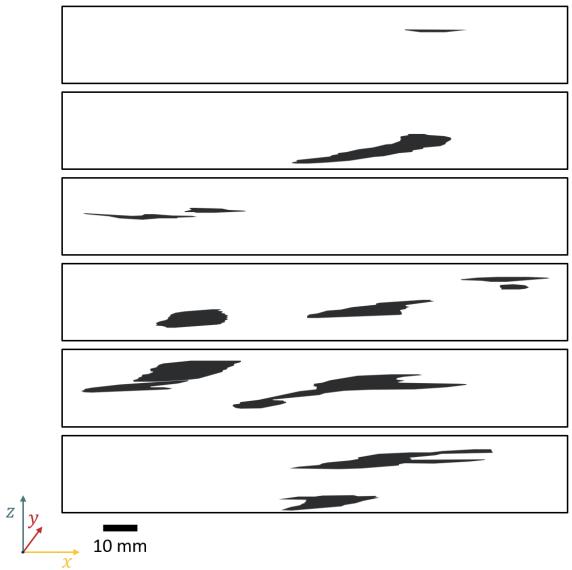

Figure 6.6: Slices of the numerically forged channel segregates observed in the xz-direction.

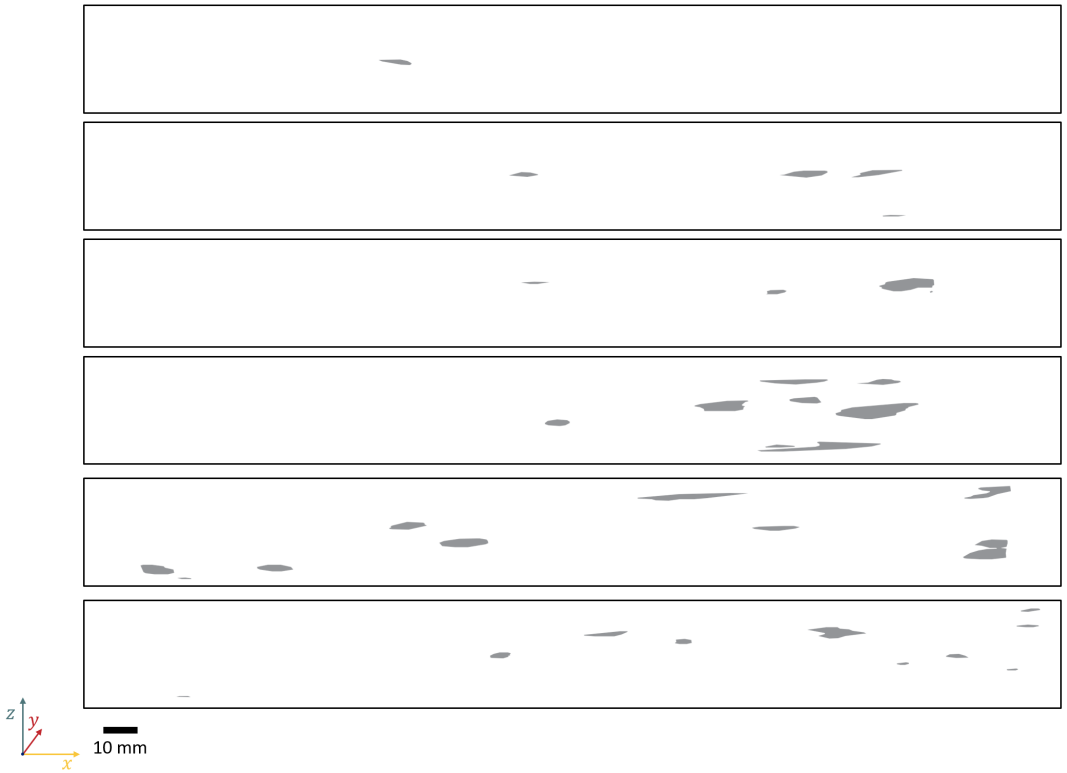

Figure 6.7: Slices of the numerically forged intermediate-scale segregations observed in the xz-direction.

6.3 Experimental and simulation results comparison

The characterisation of the forged part presented in section 6.1 can be compared to the segregations patterns observed in the *short* ingot and forged numerically with Forge NxT®. Slices were done in the numerically forged segregation patterns. Some slices have the same orientation as some samples taken in the forged part.
Figure 6.9 can be used for a direct comparison of the shape and distribution of segregation patterns in the real forged part with the forged segregation patterns. The slices of the forged segregation patterns are scaled to the µXRF segregation maps. The binary images obtained from the µXRF segregation maps forged should be handed with care since the Gaussian filter change the shape of the segregations paterns.
The observed sergegation bands, on the forged parts, are thinner and shorter than was is observed on the slices of the segregation patterns after forging simulations. The comparison of the tables 6.1 and table 6.2 supports this observations. The sizes of the observed segregations in the forged parts are one order of magnitude smaller than the one from the forging simulation, both for channel segregates and intermediate-scale segregations.
This change in shape and size can be explained by a certain homogeneisation during forging. Diffusion and solid phase transformation can contribute to the homogeneisation during forging that will cause the observed segregation to be thinner and shorter than the one simualted. In the simulated forging process, neither the diffusion nor the phase transformation are considered. Segregations patterns are also considered to be an unbreakable object in the steel. However, in reality during the forging process, the ingot faces high temperatures. The forging process requires a fully austenitic structure: the steel is heated up in the austenitic range and stays at high temperatures (900-1200 °C) for a long time (several hours). In this range of temperature and time, the Mo-diffusion length can go up to 4 µm [96]. However the segregation banding observed in the forged part is hunderds of micrometres: atomic diffusion alone cannot homogenise such distances.
However the segregation homogeneisation occurs to a certain extend during forging. Figure 6.8 compares the µXRF data of maps taken in the forged part (maps in the yz direction) with C3 samples taken in the yz direction in the as-cast short ingot (see chapter 4). The density plot of the forged part samples data set is thinner and more centred than the density plot of the as-cast material data set: this observation confirms the segregation homogenisation during the forging process. Atomic diffusion cannot explain this homogeneisation, however it the solid phase transformation (austenitisation) might redistribute the solute and homogenise the steel during the forging.
Still, the segregation homogeneisation that occurs during forging is minimal as shown by the figure 6.8. The difference between the forged part samples and the segregations forging simulation could also be explained by other phenomena: an inadequate image processing used on segregation maps, the hypothesis used for the forging simualation (isotropic material properties, unbreakable segregation patterns), ...

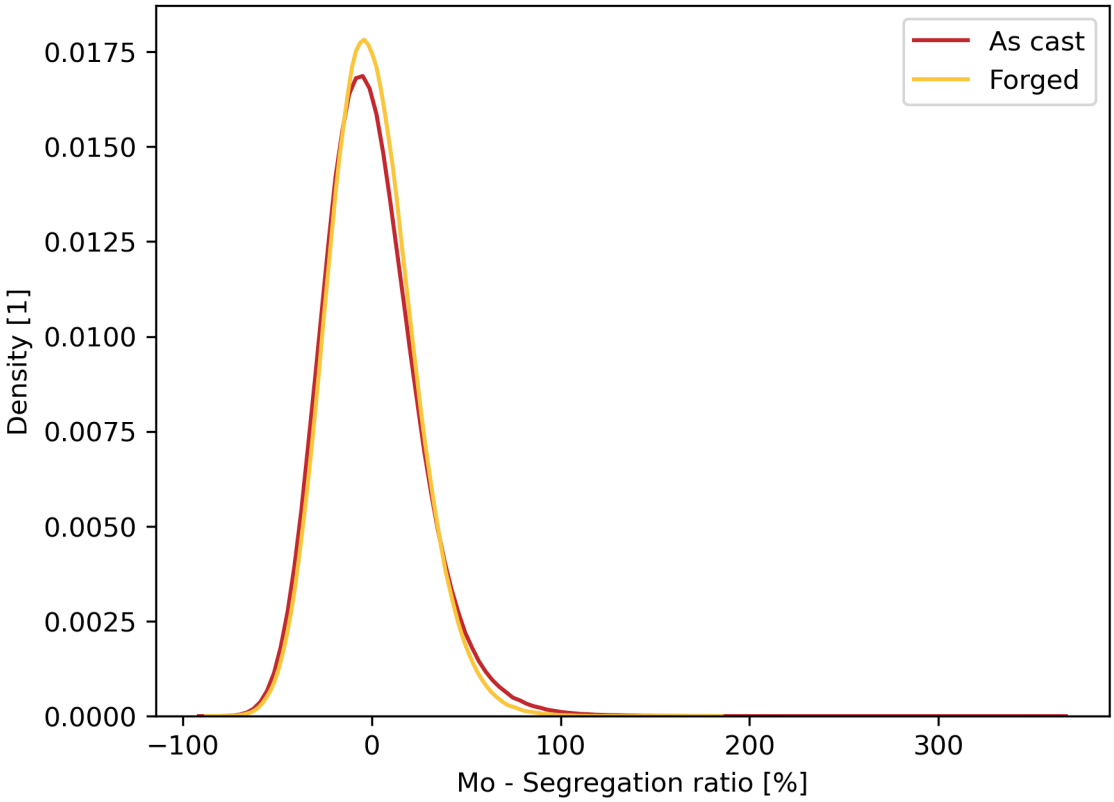

Figure 6.8: Comparision of µXRF data forged part samples against as-cast samples.

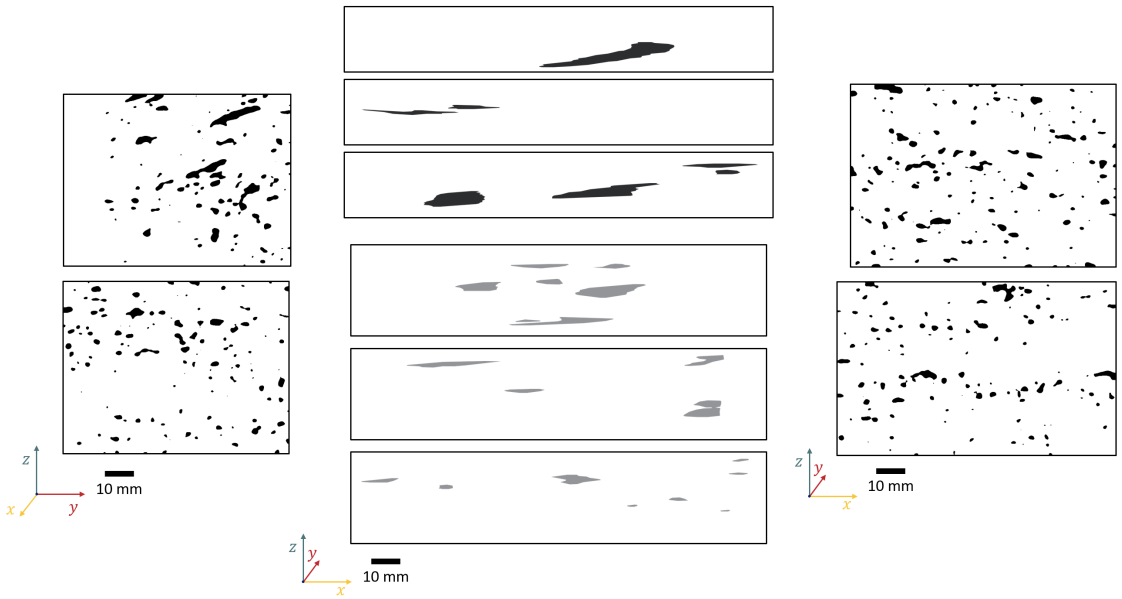

Figure 6.9: Forged channel segregates slices (in black), forged intermediate-scale segregation (in grey) and µXRF segregation ratios maps obtained from samples taken on the forged part.

6.4 Conclusion

In this chapter, two different approaches were used to study the effects of forging on segregation patterns observed in as-cast ingots. Both approaches comes with limitations. First, samples were taken in the forged part and analysed with µXRF. The obtained segregation maps were processed with an image process similar to the one used in chapter 3 to identify segregation patterns on 2D segregation maps. However, the image processing chosen is not adapted to the observation and characterisation of ellipsoidal shape segregation patterns: it distorts the segregation pattern shapes.
The second approach was to use a forging simulation software called Forge NxT® to simulate how the forging of a *short* ingot into the desired part will affect the segregation pattern observed in 3D. The innovation was to use such precise experimental data of segregation patterns as input in the forging simulation. In 2018, Loucif and coworkers [3] modelled the deformation of A-type segregates during forging, however, the A-segregates were modelled as fibres and the forging process was simpler than the one model in the current study. The forging simulation studied in this PhD made it possible to observe the effects of a complex forging process on segregation patterns with a high level of precision. One of the limitations of this approach is that the diffusion of the elements during forging is not accounted for. Even if the forging duration is not long enough to reach full homogenisation, elements diffuse during the forging process and homogenise segregation to a certain extent.
The segregation patterns observed in this work are larger and thicker than the ones reported by Delattre in this PhD work [4] (he reports 200 µm thick segregations). However, the forging process in his work is different (the forged part is not the same), and the ingot shape is different too: the ingot used is hollow (identical to the one studied in chapter 4) and we know from chapter 4 that segregation patterns shape and size can vary with the ingot shape. The lack of comparable data restricts the extensive comprehension of the effects of forging on segregation patterns.
With the current work, we can conclude that forging affects the shape and to a small extent the intensity of the segregation pattern. During the forging process, the segregation patterns are deformed. After forging, cross-section observation of segregation reveals elongated ellipsoidal shapes. The segregation patterns observed could fit some description of segregation bands already described in literature [4–7]. However, the size of the segregation bands reported in the literature is smaller than the one measured in this work. The size difference can be linked to the forging ratio and segregation initial size.
Additional measurement on both as-cast and forged part could help to understand which segregation patterns can lead to segregation banding. This work opens a way on the use of a new way to investigate segregations at a centimetric scale in both as-cast and forged parts.

Conclusions and scope for future work

Ils ne se rendent pas compte, eux,
de combien ça ferait mal.
Ils ne savent pas, eux, qu'écrire,
que poser les mots, ça pèse lourd.
Qu'écrire, c'est graver, c'est faire exister,
c'est ne plus jamais pouvoir ignorer.

Serena Giuliano,
Ciao Bella

Conclusions

The nuclear industry needs reliable construction materials to build nuclear power plants. Hence the understanding of segregation patterns from solidification to forging is crucial for Framatome. This PhD work is part of a larger research project to understand the evolution of segregation patterns along the manufacturing of the pressure vessel parts.
There was little information available on the specific segregation patterns that cause banding segregation. This study aimed to address this gap by characterising segregation patterns on an intermediate scale in large ingots. By observing segregation patterns, we could better understand their formation and adjust industrial processes to reduce the severity or frequency of such patterns. Additionally, we must investigate how segregation behaves during the forging process. To this end, this PhD work focused on 5 main points.

- We developed a new methodology for segregation characterisation at the centimetric scale. We used the µXRF technique, which was adapted for segregation mapping on centimetric scale samples.
- Segregation patterns in a $110 \times 95 \times 145 mm^3$ volume were reconstructed in 3D. In our samples, we found two kinds of segregation patterns coexisting: channel segregates and intermediate-scale segregation.
- Three different large ingots (116, 170 and 173 tons) were compared.
- Solid® simulations were used to investigate both global and local solidification conditions leading to channel segregates and intermediate-scale segregation formation.
- The effects of forging on the segregation patterns were investigated with 2 different and complementary approaches: simulation of the forging process and experimental observation of forged material.

The µXRF-based characterisation methodology provides a fast and easy way to characterise centimetric scale samples with minimal sample preparation. This technique is also non-destructive, opening wide research possibilities. The segregations patterns can be characterised on large samples before other investigations, like mechanical testing. With µXRF a new investigation scale is now available: centimetric scale mapping with a resolution up to 20 µm is now a possibility for steel samples.
Thanks to µXRF we were able to study numerous samples and reconstruct the observed segregation patterns in 3D. In the reconstructed volume channel segregates and intermediate-scale segregation coexist. The 3D reconstructions gave a new point of view on segregation shape and highlighted how complex channel segregates' shape is. The channels were found to be sinuous, to merge and to present ramifications. This 3D observation - the first of its kind, to our knowledge - showed the limitation of 2D observations for segregation characterisation.
Channel segregates and possible intermediate-scale segregation were observed on samples taken in 3 different large ingots. In each ingot under study, channel segregates were observed in equiaxed dendritic grains' areas. Our study also showed the absence of intermediate-scale segregations in the equiaxed globular region of the *hollow* ingot. Taking into account the primary microstructure when trying to understand the segregations formation is crucial.
With Solid® simulations, we studied the solidification conditions leading to the formation of channel segregates and intermediate-scale segregations in the *short* ingot. Ingots similar to the *short* ingot under study take tens of hours to reach full solid state. During the solidification, grains block each other and stay motionless for hours without solidifying. This phenomenon was observed at the emplacement where channel segregates and intermediate-scale segregations were observed. During this solidification plateau, the local segregation does not evolve much. The segregations patterns are expected to form after the solidification plateau when the thermal gradient and the fluid flow change.
Our study also highlighted the difficulty in identifying the segregation patterns that lead to segregation banding in forged parts. The limited availability of comparative material (segregation mappings of forged parts, numerical forging of segregation patterns models) was an obstacle to a comprehensive understanding. However, we show a new way to investigate the effects of forging on segregation patterns with paired investigations: experimental observations, before and after forging, together with forging simulations.

Possible future investigations

The work conducted in this PhD highlighted gaps in the scientific knowledge on solidification and led to the development of tools making new investigations possible. Here are some suggestions for future investigations:

- *A detailed investigation on intermediate-scale segregation patterns*: with this PhD work, the use of µXRF for segregation characterisation was validated. The use of µXRF gives the possibility to investigate samples on the intermediate scale. A 3D characterisation of intermediate-scale segregation is crucial to understand their formation and their behaviour during forging.

- *A criterion to distinguish channel segregates and intermediate-scale segregation in 2D cuts* would also be a great help for the industry. Nowadays, the presence of channel segregates is assessed with 2D samples, however, this PhD work showed the limitations of 2D

sampling for segregation characterisation. With a larger segregation map database, the distinction between intermediate-scale segregations and channel segregates could become easier. To help this categorisation, *geostatics* could be used. Already used in the mining industry, geostratics can help to understand and measure the scale of patterns observed on maps. Geostatistics can be used for segregation characterisation (distinction between the segregation scales), or even secondary dendritic arms spacing (SDAS). For SDAS, such tools would suppress the bias linked to the operator in manual SDAS measurements.

- *Link between segregation patterns and primary solidification structures on the intermediate scale* is also an interesting point to look at. In this work, we showed channel segregation and intermediate-scale segregation on samples with an equiaxed dendritic microstructure. A precise characterisation of the primary microstructure coupled with a segregation characterisation would help to understand the relations between the dendritic or globular grains, as well as intermediate-scale segregations and channel segregates formation.

- *Criteria for channel segregates and/or intermediate-scale segregation* should be studied. In this work, channel segregates were observed in an equaixed dendritic area, yet most of the existing criteria assume a columnar surrounding. Therefore we can ask ourselves if the existing criteria can predict the observed channel segregates. The criteria could be investigated during the solidification with SOLID®, it could also help to understand when exactely during solidification channel segregates and intermediate-scale segregation are formed.

- *New set of criteria for channel segregates and/or intermediate-scale segregation* could be imagined in case the existing ones fail to predict our experiemental observations. We can imagine a set of criteria: depending on the type of segregation pattern to predict (channel segregates or intermediate-scale segregations) and the local primary microstructure under formation during the solidification (columnar, equiaxed globular or equiaxed dendritic grains).

- *A deeper and wider investigation of the effect of forging on segregation patterns* is still needed. This PhD showed the way to a new insight into the process investigations with a combination of simulation and experimental observations to understand how the forging process affects the segregation patterns. A comprehensive understanding of these issues requires deeper investigation. Laboratory experiments could be designed to investigate the effect of the forging ratio on different segregation patterns. Forging is a high-temperature elong procedure, hence the diffusion of the elements during forging should also be studied.

References

[1] R Mehrabian, M Keane, and MC Flemings. "Interdendritic fluid flow and macrosegregation; influence of gravity". In: *Metallurgical and Materials Transactions B* 1.5 (1970), pp. 1209–1220.

[2] Alok Kumar, Miha Založnik, Hervé Combeau, Gérard Lesoult, and Arvind Kumar. "Channel segregation during columnar solidification: Relation between mushy zone instability and mush permeability". In: *International Journal of Heat and Mass Transfer* 164 (2021), p. 120602.

[3] Abdelhalim Loucif, Emna Ben Fredj, Nathan Harris, Davood Shahriari, Mohammad Jahazi, and Louis-Philippe Lapierre-Boire. "Evolution of A-type macrosegregation in large size steel ingot after multistep forging and heat treatment". In: *Metallurgical and Materials Transactions B* 49 (2018), pp. 1046–1055.

[4] Jean-Baptiste Delattre. "Etude du lien entre traitement thermique, propriétés mécaniques et amorćage de la rupture fragile par clivage d'un acier faiblement allié trempé revenue. [Manuscript submitted for publication]". PhD thesis. Université Paris sciences et lettres, 2024.

[5] EJ Pickering and HKDH Bhadeshia. "The consequences of macroscopic segregation on the transformation behavior of a pressure-vessel steel". In: *Journal of Pressure Vessel Technology* 136.3 (2014), p. 031403.

[6] Guanghua Yan, Lizhan Han, Chuanwei Li, Xiaomeng Luo, and Jianfeng Gu. "Effect of macrosegregation on the microstructure and mechanical properties of a pressure-vessel steel". In: *Metallurgical and Materials Transactions A* 48.7 (2017), pp. 3470–3481.

[7] Teruo Yamashita, Shiro Torizuka, and Kotobu Nagai. "Effect of manganese segregation on fine-grained ferrite structure in low-carbon steel slabs". In: *ISIJ international* 43.11 (2003), pp. 1833–1841.

[8] Jonathan A Dantzig and Michel Rappaz. *Solidification*. EPFL Press, 2009.

[9] Hervé Combeau and Lounès Tadrist. *Les changements de phase solide-liquide-vapeur, tome 2*. CNRS Editions, 2016.

[10] G Lesoult. "Solidification. Macrostructures et qualité des produits". In: *Techniques de l'ingénieur. Matériaux métalliques* M59 (1989), pp. M59–1.

[11] Gérard Lesoult. *Thermodynamique des matériaux: de l'élaboration des matériaux à la genèse des microstructures*. Vol. 5. PPUR Presses polytechniques, 2010.

[12] Wilfried Kurz, David J Fisher, and Michel Rappaz. *Fundamentals of Solidification 5th Edition*. Trans Tech Publ, 2023.

[13] John Campbell. *Complete casting handbook: metal casting processes, metallurgy, techniques and design*. Butterworth-Heinemann, 2015.

[14] G Lesoult. "Solidification. Cristallisation et microstructures". In: *Techniques de l'ingénieur. Matériaux métalliques* M58 (1986), pp. M58–1.

[15] George Krauss. "Solidification, segregation, and banding in carbon and alloy steels". In: *Metallurgical and Materials Transactions B* 34.6 (2003), pp. 781–792.

[16] G Lesoult. "Macrosegregation in cast steel: historical considerations on products, casting processes, and segregation models". In: *Solidification Science and Technology–Proceedings of the John Hunt International Symposium*. 2011, pp. 269–292.

[17] J Pisseloup, I Poitrault, JP Badeau, and P Bocquet. "Adaptation du type et de la géométrie du lingot à la fabrication de grosses pièces forgées. Conséquences au niveau de la ségrégation". In: *Mémoires et études scientifiques de la revue de métallurgie* 83.4 (1986), pp. 191–199.

[18] Julien Zollinger. "Influence de l'oxygène sur le comportement à la solidification d'aluminiures de titane binaires et alliés au niobium basés sur le composé intermétallique γ-TiAl". PhD thesis. Institut National Polytechnique de Lorraine, 2008.

[19] A Ludwig, M Wu, and A Kharicha. "On macrosegregation". In: *Metallurgical and Materials Transactions A* 46.11 (2015), pp. 4854–4867.

[20] EJ Pickering. "Macrosegregation in steel ingots: the applicability of modelling and characterisation techniques". In: *ISIJ international* 53.6 (2013), pp. 935–949.

[21] J Comon and P Bastien. "Etude expérimentale des relations entre la solidification et les hétérogénéités de lingots d'acier de 3 à 30 tonnes". In: *Revue de Métallurgie* 65.1 (1968), pp. 13–23.

[22] G Lesoult. "Macrosegregation in steel strands and ingots: Characterisation, formation and consequences". In: *Materials Science and Engineering: A* 413 (2005), pp. 19–29.

[23] MC Flemings. "Principles of control of soundness and homogeneity of large ingots". In: (1976).

[24] J Comon, J Delorme, and P Bastien. "Hétérogénéité des gros lingots de forge. Étude de l'influence des impuretés et des éléments d'alliage sur la ségrégation". In: *Revue de Métallurgie* 70.4 (1973), pp. 251–258.

[25] MC Flemings and GE Nereo. "Macrosegregation Part I". In: *Trans. Met. Soc. AIME* 239.9 (1967), pp. 1449–1461.

[26] K A Jackson, J D Hunt, D R Uhlmann, and T P Seward. "On Origin of Equiaxed Zone in Castings". In: *Transactions of the Metallurgical Society of Aime* 236.2 (1966), pp. 149–158.

[27] H. Neumann-Heyme, K. Eckert, and C. Beckermann. "Dendrite fragmentation in alloy solidification due to sidearm pinch-off". In: *Phys. Rev. E* 92 (6 2015), p. 060401.

[28] F Roch, H Combeau, I Poitrault, J Ch Chevrier, and G Lesoult. "Numerical model for prediction of chemical-type segregation in heavy steel ingots". In: *IISC. The Sixth International Iron and Steel Congress*. Vol. 1. 1990, pp. 665–672.

[29] RJ McDonald and JD Hunt. "Convective fluid motion within the interdendritic liquid of a casting". In: *MT* 1.6 (1970), pp. 1787–1788.

[30] Anthony F Giamei and BH Kear. "On the nature of freckles in nickel base superalloys". In: *Metallurgical Transactions* 1 (1970), pp. 2185–2192.

[31] Z. Chen, D. Senk, and F. Firsbach. "Experimental Investigations on Solidification of 500-kg Steel Ingots with Laboratory Trials". In: *Metallurgical and Materials Transactions B* 49.5 (2018), pp. 2514–2532.

[32] MC Flemings. "Solidification processing". In: *Metallurgical transactions* 5.10 (1974), pp. 2121–2134.

[33] MC Flemings, R Mehrabian, and GE Nereo. "Macrosegregation Part II". In: *Trans. Met. Soc. AIME* 242 (1968), pp. 41–49.

[34] MC Flemings and GE Nereo. "Macrosegregation Part III". In: *Trans. Met. Soc. AIME* 242 (1968), pp. 50–55.

[35] Menghuai Wu, Andreas Ludwig, and Abdellah Kharicha. "Simulation of As-Cast Steel Ingots". In: *steel research international* 89.1 (2018), p. 1700037.

[36] Nicolas Leriche, Hervé Combeau, Ch-A Gandin, and M Založnik. "Modelling of columnar-to-equiaxed and equiaxed-to-columnar transitions in ingots using a multiphase model". In: *IOP Conference Series: Materials Science and Engineering*. Vol. 84. 1. IOP Publishing. 2015, p. 012087.

[37] Thi-Thuy-My Nguyen, Charles-André Gandin, Hervé Combeau, Miha Založnik, and Michel Bellet. "Finite Element Multi-scale Modeling of Chemical Segregation in Steel Solidification Taking into Account the Transport of Equiaxed Grains". In: *Metallurgical and Materials Transactions A* 49.5 (2018), pp. 1725–1748.

[38] Benjamin Gerin, Hervé Combeau, Miha Založnik, Isabelle Poitrault, and Maya Cherif. "Prediction of solidification structures in a 9.8 tonne steel ingot". In: *IOP Conference Series: Materials Science and Engineering*. Vol. 861. 1. IOP Publishing. 2020, p. 012032.

[39] Knut Omdal Tveito, Akash Pakanati, Mohammed M'Hamdi, Hervé Combeau, and Miha Založnik. "A Simplified Three-Phase Model of Equiaxed Solidification for the Prediction of Microstructure and Macrosegregation in Castings". In: *Metallurgical and Materials Transactions A* 49.7 (2018), pp. 2778–2794.

[40] Hervé Combeau, Miha Založnik, Stéphane Hans, and Pierre Emmanuel Richy. "Prediction of macrosegregation in steel ingots: Influence of the motion and the morphology of equiaxed grains". In: *Metallurgical and materials transactions B* 40 (2009), pp. 289–304.

[41] Hervé Combeau, Miha Založnik, and Marie Bedel. "Predictive capabilities of multiphysics and multiscale models in modeling solidification of steel ingots and DC casting of aluminum". In: *Jom* 68.8 (2016), pp. 2198–2206.

[42] Miha Zaloznik and Hervé Combeau. "The influence of the morphology evolution of free-floating equiaxed grains on the macrosegregation in a 3.3-ton steel ingot". In: *Proceedings of MCWASP XII, TMS, The Minerals, Metals and Materials Society* (2009), pp. 165–172.

[43] Arvind Kumar, Bernard Dussoubs, Miha Založnik, and Hervé Combeau. "Effect of discretization of permeability term and mesh size on macro-and meso-segregation predictions". In: *Journal of Physics D: Applied Physics* 42.10 (2009), p. 105503.

[44] SM Copley, Anthony F Giamei, SM Johnson, and MF Hornbecker. "The origin of freckles in unidirectionally solidified castings". In: *Metallurgical transactions* 1 (1970), pp. 2193–2204.

[45] Koreaki SUZUKI and Kohzo TANIGUCHI. "The mechanism of reducing "a" segregates in steel ingots". In: *Transactions of the Iron and Steel Institute of Japan* 21.4 (1981), pp. 235–242.

[46] M Torabi Rad, Petr Kotas, and C Beckermann. "Rayleigh number criterion for formation of A-segregates in steel castings and ingots". In: *Metallurgical and Materials Transactions A* 44 (2013), pp. 4266–4281.

[47] C Beckermann, JP Gu, and William J Boettinger. "Development of a freckle predictor via Rayleigh number method for single-crystal nickel-base superalloy castings". In: *Metallurgical and materials transactions A* 31 (2000), pp. 2545–2557.

[48] JC Ramirez and C Beckermann. "Evaluation of a rayleigh-number-based freckle criterion for Pb-Sn alloys and Ni-base superalloys". In: *Metallurgical and Materials Transactions A* 34 (2003), pp. 1525–1536.

[49] EJ Pickering, SS Al-Bermani, and J Talamantes-Silva. "Application of criterion for A-segregation in steel ingots". In: *Materials Science and Technology* 31.11 (2015), pp. 1313–1319.

[50] M Simpson, M Yerebakan, and MC Flemings. "Influence of dendrite network defects on channel segregate growth". In: *Metallurgical Transactions A-Physical Metallurgy and Materials Science* 16 (1985).

[51] Miha Založnik and Hervé Combeau. "Thermosolutal flow in steel ingots and the formation of mesosegregates". In: *International Journal of Thermal Sciences* 49.9 (2010), pp. 1500–1509.

[52] RA Grange. "Effect of microstructural banding in steel". In: *Metallurgical Transactions* 2.2 (1971), pp. 417–426.

[53] John D Verhoeven. "A review of microsegregation induced banding phenomena in steels". In: *Journal of materials engineering and performance* 9.3 (2000), pp. 286–296.

[54] JS Kirkaldy, J von Destinon-Forstmann, and RJ Brigham. "Simulation of banding in steels". In: *Canadian Metallurgical Quarterly* 1.1 (1962), pp. 59–81.

[55] Ahmadreza Salimi, Hossein Monajati Zadeh, Mohammad Reza Toroghinejad, Davod Asefi, and Amir Ansaripour. "Influence of sample direction on the impact toughness of the api-x42 microalloyed steel with a banded structure". In: *Mater Tehnol* 47 (2013), pp. 385–389.

[56] Pierre Joly and F Roch. "Effets de la structure en bande sur la dispersion de résilience et de ténacité de produits épais pour enceintes sous pression, en acier faiblement allié type 18MND5". In: *Journées annuelles SF2M*. SF2M. 2019.

[57] Peter A Thornton and Vito J Colangelo. "Variation of mechanical properties in large steel forgings". In: *Metallurgical Transactions B* 7.3 (1976), p. 425.

[58] Jean POKORNY and T Annick POKORNY. "Métallographie". In: *Techniques de l'ingénieur. Matériaux métalliques* M90 (1994), pp. M90–2.

[59] Thierry Mazet. "Étude des structures de solidification et des ségregations dans les lingots d'acier". PhD thesis. Institut National Polytechnique de Lorraine, 1995.

[60] Ko MIYAMURA, Isamu TAGUCHI, and Hiromu SOGA. "New evaluation techniques of segregation in continuously cast steel". In: *Transactions of the Iron and Steel Institute of Japan* 24.11 (1984), pp. 883–890.

[61] Edward John Pickering. "Macrosegregation in Steel Ingots". PhD thesis. University of Cambridge, 2014.

[62] Markéta. Tkadlečková, Pavel Machovčák, Karel Gryc, Karel Michalek, Ladislav Socha, and Pavel klus. "Numerical modelling of macrosegregation in heavy steel ingot". In: *Archives of metallurgy and materials* 58.1 (2013).

[63] Pavel Machovčák, Aleš Opler, Zdeněk Carbol, Antonín Trefil, Karel Merta, J Zaoral, Markéta Tkadlečková, and Karel Michalek. "Evaluation of chemical heterogeneity of a 90-ton forging ingot". In: *Archives of Materials Science and Engineering* 58.1 (2012), pp. 22–27.

[64] Pavel Machovčák, Markéta Tkadlečková, Aleš Opler, Zdeněk Carbol, Antonín Trefil, and Karel Michalek. "The development of new type of 90 ton forging ingot". In: *Conference Proceedings: 23rd International Conference on Metallurgy and Materials, METAL*. 2014, pp. 72–80.

[65] C Maidorn and D Blind. "Solidification and segregation in heavy forging ingots". In: *Nuclear engineering and design* 84.2 (1985), pp. 285–296.

[66] Jun Li, Menghuai Wu, Andreas Ludwig, and Abdellah Kharicha. "Simulation of macrosegregation in a 2.45-ton steel ingot using a three-phase mixed columnar-equiaxed model". In: *International journal of heat and mass transfer* 72 (2014), pp. 668–679.

[67] EJ Pickering and M Holland. "Detection of macrosegregation in a large metallic specimen using XRF". In: *Ironmaking & Steelmaking* 41.7 (2014), pp. 493–499.

[68] Ed J Pickering, Connor Chesman, Sinan Al-Bermani, Melanie Holland, Peter Davies, and Jesus Talamantes-Silva. "A comprehensive case study of macrosegregation in a steel ingot". In: *Metallurgical and Materials Transactions B* 46.4 (2015), pp. 1860–1874.

[69] A Basso, Isaac Toda-Caraballo, D San-Martín, and FG Caballero. "Influence of cast part size on macro-and microsegregation patterns in a high carbon high silicon steel". In: *Journal of Materials Research and Technology* 9.3 (2020), pp. 3013–3025.

[70] Joydeep Sengupta, Jackie Leung, and Amir Noorafkan. "Calibration and Validation of X-Ray Fluorescence Technique for Mapping Centreline Segregation on Steel Slabs". In: *AISTech 2017 Proceedings* (2017), pp. 1925–38.

[71] Joydeep Sengupta and Amir Noorafkan. "Quantifying Slab Centerline Segregation: MXRF Eliminates Sample Preparation and Etching Procedures". In: *AISTech 2018 Proceedings* (2018), pp. 2637–49.

[72] Dongling Li, Xuejing Shen, Haiou Yang, Zong-xin Liu, Lei Zhao, and Haizhou Wang. "Quantitative distribution characterization of gradient composition of additive-manufactured stainless steel using micro-beam X-ray fluorescence". In: *Spectrochimica Acta Part B: Atomic Spectroscopy* 183 (2021), p. 106268.

[73] Sharhid Jabar, John A Siefert, Martin Strangwood, and Geoff D West. "The effect of micro-segregation on the quantification of microstructural parameters in grade 91 steel". In: *Metallurgical and Materials Transactions A* 52 (2021), pp. 426–437.

[74] Hui Wang, Chao Tang, Jinhui Du, Lei Zhao, and Haizhou Wang. "Characterization of the element distribution and quantitative segregation degree of nickel-based superalloy ingot". In: *At. Spectrosc* 43 (2022), pp. 423–429.

[75] S Béchet and L Beaujard. "Nouveau réactif pour la mise en évidence micrographique du grain austénitique des aciers trempés ou trempés-revenus". In: *Revue de métallurgie* 52.10 (1955), pp. 830–836.

[76] Marvin Gennesson, Dominique Daloz, Julien Zollinger, Bernard Rouat, Joëlle Demurger, and Hervé Combeau. "Effect of direct powder additions on the solidification structure and microsegregation of 42CrMo4 steel". In: *ISIJ international* 60.8 (2020), pp. 1693–1702.

[77] Nicolás E Tenaglia, Roberto E Boeri, Alejandro D Basso, and Juan M Massone. "Macro and microstructural characterisation of high Si cast steels–study of microsegregation patterns". In: *International Journal of Cast Metals Research* 30.2 (2017), pp. 103–111.

[78] Li Gao, Yohei Harada, and Shinji Kumai. "Visualization of solute distributions in dendritic and spheroidized Al grains characterized by both color etching method and electron probe microanalysis". In: *Journal of Materials Science* 49 (2014), pp. 1286–1296.

[79] Jingliang Wang, Rongtao Qian, Xiang Yang, Yong Zhong, and Chengjia Shang. "Effect of segregation on the microstructure and properties of a quenching and partitioning steel". In: *Materials Letters* 325 (2022), p. 132815.

[80] D Senk, E Erdem, and S Stratemeier. "Statistical analysis of EPMA results for numerical modelling of micro-segregation in steel". In: *International Journal of Cast Metals Research* 22.1-4 (2009), pp. 94–98.

[81] Denis Buisine and Gérard Perrat. "Soudage des matériaux des réacteurs nucléaires à eau préssurisée". In: *Techniques de l'ingénieur* 3732 (2016), pp. 1–18.

[82] *Pièces forgées en acier soudable pour chaudières et appareils à pression - Aciers alliés à haute limite d'élasticité - Nuances et qualités., NF A 36-603.* 1988. Normes Françaises.

[83] Marvin Gennesson. "Étude expérimentale de la mise en place des structures de solidification dans les lingots d'acier". PhD thesis. Université de Lorraine, 2018.

[84] George F Vander Voort. *Metallography, principles and practice.* ASM international, 1999.

[85] Cecile Fabre, Kimberly Trebus, Alexandre Tarantola, Jean Cauzid, Vincent Motto-Ros, and Panagiotis Voudouris. "Advances on microLIBS and microXRF mineralogical and elemental quantitative imaging". In: *Spectrochimica Acta Part B: Atomic Spectroscopy* 194 (2022), p. 106470.

[86] Vincente Armando Solé, Emmanuel Papillon, Marine Cotte, Ph Walter, and Jean Susini. "A multiplatform code for the analysis of energy-dispersive X-ray fluorescence spectra". In: *Spectrochimica Acta Part B: Atomic Spectroscopy* 62.1 (2007), pp. 63–68.

[87] M Ganesan, D Dye, and PD Lee. "A technique for characterizing microsegregation in multicomponent alloys and its application to single-crystal superalloy castings". In: *Metallurgical and Materials Transactions A* 36 (2005), pp. 2191–2204.

[88] Vincente Armando Solé, Emmanuel Papillon, Marine Cotte, Ph Walter, and Jean Susini. "A multiplatform code for the analysis of energy-dispersive X-ray fluorescence spectra". In: *Spectrochimica Acta Part B: Atomic Spectroscopy* 62.1 (2007), pp. 63–68.

[89] Michael Haschke. "Laboratory micro-X-ray fluorescence spectroscopy". In: *Cham: Springer International Publishing* 10 (2014), pp. 978–983.

[90] Koen HA Janssens, Freddy Adams, and Anders Rindby. *Microscopic X-ray fluorescence analysis.* Vol. 434. Wiley Chichester, 2000.

[91] Mathilde Alcaraz, Anouar Brahimi, Théotime Michez, Moussa Nana, and Alison Tonnelle. "Étude de la mise en place des structures de solidification et des ségrégations dans un lingot d'acier à destination de l'industrie nucléaire". PhD thesis. École des Mines de Nancy, 2021.

[92] Lucie Gutman, Jacob R Kennedy, François Roch, A Marceaux dit Clément, Lise Salsi, Jean Cauzid, Bernard Rouat, Hervé Combeau, Miha Založnik, and Julien Zollinger. "Characterisation of mesosegregations in large steel ingots". In: *IOP Conference Series: Materials Science and Engineering*. Vol. 1274. 1. IOP Publishing. 2023, p. 012049.

[93] Andriy Fedorov, Reinhard Beichel, Jayashree Kalpathy-Cramer, Julien Finet, Jean-Christophe Fillion-Robin, Sonia Pujol, Christian Bauer, Dominique Jennings, Fiona Fennessy, Milan Sonka, et al. "3D Slicer as an image computing platform for the Quantitative Imaging Network". In: *Magnetic resonance imaging* 30.9 (2012), pp. 1323–1341.

[94] H Yasuda, I Ohnaka, A Sugiyama, T Nagira, N Tsukihara, K Kawasaki, and K Umetani. "Time-resolved imaging of the microstructure evolution during dendritic solidification by using synchrotron radiation". In: *Modeling of Casting, Welding and Advanced Solidification Processes—XI* (2006), pp. 375–382.

[95] Laurent Heyvaert, Marie Bedel, Miha Založnik, and Hervé Combeau. "Modeling of the coupling of microstructure and macrosegregation in a direct chill cast Al-Cu billet". In: *Metallurgical and Materials Transactions A* 48 (2017), pp. 4713–4734.

[96] Jyrki Miettinen. "Calculation of solidification-related thermophysical properties for steels". In: *Metallurgical and materials transactions B* 28 (1997), pp. 281–297.

Understanding and optimising the formation of local chemical heterogeneities in large forging ingots used by the nuclear industry

Chemically segregated bands affect the mechanical properties of forged and hot-rolled steel. These bands seems to arise for the deformation of mesosegregations during forging or hot-rolling. While microsegregation (at the dendritic scale) and macrosegregation (at the ingot scale) are well understood, little is known about mesosegregation formation. Such intermediate scale segregations in large ingots have never been investigated. A precise characterisation is the first step towards understanding the formation and the behaviour of these segregations.
In this PhD, a new methodology for segregation chracterisation was developped. The methodology is based on the µXRF technique which was adapted for segregation mapping on centimetric scale samples. The µXRF-based characterisation methodology provides a fast and easy way to characterise centimetric scale samples with minimal sample preparation. This technique is also non-destructive, opening wide research possibilities.
With µXRF, segregation patterns in a $110 \times 95 \times 145 \text{mm}^3$ volume were reconstructed in 3D based on 2D sucessive segregations maps. In our samples, we found two kinds of segregation patterns coexisting: channel segregates and intermediate-scale segregation. The 3D reconstructions gave a new point of view on segregation shape and highlighted how complex channel segregates' shape is. The channels were found to be sinuous, to merge and to present ramifications. This 3D observation showed the limitation of 2D observations for segregation characterisation. µXRF was also used to investigate segregations at the centimetric scale in 3 different ingots. In each ingot under study, channel segregates were observed in equiaxed dendritic grains' areas.
To understand in which conditions such segregations patterns form. Solid® simulations were used to investigate both global and local solidification conditions leading to channel segregates and intermediate-scale segregation formation. The solidification of a 116 tons ingot was simulated. The full solidification of the ingto takes 41 hours. During the solidication, equiaxed grains can move in the liquid pool and get stuck in a coherent grains network. They can stay motionless for hours without solidifying. This phenomenon was observed at the emplacement where channel segregates and intermediate-scale segregations were observed. During this solidification plateau, the local segregation does not evolve much. The segregations patterns are expected to form after the solidification plateau when the thermal gradient and the fluid flow change.
Finally, the effects of forging on the segregation patterns were investigated with 2 different and complementary approaches: simulation of the forging process and experimental observation of forged material. µXRF was used to map sergegation on samples taken from a froged part and the 3D reconstruction of segregations patterns was numically forged to compare experimental observations with simulations of forging. The lack of comparative material is an obstacle to a fully understanding of the effects of forging on sergegations.

Compréhension et optimisation de la formation des hétérogénéités chimiques locales dans les gros lingots de forge utilisés par l'industrie nucléaire.

Les filets de ségrégations affectent les propriétés mécaniques de l'acier forgé et laminé à chaud. Ces filets semblent provenir de la déformation des mésoségrégations pendant les étapes de forgeage ou de laminage à chaud. Si la microségrégation (à l'échelle dendritique) et la macroségrégation (à l'échelle du lingot) sont bien comprises, on sait peu de choses sur la formation de la mésoségrégation. Ces ségrégations à l'échelle intermédiaire n'ont pas encore été étudiées dans les grands lingots. Afin de comprendre la formation et l'évolution de ces ségrégations, il est primordial de les caractériser avec précision.

Cette thèse développe une nouvelle approche pour la caractérisation des ségrégations. Cette approche est basée sur la µXRF qui offre un moyen rapide et facile de caractériser des échantillons de taille centimétrique, tout en nécessitant une préparation minimale de l'échantillon. Cette technique est également non destructive, ce qui ouvre de vastes possibilités de recherche.

Avec la µXRF, les ségrégations ont été reconstruites en 3D dans un volume de $110 \times 95 \times 145 \text{mm}^3$. Cette reconstruction est basée sur l'interpolation en 3D de ségrégations observées sur des échantillons centimétriques 2D. Dans le volume reconstruit, deux types de ségrégations coexistent: les canaux de ségrégation et les ségrégations d'échelle intermédiaire. La visualisation en 3D des canaux de ségrégation met en évidence la complexité de la forme des canaux: ils sont sinueux, fusionnent entre eux et certains sont ramifiés. Cette observation 3D montre également les limites de l'observation 2D pour la caractérisation des ségrégations. Les caractérisations 2D sont tout de même utilisés pour leur rapidité, elles permettent d'observer les ségrégations sur des échantillons issus de 3 lingots différents. Dans chaque lingot étudié, des canaux de ségrégations sont observés dans des zones de croissance équiaxe dendritique.

Afin de comprendre dans quelles conditions les ségrégations observées se sont formées, des simulations Solid® sont utilisées. Les conditions de solidification globales et locales d'un lingot de 116 tonnes sont étudiées. La solidification complète du lingot prend 41 heures, durant lesquelles les grains équiaxes bougent dans le puits liquide avant de s'immobiliser bloqués les uns par les autres. Ils peuvent alors rester immobiles pendant des heures sans se solidifier. Ce phénomène se produit à l'endroit où ont été observés les canaux de ségrégation et les ségrégations d'échelle intermédiaire ont été observées. Pendant ce plateau de solidification, la ségrégation locale n'évolue quasiment pas. Les ségrégations observées semblent se former en fin de solidification, lorsque le gradient thermique et l'écoulement du liquide changent.

Enfin, les effets du forgeage sur les ségrégations sont étudiés à l'aide de deux approches différentes et complémentaires: la caractérisation d'échantillons de matière forgée et la simulation du processus de forgeage sur les ségrégations précédemment reconstruites en 3D. La µXRF a été utilisée pour cartographier la ségrégation sur des échantillons prélevés sur une pièce forgée. Le manque de données auxquelles comparer nos résultats est un obstacle à la compréhension complète des effets du forgeage sur les ségrégations.